School of Science and Engineering
Department of Physics, Astronomy and Medical Radiation Sciences

Electron and Positron Scattering from Diatomic Molecules

Mark Christian Zammit

This thesis is presented for the Degree of
Doctor of Philosophy
of
Curtin University

June 2015

Declaration

To the best of my knowledge and belief this thesis contains no material previously published by any other person except where due acknowledgement has been made. This thesis contains no material which has been accepted for the award of any other degree or diploma in any university.

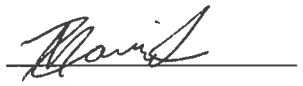

Mark Christian Zammit
26 June 2015

Summary

This thesis describes the development of the adiabatic-nuclei convergent close-coupling method and its application to electron and positron scattering from diatomic molecules. Here the method is applied to positron scattering from vibrationally excited molecular hydrogen H_2 and electron scattering from the vibrationally excited molecular hydrogen ion H_2^+ and its isotopologues (D_2^+, T_2^+, HD^+, HT^+ and TD^+).

Goals and objectives

The grand goal of this research project is to develop a general theoretical formulation and computer code that can accurately calculate electron- and positron-molecule collision data for all scattering processes at any arbitrary projectile-energy. This goal extends well beyond the time-frame of this thesis.

For this thesis the main objectives were to:

1. Develop theory and code for a single-centre convergent close-coupling approach to diatomic molecules within the adiabatic-nuclei approximation.

2. Rigorously test the developed method.

3. Demonstrate convergence in the close-coupling and projectile partial-wave expansions for electron scattering from H_2^+ and positron scattering from H_2.

4. Perform extensive comparison with existing theory and experimental results.

5. Provide accurate collision data for elastic scattering, ionisation and electronic and vibrational excitations.

Major results

1. Successfully extended the convergent close-coupling method to electron- and positron-molecule scattering.

2. For the first time, convergence is achieved in both the fixed-nuclei close-coupling (target state) and projectile partial-wave expansions of electron-molecule scattering calculations.

3. First accurate *ab initio* results presented over a broad energy-range for electron-impact dissociative excitation and dissociative ionisation cross sections of H_2^+ and its isotopologues as a function of the initial vibrational state.

4. First agreement with experiment for proton production and dissociative ionisation cross sections of electron scattering from vibrationally excited H_2^+ and its isotopologues over a broad energy-range.

5. First accurate *ab initio* results of positron-molecule scattering above the ionisation threshold.

6. Convergence is achieved for the first time in both the single-centre fixed-nuclei close-coupling (target state) and projectile partial-wave expansions of positron-molecule scattering calculations.

7. First *ab initio* grand total and total ionisation cross sections in good agreement with experiment over a broad energy range for positron scattering from H_2.

8. First accurate elastic scattering and electronic $X^1\Sigma_g^+ \rightarrow B^1\Sigma_u^+$ excitation cross sections are presented over a broad energy-range and are in good agreement with experiment.

9. First results of positron scattering from H_2 in the $v_i = 1$ vibrationally excited state.

Layout of the thesis

The layout of the thesis is as follows:

Chapter 1 introduces the concept of collision data and its application to industry and other sciences. The electron- and positron-molecule scattering field is summarised, concentrating on the successes and failures of other non-perturbative methods.

Chapter 2 describes the fundamental concepts of electron-molecule scattering, the connection between body- and lab-frames of reference and the approximations generally used in electron-molecule scattering. These approximations include the Born-Oppenheimer and adiabatic approximations. Adiabatic differential and integrated vibrational and electronic excitation cross sections are derived in terms of the partial-wave scattering amplitudes.

Chapter 3 details the formulation of molecular target states for H_2^+ and H_2 within the Born-Oppenheimer approximation. Single-centre Laguerre basis functions are used in a configuration interaction expansion to diagonalise the target Hamiltonian and construct electronic and vibrational target states. The molecular orbital (two-step diagonalisation) method is described. Comparisons are made with accurate structure calculations of H_2^+ and H_2.

Chapter 4 describes in detail the single-centre convergent close-coupling method and derives a solution of the momentum-space Lippmann-Schwinger equation via the K-matrix and T-matrix. The V-matrix elements are presented for electron/positron scattering from H_2^+ and positron scattering from H_2. The analytic Born subtraction method is formulated for orientationally averaged integrated cross sections.

Chapter 5 discusses application of the convergent close-coupling method to electron scattering from vibrationally excited H_2^+ and its isotopologues. Results are presented for dissociative excitation and dissociative ionisation cross sections as a function of the initial vibrational state of the molecular ions. Comparisons are made with other theory and experiment.

Chapter 6 describes application of the convergent close-coupling method to positron scattering from vibrationally excited H_2. Elastic, total ionisation, grand total, vibrational excitation and electronic excitation cross sections are presented. Elastic differential cross sections are also presented and comparisons are made with theory and experiment.

Chapter 7 summarises the work, results and conclusions of this thesis. Future research of this project is also outlined.

Equations are formulated primarily in the spherical coordinate system (r, θ, ϕ) and sometimes in the Cartesian coordinate (x, y, z) system. Atomic units are used throughout the thesis, for which Planck's constant $\hbar = 1$, a Bohr $a_0 = 1$, mass of an electron m_e =1 and electron charge e=-1.

List of Publications

During the candidacy of this PhD project (2011-2015) and the previous Honours year (2010-2011), fourteen manuscripts were published in refereed journals. Six of these publications emanate from the research presented in this thesis (electron- and positron-molecule scattering). Eight publications have resulted from research in the field of Debye plasmas, which was conducted in the previous Honours year and continued as a side project during the PhD. These manuscripts are listed in chronological order.

1. M. C. Zammit, D. V. Fursa, and I. Bray. Convergent calculations of positron scattering from molecular hydrogen. *J. Phys. Conf. Ser.* **635**, 012009 (2015).

2. R. Utamuratov, A. S. Kadyrov, D. V. Fursa, M. C. Zammit, and I. Bray. Two-centre close-coupling calculations of positron-molecular hydrogen scattering. *Phys. Rev. A* **92**, 032707 (2015).

3. S. Diallo, L. Gomis, I. G. Faye, M. S. Tall, I. Diedhiou, C. S. Diatta, and M. Zammit. Electron impact excitation of helium in Debye plasma. *Phys. Plasmas* **22**, 033517 (2015).

4. M. C. Zammit, D. V. Fursa, and I. Bray. Electron scattering from the molecular hydrogen ion and its isotopologues. *Phys. Rev. A* **90**, 022711 (2014).

5. B. Omar, M. A. Gonzalez, M. A. Gigosos, T. S. Ramazanov, M. C. Jelbuldina, K. N Dzhumagulova, M. C. Zammit, D. V. Fursa, and I. Bray. Spectral line shapes of He I line 3889 Angstroms. *Atoms* **2**, 277 (2014).

6. I. Bray, D. V. Fursa, A. S. Kadyrov, A.V. Lugovskoy, J. S. Savage, A.

T. Stelbovics, R. Utamuratov, and M. C. Zammit. Positron scattering from atoms and molecules. *J. Phys. Conf. Ser.* **488**, 2052 (2014).

7. S. Lorenzen, B. Omar, M. C. Zammit, D. V. Fursa, and I. Bray. Plasma pressure broadening for few electron emitters including strong electron collisions within a quantum-statistical theory. *Phys. Rev. E* **89**, 023106 (2014).

8. M. C. Zammit, D. V. Fursa, and I.Bray. Calculations of electron scattering from H_2^+. *Phys. Rev. A* **88**, 062709 (2013).

9. M. C. Zammit, D. V. Fursa, and I. Bray. Convergent-close-coupling formalism for positron scattering from molecules. *Phys. Rev. A* **87**, 020701 (2013).

10. M. C. Zammit, D. V. Fursa, and I. Bray. Electron scattering in a helium Debye plasma. *Chem. Phys.* **398**, 214 (2012).

11. S. Lorenzen, A. Wierling, H. Reinholz, G. Ropke, M. C. Zammit, D. V. Fursa, and I. Bray. Quantum-statistical line shape calculation for Lyman-α lines in dense H plasmas. *J. Phys. Conf. Ser.* **397**, 012021 (2012).

12. M. C. Zammit, D. V. Fursa, I. Bray, and R. K. Janev. Electron-helium scattering in Debye plasmas. *Phys. Rev. A* **84**, 052705 (2011).

13. M. C. Zammit, D. V. Fursa, and I. Bray. Convergent close-coupling calculations for excitation and ionization processes of electron-hydrogen collisions in Debye plasmas. *Phys. Rev. A* **82**, 052705 (2010).

14. S. Lorenzen, A. Wierling, H. Reinholz, G. Ropke, M. C. Zammit, D. V. Fursa, and I. Bray. Quantum-statistical T-matrix approach to line broadening of hydrogen in dense plasmas. *AIP Conf. Proc.* **1290**, 99 (2010).

Contents

List of Tables

List of Figures

List of Figures

Acknowledgements

It needs to be stated that this thesis, the resulting publications, invited talks and awards are a testament to the people who have played a major role in my life and education. Namely:

- My supervisor Prof. Dmitry Fursa, who has given his expertise, encouraging support and time, to teach and mentor me over the past six years, from a third-year undergraduate student through to a Research Fellow.
- My co-supervisor Prof. Igor Bray, for his advice, work ethic and passion to teach and learn new science has been inspirational.
- All the members of the Institute of Theoretical Physics at Curtin University, who have made my education a very enjoyable experience and have all at some stage offered assistance. Particularly Jeremy Savage, who proof-read this thesis and made the office fun.
- My friends, for putting up with my science stories and their consistent chat and phone calls that kept me sane (mostly).
- Most importantly my family. Their continuous encouragement to pursue any challenge has been invaluable. Their work ethic, individual expertise, support for each other and myself, has made me who I am and allowed to me to achieve my dreams and tackle even grander challenges. In particular my sister Dr. Carla Zammit, who introduced me to the world of research. She taught me new sciences, gave me career advice and provided me with assistance.

I truly appreciate all these people in my life. They drive me to want to achieve more.

Chapter 1

Introduction

Chemical reactions are the underlying processes that govern medicine, industry, nature and life. The very basis of chemistry (the interactions between atoms and molecules) is the individual collisions between photons, atomic particles, atoms and molecules. By studying individual scattering processes, resulting collision data can be used to determine the collective many body-effects of a media. Calculations of ion stage abundance, energy deposition/-transport and reactivity are just some of the properties that are required to advance other sciences and technologies. Technologies and sciences that rely on electron or positron (anti-particle of electron) collision data include electric lighting, fusion technology [50–53], materials research [54], climate science [55], astrophysics [56–58], lasers, radiotherapy [59–65] and positron emission tomography (PET) scans to detect cancers and mental illnesses [65, 66].

Although collision physics is of technological and scientific interest, accurate and efficient scattering models are not easily utilised or do not exist. Hence development of theoretical scattering techniques is important. These techniques have implications in many collision physics problems, including atomic and nuclear physics, condensed matter physics and inverse scattering problems. As well as being relatively cheap and capable of providing comprehensive collision data, theoretical studies in several cases have highlighted experimental errors and resolved discrepancies between measurements. In some cases theoretical results complement experiments that cannot resolve particular scattering processes. An example is low-energy measurements of positrons scattered to forward angles, where experiments have severe diffi-

culties in accounting for such scattering events. Hence theoretical results are used to correct measurements of low-energy integrated cross sections.

1.1 Molecular processes

Theoretical formulations of electron and positron collisions with molecules are often based on techniques developed for electron-atom scattering. Molecules, however, have the complexity of multi-centre potentials which leads to absence of spherical symmetry. In addition the rotational and vibrational degrees of freedom add to the complexity of scattering processes. *Ab initio* theoretical treatments of positron scattering are even more difficult than electron scattering. This is due to the strong electron-positron correlations and the additional channel of positronium (Ps) formation. In approximate order of lowest threshold energy, the important electron/positron-molecule/molecular-ion scattering processes include:

Elastic scattering

$$\mathrm{e}^{\pm} + \mathrm{AB}(n,v,J) \quad \rightarrow \quad \mathrm{e}^{\pm} + \mathrm{AB}(n,v,J). \tag{1.1}$$

Dissociative recombination (of molecular ions)

$$\mathrm{e}^{-} + \mathrm{AB}^{+}(n,v,J) \rightarrow \quad \mathrm{AB}^{**} \rightarrow \quad \mathrm{A} + \mathrm{B}. \tag{1.2}$$

Rotational excitation

$$\mathrm{e}^{\pm} + \mathrm{AB}(n,v,J) \quad \rightarrow \quad \mathrm{e}^{\pm} + \mathrm{AB}(n,v,J'). \tag{1.3}$$

Vibrational excitation

$$\mathrm{e}^{\pm} + \mathrm{AB}(n,v,J) \quad \rightarrow \quad \mathrm{e}^{\pm} + \mathrm{AB}(n,v',J). \tag{1.4}$$

Resonant dissociative excitation (of molecular ions)

$$\mathrm{e}^{-} + \mathrm{AB}^{+}(n,v,J) \rightarrow \quad \mathrm{AB}^{**} \rightarrow \quad \mathrm{e}^{-} + \mathrm{A}^{+} + \mathrm{B}, \tag{1.5}$$

$$\rightarrow \quad \mathrm{e}^{-} + \mathrm{A} + \mathrm{B}^{+}. \tag{1.6}$$

Dissociative attachment

$$\mathrm{e}^{-} + \mathrm{AB}(n,v,J) \quad \rightarrow \quad \mathrm{A}^{-} + \mathrm{B}, \tag{1.7}$$

$$\rightarrow \quad \mathrm{A} + \mathrm{B}^{-}. \tag{1.8}$$

Positronium formation

$$\mathrm{e}^{+} + \mathrm{AB}(n,v,J) \quad \rightarrow \quad \mathrm{Ps} + \mathrm{AB}^{+}. \tag{1.9}$$

Electronic excitation

$$\mathrm{e}^{\pm} + \mathrm{AB}(n,v,J) \quad \rightarrow \quad \mathrm{e}^{\pm} + \mathrm{AB}(n',v,J). \tag{1.10}$$

Dissociation (usually by electronic excitation)

$$\mathrm{e}^{\pm} + \mathrm{AB}(n,v,J) \quad \rightarrow \quad \mathrm{e}^{\pm} + \mathrm{AB}^{*} \quad \rightarrow \quad \mathrm{e}^{\pm} + \mathrm{A} + \mathrm{B}. \tag{1.11}$$

Dissociative excitation (of molecular ions)

$$\mathrm{e}^{\pm} + \mathrm{AB}^{+}(n,v,J) \rightarrow \quad \mathrm{e}^{\pm} + \mathrm{AB}^{+*} \rightarrow \quad \mathrm{e}^{\pm} + \mathrm{A}^{+} + \mathrm{B}, \tag{1.12}$$

$$\rightarrow \quad \mathrm{e}^{\pm} + \mathrm{A} + \mathrm{B}^{+}. \tag{1.13}$$

Ionisation

$$\mathrm{e}^{\pm} + \mathrm{AB}(n,v,J) \quad \rightarrow \quad \mathrm{e}^{\pm} + \mathrm{e}^{-} + \mathrm{AB}^{+}. \tag{1.14}$$

Dissociative ionisation (of molecular ions)

$$\mathrm{e}^{\pm} + \mathrm{AB}^{+}(n,v,J) \rightarrow \quad \mathrm{e}^{\pm} + \mathrm{e}^{-} + \mathrm{A}^{+} + \mathrm{B}^{+}. \tag{1.15}$$

Here n, v, J are the molecule's electronic, vibrational and rotational state respectively. AB^{*} indicates an excited state of AB and AB^{**} is either a doubly

excited or autoionising Rydberg state of AB with the respective dissociative asymptotic conditions. In some cases resonances drive rotational excitations (1.3), vibrational excitations (1.4), rearrangement processes (1.7), (1.8) and (1.2) and dissociation processes (1.5), (1.6) and (1.11) [67–69].

1.1.1 Resonances

Resonances in electron and positron scattering from atoms and molecules are sometimes known as "compound states" or "temporary negative ions" (in the case of projectile electrons). For positron projectiles resonances usually lead to the annihilation of a target electron and the positron. Here resonances are classified for projectile electrons. The physical process behind all resonances is the temporary attachment of the projectile to the target for times longer than the normal transit time through the target. This attachment to the target can be viewed as a non-stationary state that decays via the emission of an electron. Resonances are classified by the simultaneous/proceeding processes during/after the attachment of the projectile [70].

Atoms

Classifying resonances is a controversial topic that is in continuous development [71, 72]. Traditionally all resonances were divided into two groups, named shape and Feshbach resonances [70, 71]. However such a classification scheme of resonances (shape or Feshbach) has been recognised as an idealised description of the natural processes and can only be used as a subdivision of resonance types [71, 72]. As described by Buckman and Clark [71] resonance refers to binding an electron to a "parent" atom state or binding two electrons to a positive-ion "grandparent" state. Shape resonances are considered a one-electron phenomenon that are located energetically above the parent atom state [72]. Shape resonances are short-lived and classify the physical process of the projectile captured in a unoccupied low-lying orbital of the target [69]. During this process the target electrons remain in their initial configuration prior to attachment [67, 72]. Short-lived shape resonances are observed as a broad resonance feature as a function of projectile-energy and generally dominate the excitation cross section of the target. A class of shape resonances which are relatively long-lived are called core-excited

shape resonances. The physical process of a core-excited shape resonance is the simultaneous excitation of the target and temporary trapping of the projectile to form an excited state [67, 69]. This type of resonance is observed as a sharp resonance feature as a function of projectile-energy barely above an excitation threshold of the target [69]. As an example, a shape resonance exists in electron scattering from H [70], where a sharp resonance is observed in the elastic cross section and in the $n = 2$ excitation cross sections, within 0.3 eV above the $n = 2$ threshold [73, 74].

The physical process of a Feshbach resonance is exactly the same as a core-excited shape resonance, however, Feshbach resonances are generally found at an energy 0-0.5 eV below the target excitation threshold and are generally narrower than core-excited shape resonances [67, 70, 72]. Feshbach resonances are comparatively a sharp long-lived resonance feature and are observed in electron scattering from H and He. For H several Feshbach resonances are seen in the elastic cross section up to 0.7 eV below the $n = 2$ excitation threshold [74]. In the He 2^3S excitation cross section Feshbach resonances are observed, corresponding to the temporary states $1s2s2p\ ^2\mathrm{P}^o$ at 20.27 eV and $1s2s3d\ ^2\mathrm{D}^e$ at 20.955 eV [75]. A special case of Feshbach resonance that occurs when the energy of the state is near the very top of the potential well is called a "virtual state" [70] and is seen as resonance at the energy of a parent state (i.e. total energy $E = 0$ eV).

Molecules

For molecules, shape resonances can decay into vibrational and rotationally excited states. They also drive the dissociative attachment processes [67]. Shape resonances of electrons scattering from diatomic molecules (H_2, O_2, N_2, CO, NO) are found at low-energies between 0-4 eV and have lifetimes in the range 10^{-15}-10^{-10} s. An indication of a resonance lifetime in comparison to the molecules vibrational period (typically $\approx 10^{-14}$ s for diatomics), is seen in the vibrational excitation cross sections. For a short-lived resonance the vibrational excitation cross section exhibits a broad peak as a function of projectile-energy. When the resonance is long-lived the molecule can vibrate during this projectile attachment and a series of sharp resonance features are seen in the vibrational excitation cross section corresponding to the location of vibrational levels of the resonance state. When the lifetime is comparable to the vibrational period, several broadened spikes are observed

in the vibrational excitation cross section.

A unique class of Feshbach resonances to molecules are known as nuclear-excited Feshbach resonances. Nuclear-excited Feshbach resonances occur when a target molecule with N electrons can support one or more weakly bound states of $N + 1$ electrons. Vibrational excitation of these compound states can lead to very narrow complicated structures [69]. Nuclear-excited Feshbach resonances can decay or transfer electronic energy to the nuclei and are responsible for many of these rotational, vibrational, rearrangement and dissociation processes [67, 69]. These resonances are also a mechanism for super-elastic scattering, see Stroe and Fifirig [68] for details.

1.2 Overview of theoretical methods

Theoretical methods for electron and positron scattering from atoms and molecules can be classified into two categories: quantum mechanical perturbative methods or non-perturbative methods. Perturbative methods are generally only accurate in the high-energy region (impact-energy higher than five times ionisation threshold). Some of the most actively used quantum mechanical perturbative methods include the distorted-wave Born approximation [76, 77] and the independent-atom model screening-corrected additivity rule (IAM-SCAR) [78–80]. The distorted-wave Born approximation has been applied to electron-impact excitation and ionisation problems, calculating fully differential cross sections of orientationally averaged molecules (using orientation-averaged Dyson orbitals) [81, 82] and aligned molecules [83]. The IAM-SCAR method usually calculates elastic and total cross sections in the static-exchange approximation of relatively large molecules.

Non-perturbative methods are based on solving the Schrödinger equation using either grid based techniques or a close-coupling expansion. In principle non-perturbative methods can calculate accurate results across the entire energy region. The low-energy region (from 0 eV to ionisation threshold) for molecules is the most difficult to describe, where rotational, vibrational, electronic, dissociative and rearrangement scattering processes are important. To date completely *ab initio* electronic-rovibrational close-coupling calculations have not been performed. This method would be complicated to implement and calculations would require immense computing resources. Nuclear rotational [84], vibrational [85] and rovibrational [86] close-coupling

methods have been applied to a range of molecules by utilising phenomenological potentials. These methods solve the nuclear close-coupling problem and can only calculate accurate results for nuclear excitations (not rearrangement or electronic excitations) in the low-energy region. The multi-channel quantum defect theory (MQDT) [87] is the only *ab initio* method (utilising several approximations) that describes all processes (including rearrangement) in the low-energy region.

Currently non-perturbative methods rely on the Born-Oppenheimer approximation, they include the Schwinger multichannel (SMC) [88], Kohn variational [89], molecular R-matrix with pseudostates (MRMPS) [69], time-dependent close-coupling (TDCC) [90] and molecular convergent close-coupling (CCC) [91] methods. These methods solve the electronic close-coupling problem as opposed to the (nuclear) rovibrational close-coupling methods mentioned above. All of these non-perturbative methods utilise some approximations to reduce the complexity and computational resources required to solve the scattering problem. These approximations include the Born-Oppenheimer, adiabatic or fixed-nuclei approximations. Calculations have also been performed within the static exchange and static exchange plus polarisation approximations. All these approximations will be discussed in Chapter 2. The SMC, Kohn variational, MRMPS and molecular CCC methods utilise a fixed-nuclei close-coupling expansion to solve the scattering equations, while the TDCC method solves the fixed-nuclei time-dependent Schrödinger equation using a grid based technique. In principle these methods can accurately describe electronic transitions across the entire energy range. They have had considerable success calculating low-energy elastic cross sections and most rotational, vibrational and electronic excitation cross sections within the adiabatic-nuclei approximation.

In the intermediate-energy region (from ionisation threshold to five times ionisation threshold), elastic scattering, electronic excitation and ionisation processes are dominant. The close-coupling approximation was originally developed as a low-energy approximation, which expanded the total scattering wave function over the set of bound target states. By representing the continuum by a discretisation of positive energy pseudostates, this method was generalised to describe the entire energy range. In these calculations total ionisation cross sections are calculated by summing discrete excitation cross sections of positive energy states. Even in the Born-

Oppenheimer fixed-nuclei approximation accurate close-coupling calculations are very large and computationally expensive. This has limited the progress of non-perturbative methods, which in turn was the main motivation for the development of the molecular CCC method. To date the SMC method has not calculated ionisation cross sections but it has been capable of calculating electronic excitation cross sections in this energy region by utilising the projection operator approach [92, 93]. The MRMPS method has calculated total ionisation cross sections just above threshold for several targets, however in some cases these calculations were severely affected by pseudo-resonances [94]. The CCC and TDCC methods are currently the only non-perturbative methods suited for accurately calculating total ionisation cross sections across the entire intermediate-energy region. The MQDT and non-perturbative SMC, Kohn-variational, MRMPS, TDCC and CCC methods are discussed below.

1.2.1 Schwinger multichannel method

The Schwinger variational method [95–97] is based on the Schwinger variational principle [98] and a related variational method [99]. In this method, the Lippmann-Schwinger equation is transformed in terms of the K-matrix and total scattering wave function. The total scattering wave function is varied until a converged (stable) value of the K-matrix is obtained. The total scattering wave function is represented and varied as an expansion of square integrable basis functions. For molecular scattering the Schwinger variational method utilises Cartesian Gaussian basis functions to expand the total wave function.

The SMC method [88] is very similar to the Schwinger variational method. However the Lippmann-Schwinger equation Green's function is defined for the multichannel case, in practice only in the open-channel space P. The closed-channel component (1-P) is recovered by summing the two spaces. The definition of P space is fundamentally different from Feshbach theory, where in the SMC method the operator P is defined only in the target-space, for details see Lima and McKoy [100] and Takatsuka and McKoy [96]. Due to the large number of open channels in the intermediate-energy region and computational resources, calculations have mostly been limited to low-energy scattering [92].

In the $\tilde{C}$-functional formulation [88, 97] of the SMC method the

Lippmann-Schwinger equation is expanded to the third-order. This equation (which includes the first and second Born terms) is transformed in terms of the K-matrix and total scattering wave function. A variational principle is applied to the third term of the expanded Lippmann-Schwinger equation. The total scattering wave function is varied until a converged value of the K-matrix is obtained. This formulation has shown to produce more accurate results than the Kohn variational [101] and Schwinger variational [97] methods.

In the Schwinger iterative method [102] the total wave function is varied within the Lippmann-Schwinger equation. After each iteration, the basis set expansion of the total wave function is varied or augmented. This procedure continues until the total wave function is converged. Mu-Tao et al. [97] noted that one iteration of the Schwinger iterative method can drastically improve non-iterative K-matrix methods (described above), which leads to a result much closer to the exact value. This method has had some success in describing elastic scattering of CH_4 [103], H_2S [104] and photoionisation of N_2 [102].

These various Schwinger variational formulations have had mixed success describing low-energy electrons scattering from diatomics and relatively large polyatomic molecules. Notable investigations of diatomic molecules include H_2 [92, 105, 106] and N_2 [93], where discrepancies with experiment still remain for electron-impact excitation of H_2 and N_2. Schwinger variational studies of large polyatomic molecules utilise the static exchange and static exchange plus polarisation approximations, which use the pseudo potentials detailed in [107]. These large polyatomic molecules include furan (C_4H_4O) [108], methanol (CH_3OH) and ethanol (C_2H_5OH) [109]. Results of these studies [108, 109] elastic cross section are in reasonably good agreement with experiment.

The SMC method was extended to positron-molecule scattering by Germano and Lima [110]. This method has been applied to H_2 [32, 42], N_2 [111], CO [112] and CO_2 [113] in the low-energy region. In the study of positron-H_2 [42], the adiabatic-nuclei approximation was utilised to investigate vibrational excitations. These results of vibrational excitation cross sections were in excellent agreement with experiment. Again for larger molecules the static and static plus polarisation approximations were utilised to study positron scattering from N_2O [114], ethene (C_2H_4) [115] and ethane (C_2H_6)

[116].

In summary electron and positron scattering from small diatomic molecules to relatively large polyatomic molecules have been investigated with the SMC method. Calculations however, have been limited to describing elastic scattering and excitation processes.

1.2.2 Kohn and complex Kohn variational methods

The Kohn variational method [89] is similar in principle to the Schwinger variational method. It uses the Kohn principle [117] to treat the tangent of the scattering phase-shift $\tan(\delta_l)$ as a stationary functional. This functional is related to a trial scattering phase-shift and total scattering wave function, which is an expansion of square integrable basis functions and one-electron orbitals f_l and g_l. Functions f_l and g_l are regular and behave as Coulomb waves at asymptotic distances. From the Kato identity [118] an equation is derived, which has the stationary tangent of the scattering phase-shift proportional to matrix elements of the square integrable basis functions, f_l and g_l. The advantage of this method over the Schwinger variational method is that in this method it avoids calculation of matrix elements VG_0V.

Traditionally f_l and g_l are chosen as Coulomb functions, g_l being the irregular Coulomb wave multiplied by a suitable cut-off function to make it regular and still approach unity for large r. This choice produces singularities and is the origin of Kohn anomalies [119]. There have been various attempts to remove these singularities [119]. The most common technique to remove these singularities is the complex Kohn variational formulation.

The complex Kohn variational method [89, 120] is formulated directly from the Kohn variational method. Here g_l is chosen as a combination of Coulomb functions with the correct real boundary conditions. This choice transforms the stationary functional $\tan(\delta_l)$ into the T-matrix, which is also a stationary functional. Matrix elements are more stable with this choice and are much less likely to produce a singular matrix. Although this method produces a symmetric T-matrix, this does not guarantee a unitary S-matrix. Completeness of the trial basis functions used is checked by calculating the corresponding K-matrix and checking its symmetry and hence unitarity of the S-matrix. Practical applications of these methods divides the scattering Hamiltonian into P and Q space and a type of optical potential is constructed, for details see [89].

Notable calculations of the complex Kohn method include electron scattering from H_2 [121], H_2O [122, 123], CH_4 [124, 125] and NH_3 [126]. These results all have reasonably good agreement with experiment for elastic scattering. However excitation cross sections of H_2 [121] and H_2O [122] are in major disagreement with experiments. The complex Kohn method has also been applied to large polyatomic molecules like CH_3Cl [127], formic acid (HCOOH) [128] and tetrahydrofuran (C_4H_8O) [129], which have results in good agreement with the few experimental measurements of these systems.

The Kohn variational method has also been applied to positron scattering [130] from H_2 [131, 132] and N_2 [133]. Results of these studies were in reasonable agreement with old (inaccurate) experiments.

Like the SMC method the complex Kohn method has been able to treat electron scattering from diatomic and large polyatomic molecules. Positron scattering from diatomic molecules has also been investigated. Non-perturbative calculations have been limited to elastic scattering and excitation processes. In some cases the Kohn variational method can lead to a singular matrix in the T-matrix formula, which subsequently produces unphysical results. This anomalous behaviour is mostly avoided with the complex Kohn method [119].

1.2.3 The *R*-matrix method

The progress and formulation of the R-matrix method for electron- and positron-molecule scattering was recently reviewed by Tennyson [69]. This method is generally used to calculate low-energy collision data. The suite of R-matrix codes have been extended beyond fundamental science and have recently been privatised and can be purchased for commercial or scientific use.

The basic principle of the R-matrix method is to separate space in two, at a radius $r = a$, where $r \leq a$ is the inner-region and $r > a$ is the outer-region. For an accurate calculation it is required that the inner-region completely contains all target electrons. In the outer-region only the projectile electron can be found and the exchange interaction with the target-electrons is ignored, the interaction with the target is described by an asymptotic Coulomb charge potential in the case of an ionic-target and/or in the case of a neutral target a sum of polarisation (non-spherical) potentials. This makes the description of the outer-region relatively simple. In the inner-

region all target-electrons and the projectile-electron can exist. Here the exchange interaction is explicitly included between the target-electrons and the projectile-electron. The R-matrix method solves for the total scattering wave function in the inner-region via diagonalisation and then calculates the outer-region's electron wave function amplitude on the boundary. The outer-region's electron wave function is propagated and/or matched to the asymptotic form of a continuum wave function and K-matrix elements are determined.

Notable R-matrix calculations for electron-molecule scattering include: H_2 [134–136], water (H_2O) [137], methane (CH_4) [138] and uracil ($C_4H_4N_2O_2$) [139]. These studies have produced accurate low-energy elastic differential and integrated cross sections in good agreement with experiment. However, concerning disagreement remains for electron-impact excitation cross sections, particularly for H_2[134, 135] (which is discussed further in Section 1.3.1).

The MRMPS method uses a set of basis functions to represent the continuum in the inner-region [69]. These pseudostates play an important role of representing the polarisation effects of the target and any excitation to a pseudostate lying above the ionisation threshold is considered to be ionising. MRMPS calculations have also produced electron-impact ionisation cross sections in reasonable agreement with experiment for impact-energies $\approx$10 eV above the respective ionisation threshold. In these calculations there was a severe problem with pseudo-resonances and a convolution averaging procedure was used to smooth over results [94]. Studies of electron-impact ionisation cross sections include C_2^- [140, 141], H_2 and H_3^+ [94].

A non-adiabatic R-matrix method [142] has been used to study rotational excitation [143], vibrational excitation [144] and shape resonances of diatomic molecules caused by the coupling of nuclear motion and electronic resonances [145]. This method has been used to study electron-impact vibrational excitation of HF [144] and the N_2^- shape resonance of electron-N_2 [145].

B-spline R-matrix codes [146, 147] have had major success in electron-atom scattering [148, 149]. Currently their application to electron-molecule scattering has been limited to one-electron targets [150]. A small summary of the performance of modelling molecular targets with B-splines is given in [151]. Further research into B-spline performance of modelling electron-

molecule scattering is worth conducting.

In summary the suite of R-matrix codes are general and have been applied to electron and positron scattering from diatomic and polyatomic molecules. For electron scattering the antisymmetric scattering wave function configurations are explicitly built into the formulation. This allows the treatment of many-electron systems and closed-shell molecules. For a given basis set (which spans respective impact-energies), one computationally demanding calculation of the impact-energy independent inner-region can produce results for many impact-energies. This is because solution of the outer-region has the only impact-energy dependence. Calculations of the outer region are relatively simple and quick, which makes it a very efficient method for mapping resonances. Currently calculations are restricted to the low-energy region. The MRMPS method utilises Gaussian type orbitals (node-less) which have difficulty reproducing the nodal structure of continuum functions as a linear combination without encountering linear dependence problems (a basis function can be well represented by a linear combination of the other basis functions used in the expansion) [69]. Hence results for ionisation cross sections yield pseudo-resonances. These results require convolution, averaging over impact-energies to obtain smooth cross sections. This method is also restricted to molecules (including vibrationally excited molecules) that can fit within the inner-region space. Using Gaussian type orbitals this inner-region can extend up to 13-15 a_0 for impact-energies up to 12 eV.

1.2.4 Multi-channel quantum defect theory

The MQDT [87] is a method used to investigate low-energy excitation, dissociative recombination and dissociative excitation processes of ionic targets. The MQDT formulation is based on separating the collision space into three regions, as first proposed by Chang and Fano [152]. It uses the analytic form of the total scattering wave function in each region to propagate out a scattering solution. Having the projectile-electron and nuclear spatial coordinates indicated by r and R respectively, these regions are defined as
Region:

I This region is a short-ranged reaction zone limited to space $r < r_{\mathrm{I}}$ and $R < R_{\mathrm{I}}$ (usually within tens of atomic units). Here all short-ranged

interactions are important and the Born-Oppenheimer approximation is valid.

II The outer reaction zone, where $R < R_{\mathrm{I}}$ and $r > r_{\mathrm{I}}$ is finite. Non-central short-ranged interactions are present and therefore the angular momentum of the electron and the molecule are coupled. Hence the Born-Oppenheimer approximation is not valid in this zone.

III The asymptotic zone where $r \to \infty$ and $R \to \infty$, has only long-ranged interactions present. The angular momentum of the electron and molecule can be considered uncoupled. Asymptotic behaviour of the wave function can be used to determine a scattering solution.

In region I the MQDT solves the Lippmann-Schwinger equation perturbatively for the K-matrix. This calculation explicitly couples molecular states represented within the Born-Oppenheimer approximation. To perform these calculations the MQDT requires input of the electronic potential energy curves, electronic couplings (V-matrix elements at fixed internuclear distances [153]) and quantum defects (used to calculate resonance electron energy levels), which are obtained from resonance parameters. These quantities are usually obtained from R-matrix or complex Kohn variational scattering calculations. Upon solution of the Lippmann-Schwinger equation the resulting K-matrix is used to calculate the total wave function in region II. Contrary to Chang and Fano [152], in region II the MQDT approximates the particle interactions as isotropic (spherical). The total wave function in this region can now be expressed by the diagonalised K-matrix from region I, scattering product wave functions and Coulomb wave functions. The total wave function in region II is compared to the analytic form of the total wave function in region III. From here an expression for the S-matrix can be determined from the diagonalised region I K-matrix.

It is important to note that in most studies that use the MQDT it is assumed that the electronic couplings have no energy dependence. This allows the Lippmann-Schwinger equation to be solved perturbatively (by the second order term). An investigation of e-H_2^+ by Ngassam et al. [154] showed that solving the non-perturbative Lippmann-Schwinger equation using energy-dependent electronic couplings compared very well with the approximation described above.

Although the MQDT maybe limited by the accuracy and performance of other scattering methods it produces reasonably accurate low-energy collision data of complicated scattering processes. The MQDT has had good success in describing dissociative excitation and recombination processes of H_2^+ and its isotopologues [68, 155, 156]. Other studies have also been conducted on HeH^+ [157], BeH^+ [158] and H_3^+ [159] and also rotational [160] and vibrational super-elastic scattering [161].

1.2.5 Time-dependent close-coupling method

The TDCC method [90] is a relatively recent method which avoids some of the problems associated with the methods described above. The TDCC method starts from the time-dependent fixed-nuclei Schrödinger equation of the scattering system. The total wave function is expanded in partial waves and the projectile-electron wave function at $t = 0$ is described by a Gaussian wave-packet. The total scattering wave function is spatially propagated over time from $t = 0$ to $t \to \infty$. Scattering probabilities are calculated by projecting the appropriate process asymptotic wave function onto the antisymmetric total scattering wave function as $t \to \infty$. The ionisation probability can also be obtained by subtracting the sum of all excitation probabilities from one. Cross sections are then calculated from probabilities.

The TDCC method has had considerable success in describing electron and photon scattering from atoms and molecules [90]. Electron-impact ionisation cross sections have been calculated for the H_2^+ [17], H_2 [162] and Li_2 [163] molecules. The TDCC method has the advantage of being able to accurately calculate all kinematic parameters of a collision process. For example calculations of the triple differential ionisation cross sections of H_2 [164, 165] and fivefold (also referred to as fully) differential ionisation cross sections of aligned H_2 [166] were in good agreement with experiment.

Solution of the total scattering wave function for electron scattering from a molecule with N-electrons allows the calculation of double-photoionisation of a molecule with $N + 1$ electrons. The TDCC method has had success in modelling the double photoionisation process of H_2 [167], which also results in a Coulomb explosion. Measurements and TDCC results of fully differential double photoionisation cross sections were presented together [168, 169]. These studies observed a large dependence on the measured kinetic energy

release of the protons and hence the internuclear distance during the collision.

The TDCC method has been applied to electron scattering from quasi-one and quasi-two electron diatomic molecules. The method is general and calculations can improve accuracy by simply decreasing the time step and spatial grid spacing. It is the only non-perturbative method that can describe all kinematic electron- and photon-impact ionisation processes:

- Single-differential cross section (one outgoing particle is resolved for energy).
- Double-differential cross section (one outgoing particle is resolved for energy and direction).
- Triple-differential cross section (two outgoing particles are resolved for direction and one outgoing particle is resolved for energy).
- Fully-differential cross section (two outgoing particles are resolved for energy and direction).

Unfortunately calculations are computationally expensive. A concern with the method for quasi two-electron molecules is the use of a parameter adjusted fitting function to extrapolate partial-wave cross sections and a parameter adjusted local-exchange potential.

1.2.6 Convergent close-coupling method

The adiabatic-nuclei CCC method [91] (developed in this thesis) uses a Sturmian (Laguerre) basis to to build one-electron orbitals. Appropriate configurations are constructed and the target Hamiltonian is diagonalised to obtain negative- and positive-energy pseudostates. These pseudostates are used in a close-coupling expansion of the total wave function. The total wave function is substituted into the time-independent electronic Schrödinger equation and then transformed to a set of close-coupling equations for the T-matrix. The CCC method solves the momentum space Lippmann-Schwinger equation via a K-matrix formulation (which enforces unitarity). T-matrix elements are then obtained and cross sections are calculated.

The adiabatic-nuclei CCC method has had good success in treating positron scattering from H_2 [170], electron scattering from vibrationally ex-

cited H_2^+ [171] and its isotopologues [91]. Currently more complex diatomics are being studied.

The CCC method is suited at treating large close-coupling expansions, which is very important for positron scattering. An accurate target structure and converged expansion takes into account polarisation and higher-order effects. However these large close-coupling calculations are computationally expensive. Like the atomic CCC method it is expected that the method will be limited to treating electron scattering from quasi one- and two-electron molecules.

1.3 Current state of the field

The leading non-perturbative methods (SMC [88], Kohn variational [89], MRMPS [69] and TDCC [90]) have had mixed success for describing positron or electron scattering experiments. In this section the current state of the field is summarised (not including the works of the CCC method), concentrating on the successes and failures of these leading non-perturbative methods and experiments. This summary focuses primarily on the studies conducted in this thesis, electron scattering from H_2^+ and positron scattering from H_2. A select few studies on electron and positron scattering from diatomic and small polyatomic molecules have also been summarised. This gives the reader an indication of the need for a general and accurate scattering theory.

1.3.1 Electron scattering

Electron-H_2^+

The H_2^+ molecule is the simplest molecule to describe theoretically. Experimentally H_2^+ is produced by electron-impact ionisation of H_2 which leaves H_2^+ in a range of vibrationally excited states. Measurements of the electron-H_2^+ collision system have been taken with H_2^+ populated various vibrationally excited states [12]. Hence to compare with experiment theoretical methods need to account for the range of vibrational levels, which is difficult and computationally expensive.

In the low-energy region dissociative recombination, vibrational excitation and resonant dissociative excitation processes are important. Here the

MQDT [156] results for dissociative recombination cross sections are in excellent agreement with experiment. Their results for dissociative excitation cross sections compare reasonably well with experiment.

Proton production cross sections (which are the sum of dissociative excitation and ionisation cross sections), have been measured by several experimental groups [22–25]. These measurements vary significantly in the low-energy region, which is primarily due to the different vibrational populations of H_2^+ that they produce and use in their experiment [21]. The only theoretical investigations describing these experiments assumed a Franck-Condon distribution of the vibrational levels and utilised the adiabatic-nuclei first Born approximation [20, 172–174]. These first-order studies overestimated most experimental measurements in the low-energy region (as expected for a first-order method).

Dissociative ionisation cross sections were measured in two experiments [22, 26]. It is interesting to note that these measurements have a 20% discrepancy in the high-energy region. In this energy-region and for this process, the different experimental vibrational populations of H_2^+ should make little difference. The TDCC method is the only non-perturbative method that has studied this collision process [17]. Using the equilibrium distance of H_2^+ in the fixed-nuclei approximation (i.e. not taking into account the vibrational distribution) and performing a relatively small sized partial-wave expansion (maximum orbital angular momentum $L_{\max} = 5$ and orbital angular projection $M_{\max} = 2$) with a distorted wave top-up, this method produced results in good agreement with both experiments at the peak of the cross section. The experimental discrepancy in the high-energy region was not investigated in that study. Investigation by Zammit et al. [91] suggests that the size of the partial-wave expansion used by the TDCC method [17] is too small and overestimates the true result.

For further discussion of the electron-H_2^+ literature review, see Ref. [91].

Electron scattering from molecules

The review by Brunger and Buckman [175] summarised electron-molecule theoretical and experimental scattering results in the low- and intermediate-energy region. Brunger and Buckman [175] limited their review to cover only elastic, nuclear and electronic excitation cross sections of diatomic molecules, excluding rearrangement and ionisation processes. The review concluded

that agreement between experimental and theoretical results was "less than satisfactory" for electronic excitation integrated and differential cross sections. This poor level of agreement is also evident in electron-H_2 scattering, the most studied electron-molecule scattering problem. Accurate electron-H_2 collision data comes predominantly from experimental measurements and has been reviewed in several papers [175–179]. Results of electron-H_2 scattering are extremely important because they are used as a benchmark for theoretical and experimental studies.

Low-energy elastic differential cross sections of electron scattering from H_2 have been calculated with the R-matrix method [135]. These results are in reasonably good agreement with all experiments. Elastic and total cross sections have not been presented by a non-perturbative method over a broad energy range.

The review of [175] documents many cases of disagreement between theoretical and experimental results for electron scattering from H_2. This is of major concern considering that electron-H_2 is a relatively simple scattering system. For instance the electronic excitation differential cross sections $B^1\Sigma_u^+$, $c^3\Pi_u$, $a^3\Sigma_g^+$, $C^1\Pi_u$, $EF^1\Sigma_g^+$ and $e^3\Sigma_u^+$ are only in agreement with non-perturbative methods for particular cases. In other cases the shape and magnitude of the differential cross sections are in complete disagreement with experiments. For example results from the SMC method [92, 105] compare the best with experiment for electronic differential cross sections, however, agreement is only seen in some cases. In the experimental paper by Wrkich et al. [180] it is stated that "no theory is consistently in agreement for all the state's DCSs observed here". Even the high-energy differential and integrated cross section measurements of Kato et al. [181] are in disagreement with existing theoretical results.

Electron-impact ionisation of H_2 has been investigated by the TDCC [162] and MRMPS method [94]. The MRMPS results are limited to impact energies just above ionisation threshold and contain pseudo-resonances. The TDCC method utilised a parameter adjusted local-exchange potential and a parameter adjusted fitting function extrapolation procedure, which produced results in excellent agreement with experiment. Electron-impact ionisation triple [164, 165] and five-fold [166] differential cross section results of the TDCC method are also in good agreement with experiment. Like H_2^+ a concern with the success of the TDCC method is the size of the

partial-wave expansion (maximum orbital angular momentum $L_{\max} = 5$ and orbital angular projection $M_{\max} = 2$) and the use of parameters in the local-exchange potential and the extrapolation fitting function. TDCC results of electron-impact excitation cross sections have not been presented.

Heavier diatomic and small polyatomic molecules have been studied with the R-matrix and SMC methods, some of these include N_2 [93], O_2 [182], CH_4 [138] and H_2O [137]. Most of these studies have concentrated on the low- and intermediate-energy region elastic and electronic excitation processes. Low-energy elastic differential and integrated cross sections are generally in good agreement with experiment. In most cases electronic excitation cross sections are in disagreement with experimental measurements, however in some cases experiments disagree between each other [175].

Several experimental measurements of differential and integrated cross sections disagree with each other qualitatively and quantitatively. For example measurements of the electronic excitation differential cross sections of CO disagree with each other by as much as one order of magnitude [175]. Integrated cross sections measured for O_2 vary by as much as 100% for excitations to the $a^1\Delta_g$ and $b^1\Sigma_g$ states [175]. Measurements of the elastic differential cross section of O_2 differ by a maximum of 50% at a scattering angle of 40° [175]. These examples of disagreement are too large to be due to normalisation techniques. Also the qualitative disagreement of measurements for the electronic excitation differential cross sections of N_2 and integrated cross section of CO cannot be due to normalisation techniques.

Only recently have theoretical studies calculated total ionisation cross sections. The MRMPS method and TDCC method have investigated electron-impact ionisation of Li_2 [163], H_3^+ [94] and C_2^- [140, 141]. The MRMPS method has so far been limited to calculating reliable ionisation cross sections ≈10 eV above threshold. Further studies need to be conducted to investigate the accuracy of these calculations.

1.3.2 Positron scattering

Positron-H_2

Collision data for positron scattering from H_2 comes primarily from experimental results. Many experiments of positron-H_2 scattering have measured the total cross section [35, 37–39, 41, 183–186]. These measurements have

large discrepancies in the low-energy region, which is due to experiments different resolution of the forward angle scattering. In general the most recent measurements have better resolution and hence are expected to be more accurate. MRMPS [31] results of the total cross section range from 0 to 10 eV and are in good agreement with old experiments [38, 183]. The MRMPS results considerably underestimate the most recent measurements of Zecca et al. [37] and Machacek et al. [35]. Low-energy results calculated using the SMC [32] are in good agreement with the MRMPS calculations [31].

Measurements of the low-energy elastic differential cross section have been compared with all available non-perturbative results in Ref. [35]. In all cases there is very large disagreement in the magnitude of the differential cross section.

Positron-impact electronic excitation cross sections of H_2 have only been measured for the transition from the ground state to the $B^1\Sigma_u^+$ state [43]. The SMC method [48] has produced results in good agreement with these measurements. This calculation used a Hartree-Fock ground state wave function, while the scattering calculation was a two-state approximation.

Before the study by our group [170] there was no non-perturbative method which could consistently describe positron-H_2 experimental measurements across the entire energy range. Hence no accurate theoretical collision data existed for ionisation, positronium formation and most electronic excitations cross sections. This is problematic because some measurements either don't exist or are in disagreement with each other. For example measurements of the direct ionisation cross section vary by at least 25% at the peak [44, 46, 47].

Positron scattering from molecules

The review by Surko et al. [186] covers positron-atom and positron-molecule experimental and theoretical techniques and results. Application of theoretical methods to positron scattering from diatomic molecules have been limited to low-energy scattering from the N_2 and CO molecules. The most recent and reliable experimental measurements for N_2 and CO have been performed by Zecca et al. [187]. These measurements for N_2 are in severe disagreement with the R-matrix [188] and SMC [189] results. For CO results of the iterative Schwinger variational method [190] do not agree with the

measurements of Zecca et al. [187]. The static plus polarisation R-matrix calculations of CO [191] are in reasonably good agreement with this experiment.

Above the low-energy region the only reliable collision data is provided by experiments. For positron scattering from N_2, two separate set of measurements [192, 193] of the total ionisation cross sections have discrepancies of approximately 30% over a broad energy range. Two experimental measurements of positronium formation cross section for positron-O_2 scattering are different by 100% above ionisation threshold [193]. This discrepancy remains unresolved, however, the total ionisation cross section measurements of Marler and Surko [193] agree with earlier measurements of Laricchia et al. [194]. These discrepancies require more experimental measurements or a new theoretical method to investigate and resolve this problem.

For small polyatomic molecules like N_2O, H_2O and CO_2 the SMC method and R-matrix methods have had good success in describing low-energy scattering experiments elastic integrated and differential cross sections [113, 114, 137].

Theoretical studies of large polyatomic molecules are limited to the low-energy region. The only non-perturbative method that describes these reactions is the SMC method, which has produced results that are in severe disagreement with experiment for C_2H_4 [115] and C_2H_6 [116].

1.3.3 Summary of the field

The situation of the electron- and positron-molecule scattering field is currently similar to the electron- and positron-atom field at the beginning of 1990. Non-perturbative methods produce results that agree with experiments only for particular cases. There is also a lack of accurate collision data of elastic, excitation, ionisation and total cross sections, particularly for scattering from vibrationally excited targets (which is crucial for modelling plasmas [50, 52]). It is interesting to note that the convergence of results in terms of the partial-wave and close-coupling expansions are generally not investigated.

There does not exist reliable or sufficiently detailed collision data for electron scattering from even the simplest molecules, H_2^+ and H_2. For electron scattering from H_2, no theoretical method is able to consistently provide accurate collision data for the dominant scattering processes over the entire

energy range. This includes elastic, electronic excitation and total cross sections. Further investigations into the accuracy of the total ionisation cross sections also need to be conducted.

The status of positron scattering from H_2 is much the same as electron scattering from H_2. No non-perturbative method can describe the dominant scattering processes across the entire energy range, this includes elastic, electronic excitation, positronium formation, ionisation and total cross sections. Accurate theoretical results are crucial to resolve the experimental discrepancy of the direct ionisation cross section [44, 46, 47] and to help resolve low-energy integrated and differential cross sections.

For larger molecules theoretical electron and positron collision data is required, particularly in the intermediate-energy region and in some cases the low-energy region. This would resolve discrepancies between current measurements and in many cases provide the first accurate theoretical results.

Hence there is a demand for a non-perturbative collision theory that can accurately calculate electron and positron collision data across the entire energy range. Following the success of the atomic convergent close-coupling method [195–204], application of this method to molecules should have the same success and provide the accurate collision data required.

Chapter 2

General theory

In this Chapter non-relativistic scattering theory is derived from the foundations of quantum mechanics and applied to neutral molecular targets. The Born-Oppenheimer and adiabatic-nuclei approximations are then described and applied. The formulation here is time-independent.

Theoretical formulation of quantum mechanical scattering theory requires the consideration of a typical scattering experiment. In scattering experiments projectile particles are shot at a target molecule. The scattered particles are then counted by detectors which are positioned at asymptotic distances from the scattering centre. This detection at asymptotic distances ensures that there is no more interaction between the target and projectile, hence the system is left in a stationary state (does not change with time). A picture of an ideal time-independent laboratory frame scattering experiment is shown in Fig. 2.1. Here the initial i stationary state of the target molecule is described by the wave function $\bar{\Phi}_i(\mathfrak{R})$, where $\mathfrak{R}$ represents collectively all the target electrons and nuclei spatial and spin coordinates.

Referring to Fig. 2.1, the incident projectile-particles asymptotic stationary state is described by a plane-wave with normalisation constant N and momentum vector $\boldsymbol{q}$

$$|\boldsymbol{q}_i\rangle = N e^{i\boldsymbol{q}_i\cdot\boldsymbol{r}_0}\chi_i(\sigma_0), \tag{2.1}$$

where the index 0 refers to the projectile particle, $\boldsymbol{r}_0$ is it's spatial coordinates and $\chi(\sigma)$ is the spin-$\frac{1}{2}$ eigenfunction with angular projection σ. The normalisation constant is left arbitrary to emphasise generality. In the laboratory (lab) frame the origin of the coordinate system is set at the target

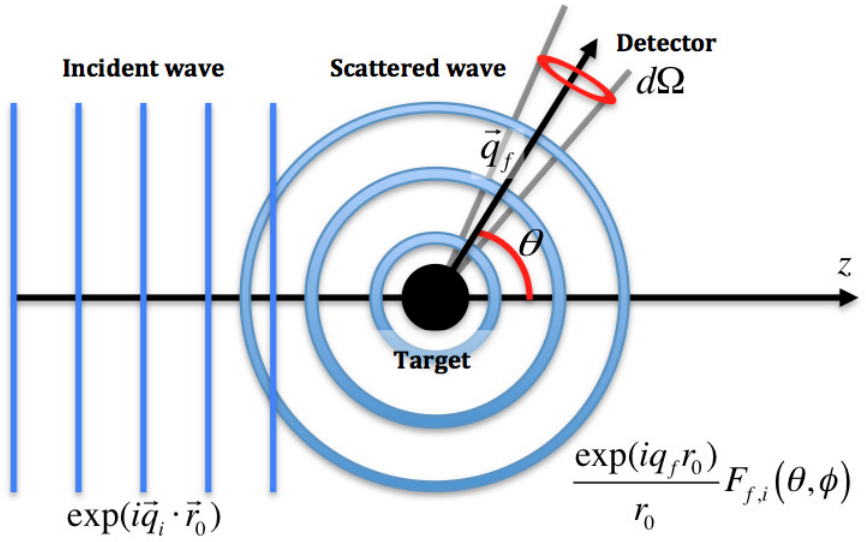

Figure 2.1: Ideal representation of a time-independent scattering experiment. The projectile incident momentum vector $\boldsymbol{q}_i$ is aligned along the laboratory frame z-axis and $F_{f,i}(\theta,\phi)$ is the scattering amplitude. Note that spin is ignored.

centre of force [205] and the projectile-particle's initial momentum vector $\boldsymbol{q}_i$ is aligned with the z-axis (i.e. $\boldsymbol{q}_i = q_i\hat{\boldsymbol{z}}$). The portion of projectile-particles scattered propagate away from the target as a spherical wave $e^{iq_f r_0}/r_0$ with linear momentum q_f, leaving the target in a final f stationary state $\bar{\Phi}_f(\mathfrak{R})$. The scattering amplitude $F^S_{f,i}(\boldsymbol{q}_f,\boldsymbol{q}_i) \equiv F^S_{f,i}(\boldsymbol{\Omega}) \equiv F^S_{f,i}(\theta,\phi)$ describes the portion of particles scattered in the direction (θ,ϕ) for a transition from the initial state i to the final state f for total spin S of the system.

For non-breakup scattering processes (dissociation by vibrational excitation (1.11) or rearrangement (1.2), (1.7) and (1.8)), the total scattering wave function $\bar{\Psi}^{S(+)}_i(\mathbf{x}_0,\mathfrak{R})$ satisfies the following asymptotic boundary condition

$$\bar{\Psi}^{S(+)}_i(\mathbf{x}_0,\mathfrak{R}) \xrightarrow[r_0\to\infty]{} N\left(e^{iq_i z_0}\chi_i(\sigma_0)\bar{\Phi}_i(\mathfrak{R}) + \sum_n \frac{e^{iq_n r_0}}{r_0}\chi_n(\sigma_0)F^S_{n,i}(\boldsymbol{q}_n,\boldsymbol{q}_i)\bar{\Phi}_n(\mathfrak{R})\right), \tag{2.2}$$

where $\mathbf{x}_0$ denotes the spatial and spin coordinates of the projectile and $(+)$ signifies outgoing spherical-wave boundary conditions. Note that the spin coupling between the projectile and the target is contained within

$F^S_{f,i}(\boldsymbol{q}_f, \boldsymbol{q}_i)$.

Scattering experiments measure currents of scattering particles and determine cross sections for a particular transition. Theoretically comparing the incident and scattered particle currents at asymptotic distances, the scattering amplitude is related to the differential and integrated cross sections, for a full derivation see Appendix A. For a scattering transition $i \to f$, the spin-resolved differential cross section (DCS) has the form

$$\frac{d\sigma^S_{f,i}}{d\Omega} = \frac{q_f}{q_i} \left| F^S_{f,i}(\boldsymbol{q}_f, \boldsymbol{q}_i) \right|^2 . \tag{2.3}$$

The integrated cross section is calculated by integrating the DCS (2.3) over all final scattering angles of the projectile

$$\sigma^S_{f,i} = \frac{q_f}{q_i} \int d\hat{q}_f \left| F^S_{f,i}(\boldsymbol{q}_f, \boldsymbol{q}_i) \right|^2 . \tag{2.4}$$

Most experiments measure the spin-averaged cross section

$$\frac{d\sigma_{f,i}}{d\Omega} = \frac{1}{2(2s_i+1)} \sum_S (2S+1) \frac{d\sigma^S_{f,i}}{d\Omega}, \tag{2.5}$$

which is calculated by averaging over the target's initial spin state s_i magnetic sub-levels and two possible spin projections of the projectile, as well as a summation over S and its projections. Hence theory's goal is to solve for $F^S_{f,i}(\boldsymbol{q}_f, \boldsymbol{q}_i)$ and $\bar{\Psi}^{S(+)}_i(\mathbf{x}_0, \mathfrak{R})$.

For neutral and ionic targets the scattering amplitude has the general form

$$\begin{aligned} F^S_{f,i}(\boldsymbol{q}_f, \boldsymbol{q}_i) &= -(2\pi)^2 \langle \boldsymbol{q}^{(-)}_f \bar{\Phi}_f | V | \bar{\Psi}^{S(+)}_i \rangle & (2.6) \\ &= -(2\pi)^2 \langle \boldsymbol{q}^{(-)}_f \bar{\Phi}_f | T^S | \bar{\Phi}_i \boldsymbol{q}^{(+)}_i \rangle, & (2.7) \end{aligned}$$

where the incoming spherical-wave boundary condition is denoted by $(-)$ and V is the sum of all interaction potentials between the projectile and the target.

Different scattering methods reflect different approaches used to solve the scattering system Schrödinger equation

$$(E^{(+)} - H) |\bar{\Psi}^{S(+)}_i\rangle = 0, \tag{2.8}$$

where E is the total energy of the scattering system and H is the total Hamiltonian of the scattering system. For a projectile with charge $z_{\rm e}$, the non-relativistic Hamiltonian H is defined as

$$\begin{aligned} H &= -\frac{1}{2}\sum_{i=0}^{N_e}\nabla_i^2 + \sum_{i=0}^{N_e}\sum_{j=1}^{N_n}\frac{z_{\rm e}Z_j}{|\boldsymbol{r}_i-\boldsymbol{R}_j|} - \sum_{j>i=0}^{N_e}\frac{z_{\rm e}}{|\boldsymbol{r}_i-\boldsymbol{r}_j|} \\ &\quad -\sum_{i=1}^{N_n}\frac{1}{2M_i}\nabla_i^2 + \sum_{j>i=1}^{N_n}\frac{Z_iZ_j}{|\boldsymbol{R}_i-\boldsymbol{R}_j|}, \end{aligned} \tag{2.9}$$

where the target molecule has N_e electrons (with charge $z_{\rm e} = -1|e|$, for $i \geq 1$), N_n nuclei with charge Z and mass M. The vectors $\boldsymbol{R}$ and $\boldsymbol{r}$ represent the nuclear and projectile/target-electronic spatial coordinates, respectively. Further details of the molecular Hamiltonian are given in [206, 207].

The total wave function $\bar{\Psi}_i^{S(+)}(\mathbf{x}_0, \mathfrak{R})$ can be expressed with the correct boundary conditions via a close-coupling expansion, which expands $\bar{\Psi}_i^{S(+)}(\mathbf{x}_0, \mathfrak{R})$ in terms of states of all asymptotic channels

$$\bar{\Psi}_i^{S(+)}(\mathbf{x}_0, \mathfrak{R}) = \mathcal{A}\sum_n f_{n,i}^{S(+)}(\mathbf{x}_0)\bar{\Phi}_n(\mathfrak{R}). \tag{2.10}$$

Here $\mathcal{A}$ is the antisymmetrisation operator

$$\mathcal{A} = 1 - \sum_{i=1}^{N_e} P_{0i}, \tag{2.11}$$

P_{0i} is the space and spin exchange operator and the multichannel functions $f_{n,i}^{S(+)}(\mathbf{x}_0)$ are regular and have the same asymptotic boundary conditions as $\bar{\Psi}_i^{S(+)}(\mathbf{x}_0, \mathfrak{R})$ in Eq. (2.2), such that

$$f_{n,i}^{S(+)}(\mathbf{x}_0) \xrightarrow[\boldsymbol{r}_0\to\infty]{} e^{iq_iz_0}\chi_i(\sigma_0)\delta_{n,i} + \frac{e^{iq_nr_0}}{r_0}\chi_n(\sigma_0)F_{n,i}^S(\boldsymbol{q}_n, \boldsymbol{q}_i). \tag{2.12}$$

Molecular states $\bar{\Phi}_n(\mathfrak{R}) \equiv \bar{\Phi}_{nvJm_J}(\mathbf{x}, \bar{\mathbf{R}})$ used in the close-coupling expansion (2.10) are characterised by their electronic state n, vibrational quantum number v, rotational quantum number J and rotational angular projection m_J, where $\mathbf{x}$ and $\bar{\mathbf{R}}$ represent all target electrons and nuclei spatial and spin coordinates respectively. Molecular states satisfy

$$\langle\bar{\Phi}_{n'v'J'm_{J'}}|H_{\rm T}|\bar{\Phi}_{nvJm_J}\rangle = \varepsilon_{nvJm_J}\delta_{n',n}\delta_{v',v}\delta_{J',J}\delta_{m_{J'},m_J}, \tag{2.13}$$

where ε_{nvJm_J} corresponds to the $nvJm_J$ state's energy and for convenience the target Hamiltonian H_{T} is defined in terms of the electronic Hamiltonian H^{Elec} and nuclear Hamiltonian H^{Nucl}

$$H_T = H^{\mathrm{Elec}} + H^{\mathrm{Nucl}}, \tag{2.14}$$

$$H^{\mathrm{Elec}} = -\frac{1}{2}\sum_{i=1}^{N_e}\nabla_i^2 - \sum_{i=1}^{N_e}\sum_{j=1}^{N_n}\frac{Z_j}{|\boldsymbol{r}_i - \boldsymbol{R}_j|} + \sum_{j>i=0}^{N_e}\frac{1}{|\boldsymbol{r}_i - \boldsymbol{r}_j|}, \tag{2.15}$$

$$H^{\mathrm{Nucl}} = -\sum_{i=1}^{N_n}\frac{1}{2M_i}\nabla_i^2 + \sum_{j>i=1}^{N_n}\frac{Z_i Z_j}{|\boldsymbol{R}_i - \boldsymbol{R}_j|}. \tag{2.16}$$

Even for the simplest diatomic molecule H_2^+ a complete electronic-rovibrational close-coupling calculation (2.10) is computationally unfeasable. This is due to the large number of energetically finely spaced rotational and vibrational states. To reduce the size of the computation a commonly used approach detailed by Lane [208] is to apply the Born-Oppenheimer approximation to the total scattering wave function.

2.1 Born-Oppenheimer and adiabatic-nuclei approximations

Neglecting electronic and nuclear spin, the Born-Oppenheimer approximation (ansatz)

$$\bar{\Phi}_{nvJm_J}(\boldsymbol{r}, \boldsymbol{R}) \approx \Phi_n(\boldsymbol{r}; \boldsymbol{R})\Xi_{nvJm_J}(\boldsymbol{R}), \tag{2.17}$$

separates the electronic vectors $\boldsymbol{r}$ and nuclear vectors $\boldsymbol{R}$ so that the electronic wave functions $\Phi_n(\boldsymbol{r}; \boldsymbol{R})$ depends parametrically on $\boldsymbol{R}$. The nuclear wave function can also be written as a product of the vibrational $\nu_{nv_nJ_n}(R)$ and rotational $R_{nJ_nm_{J_n}}(\hat{\boldsymbol{R}})$ wave functions

$$\Xi_{nv_nJ_nm_{J_n}}(\boldsymbol{R}) = \nu_{nv_nJ_n}(R)R_{nJ_nm_{J_n}}(\hat{\boldsymbol{R}}). \tag{2.18}$$

The Born-Oppenheimer approximation (2.17) relies on the property that in a molecule the electrons are very light compared to the heavy nuclei and hence are moving much more rapidly. This means that for even a small variation in the position of the nuclei, the electrons can respond and adjust (approximately) instantaneously to the nuclei potential. From a nuclear point of

view, the electrons are moving much faster than the nuclei, hence the nuclei respond to the average distribution of electron density. These are strong arguments that the electron-nuclei potential can be treated parametrically.

The Born-Oppenheimer approximation allows $\Phi_n(\boldsymbol{r};\boldsymbol{R})$ to be calculated first at any number of fixed internuclear distances $\boldsymbol{R}$. Substituting Born-Oppenheimer molecular states (2.17) and H_T (2.14) into Eq. (2.13), we obtain

$$\left\langle \Xi_{n'v'J'm_{J'}} \left| H^{\mathrm{Nucl}} + \left\langle \Phi_{n'} \left| H^{\mathrm{Elec}} \right| \Phi_n \right\rangle_{\boldsymbol{r}} \right| \Xi_{nvJm_J} \right\rangle_{\boldsymbol{R}} = \varepsilon_{nvJm_J}\delta_{n',n}\delta_{v',v}\delta_{J',J}\delta_{m_{J'},m_J}. \quad (2.19)$$

It is common practice to firstly calculate the potential energy surface $\varepsilon_n(\boldsymbol{R})$

$$\varepsilon_n(\boldsymbol{R}) = \left\langle \Phi_n \left| \sum_{j>i=1}^{N_n} \frac{Z_i Z_j}{|\boldsymbol{R}_i - \boldsymbol{R}_j|} + H^{\mathrm{Elec}} \right| \Phi_n \right\rangle_{\boldsymbol{r}}, \quad (2.20)$$

so now Eq. (2.19) becomes

$$\left\langle \Xi_{n'v'J'm_{J'}} \left| -\sum_{i=1}^{N_n} \frac{1}{2M_i}\nabla_i^2 + \varepsilon_n(\boldsymbol{R}) \right| \Xi_{nvJm_J} \right\rangle = \varepsilon_{nvJm_J}\delta_{n',n}\delta_{v',v}\delta_{J',J}\delta_{m_{J'},m_J}. \quad (2.21)$$

2.1.1 Adiabatic-nuclei approximation

From a classical point of view if the collision time t_c is much less than the molecule's vibrational period τ_v ($\approx 10^{-14}$ s) and rotational period τ_R ($>\approx 10^{-12}$ s) [208], the total scattering wave function should be well represented within the Born-Oppenheimer approximation

$$\bar{\Psi}_i^{S(+)}(\mathbf{x}_0, \mathbf{x}, \bar{\mathbf{R}}) \approx \Psi_i^{S(+)}(\mathbf{x}_0, \mathbf{x}; \boldsymbol{R})\Xi_{iv_iJ_im_{J_i}}(\bar{\mathbf{R}}). \quad (2.22)$$

Substituting Born-Oppenheimer molecular states (2.17) and the total scattering wave function (2.22) into the scattering amplitude (2.6), we obtain

the adiabatic-nuclei scattering amplitude

$$F^S_{fv_fJ_fm_{J_f},iv_iJ_im_{J_i}}(\boldsymbol{q}_f,\boldsymbol{q}_i)$$
$$= -(2\pi)^2\langle \boldsymbol{q}_f^{(-)}\Xi_{fv_fJ_fm_{J_f}}\Phi_f|V|\Psi_i^{S(+)}\Xi_{iv_iJ_im_{J_i}}\rangle \quad (2.23)$$
$$= -(2\pi)^2\langle \Xi_{fv_fJ_fm_{J_f}}|T^S_{f,i}(\boldsymbol{q}_f,\boldsymbol{q}_i;\boldsymbol{R})|\Xi_{iv_iJ_im_{J_i}}\rangle \quad (2.24)$$

where the fixed-nuclei T-matrix $T^S_{f,i}(\boldsymbol{q}_f,\boldsymbol{q}_i;\boldsymbol{R})$

$$T^S_{f,i}(\boldsymbol{q}_f,\boldsymbol{q}_i;\boldsymbol{R}) = \langle \boldsymbol{q}_f^{(-)}\Phi_f|V|\Psi_i^{S(+)}\rangle \quad (2.25)$$
$$\equiv \langle \boldsymbol{q}_f^{(-)}\Phi_f|T^S_{f,i}|\Phi_i\boldsymbol{q}_i^{(+)}\rangle. \quad (2.26)$$

Like the close-coupling expansion of $\bar{\Psi}_i^{S(+)}(\mathbf{x}_0,\mathbf{x},\bar{\mathbf{R}})$ in Eq. (2.10), the fixed-nuclei total scattering wave function $\Psi_i^{S(+)}(\mathbf{x}_0,\mathbf{x};\boldsymbol{R})$ can be expressed in a similar way

$$\Psi_i^{S(+)}(\mathbf{x}_0,\mathbf{x};\boldsymbol{R}) = \mathcal{A}\sum_n f_{n,i}^{S(+)}(\mathbf{x}_0;\boldsymbol{R})\Phi_n(\mathbf{x};\boldsymbol{R}), \quad (2.27)$$

where

$$f_{n,i}^{S(+)}(\mathbf{x}_0;\boldsymbol{R})\xrightarrow[\boldsymbol{r}_0\to\infty]{} e^{iq_iz_0}\chi_i(\sigma_0)\delta_{n,i} + \frac{e^{iq_nr_0}}{r_0}\chi_n(\sigma_0)F^S_{n,i}(\boldsymbol{q}_n,\boldsymbol{q}_i;\boldsymbol{R}) \quad (2.28)$$

and $F^S_{n,i}(\boldsymbol{q}_n,\boldsymbol{q}_i;\boldsymbol{R})$ is the fixed-nuclei scattering amplitude

$$F^S_{f,i}(\boldsymbol{q}_f,\boldsymbol{q}_i;\boldsymbol{R}) = -(2\pi)^2\langle \boldsymbol{q}_f^{(-)}\Phi_n|V|\Psi_i^{S(+)}\rangle \quad (2.29)$$
$$= -(2\pi)^2 T^S_{f,i}(\boldsymbol{q}_f,\boldsymbol{q}_i;\boldsymbol{R}). \quad (2.30)$$

In the adiabatic nuclei rotation approximation electronic and vibrational motion are coupled and only rotational motion is treated adiabatically. The total scattering wave function is parameterised in terms of the nuclei orientation $\hat{\boldsymbol{R}}$ [208] and the scattering amplitude is defined as

$$F^S_{fv_fJ_fm_{J_f},iv_iJ_im_{J_i}}(\boldsymbol{q}_f,\boldsymbol{q}_i)$$
$$= -(2\pi)^2\langle R_{fJ_fm_{J_f}}|T^S_{fv_f,iv_i}(\boldsymbol{q}_f,\boldsymbol{q}_i;\hat{\boldsymbol{R}})|R_{iJ_im_{J_i}}\rangle \quad (2.31)$$

where

$$T^S_{fv_f,iv_i}(\boldsymbol{q}_f,\boldsymbol{q}_i;\hat{\boldsymbol{R}}) = \langle \boldsymbol{q}_f^{(-)}\nu_{fv_fJ_f}\Phi_f|T^S_{fv_f,iv_i}|\Phi_i\nu_{iv_iJ_i}\boldsymbol{q}_i^{(+)}\rangle, \tag{2.32}$$

and the vibrational wave functions have a very minor dependence on J. Sometimes the adiabatic nuclei rotation approximation is synonymous with the adiabatic-nuclei [208] or fixed-nuclei approximation [69, 209], in which case electronic and vibrational motion are not coupled.

2.1.2 Accuracy of the adiabatic approximation

The adiabatic-nuclei approximation is expected to fail when the collision time t_c is comparable to the vibrational τ_v and rotational τ_R periods [208]. This can occur in the impact-energy region near a resonance or when the impact-energy is very near excitation threshold. Also in the adiabatic-nuclei approximation excitation threshold energies are not treated adequately, all vibrational and rotational transitions at a fixed R are treated as degenerate.

Several methods have investigated the accuracy of the adiabatic-nuclei method. Peek and Green [19] investigated electron scattering from vibrationally excited H_2^+ within the Born approximation calculating integrated cross sections for the transition $iv_i \rightarrow f$. They formulated the total scattering wave function and molecular states of H_2^+ without the use of the Born-Oppenheimer approximation. These results were compared with calculations that utilised the adiabatic-nuclei approximation. They showed that these results agreed with each other in almost all cases. Inaccuracies in the adiabatic-nuclei approximation were found when considering scattering from highly excited vibrational states of H_2^+.

For ions Faure et al. [209] have shown that by multiplying the rotational excitation cross sections by the Heaviside step function, the fixed-nuclei approximation is sufficiently accurate even at energies near threshold, except in the presence of large Rydberg resonances. The Heaviside step function is used to force the rotational excitation cross sections to zero at the respective excitation threshold energy. Chang and Temkin [210] have investigated the accuracy of e^--H_2 rotational excitation cross sections in the fixed-nuclei approximation. Even at energies close to threshold these results qualitatively agreed with rotational close-coupling results.

Mazevet et al. [85] have reviewed the accuracy of vibrational excita-

tion cross sections by utilising different energy correction methods of the adiabatic-nuclei approximation. These methods include the first-order non-degenerate adiabatic approximation (FONDA), the energy modified adiabatic approximation (EMA) [211], energy-modified adiabatic phase matrix (EMAP) method and an energy corrected adiabatic nuclear vibration method, referred to as ANVf. Investigating results of electron scattering from H_2 and comparing with vibrational close-coupling results, Mazevet et al. [85] concluded that the relatively simple EMAP method produces reasonably accurate vibrational excitation cross sections at energies away from threshold and non-adiabatic resonances. For very accurate excitation cross sections near threshold the FONDA method is better suited, it retains energy conservation and produces results with the correct threshold behaviour.

2.2 Diatomic molecule adiabatic cross sections

Initially the adiabatic scattering amplitudes (2.24) and (2.31) look like they require data of the T-matrix for many orientations of $\hat{\boldsymbol{R}}$. For a molecular target with a given symmetry (i.e. diatomics), analytic integration over $\hat{\boldsymbol{R}}$ can be carried out by utilising the rotation matrix to rotate the coordinate system. The method applied here requires the T-matrix to be expressed in partial-wave form and is applicable to both the adiabatic-nuclei approximation (2.24) and adiabatic nuclear rotation approximation of Lane [208] (electronic and vibrational coupling). In the equations presented below the adiabatic-nuclei scattering amplitude (2.24) is assumed.

Utilising the target molecule's symmetry and the rotation matrix, the T-matrix $T^S_{f,i}(\boldsymbol{q}_f, \boldsymbol{q}_i; \boldsymbol{R})$ only needs to be calculated for one-orientation of the molecule $\hat{\boldsymbol{R}}$. This single orientation of the molecule is chosen as the most convenient and is formulated in the body-frame of reference (labelled by superscript $^{(\mathrm{b})}$), see Fig. 2.2. In this frame of reference for homonuclear diatomic molecules it is convenient to set the origin halfway between the nuclei and to align the internuclear axis with the z-axis i.e. $\hat{\boldsymbol{R}}^{(\mathrm{b})} = \hat{\boldsymbol{z}}^{(\mathrm{b})}$. For homonuclear diatomic molecules this choice of coordinate system ensures that electronic target states can be characterised by spin, parity and orbital angular momentum projection.

The three-dimensional body-frame fixed-nuclei T-matrix $T^S_{f,i}(\boldsymbol{q}_f^{(\mathrm{b})}, \boldsymbol{q}_i^{(\mathrm{b})}; R)$ is still computationally demanding to calculate. In

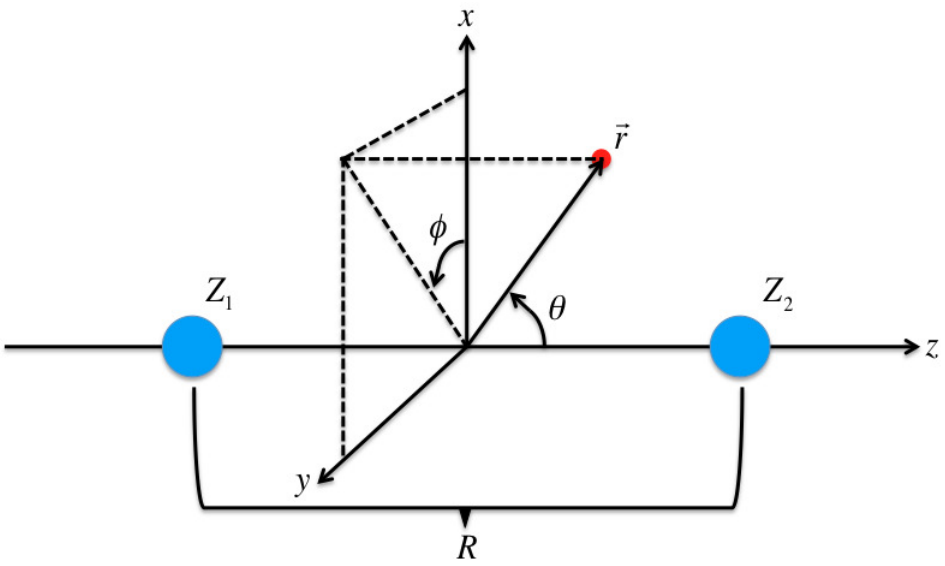

Figure 2.2: Body-frame coordinate system for a diatomic molecule.

order to reduce the computational resources required, $T^S_{f,i}(\boldsymbol{q}_f^{(\mathrm{b})}, \boldsymbol{q}_i^{(\mathrm{b})}; R)$ is expanded in partial waves of the projectile. In the convergent close-coupling method $T^S_{f,i}(\boldsymbol{q}_f^{(\mathrm{b})}, \boldsymbol{q}_i^{(\mathrm{b})}; R)$ is conveniently expressed as

$$T^S_{f,i}(\boldsymbol{q}_f^{(\mathrm{b})}, \boldsymbol{q}_i^{(\mathrm{b})}; R) = (q_f q_i)^{-1} \sum_{\substack{L_f, L_i \\ M_f, M_i}} i^{L_i - L_f} e^{i(\sigma_{L_i} + \sigma_{L_f})} \times T^{S(\mathrm{b})}_{fL_fM_f, iL_iM_i}(q_f, q_i; R) Y_{L_fM_f}(\hat{\boldsymbol{q}}_f^{(\mathrm{b})}) Y^*_{L_iM_i}(\hat{\boldsymbol{q}}_i^{(\mathrm{b})}), \tag{2.33}$$

where the scattered particle orbital angular momentum L and angular projection M are indexed i and f for initial and final states respectively, σ_L is the Coulomb phase shift of the Coulomb wave function and $\boldsymbol{q}^{(\mathrm{b})}$ indicates the scattered particle momentum vector in the body-frame. Fixed-nuclei body-frame T-matrix elements $T^{S(\mathrm{b})}_{fL_fM_f,iL_iM_i}(q_f, q_i; R)$ are formulated in Chapter 4. Some experiments measure cross sections of aligned target molecules [166]. To compare with these experiments the scattering amplitude in the DCS (2.3) is formulated in the body-frame $F^S_{f,i}(\boldsymbol{q}_f^{(\mathrm{b})}, \boldsymbol{q}_i^{(\mathrm{b})})$ and is calculated for an appropriate angle of $\hat{\boldsymbol{q}}_i^{(\mathrm{b})}$.

It is important to note that the good quantum numbers of the electronic target states (for homonuclear diatomic molecules spin, parity and orbital angular momentum projection) are the same for $T^{S(\mathrm{b})}_{fL_fM_f,iL_iM_i}(q_f, q_i; R)$.

Hence the formulation of $T^{S(\mathrm{b})}_{fL_fM_f,iL_iM_i}(q_f, q_i; R)$ is also dependent upon the choice of the body-frame. For example for homonuclear diatomic molecules, there is no conservation of total orbital angular projection if one chooses $\hat{\boldsymbol{R}}^{(\mathrm{b})}$ to be unaligned with $\hat{\boldsymbol{z}}^{(\mathrm{b})}$, there is also no conservation of parity if the origin is not chosen halfway between the nuclei.

Most experiments take measurements of unaligned target molecules. In this case, the scattering amplitude in the DCS Eq. (2.3) is defined in the lab-frame of reference $F^S_{f,i}(\boldsymbol{q}_f^{(\mathrm{lab})}, \boldsymbol{q}_i^{(\mathrm{lab})})$ and hence is a function of $T^S_{f,i}(\boldsymbol{q}_f^{(\mathrm{lab})}, \boldsymbol{q}_i^{(\mathrm{lab})}; \boldsymbol{R}^{(\mathrm{lab})})$, where $\boldsymbol{q}^{(\mathrm{lab})}$ indicates the scattered particle momentum vector in the lab-frame (and superscript $^{(\mathrm{lab})}$ refers to the lab-frame of reference). Therefore the body-frame T-matrix $T^S_{f,i}(\boldsymbol{q}_f^{(\mathrm{b})}, \boldsymbol{q}_i^{(\mathrm{b})}; R)$ needs to be transformed to the lab-frame. To rotate and align $\hat{\boldsymbol{q}}^{(\mathrm{b})}$ to $\hat{\boldsymbol{q}}^{(\mathrm{lab})}$, the following definitions are utilised

$$Y_{LM}(\Omega') = \sum_{\kappa} D^L_{\kappa,M}(\boldsymbol{\beta}) Y_{L\kappa}(\Omega), \tag{2.34}$$

$$Y^*_{LM}(\Omega') = \sum_{\kappa} D^{L*}_{\kappa,M}(\boldsymbol{\beta}) Y^*_{L\kappa}(\Omega), \tag{2.35}$$

where $D^{L*}_{\kappa,M}(\boldsymbol{\beta})$ are the Wigner-D rotation matrices and $\boldsymbol{\beta} \equiv (\alpha, \beta, \gamma)$ are the Euler angles. Here we adopt the conventions of Edmonds [212], where the original reference frame C can be transformed by three consecutive rotations designated by the frames of reference C', C'' and C''', respectively. The order of rotation: is first a rotation about the z-axis by angle α transforming $C \rightarrow C'$, the second is a rotation about the y'-axis by angle β transforming $C' \rightarrow C''$ and lastly, a rotation about the z''-axis by angle γ transforming $C'' \rightarrow C'''$. A positive rotation angle is designated by the right-handed screw rule about the axis of rotation.

In definitions (2.34) and (2.35) the Euler angles are chosen to align the body-frame internuclear axis ($\hat{\boldsymbol{R}}^{(\mathrm{b})} = \hat{\boldsymbol{z}}^{(\mathrm{b})}$) with the lab-frame internuclear axis $\hat{\boldsymbol{R}}^{(\mathrm{lab})}$. Referring to Fig. 2.3, this only requires two rotations such that the Euler angles are $\boldsymbol{\beta} = (\phi_{\hat{\boldsymbol{R}}}, \theta_{\hat{\boldsymbol{R}}}, 0) = \hat{\boldsymbol{R}}^{(\mathrm{lab})}$. The body-frame is originally designated by the frame of reference C. First a rotation about the z-axis by angle $\alpha = \phi_{\hat{\boldsymbol{R}}}$ rotates the z,x-plane to the z,x'-plane, which is in the same plane as the lab-frame internuclear axis. Secondly a rotation about the new y'-axis by angle $\beta = \theta_{\hat{\boldsymbol{R}}}$ brings the new body-frame internuclear axis ($\hat{\boldsymbol{z}}$') in line with the lab-frame internuclear axis ($\hat{\boldsymbol{z}}$"). After these rota-

tions, the body-frame has been rotated to C'' and the lab-frame coordinate system is now designated by C. Note that the lab-frame incident projectile-momentum is along the z-axis. Alternatively these rotations can be thought of as rotating $\hat{\boldsymbol{q}}_i^{(\mathrm{b})}$ to be aligned with the lab-frame z-axis, i.e. $\hat{\boldsymbol{q}}_i^{(\mathrm{lab})} = \hat{\boldsymbol{z}}^{(\mathrm{lab})}$.

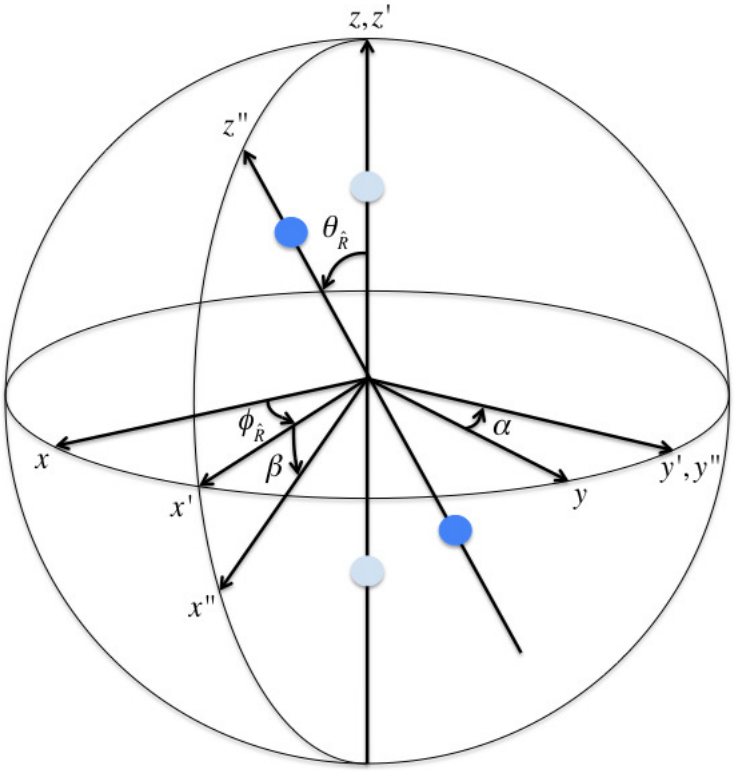

Figure 2.3: A figure of the body-frame coordinate system originally designated by the frame of reference C, rotated by Euler angles to align the body-frame internuclear axis z with the lab-frame internuclear axis z''. See text for further details.

For our application having $\boldsymbol{\beta} = (\phi_{\hat{\boldsymbol{R}}}, \theta_{\hat{\boldsymbol{R}}}, 0) = \hat{\boldsymbol{R}}^{(\mathrm{lab})}$, transforms definitions (2.34) and (2.35) to

$$Y_{LM}(\hat{\boldsymbol{q}}^{(\mathrm{b})}) = \sum_{\kappa} D^{L}_{\kappa,M}(\hat{\boldsymbol{R}}^{(\mathrm{lab})}) Y_{L\kappa}(\hat{\boldsymbol{q}}^{(\mathrm{lab})}), \tag{2.36}$$

$$Y^{*}_{LM}(\hat{\boldsymbol{q}}^{(\mathrm{b})}) = \sum_{\kappa} D^{L*}_{\kappa,M}(\hat{\boldsymbol{R}}^{(\mathrm{lab})}) Y^{*}_{L\kappa}(\hat{\boldsymbol{q}}^{(\mathrm{lab})}). \tag{2.37}$$

Utilising these definitions and noting that the lab-frame incident projectile-momentum is aligned along the z-axis (refer Appendix C Eq. (C.30)),

$T^S_{f,i}(\boldsymbol{q}_f^{(\mathrm{b})}, \boldsymbol{q}_i^{(\mathrm{b})}; R)$ is transformed to $T^S_{f,i}(\boldsymbol{q}_f^{(\mathrm{lab})}, \boldsymbol{q}_i^{(\mathrm{lab})}; \boldsymbol{R}^{(\mathrm{lab})})$. The lab-frame fixed-nuclei T-matrix is now expressed as

$$T^S_{f,i}(\boldsymbol{q}_f^{(\mathrm{lab})}, \boldsymbol{q}_i^{(\mathrm{lab})}; \boldsymbol{R}^{(\mathrm{lab})}) = (q_f q_i \sqrt{4\pi})^{-1} \sum_{\substack{L_f, L_i \\ M_f, M_i}} \hat{L}_i i^{L_i - L_f} e^{i(\sigma_{L_i} + \sigma_{L_f})} \tag{2.38}$$

$$\times T^{S(\mathrm{b})}_{fL_fM_f, iL_iM_i}(q_f, q_i; R) \sum_\kappa D^{L_f}_{\kappa, M_f}(\hat{\boldsymbol{R}}^{(\mathrm{lab})}) Y_{L_f\kappa}(\hat{\boldsymbol{q}}_f^{(\mathrm{lab})}) D^{L_i *}_{0, M_i}(\hat{\boldsymbol{R}}^{(\mathrm{lab})}),$$

where $\hat{L}_i = \sqrt{(2L_i + 1)}$. Now $F^S_{f,i}(\boldsymbol{q}_f^{(\mathrm{lab})}, \boldsymbol{q}_i^{(\mathrm{lab})})$ in (2.3) is conveniently expressed in partial-wave form for the transition $iv_iJ_im_{J_i} \to fv_fJ_fm_{J_f}$

$$F^S_{fv_fJ_fm_{J_f}, iv_iJ_im_{J_i}}(\boldsymbol{q}_f^{(\mathrm{lab})}, \boldsymbol{q}_i^{(\mathrm{lab})}) = (\sqrt{4\pi})^{-1} \sum_{\substack{L_f, L_i \\ M_f, M_i}} \hat{L}_i \tag{2.39}$$

$$\times \langle \Xi_{fv_fJ_fm_{J_f}} | A^{S(\mathrm{b})}_{fL_fM_f, iL_iM_i} \sum_\kappa D^{L_f}_{\kappa, M_f} D^{L_i *}_{0, M_i} | \Xi_{iv_iJ_im_{J_i}} \rangle_{\bar{\mathbf{R}}^{(\mathrm{lab})}} Y_{L_f\kappa}(\hat{\boldsymbol{q}}_f^{(\mathrm{lab})}),$$

where nuclear wave functions $\Xi_{nv_nJ_nm_{J_n}}(\bar{\mathbf{R}}^{(\mathrm{lab})})$ are formulated in the lab-frame and

$$A^{S(\mathrm{b})}_{fL_fM_f, iL_iM_i}(R) = -(2\pi)^2 (q_f q_i)^{-1} i^{L_i - L_f} \tag{2.40}$$

$$\times e^{i(\sigma_{L_i} + \sigma_{L_f})} T^{S(\mathrm{b})}_{fL_fM_f, iL_iM_i}(q_f, q_i; R).$$

The form of $F^S_{fv_fJ_fm_{J_f}, iv_iJ_im_{J_i}}(\boldsymbol{q}_f^{(\mathrm{lab})}, \boldsymbol{q}_i^{(\mathrm{lab})})$ (2.39) is general and can be applied to other definitions of the scattering T-matrix. Substituting the nuclear wave function (2.18) into Eq. (2.39) and noting the orthogonality of nuclear spin functions, the integral can now be separated into radial and angular integration terms

$$F^S_{fv_fJ_fm_{J_f}, iv_iJ_im_{J_i}}(\boldsymbol{q}_f^{(\mathrm{lab})}, \boldsymbol{q}_i^{(\mathrm{lab})}) \tag{2.41}$$

$$= (\sqrt{4\pi})^{-1} \sum_{\substack{L_f, L_i \\ M_f, M_i}} \hat{L}_i \langle \nu_{fv_fJ_f} | A^{S(\mathrm{b})}_{fL_fM_f, iL_iM_i} | \nu_{iv_iJ_i} \rangle_R$$

$$\times \langle R_{fJ_fm_{J_f}} | \sum_\kappa D^{L_f}_{\kappa, M_f} D^{L_i *}_{0, M_i} | R_{iJ_im_{J_i}} \rangle_{\hat{\boldsymbol{R}}^{(\mathrm{lab})}} Y_{L_f\kappa}(\hat{\boldsymbol{q}}_f^{(\mathrm{lab})}),$$

and it is now clear that $A^{S(\mathrm{b})}_{fL_fM_f, iL_iM_i}(R)$ is calculated for only one orientation of the molecule $\hat{\boldsymbol{R}}^{(\mathrm{b})}$.

Non-rigid (vibrating) linear molecules behave like symmetric-top molecules [206], the rotational wave function is written as

$$R_{nJ_nm_{J_n}}(\hat{\boldsymbol{R}}) = \sqrt{\frac{(2J_n+1)}{8\pi^2}} D^{J_n*}_{m_{J_n},m_n}(\hat{\boldsymbol{R}}), \tag{2.42}$$

where m_{J_n} is the angular projection of J_n and m_n is the orbital angular projection of the electronic state. Hund's coupling cases are idealised situations of describing the total molecular wave function and can lead to various forms of the rotational wave function [206].

In the rigid (non-vibrating) rotor approximation the rotational wave function is given by

$$R_{nJ_nm_{J_n}}(\hat{\boldsymbol{R}}) = Y_{J_nm_{J_n}}(\hat{\boldsymbol{R}}), \tag{2.43}$$

which is spherically symmetric for $J_n = 0$. Some studies utilise the rigid rotor approximation to formulate the DCS [84, 213]. Substituting an appropriate rotational wave function (for the molecular target) into the scattering amplitude of (2.41), the integration over $\hat{\boldsymbol{R}}^{(\mathrm{lab})}$ can be carried out analytically. Then the DCS (2.3) resolved for the transition $iv_iJ_im_{J_i} \to fv_fJ_fm_{J_f}$ can be formulated [208].

2.2.1 Classical orientation averaging

As most scattering experiments do not resolve rotational transitions, here rotational excitation cross sections are not calculated and instead the classical orientation averaging procedure is adopted [214]. In the classical orientation averaging procedure the target diatomic molecule has equal probability of being oriented in an arbitrary direction. The DCS for the transition $iv_i \to fv_f$ is calculated by averaging over all orientations of the molecule [93, 214–216]. In this method the body-frame scattering amplitude is defined for the transition $iv_i \to fv_f$

$$F^S_{fv_f,iv_i}(\boldsymbol{q}_f^{(\mathrm{b})}, \boldsymbol{q}_i^{(\mathrm{b})}) = \sum_{\substack{L_f,L_i \\ M_f,M_i}} \langle \nu_{fv_f} | A^{S(\mathrm{b})}_{fL_fM_f,iL_iM_i} | \nu_{iv_i} \rangle_R \times Y_{L_fM_f}(\hat{\boldsymbol{q}}_f^{(\mathrm{b})}) Y^*_{L_iM_i}(\hat{\boldsymbol{q}}_i^{(\mathrm{b})}). \tag{2.44}$$

Note that vibrational wave functions $\nu_{nvJ}(R)$ have a very minor dependence on J. Hence it can be assumed the vibrational wave functions are independent of J, i.e. ν_{fv_f}. $F^S_{fv_f,iv_i}(\boldsymbol{q}_f^{(\mathrm{b})}, \boldsymbol{q}_i^{(\mathrm{b})})$ is transformed to the lab-frame utilising the method described in the previous Section and definitions (2.36) and (2.37)

$$F^S_{fv_f,iv_i}(\boldsymbol{q}_f^{(\mathrm{lab})}, \boldsymbol{q}_i^{(\mathrm{lab})}, \hat{\boldsymbol{R}}^{(\mathrm{lab})}) = (\sqrt{4\pi})^{-1} \sum_{\substack{L_f,L_i \\ M_f,M_i}} \hat{L}_i \tag{2.45}$$

$$\times \langle \nu_{fv_f} | A^{S(\mathrm{b})}_{fL_fM_f,iL_iM_i} | \nu_{iv_i} \rangle_R \sum_{\kappa} D^{L_f}_{\kappa,M_f}(\hat{\boldsymbol{R}}^{(\mathrm{lab})}) D^{L_i*}_{0,M_i}(\hat{\boldsymbol{R}}^{(\mathrm{lab})}) Y_{L_f\kappa}(\hat{\boldsymbol{q}}_f^{(\mathrm{lab})}).$$

The lab-frame scattering amplitude $F^S_{fv_f,iv_i}(\boldsymbol{q}_f^{(\mathrm{lab})}, \boldsymbol{q}_i^{(\mathrm{lab})}, \hat{\boldsymbol{R}}^{(\mathrm{lab})})$ is substituted into the DCS Eq. (2.3) and averaged over all orientations of the molecule

$$\frac{d\sigma^S_{fv_f,iv_i}}{d\Omega^{(\mathrm{lab})}} = \frac{q_f}{q_i} \frac{1}{4\pi} \int_0^{2\pi} \int_0^{\pi} |F^S_{fv_f,iv_i}(\boldsymbol{q}_f^{(\mathrm{lab})}, \boldsymbol{q}_i^{(\mathrm{lab})}, \hat{\boldsymbol{R}}^{(\mathrm{lab})})|^2 d\Omega_{R^{(\mathrm{lab})}}. \tag{2.46}$$

The orientationally averaged DCS (2.46) is evaluated in Appendix B, and the final form is

$$\frac{d\sigma^S_{fv_f,iv_i}}{d\Omega^{(\mathrm{lab})}} = \frac{q_f}{q_i} \frac{1}{(4\pi)^2} \sum_{\substack{L_f,L_i \\ M_f,M_i}} \sum_{\substack{L'_f,L'_i \\ M'_f,M'_i}} (-1)^{M'_f - M'_i} \hat{L}_i \hat{L}'_i \hat{L}_f \hat{L}'_f \tag{2.47}$$

$$\times \langle \nu_{fv_f} | A^{S(\mathrm{b})}_{fL_fM_f,iL_iM_i} | \nu_{iv_i} \rangle_R \langle \nu^*_{fv_f} | A^{S(\mathrm{b})*}_{fL'_fM'_f,iL'_iM'_i} | \nu^*_{iv_i} \rangle_{R'}$$

$$\times \sum_j (2j+1)^{-1} C^{j0}_{L_i0,L'_i0} C^{jM'_i - M_i}_{L_i - M_i,L'_iM'_i} C^{jM_f - M'_f}_{L_fM_f,L'_f - M'_f} C^{j0}_{L_f0,L'_f0}$$

$$\times P_j(\cos(\theta^{(\mathrm{lab})})) \delta_{M_i - M'_i, M_f - M'_f}.$$

For a molecule in the $J_i = 0$ state, this form of the DCS (2.46) and (2.47), is equivalent to substituting the lab-frame scattering amplitude (2.41) and rigid rotor rotational wave function (2.43) into the DCS (2.3) and summing transitions over all final rotational states.

Utilising Eq. (2.4) the integrated cross sections are calculated by integrating the DCS in Eq. (2.47) over all final angles. Orientationally averaged

integrated cross sections have the final form

$$\sigma^S_{fv_f,iv_i} = \frac{q_f}{q_i}\frac{1}{4\pi}\sum_{\substack{L_f,L_i\\M_f,M_i}} |\langle \nu_{fv_f}|A^{S(\mathrm{b})}_{fL_fM_f,iL_iM_i}|\nu_{iv_i}\rangle_R|^2, \tag{2.48}$$

$$= 4\pi^3\frac{1}{q_f q_i^3}\sum_{\substack{L_f,L_i\\M_f,M_i}} |\langle \nu_{fv_f}|T^{S(\mathrm{b})}_{fL_fM_f,iL_iM_i}(q_f,q_i;R)|\nu_{iv_i}\rangle_R|^2, \tag{2.49}$$

where $T^{S(\mathrm{b})}_{fL_fM_f,iL_iM_i}(q_f,q_i;R)$ is the body-frame fixed-nuclei T-matrix elements from Eq. (2.38). This form of the integrated cross section is consistent with Lane [208], who calculated the integrated cross section using the scattering amplitude defined in Eq. (2.41).

Some experiments measure cross sections resolved for the transition $iv_i \to f$. This cross section is the sum of transitions to all final vibrational levels, for example measurements of the total cross section. The closure property of the vibrational wave functions

$$\sum\!\!\!\!\!\!\int_{v_f} \nu^*_{fv_f}(R)\nu_{fv_f}(R') = \frac{1}{R'^2}\delta(R-R'), \tag{2.50}$$

is utilised to sum integrated cross sections in Eq. (2.48) over all final vibrational states

$$\begin{aligned}\sigma^S_{f,iv_i} &= \sum\!\!\!\!\!\!\int_{v_f} \sigma^S_{fv_f,iv_i}\\ &= \frac{q_f}{q_i}\frac{1}{4\pi}\sum_{\substack{L_f,L_i\\M_f,M_i}}\int R^2dR|A^{S(\mathrm{b})}_{fL_fM_f,iL_iM_i}(R)|^2|\nu_{iv_i}(R)|^2.\end{aligned} \tag{2.51}$$

For convenience the integrated cross section in Eq. (2.51) can be expressed in the alternative form

$$\sigma^S_{f,iv_i} = \int R^2dR\ \sigma^S_{f,i}(R)|\nu_{iv_i}(R)|^2, \tag{2.52}$$

where $\sigma^S_{f,i}(R)$ is the fixed-nuclei integrated cross section at the internuclear

distance R

$$\sigma^S_{f,i}(R) = \frac{q_f}{q_i}\frac{1}{4\pi}\sum_{\substack{L_f,L_i\\M_f,M_i}} |A^{S(\mathrm{b})}_{fL_fM_f,iL_iM_i}(R)|^2 \tag{2.53}$$

$$= 4\pi^3\frac{1}{q_f q_i^3}\sum_{\substack{L_f,L_i\\M_f,M_i}} |T^{S(\mathrm{b})}_{fL_fM_f,iL_iM_i}(q_f,q_i;R)|^2. \tag{2.54}$$

Because the probability density function of the vibrational ground state ($v = 0$) is approximately a Gaussian function, a common approximation is to replace the integration in Eq. (2.52) with a fixed-nuclei cross section chosen at an appropriate value of $R = R_c$. This value R_c is generally chosen as the equilibrium distance $R = R_0$, which is localised at the position near the peak of the vibrational ground state wave function. Referred to as the fixed-nuclei approximation Eq. (2.52) becomes

$$\sigma^S_{f,iv_i=0} \approx \sigma^S_{f,i}(R_0) \tag{2.55}$$

$$= \frac{q_f}{q_i}\frac{1}{4\pi}\sum_{\substack{L_f,L_i\\M_f,M_i}} |A^{S(\mathrm{b})}_{fL_fM_f,iL_iM_i}(R_0)|^2.$$

Here the choice of the arbitrary fixed-nuclei distance R_c is investigated. Expressing the fixed-nuclei cross section as a Taylor series expansion about the arbitrary internuclear distance R_c

$$\sigma^S_{f,i}(R) = \sigma^S_{f,i}(R_c) + (R - R_c)\left(\frac{d\sigma^S_{f,i}}{dR}\right)_{R=R_c} + \cdots. \tag{2.56}$$

Substituting this expression into Eq. (2.52) to the first order variations about R_c

$$\sigma^S_{f,iv_i} = \sigma^S_{f,i}(R_c) \tag{2.57}$$

$$+ \left(\frac{d\sigma^S_{f,i}}{dR}\right)_{R=R_c}\int R^2 dR\ (R - R_c)|\nu_{iv_i}(R)|^2.$$

By choosing R_c to be the mean internuclear distance R_m of the initial vibrational wave function (v_i), the integral is zero. Hence in the fixed-nuclei approximation the equilibrium distance is more accurately replaced by the

mean internuclear distance of the vibrational ground state $R = R_m$ [28, 29], where

$$R_m = \langle R \rangle_{iv_i=0} = \langle \nu_{iv_i=0} | R | \nu_{iv_i=0} \rangle. \tag{2.58}$$

2.3 Types of scattering models

Many studies have utilised the first Born approximation (FBA), distorted-wave Born approximation (DWBA), unitarised Born approximation (UBA), Born expansion approximation, static exchange (SE) and static exchange plus polarisation (SEP) approximations for computationally demanding calculations. Contrary to electron-scattering, a positron projectile does not have the exchange interaction with the target electrons, hence the term "exchange" is dropped when describing these approximations in positron-scattering. The SE and SEP approximations have been described in detail by Tennyson [69], while the Born approximations have been described by Bray and Stelbovics [217]. Here a brief overview of their definition and accuracy is given.

2.3.1 First Born approximation

The FBA is an approximation of the Lippmann-Schwinger equation for the T-matrix $T = V + VG_0T$, where V is the interaction-potential matrix and G_0 is the Greens function matrix. In the FBA the T-matrix is approximated by $T = V$ and hence neglects channel coupling. Formally in the FBA, plane-waves are used to describe the projectile wave function before and after the collision. Hence distortion of the incident channel functions by the interaction potential is ignored. The exchange-interaction potential is formally omitted and a distorting potential U is not used. This approximation is not unitary but works well for high impact energies as G_0 is inversely proportional to the total energy of the scattering system. The Born approximation is typically accurate at 10 times the threshold energy of the transition of interest. The Born approximation can be improved by including the exchange-interaction, enforcing unitarity and utilising incident projectile wave functions that have distortion similar to that of the interaction potential.

2.3.2 Distorted-wave Born approximation

The DWBA includes distortion of the incident projectile-wave to improve on the FBA. Distorted-waves are the solution of the free particle minus short-ranged potential U Schrödinger equation. The physical interaction potential V is expressed as $V = (V - U) + U$ and the physical T-matrix $T \equiv \langle Q_f^{(-)}|T|Q_i^{(+)}\rangle$ is then calculated by

$$\langle Q_f^{(-)}|T|Q_i^{(+)}\rangle = \langle X_f^{(-)}|(V-U)|X_i^{(+)}\rangle + \langle X_f^{(-)}|U|Q_i^{(+)}\rangle, \tag{2.59}$$

where $X^{(\pm)}$ are the distorted-wave channel functions [196]. The distorting potential should be chosen such that $V - U$ is small [218]. If results of the DWBA are very similar to the FBA these approximations are likely to be accurate. The DWBA is not unitary.

2.3.3 Unitarised Born approximation

In the UBA the K-matrix is approximated by $K = V$. Transforming the K-matrix to the T-matrix unitarity is enforced. This approximation can include the exchange-interaction, which is referred to as the UBA with exchange and improves the energy range of validity of the UBA. It can also utilise distorted-waves to approximate the incident projectile wave function.

2.3.4 Born expansion approximation

The Born expansion approximation is an improvement of the FBA, where the T-matrix is calculated by an iterative procedure. The n-order Born approximation is given as $T^{(n)} = V + VGT^{(n-1)}$, where the first-order Born approximation (or FBA) has $T^{(1)} = V$. Though the matrix elements of the $n \geq 2$ approximation are relatively complicated to formulate, high-order effects are important. For example for elastic scattering the effects of dipole polarisation are important. Dipole polarisation effects are not included in the FBA approximation and only take effect at the second-order Born approximation level. This approximation is more accurate than the FBA at lower-energies. At high orders of the Born approximation the matrix elements become more complicated than numerically solving the scattering equations. Unitarity can be imposed by performing the series expansion for the K-matrix rather than T-matrix.

2.3.5 Static exchange approximation

The following approximations are all based on the close-coupling method and are therefore unitary. In the SE approximation only one target state wave function is included in the close-coupling expansion. This state is usually described within the Hartree-Fock (also known as the self-consistent field) approximation. Exchange between the projectile-electron and target electrons is explicitly included. The SE approximation cannot treat electronic excitation processes and hence Feshbach resonances, which implicitly involve electronic excitation. Shape resonances can be treated within this approximation, although the resulting positions are usually too high in energy.

2.3.6 Static exchange plus polarisation approximation

The SEP approximation only includes one target state wave function in the close-coupling expansion, however target polarisation effects are included by utilising either an optical potential or local polarisation potential. Some methods (like the R-matrix method) include polarisation effects by including singly excited target-state configurations, promoting a target electron and the projectile-electron to virtual orbitals. This is called two particle, one hole (2p,1h) configurations and is sometimes known as the polarised self-consistent field method. In the Hartree-Fock approximation these singly excited target-state configurations do not improve the ground-state Hartree-Fock wave function. Although this method cannot explicitly treat electronic excitation, it can resolve both Feshbach and shape resonances. Compared to the SE approximation, inclusion of polarisation effects in the SEP approximation lowers the shape resonance position.

2.3.7 Close-coupling

To improve on these approximations many target states can be included into the close-coupling expansion. This method is attractive because it explicitly includes electronic excitations and implicitly includes polarisation and high-order effects. Convergence and accuracy of the results can also be investigated in a systematic approach by increasing the number of target states included in the close-coupling expansion. This method has been widely used in atomic scattering with great success [195–199, 203, 204, 219].

For molecules calculations using a complete close-coupling expansion is computationally expensive. An inherent issue in this method is the choice of configurations used to represent a complete close-coupling expansion.

2.3.8 Positron scattering single-centre expansion

For a complete description of positron scattering, the total asymptotic scattering wave function must include positronium formation. In a close-coupling expansion of the total wave function, a two centre expansion is required. The first expansion is over the target, while the second expansion is over the positronium states. This method is complicated to implement and calculations are computationally expensive. For atomic targets this method has also been known to suffer from ill conditioning [220, 221]. Until recently [222], the only two centre expansion molecular calculation utilised a two-state expansion, one-state for H_2 and one-state for positronium [223].

In the single-centre expansion the total scattering wave function is expanded just over target states of the molecule. This close-coupling expansion includes positronium formation implicitly by including configurations that have an electron and positron in the continuum, which corresponds to both the direct ionisation and positronium formation channels. Hence the single-centre expansion includes these channels indirectly and results of the total ionisation cross section (sum of the direct ionisation and positronium formation cross sections) can be calculated by summing over individual excitation cross sections to positive energy states.

It is important to note that contrary to the electron-electron interaction, the positron-electron interaction is attractive and hence strongly correlated [69]. To describe long-ranged correlations of the positron-electron potential (in the single-centre expansion method) a relatively large partial-wave expansion of the potential is required. These large partial waves are constructed from target state orbitals that have large orbital angular momentum.

Compared to the two-centre expansion, the single-centre expansion is simple to implement, computationally efficient and numerically stable. However there are several minor drawbacks of this method, the first of which is that the positronium formation and direct ionisation channels are indistinguishable. In the energy-region between the positronium formation threshold (6.8 eV below ionisation threshold) and the ionisation threshold, incor-

rect cross sections are calculated. This is because an electron can be in the continuum below the direct ionisation threshold (positronium formation), which causes a mismatch of boundary conditions in the single-centre expansion cross sections. Performing single-centre calculations with target state orbitals that have small values of orbital angular momentum, an estimate of the cross sections in this energy-region can be obtained.

Chapter 3

Single-centre molecular target structure

In this Chapter H_2^+ and H_2 molecular target states are formulated in a single-centre expansion. Here the Born-Oppenheimer approximation (2.17) is utilised and the formulation concentrates primarily on calculating electronic wave functions $\Phi_n(\boldsymbol{r};\boldsymbol{R})$ used in the molecular convergent close-coupling method [91, 170, 171]. Equations are formulated in the body-frame of reference shown in Fig. 2.2, i.e. for homonuclear diatomic molecules the origin of the coordinate system is set at the nuclei centre of mass, or for heteronuclear diatomic molecules the origin of the coordinate system is set at the geometrical centre of the nuclei.

Starting from Eq. (2.14), the total kinetic energy of a diatomic molecule in the nuclei centre of mass coordinate system $K_T^{(\mathrm{com})}$ is [206]

$$K_T^{(\mathrm{com})} = -\frac{1}{2\mu}\nabla_R^2 - \frac{1}{2}\sum_{i=1}^{N_e}\nabla_i^2 - \frac{1}{2(M_1+M_2)}\sum_{i,j=1}^{N_e}\nabla_i\cdot\nabla_j, \tag{3.1}$$

where M_i are the mass of the individual nuclei and the reduced mass $\mu = M_1M_2/(M_1+M_2)$. Here the last term (known as the mass polarisation correction term) comes in at the adiabatic level approximation [207] and is neglected in the calculation of Born-Oppenheimer electronic wave functions. The total kinetic energy of a diatomic molecule in the geometrical centre of

the nuclei coordinate system $K_T^{(\mathrm{gc})}$ is [206]

$$K_T^{(\mathrm{gc})} = -\frac{1}{2\mu}\nabla_R^2 - \frac{1}{2}\sum_{i=1}^{N_e}\nabla_i^2 - \frac{1}{8\mu}\sum_{i,j=1}^{N_e}\nabla_i\cdot\nabla_j - \frac{1}{2\mu_\alpha}\nabla_R\cdot\sum_{i=1}^{N_e}\nabla_i, \quad (3.2)$$

where $\mu_\alpha = M_1M_2/(M_1 - M_2)$. Note that the third term in Eq. (3.2) is an adiabatic correction to the Born-Oppenheimer potential energy [207] and the last term in Eq. (3.2) only participates for heteronuclear diatomic molecules and is only accounted for in a nonadiabatic treatment [207]. Hence the last two terms in Eq. (3.2) are neglected in the calculation of Born-Oppenheimer electronic wave functions.

3.1 H_2^+ electronic target states

Referring to Section 2.1 it is common practice in the Born-Oppenheimer approximation to formulate electronic target states that satisfy (2.20). Here the target electronic Hamiltonian $H_{\mathrm{T}}^{\mathrm{Elec}}$ of H_2^+ describes an electron in the Coulomb potential of two protons that are fixed at a distance R and is defined as

$$H_{\mathrm{T}}^{\mathrm{Elec}} = H_1^{\mathrm{Elec}} + 1/R, \quad (3.3)$$

where, the internuclear Coulomb repulsion term $1/R$ comes from Eq. (2.16) for homogeneous diatomic molecules

$$\frac{Z_iZ_j}{|\boldsymbol{R}_i - \boldsymbol{R}_j|} = \frac{Z^2}{R}, \quad (3.4)$$

where Z is the charge of the individual nuclei (in this case $Z = 1|e|$). The one-electron (or positron) electronic Hamiltonian H_i^{Elec} for homonuclear diatomic molecules is

$$H_i^{\mathrm{Elec}} = K_i(\boldsymbol{r}_i) + V_i(\boldsymbol{r}_i;\boldsymbol{R}), \quad (3.5)$$

where,

$$K_i(\boldsymbol{r}_i) = -\frac{1}{2}\frac{d^2}{dr_i^2} + \frac{l(l+1)}{2r_i^2}, \quad (3.6)$$

$$V_i(\boldsymbol{r}_i;\boldsymbol{R}) = \left(\frac{z_{\mathrm{e}}}{\left|\boldsymbol{r}_i + \frac{\boldsymbol{R}}{2}\right|} + \frac{z_{\mathrm{e}}}{\left|\boldsymbol{r}_i - \frac{\boldsymbol{R}}{2}\right|}\right), \quad (3.7)$$

$z_e = -1|e|$ for the charge of an electron or $z_e = 1|e|$ for the charge of a positron. The electron-nuclei (or positron-nuclei) potential (3.7) in the Born-Oppenheimer approximation is expanded in partial waves

$$V_i(\boldsymbol{r}_i;\boldsymbol{R}) = 2z_e \sum_{\lambda=0,2,4,..}^{\infty} \sqrt{\frac{4\pi}{(2\lambda+1)}} v_\lambda(r_i, R/2) Y_{\lambda 0}(\hat{\boldsymbol{r}}_i), \tag{3.8}$$

where

$$v_\lambda(r_i, r_j) = \frac{r_<^\lambda}{r_>^{\lambda+1}}, \tag{3.9}$$

$r_< = \min(r_i, r_j)$ and $r_> = \max(r_i, r_j)$.

The electronic target states of H_2^+ are characterised by the projection of orbital angular momentum m and parity π. The electronic wave function of H_2^+ is represented by an expansion over one-electron orbitals

$$\Phi^{m\pi}(\mathbf{x}_1) = \sum_{j=1}^{N} C_j \phi_j^{m\pi}(\mathbf{x}_1), \tag{3.10}$$

where $\mathbf{x}$ denotes the electronic spin and spatial coordinates, N is the number of orbitals and C_j are the expansion coefficients. For H_2^+, one-electron orbitals $\phi_j^{m\pi}(\mathbf{x})$ are represented by

$$\phi_j^{m\pi}(\mathbf{x}) = \frac{1}{r} \varphi_{k_j l_j}(r) Y_{l_j m_j}(\hat{\boldsymbol{r}}) \chi(\sigma), \tag{3.11}$$

with $m_j = m$, $(-1)^{l_j} = \pi$ and $\chi(\sigma)$ is the spin-$\frac{1}{2}$ eigenfunction with angular projection σ. The radial functions $\varphi_{k_j l_j}(r)$ are the Laguerre functions

$$\varphi_{kl}(r) \;=\; \sqrt{\frac{\alpha_l (k-1)!}{(k+l)(k+2l)!}} (2\alpha_l r)^{l+1} \exp(-\alpha_l r)\, L_{k-1}^{2l+1}(2\alpha_l r), \tag{3.12}$$

where α_l is the exponential fall-off parameter, L_{k-1}^{2l+1} are the associated Laguerre polynomials and k ranges from 1 to N_l. N_l is the number of Laguerre basis function per orbital angular momentum l, where the largest value of l is $l_{\max}$. Analytic properties of Laguerre basis functions of order $2l+1$ [224] have extensively been used in the J-matrix method [225] to evaluate matrix elements of the target Hamiltonian (3.3). These matrix elements are given in Section 3.3. Note that each Laguerre basis function constructs $2l+1$

one-electron orbitals and electronic target states.

For each combination of m and π the generalised eigenvalue problem (for either an orthogonal or non-orthogonal basis)

$$\sum_{j=1}^{N}\left(\langle\phi_i|H_{\mathrm{T}}^{\mathrm{Elec}}|\phi_j\rangle - \varepsilon^{\mathrm{Elec}}(R)\langle\phi_i|\phi_j\rangle\right)C_j = 0, \tag{3.13}$$

is solved via diagonalisation of the target electronic Hamiltonian (3.3) to obtain energies $\varepsilon^{\mathrm{Elec}}(R)$ (eigenvalues) and expansion coefficients C_j (eigenvectors). Once these are obtained, electronic target states are constructed

$$\Phi_n^{m\pi}(\mathbf{x}_1) = \sum_{j=1}^{N} C_j^{(n)}\phi_j^{m\pi}(\mathbf{x}_1). \tag{3.14}$$

By expanding one-electron orbitals (3.11) in Eq. (3.14), the target states are represented in a more compact form

$$\Phi_n^{m\pi}(\mathbf{x}_1) = \frac{1}{r_1}\sum_{l=0}^{l_{\max}}\left(\sum_{j=1}^{N_l} C_{j_l}^{(n)}\varphi_{k_j l}(r_1)\right)Y_{lm}(\hat{\boldsymbol{r}}_1)\chi(\sigma_1) \tag{3.15}$$

$$= \frac{1}{r_1}\sum_{l=0}^{l_{\max}}\bar{\varphi}_{nl}(r_1)Y_{lm}(\hat{\boldsymbol{r}}_1)\chi(\sigma_1). \tag{3.16}$$

The lack of spherical symmetry of the system leads to a substantial increase in the number of states generated when compared to the atomic case for the same size of the Laguerre basis (3.12).

3.1.1 Molecular orbital basis

The multi-centre nature of the H_2^+ and H_2 molecules leads to a slow convergence rate of the calculated wave functions with respect to the orbital angular momentum l of the one-electron orbitals. This is only an issue for the ground and few lowest-lying excited states, other states are usually hydrogenic and are well represented in a single-centre Laguerre basis formulation.

Specifically for H_2^+ there is a slow convergence rate of the $1s\sigma_g$ ground state and $2p\sigma_u$ excited state. For H_2 only the ground state converges slowly. To improve accuracy and save on computational resources, structure calcu-

lations are performed in two steps. Firstly, a large Laguerre basis is used to diagonalise the H_2^+ target Hamiltonian (3.3) and generate accurate $1s\sigma_g$ and $2p\sigma_u$ states of H_2^+. Secondly, a new Laguerre basis is produced with smaller values of l and N_l. If both Laguerre bases are chosen to have the same values of exponential fall-offs matrix elements are evaluated using analytic properties of the Laguerre basis functions (see Section 3.3), otherwise these matrix elements are evaluated numerically.

For H_2^+ the $1s\sigma_g$ and $2p\sigma_u$ orbitals of this new basis are replaced with the accurate $1s\sigma_g$ and $2p\sigma_u$ states calculated at the first step. For H_2 the $1s\sigma_g$ orbital of this new basis is replaced with the accurate $1s\sigma_g$ target state of H_2^+ calculated at the first step. This new basis is then used to diagonalise the respective target Hamiltonian and generate electronic states that are then used in scattering calculations.

3.1.2 Accuracy of the H_2^+ structure

Here the accuracy of the H_2^+ electronic structure is investigated as a function of internuclear distance R for the methods described above. Firstly, target states calculated without the use of molecular orbital method were produced via diagonalisation of the target electronic Hamiltonian with a Laguerre basis that had $N_l = 17 - l$, $l_{\max} = 4$ and $\alpha_l = 1.4$. This calculation is denoted "structure a".

Structure b improves on a by obtaining accurate $1s\sigma_g$ and $2p\sigma_u$ states utilising a large Laguerre basis. This basis had $N_l = 60 - l$ functions with $l_{\max} = 9$ and $\alpha_l = 1.4$, and produced accurate $1s\sigma_g$ and $2p\sigma_u$ target states through to $R = 5.5\ a_0$. In the second step the original basis a was used except that the $1s\sigma_g$ and $2p\sigma_u$ orbitals were replaced with the accurate $1s\sigma_g$ and $2p\sigma_u$ states calculated at the first step.

Both structure models generate a total of 355 states. Structure a and structure b energies are plotted in Fig. 3.1 for the first few low lying target states as a function of R, and are compared with the exact spheroidal method (private communication [14]). It is seen that structure b results are a major improvement on structure a, particularly at larger values of R.

In this thesis target states generated with the structure b model are used to perform e^--H_2^+ scattering calculations. The highest-energy pseudostates in a convergent close-coupling calculation can usually be omitted without changing the final results. This ensures that high-energy highly oscillatory

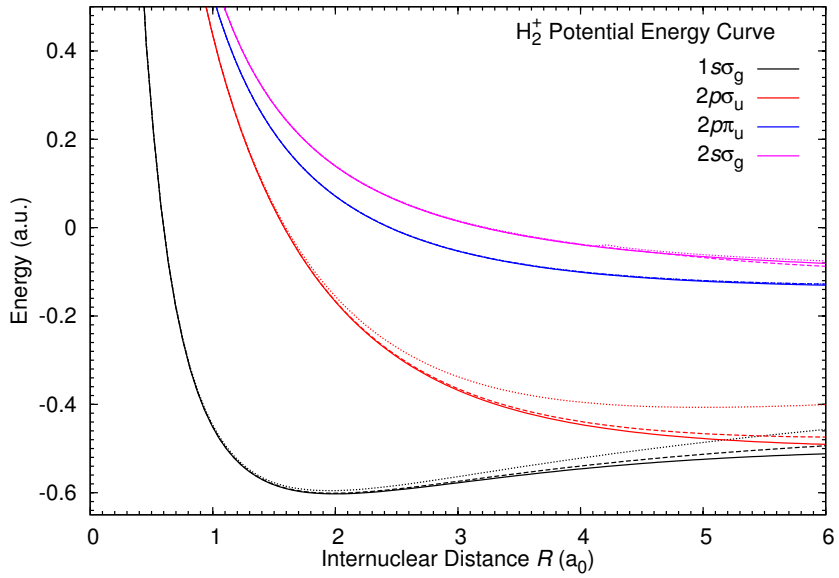

Figure 3.1: The $1s\sigma_g$, $2p\sigma_u$, $2p\pi_u$ and $2s\sigma_g$ target state energies of H_2^+ are presented as a function of internuclear distance R. The exact spheroidal results [14] are denoted by solid lines. Structure a and b, see text, are denoted by dotted and dashed lines, respectively.

pseudostates do not result in inaccurate V-matrix elements and subsequently do not destabilise the solution to non-uniqueness. For e^--H_2^+ scattering the four highest energy pseudostates were omitted, and is referred to as the 351-state calculations. Structure b target state energies, oscillator strengths and static dipole polarisability are presented as a function of R in Tables 3.1, 3.2 and 3.3, respectively. This structure model is in excellent agreement with accurate calculations of target state energies [1], oscillators strengths [2–4], and static dipole polarisability [3] for internuclear distances ranging from the united atom limit ($R = 0$ a_0) to the equilibrium distance $R_0 = 2.0$ a_0. For larger internuclear distances the accuracy of the structure model deteriorates, however it is sufficiently accurate for scattering calculations in the range $0 \leq R \leq 5.5$ a_0.

Oscillator strengths are calculated in the length and velocity gauges for parallel and perpendicular transitions [226]. For parallel transitions ($m_i = m_f$ and $\pi_i = -\pi_f$) the length gauge oscillator strength is defined as

$$\mathcal{L}^{\parallel}_{f,i}(R) = \frac{2g^{\parallel}E_{f,i}(R)}{3} \left|\langle \Phi_f | z | \Phi_i \rangle\right|^2 , \tag{3.17}$$

where the degeneracy factor $g^{\parallel} = 1$, $z = r\cos(\theta)$,

$$\langle \Phi_f | z | \Phi_i \rangle = \sum_{\alpha\gamma} C_{\alpha}^{(f)} C_{\gamma}^{(i)} \mathcal{K}^{\parallel}_{l_\alpha m_\alpha, l_\gamma m_\gamma} \int_0^\infty dr\ \varphi_\alpha(r) r \varphi_\gamma(r) \tag{3.18}$$

and

$$\mathcal{K}^{\parallel}_{l_\alpha m_\alpha, l_\gamma m_\gamma} = \begin{cases} \sqrt{\frac{(l_\gamma+1)^2 - m_\gamma^2}{(2l_\gamma+3)(2l_\gamma+1)}}, & l_\alpha = l_\gamma + 1 \text{ and } m_\alpha = m_\gamma \\ \sqrt{\frac{l_\gamma^2 - m_\gamma^2}{(2l_\gamma+1)(2l_\gamma-1)}}, & l_\alpha = l_\gamma - 1 \text{ and } m_\alpha = m_\gamma \\ 0 \quad , & \text{otherwise} \end{cases}. \tag{3.19}$$

The velocity gauge for parallel transitions

$$\mathcal{V}^{\parallel}_{f,i}(R) = \frac{2g^{\parallel}}{3E_{f,i}(R)} \left| \left\langle \Phi_f \left| \frac{\partial}{\partial z} \right| \Phi_i \right\rangle \right|^2, \tag{3.20}$$

where $\frac{\partial}{\partial z} = \nabla_0 = \cos(\theta)\frac{\partial}{\partial r} - \frac{1}{r}\sin(\theta)\frac{\partial}{\partial \theta}$,

$$\left\langle \Phi_f \left| \frac{\partial}{\partial z} \right| \Phi_i \right\rangle = \sum_{\alpha\gamma} C_{\alpha}^{(f)} C_{\gamma}^{(i)} \mathcal{K}^{\parallel}_{l_\alpha m_\alpha, l_\gamma m_\gamma} \mathcal{R}_{\alpha l_\alpha, \gamma l_\gamma} \tag{3.21}$$

and

$$\mathcal{R}_{\alpha l_\alpha, \gamma l_\gamma} = \begin{cases} \int_0^\infty dr\ \varphi_\alpha(r) \left(\frac{d}{dr} - \frac{(l_\gamma+1)}{r} \right) \varphi_\gamma(r), & l_\alpha = l_\gamma + 1 \\ \int_0^\infty dr\ \varphi_\alpha(r) \left(\frac{d}{dr} + \frac{l_\gamma}{r} \right) \varphi_\gamma(r) \quad , & l_\alpha = l_\gamma - 1 \end{cases}. \tag{3.22}$$

The length gauge oscillator strength for perpendicular transitions ($m_i = m_f \pm 1$ and $\pi_i = -\pi_f$)

$$\mathcal{L}^{\perp}_{f,i}(R) = \frac{2g^{\perp} E_{f,i}(R)}{3} \left| \left\langle \Phi_f \left| \mp \frac{1}{\sqrt{2}}(x \pm iy) \right| \Phi_i \right\rangle \right|^2 \tag{3.23}$$

where the degeneracy factor $g^{\perp} = 2$, $x \pm iy = r\sin(\theta)e^{\pm i\phi}$,

$$\left\langle \Phi_f \left| \mp \frac{1}{\sqrt{2}}(x \pm iy) \right| \Phi_i \right\rangle = \mathcal{K}^{\perp}_{l_\alpha m_\alpha, l_\gamma m_\gamma} \int_0^\infty dr\ \varphi_\alpha(r) r \varphi_\gamma(r) \tag{3.24}$$

and

$$\mathcal{K}^{\perp}_{l_\alpha m_\alpha, l_\gamma m_\gamma} = \begin{cases} \sqrt{\frac{(l_\gamma \pm m_\gamma + 2)(l_\gamma \pm m_\gamma + 1)}{2(2l_\gamma+3)(2l_\gamma+1)}}, & l_\alpha = l_\gamma + 1 \text{ and } m_\alpha = m_\gamma \pm 1 \\ -\sqrt{\frac{(l_\gamma \mp m_\gamma)(l_\gamma \mp m_\gamma - 1)}{2(2l_\gamma+1)(2l_\gamma-1)}} & , \quad l_\alpha = l_\gamma - 1 \text{ and } m_\alpha = m_\gamma \pm 1 \\ 0 & , \quad \text{otherwise} \end{cases} . \tag{3.25}$$

The velocity gauge for perpendicular transitions

$$\mathcal{V}^{\perp}_{f,i}(R) = \frac{2g^{\perp}}{3E_{f,i}(R)} \left| \left\langle \Phi_f \left| \mp \frac{1}{\sqrt{2}} \left(\frac{\partial}{\partial x} \pm i \frac{\partial}{\partial y} \right) \right| \Phi_i \right\rangle \right|^2 , \tag{3.26}$$

where

$$\begin{aligned} \nabla_{\pm 1} &= \mp \frac{1}{\sqrt{2}} \left(\frac{\partial}{\partial x} \pm i \frac{\partial}{\partial y} \right) \\ &= \mp \frac{e^{\pm i\phi}}{\sqrt{2}} \left(\sin(\theta) \frac{\partial}{\partial r} + \frac{\cos(\theta)}{r} \frac{\partial}{\partial \theta} \pm \frac{i}{r \sin(\theta)} \frac{\partial}{\partial \phi} \right) , \end{aligned} \tag{3.27}$$

and

$$\left\langle \Phi_f \left| \mp \frac{1}{\sqrt{2}} \left(\frac{\partial}{\partial x} \pm i \frac{\partial}{\partial y} \right) \right| \Phi_i \right\rangle = \sum_{\alpha\gamma} C^{(f)}_{\alpha} C^{(i)}_{\gamma} \mathcal{R}_{\alpha l_\alpha, \gamma l_\gamma} \mathcal{K}^{\perp}_{l_\alpha m_\alpha, l_\gamma m_\gamma} . \tag{3.28}$$

The total static dipole polarisability α is calculated from the parallel $\alpha_{\parallel}$ and perpendicular $\alpha_{\perp}$ components such that

$$\alpha = \frac{1}{3}\alpha_{\parallel} + \frac{2}{3}\alpha_{\perp} . \tag{3.29}$$

The static dipole polarisability is calculated from the oscillator strengths. Here the length gauge is used

$$\alpha_{\parallel}(R) = \sum_{n=1}^{N} \frac{3\mathcal{L}^{\parallel}_{n,i}(R)}{g^{\parallel}(E_n(R) - E_i(R))^2} , \tag{3.30}$$

$$\alpha_{\perp}(R) = \sum_{n=1}^{N} \frac{3\mathcal{L}^{\perp}_{n,i}(R)}{2g^{\perp}(E_n(R) - E_i(R))^2} . \tag{3.31}$$

The division by $g^{\parallel}$ and $g^{\perp}$ is due to the degeneracy of the states.

Table 3.1: Total energy of the structure b (see text) electronic target states of H_2^+ are presented as a function of internuclear distances R for the states $1s\sigma_g$, $2p\sigma_u$, and $2p\pi_u$. Comparisons are made with the accurate calculations of Bates et al. [1]. All values are in atomic units.

	$1s\sigma_g$		$2p\sigma_u$		$2p\pi_u$	
R	Present	[1]	Present	[1]	Present	[1]
0*	-2.0000	-2.0000	-0.5000	-0.5000	-0.5000	-0.5000
0.4	0.6996	0.6992	1.9892	1.9892	2.0050	2.0050
0.8	-0.3038	-0.3045	0.7073	0.7072	0.7678	0.7678
1.2	-0.5282	-0.5290	0.2450	0.2447	0.3680	0.3679
1.6	-0.5898	-0.5909	-0.0080	-0.0086	0.1780	0.1779
2.0	-0.6010	-0.6026	-0.1661	-0.1675	0.0714	0.0712
2.4	-0.5944	-0.5965	-0.2699	-0.2719	0.0058	0.0056
2.8	-0.5814	-0.5844	-0.3389	-0.3420	-0.0368	-0.0372
3.2	-0.5670	-0.5707	-0.3857	-0.3897	-0.0657	-0.0663
3.6	-0.5529	-0.5577	-0.4175	-0.4226	-0.0857	-0.0865
4.0	-0.5396	-0.5461	-0.4387	-0.4456	-0.0999	-0.1008
4.4	-0.5279	-0.5362	-0.4532	-0.4616	-0.1099	-0.1111
5.0	-0.5130	-0.5244	-0.4661	-0.4773	-0.1198	-0.1214
5.5	-0.5027	-0.5172	-0.4718	-0.4854	-0.1248	-0.1268

*This entry is the combined nuclear limit of H_2^+, which omits the internuclear Coulomb repulsion term $1/R$ and is equivalent to He^+.

3.2 H_2 electronic target states

The H_2 target electronic Hamiltonian H_T^{Elec} in the Born-Oppenheimer approximation describes two electrons in the Coulomb potential of two protons that are fixed at a distance R and is defined as

$$H_T^{Elec} = H_1^{Elec} + H_2^{Elec} + V_{12} + 1/R \tag{3.32}$$

Table 3.2: Structure b oscillator strengths obtained in the length (L) and velocity (V) gauges are presented for transitions involving the $n = 1$, 2 levels of H_2^+ at various internuclear distances R. Results are compared with the accurate calculations of Bates [2], Bishop and Cheung [3] and Bates et al. [4]. All values are in atomic units.

	$1s\sigma_g \rightarrow 2p\sigma_u$			$1s\sigma_g \rightarrow 2p\pi_u$			$2p\sigma_u \rightarrow 2s\sigma_g$		
R	L	V	[2]	L	V	[3]	L	V	[4]
0*	0.139	0.138	0.139	0.277	0.276				0
0.4	0.175	0.173	0.175	0.319	0.317	0.319	0.053	0.048	0.053
0.8	0.239	0.236	0.240	0.372	0.369	0.372	0.124	0.121	0.124
1.2	0.293	0.288	0.292	0.412	0.409	0.412	0.156	0.155	0.156
1.6	0.317	0.310	0.317	0.441	0.437	0.441	0.152	0.153	0.152
2.0	0.320	0.311	0.319	0.461	0.456	0.460	0.137	0.139	0.136
2.4	0.310	0.301	0.310	0.473	0.467	0.472	0.121	0.123	
2.8	0.295	0.287	0.297	0.479	0.472	0.478	0.108	0.110	
3.2	0.277	0.269	0.281	0.480	0.471	0.478	0.097	0.099	
3.6	0.256	0.250	0.261	0.476	0.465	0.473	0.085	0.086	
4.0	0.234	0.231	0.238	0.469	0.455	0.465	0.066	0.067	0.081
4.4	0.210	0.211	0.213	0.458	0.441		0.023	0.026	
5.0	0.172	0.183	0.175	0.436	0.414	0.430	0.035	0.017	0.077
5.5	0.140	0.162	0.144	0.415	0.388		0.057	0.027	

*This entry is the combined nuclear limit of H_2^+, which omits the internuclear Coulomb repulsion term $1/R$ and is equivalent to He^+.

where V_{12} is the electron-electron (or positron-electron) potential expanded in partial waves

$$V_{i,j} = -\frac{z_e}{|\boldsymbol{r}_i - \boldsymbol{r}_j|} \tag{3.33}$$

$$= -z_e \sum_{\lambda\mu}^{\infty} (-1)^\mu \frac{4\pi}{(2\lambda+1)} v_\lambda(r_i, r_j) Y_{\lambda -\mu}(\hat{\boldsymbol{r}}_i) Y_{\lambda\mu}(\hat{\boldsymbol{r}}_j), \tag{3.34}$$

$v_\lambda(r_i, r_j)$ is defined in Eq. (3.9) and again $1/R$ is the internuclear Coulomb repulsion term.

Electronic target states of H_2 are constructed using a similar method to that described in Section 3.1 for H_2^+. The target Hamiltonian (3.32) is

Table 3.3: Static dipole polarisability of the structure b (see text) H_2^+ ground state is presented as a function of internuclear distance R. Comparing with the accurate calculations of Bishop and Cheung [3]. All values are in atomic units. The number in parentheses indicates that the entry is multiplied by 10 to the power of the number in parentheses.

	$\alpha_\parallel$		$\alpha_\perp$		α	
R	Present	[3]	Present	[3]	Present	[3]
0*	0.2812(0)		0.2812(0)		0.2812(0)	0.2812(0)
0.4	0.4259(0)	0.4257(0)	0.3953(0)	0.3951(0)	0.4055(0)	0.4504(0)
0.8	0.8105(0)	0.8096(0)	0.6293(0)	0.6283(0)	0.6897(0)	0.6887(0)
1.2	0.1540(1)	0.1538(1)	0.9446(0)	0.9426(0)	0.1143(1)	0.1141(1)
1.6	0.2842(1)	0.2837(1)	0.1328(1)	0.1324(1)	0.1833(1)	0.1828(1)
2.0	0.5084(1)	0.5078(1)	0.1767(1)	0.1758(1)	0.2873(1)	0.2865(1)
2.4	0.8865(1)	0.8860(1)	0.2240(1)	0.2224(1)	0.4449(1)	0.4436(1)
2.8	0.1514(2)	0.1515(2)	0.2731(1)	0.2701(1)	0.6868(1)	0.6851(1)
3.2	0.2545(2)	0.2552(2)	0.3212(1)	0.3165(1)	0.1063(2)	0.1062(2)
3.6	0.4228(2)	0.4248(2)	0.3663(1)	0.3593(1)	0.1653(2)	0.1656(2)
4.0	0.6948(2)	0.7005(2)	0.4075(1)	0.3964(1)	0.2588(2)	0.2599(2)
4.4	0.1136(3)		0.4424(1)		0.4081(2)	
5.0	0.2364(3)	0.2375(3)	0.4821(1)	0.4579(1)	0.8201(2)	0.8222(2)
5.5	0.4390(3)		0.5035(1)		0.1497(3)	

*This entry is the combined nuclear limit of H_2^+, which omits the internuclear Coulomb repulsion term $1/R$ and is equivalent to He^+. $R = 0$ a_0 is compared with the calculations of Qi et al. [227] for He^+.

diagonalised in a set of two-electron configurations and then target states are constructed. H_2 electronic target states are characterised by their orbital angular momentum projection m, parity π and spin s. For H_2 two-electron configurations $\bar{\phi}^{m\pi s}(\mathbf{x}_1, \mathbf{x}_2)$

$$\bar{\phi}^{m\pi s}_{\gamma,\delta}(\mathbf{x}_1, \mathbf{x}_2) \quad = \quad \frac{1}{\sqrt{2(1+\delta_{\gamma,\delta})}} \mathcal{A} |\phi_\gamma(\mathbf{x}_1)\phi_\delta(\mathbf{x}_2) : m\pi s m_s\rangle, \quad (3.35)$$

are constructed from antisymmetric combinations of one-electron orbitals $\phi(\mathbf{x})$, which are given by Eq. (3.11). The antisymmetrisation operator $\mathcal{A} = 1 - P_{12}$, is Hermitian i.e. $\mathcal{A} = \mathcal{A}^\dagger$ and hence $\mathcal{A}^\dagger\mathcal{A} = 2(1 - P_{12})$. Some

useful definitions of the two-electron configurations (3.35) are

$$P_{12}|\phi_\gamma(\mathbf{x}_1)\phi_\delta(\mathbf{x}_2):m\pi s m_s\rangle = -(-1)^s|\phi_\delta(\mathbf{x}_1)\phi_\gamma(\mathbf{x}_2):m\pi s m_s\rangle \quad (3.36)$$

$$= -(-1)^s P_{\gamma,\delta}|\phi_\gamma(\mathbf{x}_1)\phi_\delta(\mathbf{x}_2):m\pi s m_s\rangle, \quad (3.37)$$

where the operator $P_{\gamma,\delta}$ interchanges indices γ and δ. Note that using (3.35) and (3.37) the two-electron configuration

$$\bar{\phi}^{m\pi s}_{\gamma,\gamma}(\mathbf{x}_1,\mathbf{x}_2) = |\phi_\gamma(\mathbf{x}_1)\phi_\gamma(\mathbf{x}_2):m\pi s m_s\rangle, \quad (3.38)$$

where in this case $s=0$ (otherwise from (3.35) the configuration is a zero function), $m_s=0$ due to the Pauli exclusion principle and $\pi=+$. From the above definitions the following overlaps are derived

$$\langle\bar{\phi}^{m\pi s}_{\alpha,\beta}|\bar{\phi}^{m\pi s}_{\gamma,\delta}\rangle = \langle\phi_\alpha|\phi_\gamma\rangle\langle\phi_\beta|\phi_\delta\rangle + (-1)^s\langle\phi_\alpha|\phi_\delta\rangle\langle\phi_\beta|\phi_\gamma\rangle, \quad (3.39)$$

$$\langle\bar{\phi}^{m\pi s}_{\alpha,\beta}|\bar{\phi}^{m\pi s}_{\gamma,\gamma}\rangle = \sqrt{2}\langle\phi_\alpha|\phi_\gamma\rangle\langle\phi_\beta|\phi_\gamma\rangle, \quad (3.40)$$

$$\langle\bar{\phi}^{m\pi s}_{\alpha,\alpha}|\bar{\phi}^{m\pi s}_{\gamma,\gamma}\rangle = \langle\phi_\alpha|\phi_\gamma\rangle\langle\phi_\alpha|\phi_\gamma\rangle. \quad (3.41)$$

Matrix elements of the target Hamiltonian (3.32) are now evaluated for the following cases

$$\begin{aligned}\langle\bar{\phi}^{m\pi s}_{\alpha,\beta}|H_{\rm T}^{\rm Elec}|\bar{\phi}^{m\pi s}_{\gamma,\delta}\rangle &= \langle\phi_\alpha|H_1^{\rm Elec}|\phi_\gamma\rangle\langle\phi_\beta|\phi_\delta\rangle \\ &+\langle\phi_\beta|H_2^{\rm Elec}|\phi_\delta\rangle\langle\phi_\alpha|\phi_\gamma\rangle + \langle\phi_\alpha\phi_\beta|V_{12}|\phi_\gamma\phi_\delta\rangle \\ &+1/R\langle\phi_\alpha|\phi_\gamma\rangle\langle\phi_\beta|\phi_\delta\rangle + (-1)^s\Big(\langle\phi_\alpha|H_1^{\rm Elec}|\phi_\delta\rangle\langle\phi_\beta|\phi_\gamma\rangle \\ &+\langle\phi_\beta|H_2^{\rm Elec}|\phi_\gamma\rangle\langle\phi_\alpha|\phi_\delta\rangle + \langle\phi_\alpha\phi_\beta|V_{12}|\phi_\delta\phi_\gamma\rangle \\ &+1/R\langle\phi_\alpha|\phi_\delta\rangle\langle\phi_\beta|\phi_\gamma\rangle\Big),\end{aligned} \quad (3.42)$$

$$\begin{aligned}\langle\bar{\phi}^{m\pi s}_{\alpha,\beta}|H_{\rm T}^{\rm Elec}|\bar{\phi}^{m\pi s}_{\gamma,\gamma}\rangle &= \sqrt{2}\Big(\langle\phi_\alpha|H_1^{\rm Elec}|\phi_\gamma\rangle\langle\phi_\beta|\phi_\gamma\rangle \\ &+\langle\phi_\beta|H_2^{\rm Elec}|\phi_\gamma\rangle\langle\phi_\alpha|\phi_\gamma\rangle + \langle\phi_\alpha\phi_\beta|V_{12}|\phi_\gamma\phi_\gamma\rangle \\ &+1/R\langle\phi_\alpha|\phi_\gamma\rangle\langle\phi_\beta|\phi_\gamma\rangle\Big),\end{aligned} \quad (3.43)$$

$$\begin{aligned}\langle\bar{\phi}^{m\pi s}_{\alpha,\alpha}|H_{\rm T}^{\rm Elec}|\bar{\phi}^{m\pi s}_{\gamma,\gamma}\rangle &= 2\langle\phi_\alpha|H_1^{\rm Elec}|\phi_\gamma\rangle\langle\phi_\alpha|\phi_\gamma\rangle \\ &+\langle\phi_\alpha\phi_\alpha|V_{12}|\phi_\gamma\phi_\gamma\rangle + 1/R\langle\phi_\alpha|\phi_\gamma\rangle\langle\phi_\alpha|\phi_\gamma\rangle\end{aligned} \quad (3.44)$$

By using definition (C.40) and dropping overlaps of the spin functions

$$\langle\phi_\alpha|\phi_\gamma\rangle = \delta_{l_\alpha,l_\gamma}\delta_{m_\alpha,m_\gamma}\int_0^\infty dr\varphi_{k_\alpha l_\alpha}(r)\varphi_{k_\gamma l_\gamma}(r), \tag{3.45}$$

$$\begin{aligned}\langle\phi_\alpha\phi_\beta|V_{12}|\phi_\gamma\phi_\delta\rangle = &\sum_{\lambda\mu}(-1)^\mu C^{l_\gamma 0}_{l_\alpha 0,\lambda 0}C^{l_\alpha m_\alpha}_{l_\gamma m_\gamma,\lambda-\mu}C^{l_\delta 0}_{l_\beta 0,\lambda 0}C^{l_\beta m_\beta}_{l_\delta m_\delta,\lambda\mu} \\ &\times\int_0^\infty dr_2\varphi_{k_\beta l_\beta}(r_2)\varphi_{k_\delta l_\delta}(r_2)\left(\int_0^{r_2}dr_1\varphi_{k_\alpha l_\alpha}(r_1)\frac{r_1^\lambda}{r_2^{\lambda+1}}\varphi_{k_\gamma l_\gamma}(r_1)\right. \\ &\left.+\int_{r_2}^\infty dr_1\varphi_{k_\alpha l_\alpha}(r_1)\frac{r_2^\lambda}{r_1^{\lambda+1}}\varphi_{k_\gamma l_\gamma}(r_1)\right),\end{aligned} \tag{3.46}$$

where $C^{lm}_{l_1m_1,l_2m_2}$ denotes Clebsch-Gordan coefficients and the one-electron matrix elements $\langle\phi_\alpha|H_1^{\rm Elec}|\phi_\gamma\rangle$ are evaluated in Section 3.3.

Diagonalising the H_2 target Hamiltonian, eigenvectors $C^{(n)}_{\gamma,\delta}$ and eigenvalues are obtained. H_2 target states are then constructed

$$\Phi_n^{m\pi s}(\mathbf{x}_1,\mathbf{x}_2) = \sum_{\gamma\le\delta}C^{(n)}_{\gamma,\delta}\bar{\phi}^{m\pi s}_{\gamma,\delta}(\mathbf{x}_1,\mathbf{x}_2), \tag{3.47}$$

$$= \sum_{\gamma\le\delta}\frac{C^{(n)}_{\gamma,\delta}}{\sqrt{2(1+\delta_{\gamma,\delta})}}\left(\phi_\gamma(\boldsymbol{r}_1)\phi_\delta(\boldsymbol{r}_2)+(-1)^s\phi_\delta(\boldsymbol{r}_1)\phi_\gamma(\boldsymbol{r}_2)\right)X^s_{m_s}, \tag{3.48}$$

where

$$X^s_{m_s} = \sum_{\sigma_1\sigma_2}C^{sm_s}_{\frac{1}{2}\sigma_1,\frac{1}{2}\sigma_2}\chi(\sigma_1)\chi(\sigma_2). \tag{3.49}$$

For brevity of notation the H_2 two-electron target states are represented by

$$\Phi_n^{m\pi s}(\mathbf{x}_1,\mathbf{x}_2) = \sum_{\gamma\le\delta}C^{(n)}_{\gamma,\delta}|\phi_\gamma(\mathbf{x}_1)\phi_\delta(\mathbf{x}_2):m\pi s m_s\rangle \tag{3.50}$$

$$= \frac{1}{r_1r_2}\sum_{\gamma\le\delta}C^{(n)}_{\gamma,\delta}\varphi_\gamma(r_1)\varphi_\delta(r_2)Y_{l_\gamma m_\gamma}(\hat{\boldsymbol{r}}_1)Y_{l_\delta m_\delta}(\hat{\boldsymbol{r}}_2)X^s_{m_s}. \tag{3.51}$$

3.2.1 Accuracy of the H_2 structure

The H_2 structure model needs to allow for an expansion over the two electrons $(nlm, n'l'm')$. The structure model chosen here represents the "outer" electron $(n'l'm')$ by one-electron orbitals. These one-electron orbitals were constructed from a Laguerre basis that had $N_l = 17-l$ functions up to $l = 7$

and $N_{l=8} = 10$ with $l_{\max} = 8$, exponential fall-offs $\alpha_l = 1.2$ for $l \leq 4$ and $\alpha_l = 1.0$ for $l \geq 5$. In the frozen-core model, the "inner" electron of H_2 is restricted to the $1s\sigma_g$ orbital of H_2^+ $(1s\sigma, n'l'm')$. This model is not sufficiently accurate to obtain the ground state energy, instead a more accurate model is chosen. Here the "inner" electron is expanded by all $n \leq 3$ one-electron orbitals. These orbitals ($n \leq 3$ and $n' \leq 3$) are replaced by short-ranged one-electron orbitals that have Laguerre basis functions with exponential-fall offs of $\alpha_l = 1.9$. The $1s\sigma$ orbital ($n = n' = 1$) is represented by a converged (at an internuclear distance of $R = 1.4\ a_0$) molecular-orbital of H_2^+ that was constructed from a Laguerre basis that had $N_l = 60 - l$, $\alpha_l = 1.7$ functions up to $l_{\max} = 8$. Two-electron configurations with $|m| \geq 2$ are restricted to the frozen-core model $(1s\sigma, n'l'm')$. Hence the largest angular projection $m_{\max} = l_{\max} = 8$.

Diagonalising the target Hamiltonian with two-electron configurations built from the above model generates $N = 1014$ singlet $s = 0$ target states. For scattering calculations the highest energy $m = 0$ $\pi = 1$ $s = 0$ pseudostate (highly oscillatory) was omitted because highly oscillatory pseudostates can potentially cause numerical inaccuracies in the scattering V-matrix elements. This 1013-state model is used in the scattering calculations of positron collisions with H_2 in the $v = 0$ and $v = 1$ vibrational states. Referring to Fig. 3.3 the $v = 1$ vibrational wave function approximately spans the range $0.9 \leq R \leq 2.2\ a_0$. In Tables 3.4 and 3.5 the H_2 electronic states two-electron energy and ground state static dipole polarisability are presented as a function of R. At the equilibrium distance of $R_0 = 1.4\ a_0$, the static dipole polarisability of this model is $\alpha_{\parallel} = 6.3775\ a_0^3$ and $\alpha_{\perp} = 4.6346\ a_0^3$ for the ground state, which are both in good agreement with the accurate calculations of Kolos and Wolniewicz [7] ($\alpha_{\parallel} = 6.3805\ a_0^3$ and $\alpha_{\perp} = 4.5777\ a_0^3$). As R increases beyond the equilibrium distance of $R_0 = 1.4\ a_0$, the ground and low-lying excited states of H_2 start to become more diffuse and the present structure model becomes less accurate. For the purpose of scattering calculations the current structure model is sufficiently accurate to describe H_2 in the $v = 0$ and $v = 1$ states, which is confirmed in Chapter 6. Electronic excited states two-electron energies and oscillator strengths are presented for H_2 at the equilibrium internuclear distance of $R_0 = 1.4\ a_0$ in Tables 3.6 and 3.7. At $R_0 = 1.4\ a_0$ these excited states are hydrogenic and are well represented in the single-centre expansion. The

present low-lying electronic excited states energies are within 1.5% of the accurate values [5, 6, 8, 9]. The dominant oscillator strengths are also well represented in the present model. It is important to note that at $R_0 = 1.4$ a_0 this model resulted in the most accurate ground-state energy and static dipole polarisability compared to other non-perturbative scattering calculations that utilise a close-coupling expansion.

Table 3.4: Two-electron energy of the H_2 electronic target states $X^1\Sigma_g^+$, $B^1\Sigma_u^+$, and $C^1\Pi_u$ as a function of the internuclear distances R. Comparisons are made with the accurate calculations of Kolos et al. [5] and Wolniewicz and Dressler [6]. All values are in atomic units.

	$X^1\Sigma_g^+$		$B^1\Sigma_u^+$		$C^1\Pi_u$	
R	Present	[5]	Present	[6]	Present	[6]
0*	-2.8990	-2.9033	-2.1235	-2.1331	-2.1235	-2.1331
0.2	2.2142	2.1978	2.9597		2.9600	
0.4	-0.1148	-0.1202	0.5763		0.5777	
0.6	-0.7647	-0.7696	-0.1290		-0.1258	
0.8	-1.0154	-1.0201	-0.4300		-0.4246	
1.0	-1.1198	-1.1245	-0.5790	-0.5813	-0.5706	-0.5725
1.2	-1.1599	-1.1649	-0.6583	-0.6613	-0.6465	-0.6487
1.4	-1.1688	-1.1745	-0.7020	-0.7058	-0.6861	-0.6887
1.6	-1.1626	-1.1686	-0.7248	-0.7308	-0.7050	-0.7086
1.8	-1.1472	-1.1551	-0.7379	-0.7447	-0.7134	-0.7169
2.0	-1.1288	-1.1381	-0.7432	-0.7521	-0.7142	-0.7182
2.2	-1.1076	-1.1201	-0.7441	-0.7556	-0.7107	-0.7155

*This entry is the combined nuclear limit of H_2, which omits the internuclear Coulomb repulsion term $1/R$ and is equivalent to He. $R = 0$ a_0 energies are compared to the measurements of Moore [228] for the He atom.

3.3 One-electron matrix elements

Matrix elements of the target Hamiltonian (3.3)

$$\langle\phi_i|H_T^{\rm Elec}|\phi_j\rangle \quad = \quad \langle\phi_i|(K + V + 1/R)|\phi_j\rangle, \tag{3.52}$$

Table 3.5: Parallel $\alpha_{\parallel}$, perpendicular $\alpha_{\perp}$ and total α static dipole polarisability of the H_2 ground state presented as a function of the internuclear distance R. Comparing with the accurate calculations of Kolos and Wolniewicz [7]. All values are in atomic units.

	$\alpha_{\parallel}$		$\alpha_{\perp}$		α	
R	Present	[7]	Present	[7]	Present	[7]
0*	1.3966		1.3966		1.3966	1.3832
0.2	1.5654		1.5479		1.5537	
0.4	1.9566	1.9289	1.8764	1.8503	1.9031	1.8765
0.6	2.5113	2.4900	2.3049	2.2825	2.3737	2.3517
0.8	3.2248	3.2043	2.8083	2.7825	2.9471	2.9231
1.0	4.1010	4.0878	3.3706	3.3410	3.6141	3.5899
1.2	5.1497	5.1465	3.9832	3.9440	4.3720	4.3448
1.4	6.3755	6.3805	4.6346	4.5777	5.2149	5.1786
1.6	7.7080	7.7807	5.2796	5.2276	6.0891	6.0786
1.8	9.3703	9.3204	6.0090	5.8780	7.1294	7.0255
2.0	11.1174	10.9644	6.6992	6.5109	8.1719	7.9954
2.2	13.1692	12.6376	7.4248	7.1097	9.3396	8.9523

*This entry is the combined nuclear limit of H_2, which omits the internuclear Coulomb repulsion term $1/R$ and is equivalent to He. The $R = 0$ a_0 polarisability is compared with the calculations of Kar and Ho [229] for atomic He.

are evaluated using analytic properties of the Laguerre basis functions. Laguerre functions of order $2l + 1$ satisfy the following equation

$$\left(-\frac{1}{2}\frac{d^2}{dr^2} + \frac{l(l+1)}{2r^2}\right)\varphi_{kl}(r) = \left(\frac{\alpha_l(k+l)}{r} - \frac{\alpha_l^2}{2}\right)\varphi_{kl}(r), \tag{3.53}$$

Table 3.6: Two-electron energy of singlet $s = 0$ electronic target states of H_2 at the internuclear distance of $R_0 = 1.4\ a_0$. Comparisons are made with accurate calculations [5, 6, 8, 9]. All values are in atomic units.

State	Present	Reference Energy	Reference
$EF^1\Sigma_g^+$	-0.6891	-0.6920	[8]
$B'^1\Sigma_u^+$	-0.6269	-0.6287	[8]
$GK^1\Sigma_g^+$	-0.6250	-0.6265	[8]
$D^1\Pi_u$	-0.6220	-0.6236	[6]
$B''^1\Sigma_u^+$	-0.5965	-0.6025	[8]
$D'^1\Pi_u$	-0.5927	-0.6002	[9]

where, the left hand side has the same form as the kinetic energy operator $K(\boldsymbol{r})$ (3.6). Utilising the properties

$$\int_0^\infty dr\varphi_{kl}(r)\varphi_{kl}(r) = 1, \tag{3.54}$$

$$\int_0^\infty dr\varphi_{k'l}(r)\varphi_{kl}(r) = \begin{cases} 0 & , \quad k > k'+1 \\ -\frac{1}{2}\sqrt{1-\frac{l(l+1)}{(k'+l)(k'+l+1)}}, & k = k'+1 \end{cases}, \tag{3.55}$$

$$\int_0^\infty dr\varphi_{k'l}(r)\frac{1}{r}\varphi_{kl}(r) = \frac{\alpha_l}{(k+l)}\delta_{k',k}, \tag{3.56}$$

the kinetic energy matrix element and Coulomb repulsion term are evaluated analytically

$$\langle\phi_i|K|\phi_j\rangle = \delta_{l_i,l_j}\delta_{m_i,m_j}\left(\alpha_{l_j}^2\delta_{k_i,k_j} - \frac{\alpha_{l_j}^2}{2}\int_0^\infty dr\varphi_{k_il_i}(r)\varphi_{k_jl_j}(r)\right) \tag{3.57}$$

$$\langle\phi_i|1/R|\phi_j\rangle = \delta_{l_i,l_j}\delta_{m_i,m_j}\frac{1}{R}\int_0^\infty dr\varphi_{k_il_i}(r)\varphi_{k_jl_j}(r). \tag{3.58}$$

The electron-nuclei (or positron-nuclei) potential term is evaluated using (C.40) to integrate over angular terms analytically

$$\begin{aligned}\langle\phi_i|V|\phi_j\rangle &= 2z_eZ\delta_{m_i,m_j}\sum_{\lambda=0,2,4,..}^{\infty}(-1)^\lambda C_{l_i0,\lambda0}^{l_j0}C_{l_jm_j,\lambda0}^{l_im_i} \\ &\quad\times\int_0^\infty dr\varphi_{k_il_i}(r)v_\lambda(r,R/2)\varphi_{k_jl_j}(r),\end{aligned} \tag{3.59}$$

Table 3.7: Oscillator strengths for transitions from the ground state to the lowest lying $^1\Sigma_u$ and $^1\Pi_u$ states of H_2 at the internuclear distance $R_0 = 1.4$ a_0. Comparisons are made with the calculations of Branchett and Tennyson [10]. All values are in atomic units.

Transition	Length	Velocity	[10]
$X^1\Sigma_g^+ \rightarrow B^1\Sigma_u^+$	0.2931	0.2884	0.2995
$X^1\Sigma_g^+ \rightarrow C^1\Pi_u$	0.3545	0.3508	0.3508
$X^1\Sigma_g^+ \rightarrow B'^1\Sigma_u^+$	0.0577	0.0566	0.0603
$X^1\Sigma_g^+ \rightarrow D^1\Pi_u$	0.0871	0.0861	0.0913
$X^1\Sigma_g^+ \rightarrow B''^1\Sigma_u^+$	0.0364	0.0354	0.0353
$X^1\Sigma_g^+ \rightarrow D'^1\Pi_u$	0.0673	0.0665	0.0534

where $v_\lambda(r_i, r_j)$ is defined in Eq. (3.9). Note that the above matrix elements drop the overlap of the spin eigenfunctions.

3.4 Vibrational wave functions

Performing structure calculations at various R and interpolating, Born-Oppenheimer potential energy curves $\varepsilon_n^{\rm Elec}(R)$ are obtained (as defined in [207]). Referring to Eq. (3.1) or (3.2) adiabatic and/or nonadiabatic correction terms can be included, however they are not included here. The adiabatic and nonadiabatic correction terms are expected to have only a very minor effect on the molecular structure and major electronic scattering cross sections. A study by Bishop and Wetmore [230, 231] showed that the adiabatic and nonadiabatic correction terms of H_2^+, D_2^+ and H_2 do indeed have a negligible effect on the electronic ground state vibrational energy levels, even for relatively highly excited vibrational levels. The total Born-Oppenheimer Hamiltonian for a diatomic molecule

$$H_n^{\rm BO} \;=\; -\frac{1}{2\mu}\nabla_R^2 + \varepsilon_n^{\rm Elec}(R), \tag{3.60}$$

where the reduced mass $\mu = M_1 M_2/(M_1 + M_2)$, M_i is the mass of the individual nuclei; M_i=1836.152 m_e for a proton, M_i=3670.483 m_e for deuteron and M_i=5496.922 m_e for triton. Nuclear wave functions $\Xi_{nvJm_J}(\boldsymbol{R})$ of the

electronic ground state are calculated via diagonalisation of the total Hamiltonian (3.60) for each rotational angular momentum J using a set of nuclear orbitals

$$\xi_j(\boldsymbol{R}) = \frac{1}{R}\varphi_{k_j J_j}(R) Y_{J_j m_j}(\hat{\boldsymbol{R}}). \tag{3.61}$$

Here $\varphi_{k_j J_j}(R)$ are Laguerre basis functions (3.12).

3.4.1 Accuracy of H_2, H_2^+ and its isotopologues molecular states

In this thesis adiabatic-nuclei scattering calculations of positron scattering from vibrationally excited H_2 and electron scattering from vibrationally excited H_2^+ and its isotopologues require knowledge of the vibrational wave functions.

Firstly for H_2^+, the accurate electronic ground state potential energy curve $\varepsilon_1^{\text{Elec}}(R)$ of Wolniewicz and Poll [232] (private communication) is utilised in the total Born-Oppenheimer Hamiltonian (3.60), which is subsequently diagonalised with a set of $J = 0$ nuclear orbitals that was taken to convergence. The potential energy curve of Wolniewicz and Poll [232] was used because at large values of R the single-centre formulation requires large expansions to obtain accurate $1s\sigma_g$ electronic state energies, as discussed in Section 3.1.1. Franck-Condon (FC) factors are also calculated for the single-ionisation transition from the neutral molecule to its ion, this approximates the vibrational population of the H_2^+ beam produced in scattering experiments [12]. Here the respective neutral molecule's vibrational and rotational ground state was calculated using the same procedure described above for H_2^+, however an accurate Born-Oppenheimer electronic potential energy curve of $H_2(X^1\Sigma_g^+)$ was taken from Kolos et al. [5] and used in Eq. (3.60). H_2 molecular state energies are compared with the accurate calculations of Kolos and Wolniewicz [11] in Table 3.8. The calculations of Kolos and Wolniewicz [11] utilised the same Born-Oppenheimer potential energy curves as those used here. The present total energies are in excellent agreement with the accurate calculations [11]. FC factors

$$\text{FC}_{fv_f J_f m_{J_f}, iv_i J_i m_{J_i}} = \left| \int d\boldsymbol{R}\; \Xi^*_{fv_f J_f m_{J_f}}(\boldsymbol{R}) \Xi_{iv_i J_i m_{J_i}}(\boldsymbol{R}) \right|^2, \tag{3.62}$$

and molecular state energies are presented and compared with the accurate

Table 3.8: Born-Oppenheimer molecular state energy levels of $H_2(X^1\Sigma_g^+, v, 0)$. Results are compared with the calculations of Kolos and Wolniewicz [11].

	Energy (eV)			Energy (eV)	
v	Present	[11]	v	Present	[11]
0	-31.68803	-31.68901	8	-28.35930	-28.36170
1	-31.17156	-31.17299	9	-28.07359	-28.07732
2	-30.68448	-30.68615	10	-27.82107	-27.82604
3	-30.22652	-30.22790	11	-27.60474	-27.61066
4	-29.79632	-29.79784	12	-27.42923	-27.43516
5	-29.39387	-29.39586	13	-27.29998	-27.30511
6	-29.02026	-29.02212	14	-27.22597	-27.22822
7	-28.67495	-28.67709			

calculations of Wünderlich and Fantz [13] in Tables 3.9 for H_2^+, 3.10 for D_2^+ and 3.11 for T_2^+. A plot of the FC factors is given in Fig. 3.2. The present energies and FC factors of H_2^+, D_2^+ and T_2^+ are in excellent agreement with the calculations of Wünderlich and Fantz [13]. There is however a minor discrepancy in the number of vibrational bound states, which is likely to be due to minor numerical inaccuracies in the present model's diagonalisation procedure. Because these extra bound states have a very minor FC weighting they will have a negligible effect on final scattering results.

Table 3.9: Born-Oppenheimer molecular state energy levels of $H_2^+(1s\sigma_g, v, 0)$. Franck-Condon (FC) factors and von Busch and Dunn [12] (BD) weights are given for the transition $H_2(X^1\Sigma_g^+, 0, 0) \rightarrow H_2^+(1s\sigma_g, v, 0)$. Results are compared with the calculations of Wünderlich and Fantz [13].

	Energy (eV)		Weighting		
v	Present	[13]	Present FC	FC [13]	BD [12]
0	-16.25594	-16.25498	0.0909007	0.0911850	0.11916
1	-15.98416	-15.98338	0.1600668	0.1605800	0.18994
2	-15.72816	-15.72753	0.1739719	0.1742600	0.18791
3	-15.48744	-15.48685	0.1525290	0.1521300	0.15173
4	-15.26153	-15.26086	0.1193440	0.1190800	0.11097
5	-15.05009	-15.04958	0.0876249	0.0875530	0.07732
6	-14.85282	-14.85237	0.0621211	0.0619910	0.05270
7	-14.66951	-14.66909	0.0432688	0.0431950	0.03564
8	-14.50006	-14.49974	0.0299371	0.0299210	0.02411
9	-14.34441	-14.34421	0.0207168	0.0207080	0.01638
10	-14.20260	-14.20250	0.0143968	0.0143850	0.01121
11	-14.07479	-14.07476	0.0100634	0.0100560	0.00773
12	-13.96122	-13.96126	0.0070698	0.0070679	0.00536
13	-13.86222	-13.86239	0.0049739	0.0049789	0.00374
14	-13.77832	-13.77860	0.0034781	0.0034841	0.00258
15	-13.71018	-13.71057	0.0023777	0.0023826	0.00175
16	-13.65863	-13.65909	0.0015287	0.0015298	0.00109
17	-13.62460	-13.62566	0.0008294	0.0007257	0.00056
18	-13.60854	*	0.0002434	*	0.00012

*Stated as unbound by potential energy curve

Table 3.10: Born-Oppenheimer molecular state energy levels of $D_2^+(1s\sigma_g, v, 0)$. Franck-Condon (FC) factors are given for the transition $D_2(X^1\Sigma_g^+, 0, 0) \rightarrow D_2^+(1s\sigma_g, v, 0)$. Results are compared with the calculations of Wünderlich and Fantz [13].

	Energy (eV)		Weighting			Energy (eV)		Weighting	
v	Present	[13]	Present FC	FC[13]	v	Present	[13]	Present FC	FC[13]
0	-16.29734	-16.29634	0.0344701	0.0346030	14	-14.23559	-14.23575	0.0080059	0.0080244
1	-16.10177	-16.10084	0.0859598	0.0863810	15	-14.14066	-14.14152	0.0058199	0.0058630
2	-15.91421	-15.91357	0.1247462	0.1251600	16	-14.05241	-14.05432	0.0043019	0.0043087
3	-15.73448	-15.73368	0.1390024	0.1387300	17	-13.97120	-13.97429	0.0032599	0.0031850
4	-15.56240	-15.56166	0.1325658	0.1325300	18	-13.89749	-13.90154	0.0024991	
5	-15.39779	-15.39701	0.1144811	0.1141200	19	-13.83148	-13.83622	0.0018842	
6	-15.24052	-15.23974	0.0925865	0.0924670	20	-13.77324	-13.77855	0.0013713	
7	-15.09046	-15.08978	0.0716467	0.0715630	21	-13.72300	-13.72875	0.0009640	
8	-14.94752	-14.94684	0.0538533	0.0537870	22	-13.68126	-13.68711	0.0006583	
9	-14.81160	-14.81097	0.0397230	0.0397380	23	-13.64857	-13.65394	0.0004321	
10	-14.68264	-14.68209	0.0289739	0.0289910	24	-13.62536	-13.62969	0.0002588	
11	-14.56060	-14.56013	0.0210232	0.0210130	25	-13.61170	*	0.0001202	*
12	-14.44543	-14.44507	0.0152415	0.0152160	26	-13.60659	*	0.0000265	*
13	-14.33713	-14.33695	0.0110512	0.0110340					

*Stated as unbound by potential energy curve

Table 3.11: Born-Oppenheimer molecular state energy levels of $T_2^+(1s\sigma_g, v, 0)$. Franck-Condon (FC) factors are given for the transition $T_2(X^1\Sigma_g^+, 0, 0) \rightarrow T_2^+(1s\sigma_g, v, 0)$. Results are compared with the calculations of Wünderlich and Fantz [13].

	Energy (eV)		Weighting			Energy (eV)		Weighting	
v	Present	[13]	Present FC	FC[13]	v	Present	[13]	Present FC	FC[13]
0	-16.31572	-16.31470	0.0164282	0.0164670	17	-14.25558	-14.25539	0.0053657	0.0053434
1	-16.15469	-16.15369	0.0501630	0.0505410	18	-14.17672	-14.17672	0.0039946	
2	-15.99905	-15.99841	0.0867873	0.0871240	19	-14.10236	-14.10273	0.0029681	
3	-15.84869	-15.84784	0.1126303	0.1126800	20	-14.03241	-14.03347	0.0022145	
4	-15.70352	-15.70281	0.1225468	0.1223600	21	-13.96697	-13.96903	0.0016841	
5	-15.56342	-15.56257	0.1185671	0.1183400	22	-13.90637	-13.90944	0.0013151	
6	-15.42833	-15.42754	0.1056883	0.1055500	23	-13.85092	-13.85479	0.0010416	
7	-15.29814	-15.29732	0.0888531	0.0886560	24	-13.80080	-13.80521	0.0008156	
8	-15.17280	-15.17202	0.0716072	0.0715640	25	-13.75603	-13.76082	0.0006189	
9	-15.05225	-15.05152	0.0559802	0.0559270	26	-13.71668	-13.72173	0.0004539	
10	-14.93643	-14.93571	0.0428184	0.0428000	27	-13.68299	-13.68815	0.0003240	
11	-14.82530	-14.82462	0.0322589	0.0322840	28	-13.65526	-13.66020	0.0002255	
12	-14.71883	-14.71819	0.0240594	0.0240790	29	-13.63378	-13.63809	0.0001502	
13	-14.61699	-14.61638	0.0178323	0.0178500	30	-13.61870	-13.62273	0.0000906	
14	-14.51976	-14.51920	0.0131779	0.0131970	31	-13.60993	*	0.0000424	*
15	-14.42711	-14.42665	0.0097356	0.0097472	32	-13.60652	*	0.0000110	*
16	-14.33904	-14.33871	0.0072128	0.0072057	33	-13.60573	*	0.0000035	*

*Stated as unbound by potential energy curve

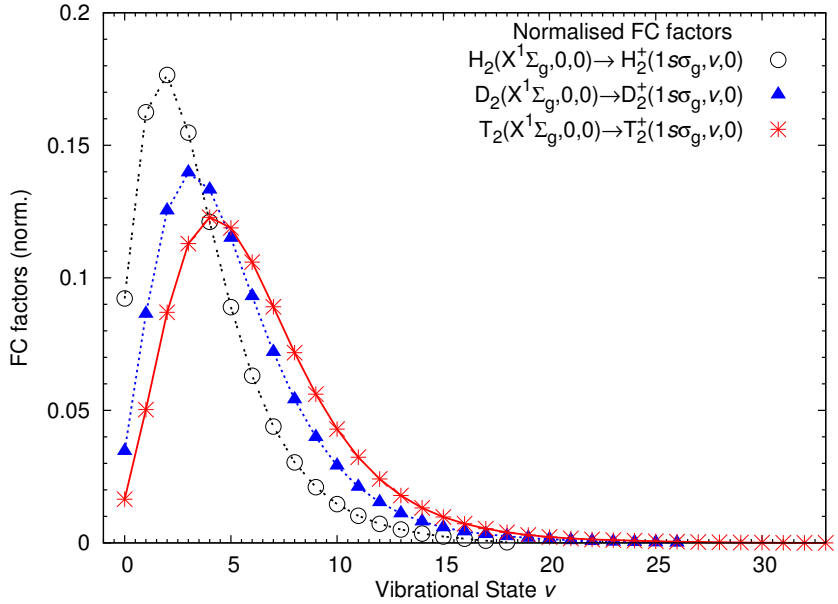

Figure 3.2: Normalised Franck-Condon (FC) factors of $H_2(X^1\Sigma_g^+, 0, 0) \rightarrow H_2^+(1s\sigma_g, v, 0)$, $D_2(X^1\Sigma_g^+, 0, 0) \rightarrow D_2^+(1s\sigma_g, v, 0)$ and $T_2(X^1\Sigma_g^+, 0, 0) \rightarrow T_2^+(1s\sigma_g, v, 0)$.

The $v = 0$ and $v = 1$ vibrational states probability density functions of H_2^+, H_2 and their isotopologues are presented in Fig. 3.3. It is seen that the lighter isotopologues have a more diffuse vibrational wave function. Note that the peak of the ground vibrational states probability density function is at a slightly higher R value than the equilibrium distance R_0. For example the H_2^+ equilibrium internuclear distance is at $R_0 = 2.0\ a_0$, while the peak of vibrational ground state probability density function is situated at approximately $R = 2.05\ a_0$, which is closer to the mean internuclear distance of the vibrational ground state $R_m = 2.063\ a_0$.

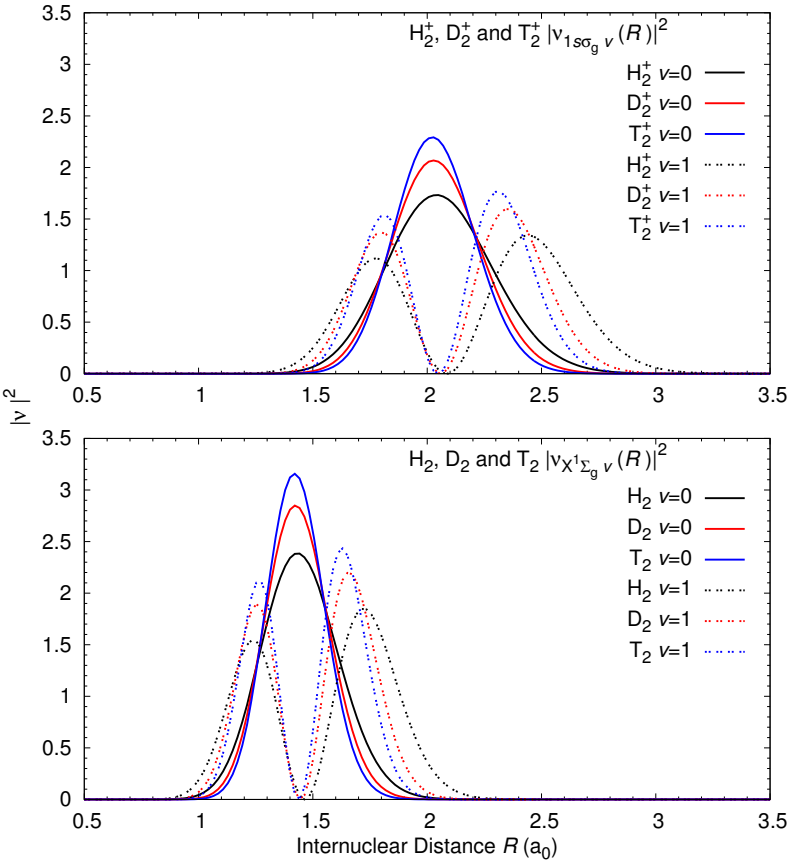

Figure 3.3: Vibrational probability density functions of the $H_2^+(1s\sigma_g, v, 0)$, $D_2^+(1s\sigma_g, v, 0)$, $T_2^+(1s\sigma_g, v, 0)$, $H_2(X^1\Sigma_g^+, v, 0)$, $D_2(X^1\Sigma_g^+, v, 0)$ and $T_2(X^1\Sigma_g^+, v, 0)$ molecules for the $v = 0$ and $v = 1$ states.

Chapter 4

Convergent close-coupling method

Here the convergent close-coupling (CCC) method is formulated in a general form for electron and positron scattering from symmetric linear molecules (H_2^+, H_2, Li_2, C_2, BeH_2, BeH_2^+, CO_2, etc and their respective isotopologues). This method can be extended simply to asymmetric linear molecules (HeH^+, BeH^+, BeH, LiH, OH, CO, etc and their respective isotopologues). However here non-uniqueness is only solved for one-electron targets.

Starting with the adiabatic-nuclei approximation introduced in Chapter 2, the scattering system Schrödinger equation is formulated in the body-frame for a fixed internuclear distance R and orientation of the diatomic molecule

$$(E^{(+)} - H)|\Psi_i^{S(+)}\rangle = 0, \tag{4.1}$$

where E is the total energy of the scattering system, $(+)$ denotes outgoing spherical-wave boundary conditions and i denotes the initial state of the system. Here the scattering Hamiltonian H is a sum of the single-particle Hamiltonian for the projectile $H_0^{\rm Elec}$ (3.5), the projectile-target electron potential terms V_{0j} (3.34) and the target Hamiltonian $H_{\rm T}^{\rm Elec}$ given in Eq. (3.3) for H_2^+ and Eq. (3.32) for H_2

$$H = H_{\rm T}^{\rm Elec} + H_0^{\rm Elec} + \sum_{j=1}^{N_e} V_{0j}, \tag{4.2}$$

where index 0 denotes the projectile coordinate space. A general form of

the scattering system asymptotic Hamiltonian $H_{\rm asy}$ is chosen such that

$$H_{\rm asy} = H_{\rm T}^{\rm Elec} + K_0^{\rm Elec} + \frac{z_{\rm e} Z_{\rm Ion}}{r_0} + U_0, \tag{4.3}$$

where $z_{\rm e}$ is the charge of the projectile ($z_{\rm e} = -1|e|$ for a projectile-electron and $z_{\rm e} = 1|e|$ for a positron-projectile). This form of $H_{\rm asy}$ allows for scattering from ionic targets with asymptotic charge $Z_{\rm Ion}$ (for H_2^+ $Z_{\rm Ion} = 1|e|$). The method described here is also suitable for asymptotically neutral targets by taking $Z_{\rm Ion} = 0|e|$ (as is the case for H_2). An optional short-ranged distorting potential U_0 is used purely for numerical stability of the solution and does not change final CCC results.

The close-coupling method utilises an explicitly antisymmetrised multichannel expansion. For this choice of $H_{\rm asy}$ (4.3) the fixed-nuclei total scattering wave function $\Psi_i^{S(+)}(\mathbf{x}_0, \mathbf{x}; R)$ is expanded over the complete set of positive- and negative-energy pseudostates $\Phi_n^N(\mathbf{x}; R)$ of the target (formulated in Chapter 3)

$$\begin{aligned} \Psi_i^{S(+)}(\mathbf{x}_0, \mathbf{x}; R) &= \mathcal{A} \sum_{n=1}^{N} \Phi_n^N(\mathbf{x}; R) f_{ni}^{SN(+)}(\mathbf{x}_0; R) \\ &= \mathcal{A} \psi_i^{SN(+)}(\mathbf{x}_0, \mathbf{x}; R), \end{aligned} \tag{4.4}$$

where $\mathbf{x}$ is collectively all target electronic spatial and spin coordinates, $\mathcal{A}$ is the antisymmetrisation operator given in Eq. (2.11) and $f_{ni}^{SN(+)}(\mathbf{x}_0; R)$ are the multichannel functions. The CCC method relies on the completeness of the Laguerre basis and hence pseudostates $\Phi_n^N(\mathbf{x}; R)$ such that

$$\lim_{N \to \infty} \Psi_i^{SN(+)}(\mathbf{x}_0, \mathbf{x}; R) = \Psi_i^{S(+)}(\mathbf{x}_0, \mathbf{x}; R). \tag{4.5}$$

4.1 Non-uniqueness

The antisymmetric total wave function $\Psi_i^{SN(+)}(\mathbf{x}_0, \mathbf{x}; R)$ in Eq. (4.4) is unique, however $\psi_i^{SN(+)}(\mathbf{x}_0, \mathbf{x}; R)$ is not unique since the antisymmetrisation operator can transform two different functions into one single function. Hence expression (4.4) is too general and leads to non-unique solutions [233].

For example suppose functions $g_n^{SN}(\mathbf{x}_0; R)$ are of the form

$$0 = \mathcal{A} \sum_{n=1}^{N} \Phi_n^N(\mathbf{x}; R) g_n^{SN}(\mathbf{x}_0; R) \tag{4.6}$$

then there are solutions

$$\Psi_i^{SN(+)}(\mathbf{x}_0, \mathbf{x}; R) = \mathcal{A} \sum_{n=1}^{N} \Phi_n^N(\mathbf{x}; R) \left(f_{ni}^{SN(+)}(\mathbf{x}_0; R) + B g_n^{SN}(\mathbf{x}_0; R) \right), \tag{4.7}$$

for any constant B.

In practice this non-unique expansion can lead to numerical instabilities in the half-on-shell K-matrix and consequently the on-shell T-matrix. Non-uniqueness becomes evident when a small variation in the momentum quadrature points (k-grid) leads to a large variation in the on-shell T-matrix results. This is a purely numerical problem that has been addressed for atomic and ionic targets [195, 196, 219], a similar technique is applied to molecules.

4.1.1 Solving non-uniqueness of H_2^+

For electron scattering from H_2^+ the expansion in Eq. (4.7) is written as

$$\begin{aligned} \Psi_i^{SN(+)}(\boldsymbol{r}_0, \boldsymbol{r}_1; R) &= [1 + (-1)^S P_{\boldsymbol{r}_0, \boldsymbol{r}_1}] \psi_i^{SN(+)}(\boldsymbol{r}_0, \boldsymbol{r}_1; R) && (4.8) \\ &= [1 + (-1)^S P_{\boldsymbol{r}_0, \boldsymbol{r}_1}] && (4.9) \\ &\quad \times \sum_{n=1}^{N} \Phi_n^N(\boldsymbol{r}_1; R) \left(f_{ni}^{SN(+)}(\boldsymbol{r}_0; R) + B g_n^{SN}(\boldsymbol{r}_0; R) \right), \end{aligned}$$

where $g_n^{SN}(\boldsymbol{r}_0; R)$ satisfies

$$0 = [1 + (-1)^S P_{\boldsymbol{r}_0, \boldsymbol{r}_1}] \sum_{n=1}^{N} \Phi_n^N(\boldsymbol{r}_1; R) g_n^{SN}(\boldsymbol{r}_0; R). \tag{4.10}$$

For the $S = 0$ channel $g_n^{0N}(\boldsymbol{r}_0; R) = 0$, while for the $S = 1$ channel $g_n^{1N}(\boldsymbol{r}_0; R)$ must be spanned by the target states $\Phi_n^N(\boldsymbol{r}_0; R)$ to satisfy (4.10). Hence the non-uniqueness problem only needs to be solved in the space spanned by the target states.

The non-uniqueness problem is solved by forcing $g_n^{SN}(\boldsymbol{r}_0; R) = 0$.

This is accomplished by making $\psi_i^{SN(+)}(\boldsymbol{r}_0, \boldsymbol{r}_1; R)$ antisymmetric like $\Psi_i^{SN(+)}(\boldsymbol{r}_0, \boldsymbol{r}_1; R)$ (note that the antisymmetrisation operator acting on an antisymmetric function results in an antisymmetric function). Utilising this antisymmetric property of $\psi_i^{SN(+)}(\boldsymbol{r}_0, \boldsymbol{r}_1; R)$

$$\psi_i^{SN(+)}(\boldsymbol{r}_0, \boldsymbol{r}_1; R) = (-1)^S P_{\boldsymbol{r}_0, \boldsymbol{r}_1} \psi_i^{SN(+)}(\boldsymbol{r}_0, \boldsymbol{r}_1; R), \tag{4.11}$$

the multichannel expansion (4.8) can be rewritten as

$$\begin{aligned}
&\Psi_i^{SN(+)}(\boldsymbol{r}_0, \boldsymbol{r}_1; R) \\
&\quad = \left[1 + (-1)^S P_{\boldsymbol{r}_0, \boldsymbol{r}_1}(1 - \theta + \theta)\right] \psi_i^{SN(+)}(\boldsymbol{r}_0, \boldsymbol{r}_1; R) \\
&\quad = \left[(1 + \theta) + (-1)^S P_{\boldsymbol{r}_0, \boldsymbol{r}_1}(1 - \theta)\right] \psi_i^{SN(+)}(\boldsymbol{r}_0, \boldsymbol{r}_1; R) \qquad (4.12) \\
&\quad = \sum_{n=1}^{N} \Big[(1 + \theta)\Phi_n^N(\boldsymbol{r}_1; R) \left(f_{ni}^{SN(+)}(\boldsymbol{r}_0; R) + B g_n^{SN}(\boldsymbol{r}_0; R)\right) \qquad (4.13) \\
&\qquad + (-1)^S (1 - \theta)\Phi_n^N(\boldsymbol{r}_0; R) \left(f_{ni}^{SN(+)}(\boldsymbol{r}_1; R) + B g_n^{SN}(\boldsymbol{r}_1; R)\right)\Big].
\end{aligned}$$

From the above the function $g_n^{SN}(\boldsymbol{r}_0; R)$ must now satisfy

$$\begin{aligned}
0 &= \sum_{n=1}^{N} \big[(1 + \theta)\Phi_n^N(\boldsymbol{r}_1; R) g_n^{SN}(\boldsymbol{r}_0; R) \\
&\quad + (-1)^S (1 - \theta)\Phi_n^N(\boldsymbol{r}_0; R) g_n^{SN}(\boldsymbol{r}_1; R)\big] \\
&= \sum_{n=1}^{N} \big[\Phi_n^N(\boldsymbol{r}_1; R) g_n^{SN}(\boldsymbol{r}_0; R) + (-1)^S \Phi_n^N(\boldsymbol{r}_0; R) g_n^{SN}(\boldsymbol{r}_1; R) \qquad (4.14) \\
&\quad + \theta \left(\Phi_n^N(\boldsymbol{r}_1; R) g_n^{SN}(\boldsymbol{r}_0; R) - (-1)^S \Phi_n^N(\boldsymbol{r}_0; R) g_n^{SN}(\boldsymbol{r}_1; R)\right)\big],
\end{aligned}$$

which forces $g_n^{SN}(\boldsymbol{r}; R) = 0$ for non-zero θ. By having $\psi_i^{SN(+)}(\boldsymbol{r}_0, \boldsymbol{r}_1; R)$ antisymmetric (4.11), the following condition is also true

$$\langle \Phi_m^N | f_{ni}^{SN} \rangle = (-1)^S \langle \Phi_n^N | f_{mi}^{SN} \rangle. \tag{4.15}$$

Condition (4.15) leads to the following property

$$(-1)^S \langle \boldsymbol{k}_f^{(-)} \Phi_f^N | P_{\boldsymbol{r_0}, \boldsymbol{r_1}} | \psi_i^{SN} \rangle = \langle \boldsymbol{k}_f^{(-)} \Phi_f^N | I_0^N | \psi_i^{SN} \rangle, \tag{4.16}$$

which is implemented within the energy term of the V-matrix elements

$$\begin{aligned}(-1)^S E\langle \boldsymbol{k}_f^{(-)}\Phi_f^N|P_{\boldsymbol{r_0},\boldsymbol{r_1}}|\psi_i^{SN}\rangle \\ &= (-1)^S(1-\theta+\theta)E\langle \boldsymbol{k}_f^{(-)}\Phi_f^N|P_{\boldsymbol{r_0},\boldsymbol{r_1}}|\psi_i^{SN}\rangle \\ &= (-1)^S(1-\theta)E\langle \boldsymbol{k}_f^{(-)}\Phi_f^N|P_{\boldsymbol{r_0},\boldsymbol{r_1}}|\psi_i^{SN}\rangle \\ &\quad +\theta E\langle \boldsymbol{k}_f^{(-)}\Phi_f^N|I_0^N|\psi_i^{SN}\rangle,\end{aligned} \tag{4.17}$$

where the projection operator I_0^N is expressed as an expansion over the electronic target states of H_2^+

$$I_0^N = \sum_{n=1}^{N} |\Phi_n^N\rangle\langle\Phi_n^N|. \tag{4.18}$$

Hence condition (4.11) is implemented within the energy term of the V-matrix elements for non-zero θ. Final CCC results are found to be independent of the choice of non-zero θ.

4.2 Momentum-space coupled-channel Lippmann-Schwinger equation

The CCC method utilises the close-coupling expansion (4.4) and transforms the Schrödinger equation (4.1) into the momentum-space coupled-channel Lippmann-Schwinger equation. Here the dependence on R is omitted from the notation unless it is explicitly indicated.

Substituting $\Psi_i^{SN(+)}(\mathbf{x}_0, \mathbf{x}; R)$ (4.4), the scattering Hamiltonian H (4.2) into the Schrödinger Eq. (4.1) and rearranging to have the asymptotic Hamiltonian $H_{\rm asy}$ (4.3) on the left-hand-side

$$\begin{aligned}(E^{(+)} - H_{\rm T} - K_0^{\rm Elec})|\psi_i^{(+)}\rangle \\ &= \left(V_0 + \sum_{j=1}^{N_e} V_{0j} + (E-H)\sum_{j=1}^{N_e} P_{0j}\right)|\psi_i^{(+)}\rangle.\end{aligned} \tag{4.19}$$

Subtracting the asymptotic target ion potential $\frac{z_{\rm e}Z_{\rm Ion}}{r_0}$ and short-ranged distorting potential U_0 on both sides

$$(E^{(+)} - H_{\rm asy})|\psi_i^{(+)}\rangle = V_U|\psi_i^{(+)}\rangle, \tag{4.20}$$

where

$$V_U = V_0 + \sum_{j=1}^{N_e} V_{0j} - \frac{z_{\rm e} Z_{\rm Ion}}{r_0} - U_0 + (E - H) \sum_{j=1}^{N_e} P_{0j}. \tag{4.21}$$

Utilising (4.17) for H_2^+, condition (4.11) is implemented within the V-matrix elements and the interaction potential (4.21) becomes

$$\begin{aligned} V_U^{SN}(\theta) = V_0 + V_{01} - \frac{z_{\rm e} Z_{\rm Ion}}{r_0} - U_0 \\ -E\theta I_0^N + (E(1-\theta) - H)\, P_{01}. \end{aligned} \tag{4.22}$$

For the asymptotic Hamiltonian $H_{\rm asy}$ (4.3) the Green's function approach is utilised to transform the Schrödinger equation (4.1) to the momentum-space Lippmann-Schwinger equation

$$|\psi_i^{SN}\rangle = |\Phi_i^N \boldsymbol{k}_i^{(+)}\rangle + \sum_{n=1}^{N} \sum\!\!\!\!\!\!\int_k d^3k \frac{|\Phi_n^N \boldsymbol{k}^{(-)}\rangle\langle \boldsymbol{k}^{(-)} \Phi_n^N | V_U^{SN}(\theta) | \psi_i^{SN}\rangle}{E^{(+)} - \varepsilon_k - \varepsilon_n^N + i0}, \tag{4.23}$$

where $|\boldsymbol{k}^{(\pm)}\rangle$ denotes a distorted-wave which is a solution of the equation

$$(\varepsilon_k^{(\pm)} - K_0 - z_{\rm e} Z_{\rm Ion}/r_0 - U_0)|\boldsymbol{k}^{(\pm)}\rangle = 0, \tag{4.24}$$

and $|\Phi_n^N \boldsymbol{k}^{(+)}\rangle$ satisfy the asymptotic Hamiltonian $H_{\rm asy}$ (4.3)

$$\begin{aligned} 0 &= (E^{(+)} - K_0 - z_{\rm e} Z_{\rm Ion}/r_0 - U_0 - \varepsilon_n^N)|\Phi_n^N \boldsymbol{k}^{(+)}\rangle \\ &= (E^{(+)} - \varepsilon_k - \varepsilon_n^N)|\Phi_n^N \boldsymbol{k}^{(+)}\rangle. \end{aligned} \tag{4.25}$$

Premultiplying Eq. (4.23) by $\langle \boldsymbol{k}_f^{(-)} \Phi_f^N | V_U^{SN}(\theta)$, the coupled Lippmann-Schwinger equation for the distorted-wave T-matrix is obtained

$$\begin{aligned} &\langle \boldsymbol{k}_f^{(-)} \Phi_f^N | T_U^{SN} | \Phi_i^N \boldsymbol{k}_i^{(+)}\rangle = \langle \boldsymbol{k}_f^{(-)} \Phi_f^N | V_U^{SN}(\theta) | \Phi_i^N \boldsymbol{k}_i^{(+)}\rangle \\ &+ \sum_{n=1}^{N} \sum\!\!\!\!\!\!\int_k d^3k \frac{\langle \boldsymbol{k}_f^{(-)} \Phi_f^N | V_U^{SN}(\theta) | \Phi_n^N \boldsymbol{k}^{(-)}\rangle\langle \boldsymbol{k}^{(-)} \Phi_n^N | T_U^{SN} | \Phi_i^N \boldsymbol{k}_i^{(+)}\rangle}{E^{(+)} - \varepsilon_k - \varepsilon_n^N + i0}, \end{aligned} \tag{4.26}$$

where f denotes the final state of the system and

$$\langle \boldsymbol{k}_f^{(-)} \Phi_f^N | T_U^{SN} | \Phi_i^N \boldsymbol{k}_i^{(+)}\rangle \equiv \langle \boldsymbol{k}_f^{(-)} \Phi_f^N | V_U^{SN}(\theta) | \psi_i^{SN}\rangle. \tag{4.27}$$

The short-ranged distorting potential U_0 in equations (4.24) and (4.25) can lead to a number of projectile bound states. For ionic targets there are an infinite number of projectile bound states, while for neutral targets U_0 can support a number of projectile bound states. Projectile bound states are included into the Green's function until convergence is reached. The form of U_0 will be discussed later. Referring to Eq. (4.27) the distorted-wave T-matrix $\langle \boldsymbol{k}_f^{(-)} \Phi_f^N | T_U^{SN} | \Phi_i^N \boldsymbol{k}_i^{(+)} \rangle$ is defined for the potential $V_U^{SN}(\theta) = V^{SN}(\theta) - U_0$ and hence does not give physical results. The physical T-matrix T^{SN} is extracted via the relation [196]

$$\begin{aligned} &\langle \boldsymbol{q}_f^{(-)} \Phi_f^N | T^{SN} | \Phi_i^N \boldsymbol{q}_i^{(+)} \rangle \\ &\qquad \equiv \langle \boldsymbol{q}_f^{(-)} \Phi_f^N | V^{SN} | \psi_i^{SN} \rangle \\ &\qquad = \langle \boldsymbol{k}_f^{(-)} \Phi_f^N | T_U^{SN} | \Phi_i^N \boldsymbol{k}_i^{(+)} \rangle + \delta_{f,i} \langle \boldsymbol{k}_f^{(-)} | U_0 | \boldsymbol{q}_i^{(+)} \rangle, \quad (4.28) \end{aligned}$$

where $\boldsymbol{q}^{(\pm)}$ refers to a Coulomb wave function for an ionic target or a plane-wave for a neutral target. For a neutral target and choosing to have $U_0 = 0$, the sum and integrand over d^3k in Eq. (4.26) is replaced with just an integration over d^3k, where resulting on-shell T-matrix elements are physical and are used to calculate body-frame scattering amplitudes. Note that although V-matrix elements in Eq. (4.26) have a dependence on an arbitrary θ, the resultant on-shell T-matrix elements do not.

4.2.1 Solving the coupled Lippmann-Schwinger equation

A partial-wave expansion of the projectile wave function allows the three-dimensional Lippmann-Schwinger equation (4.26) to be solved in effectively one-dimension. The distorted-wave partial-wave expansion is

$$|\boldsymbol{k}^{(\pm)}\rangle \;=\; \frac{\sqrt{2}}{kr\sqrt{\pi}} \sum_{L,M} i^L e^{\pm i(\sigma_L + \delta_L)} u_L(r; k; Z_{\mathrm{Ion}}) Y_{LM}(\hat{\boldsymbol{r}}) Y_{LM}^*(\hat{\boldsymbol{k}}), \quad (4.29)$$

where σ_L and δ_L are the Coulomb and distorting phase shifts, respectively. Angular terms in the matrix elements of the Lippmann-Schwinger equation can now be evaluated analytically. This allows us to perform accurate, large-scale multichannel calculations and minimises computational resources required.

Projectile wave functions with large values of momentum k are highly

oscillatory and hence can lead to a loss of accuracy in the calculation of the V-matrix elements $\langle \boldsymbol{k}_f^{(-)} \Phi_f^N | V_U^{SN}(\theta) | \Phi_i^N \boldsymbol{k}_i^{(\pm)} \rangle$. Therefore it is numerically favourable to have the most detailed structure of the integrand in the smaller values of k (in the k-grid) when evaluating the Lippmann-Schwinger equation (4.26). As Z increases, the projectile-nuclei term V_0 in Eq. (4.22) is responsible for making V-matrix elements with larger values of k more important. To minimise this numerical issue, a short-ranged distorting potential U_0 is chosen such that it cancels the spherical part of the V_0 potential. Using the antisymmetrisation property of the target states, the distorting potential can be written as

$$U_0 = 2 z_\mathrm{e} Z v_0(r_0, R/2) - \frac{z_\mathrm{e} Z_\mathrm{Ion}}{r_0} - z_\mathrm{e} N_e \int d^3 r |\Phi_n(\boldsymbol{r})|^2 v_0(r_0, r_1), \qquad (4.30)$$

where $\boldsymbol{r}$ is collectively all target electronic spatial coordinates, n is typically the electronic ground state and $v_0(r_0, r_1)$ is defined in Eq. (3.9). This form of U_0 is spherically symmetric, short-ranged and ensures the shortest-range V-matrix elements by removing the projectile-nuclei term V_0 for the $\lambda = 0$ partial-wave [referring to Eq. (3.8)]. The use of a distorting potential is a purely numerical technique which saves on computational resources when solving the integral in Eq. (4.26). Results of T^{SN} from Eq. (4.28) must be independent of U_0.

Utilising the partial-wave expansion of the projectile wave function (4.29) and analysing the V-matrix elements $\langle \boldsymbol{k}_f^{(-)} \Phi_f^N | V_U^{SN}(\theta) | \Phi_i^N \boldsymbol{k}_i^{(\pm)} \rangle$ in the Lippmann-Schwinger equation (4.26), it can be shown that symmetric linear molecules and their isotopologues conserve the scattering system total electronic orbital angular projection M, parity Π and spin S (in the body-frame). The partial-wave expansion of the V- (or T-) matrix for an incident electron with linear momentum k_i, orbital angular momentum L_i and orbital angular projection M_i has the form

$$\langle \boldsymbol{k}_f^{(-)} \Phi_f^N | V_U^{SN}(\theta) | \Phi_i^N \boldsymbol{k}_i^{(\pm)} \rangle = (k_f k_i)^{-1} \sum_{\substack{L_f, L_i \\ M_f, M_i}} i^{L_i - L_f} \qquad (4.31)$$

$$\times e^{i(\sigma_{L_f} + \delta_{L_f} \pm \sigma_{L_i} \pm \delta_{L_i})} V^{M\Pi S}_{f L_f M_f, i L_i M_i}(k_f, k_i) Y_{L_f M_f}(\hat{\boldsymbol{k}}_f^{(\mathrm{b})}) Y^*_{L_i M_i}(\hat{\boldsymbol{k}}_i^{(\mathrm{b})}),$$

or alternatively as

$$V^{M\Pi S}_{L_fM_f,L_iM_i}(k_f,k_i) = (k_fk_i)i^{L_f-L_i}e^{-i(\sigma_{L_f}+\delta_{L_f}\pm\sigma_{L_i}\pm\delta_{L_i})} \times \int d\hat{\boldsymbol{k}}_f \int d\hat{\boldsymbol{k}}_i Y^*_{L_fM_f}(\hat{\boldsymbol{k}}^{(\mathrm{b})}_f)Y_{L_iM_i}(\hat{\boldsymbol{k}}^{(\mathrm{b})}_i)\langle \boldsymbol{k}^{(-)}_f\Phi^N_f|V^{SN}_U(\theta)|\Phi^N_i\boldsymbol{k}^{(\pm)}_i\rangle, \tag{4.32}$$

where $V^{M\Pi S}_{fL_fM_f,iL_iM_i}(k_f,k_i)$ are the real V-matrix elements, $M = M_f + m_f = m_i + M_i$, $\Pi = \pi_f(-1)^{L_f} = \pi_i(-1)^{L_i}$ and $\hat{\boldsymbol{k}}^{(\mathrm{b})}$ refers to the electron momentum vector in the body-frame. Substituting Eq. (4.31) into the Lippmann-Schwinger equation (4.26), complex phases $i^{L_i-L_f}e^{i(\sigma_{L_f}+\delta_{L_f}\pm\sigma_{L_i}\pm\delta_{L_i})}$, constants $(k_fk_i)^{-1}$ and angular functions $Y_{L_fM_f}(\hat{\boldsymbol{k}}^{(\mathrm{b})}_f)Y^*_{L_iM_i}(\hat{\boldsymbol{k}}^{(\mathrm{b})}_i)$ can be factored out. Performing the integration over $d\hat{k}$ in the Lippmann-Schwinger equation (4.26), the partial-wave Lippmann-Schwinger equation for the distorted-wave T-matrix can be written as

$$T^{M\Pi S}_{fL_fM_f,iL_iM_i}(k_f,k_i) = V^{M\Pi S}_{fL_fM_f,iL_iM_i}(k_f,k_i) + \sum_{n=1}^{N}\sum_{L'M'}\sum\!\!\!\!\!\!\int_k dk \frac{V^{M\Pi S}_{fL_fM_f,nL'M'}(k_f,k)T^{M\Pi S}_{nL'M',iL_iM_i}(k,k_i)}{E^{(+)}-\varepsilon_k-\varepsilon^N_n+i0}. \tag{4.33}$$

The Lippmann-Schwinger equation (4.33) has been efficiently solved for scattering from atomic and ionic targets [195, 196, 202], here the same standard techniques are utilised. The loss of total angular momentum conservation in Eq. (4.33) is the major difference between solving Eq. (4.33) for diatomic molecules and atoms. Equation (4.33) is also applicable to scattering from heterogeneous linear molecules, however the T- and V-matrix elements will lose conservation in parity Π (in the body-frame).

Evaluating the singularity in Eq. (4.33) analytically, it becomes

$$\begin{aligned} T^{M\Pi S}_{fL_fM_f,iL_iM_i}(k_f,k_i) &= V^{M\Pi S}_{fL_fM_f,iL_iM_i}(k_f,k_i) \\ &+ \sum_{n=1}^{N}\sum_{L'M'} P\sum\!\!\!\!\!\!\int_k dk \frac{V^{M\Pi S}_{fL_fM_f,nL'M'}(k_f,k)T^{M\Pi S}_{nL'M',iL_iM_i}(k,k_i)}{E^{(+)}-\varepsilon_k-\varepsilon_n} \\ &- i\pi\sum_{n=1}^{N_0}\sum_{L'M'} k_n^{-1}V^{M\Pi S}_{fL_fM_f,nL'M'}(k_f,k_n)T^{M\Pi S}_{nL'M',iL_iM_i}(k_n,k_i), \end{aligned} \tag{4.34}$$

where, P indicates the integral is of principal value type, the total energy is $E = \varepsilon_i + \varepsilon_{k_i} = \varepsilon_f + \varepsilon_{k_f}$, the on-shell momentum $k_n = \sqrt{2(E-\varepsilon_n)}$ and

is always real. N_0 is the number of open states, a state is open if $\varepsilon_n \leq E$. To obtain a symmetric, unitary T-matrix and to save on computational resources, the K-matrix formulation is introduced to solve (4.34) using real arithmetic

$$K^{M\Pi S}_{nLM,iL_iM_i}(k_n,k_i) = \sum_{n'=1}^{N_0}\sum_{L'M'} T^{M\Pi S}_{nLM,n'L'M'}(k_n,k_{n'}) \times \left(\delta_{n_i,n'}\delta_{L_i,L'}\delta_{M_i,M'} + i\pi k_{n'}^{-1} K^{M\Pi S}_{n'L'M',iL_iM_i}(k_{n'},k_i)\right). \tag{4.35}$$

Summing over all initial channels in (4.34), performing some algebra and substituting (4.35), one obtains

$$K^{M\Pi S}_{fL_fM_f,iL_iM_i}(k_f,k_i) = V^{M\Pi S}_{fL_fM_f,iL_iM_i}(k_f,k_i) + \sum_{n=1}^{N}\sum_{L'M'} P\!\!\int\!\!\!\!\!\!\sum_{k} dk \frac{V^{M\Pi S}_{fL_fM_f,nL'M'}(k_f,k)K^{M\Pi S}_{nL'M',L_iM_i}(k,k_i)}{E^{(+)}-\varepsilon_k-\varepsilon_n^N}. \tag{4.36}$$

Letting the indexes i and f refer to channels $|n_im_i\pi_is_i,k_iL_iM_i : M\Pi S\rangle$ and $|n_fm_f\pi_fs_f,k_fL_fM_f : M\Pi S\rangle$, respectively, the coupled integral equations are solved by replacing the integrand with a quadrature rule

$$K^{M\Pi S}_{fi} = V^{M\Pi S}_{fi} + \sum_{n=1} w_n V^{M\Pi S}_{fn} K^{M\Pi S}_{ni}, \tag{4.37}$$

where, w_n contain the Gaussian type weights divided by the Greens function denominator (energy terms) and n now runs over all combinations of off-shell momentum quadrature (k-grid) points and channels $|nm\pi s,kL'M' : M\Pi S\rangle$ for a particular partial-wave. Here the bound states of the projectile come like extra quadrature points in Eq. (4.37), for more details see Bray [196]. Equation (4.37) is rearranged to form a linear system of equations $Ax = b$ by letting channels f run over the same range as n. This is indicated by replacing index f with n', Eq. (4.37) is now rearranged in the form

$$\sum_{n=1}(\delta_{n'n} - w_n V^{M\Pi S}_{n'n})K^{M\Pi S}_{ni} = V^{M\Pi S}_{n'i}. \tag{4.38}$$

Equation (4.38), is solved for the half-on-shell K-matrix elements $K^{M\Pi S}_{ni}$ using a standardised linear equation solver, in this case SCALAPACK was used. Substitution of $K^{M\Pi S}_{ni}$ into Eq. (4.37) allows solution of $K^{M\Pi S}_{fi}$. The

real on-shell K-matrix elements are then used to solve the linear system of equations for the complex distorted-wave T-matrix elements

$$\sum_{n=1}^{N_0}(\delta_{n,i}+i\pi k_n K_{ni}^{M\Pi S})T_{fn}^{M\Pi S}=K_{fi}^{M\Pi S}, \tag{4.39}$$

here, n is the on-shell combinations of $|nm\pi s,k_nL'M'\rangle$ and N_0 is the total number of open on-shell channels.

The distorted-wave T-matrix elements are used to obtain physical ($U_0=0$) T-matrix elements $T^{M\Pi S}_{fL_fM_f,iL_iM_i}(q_f,q_i)$ via Eq. (4.28)

$$\begin{aligned} T^{M\Pi S}_{fL_fM_f,iL_iM_i}(q_f,q_i) &= T^{M\Pi S}_{fL_fM_f,iL_iM_i}(k_f,k_i)e^{i(\delta_{L_i}+\delta_{L_f})} \\ &\quad -\delta_{f,i}\delta_{L_f,L_i}\delta_{M_f,M_i}q_i\pi^{-1}e^{i\delta_{L_i}}\sin(\delta_{L_i}), \end{aligned} \tag{4.40}$$

where q is the linear momentum of the electron and indicates the physical T-matrix elements. The physical T-matrix can then be expressed as

$$\begin{aligned} &\langle \boldsymbol{q}_f^{(-)}\Phi_f^N|T^{SN}|\Phi_i^N\boldsymbol{q}_i^{(+)}\rangle=(q_fq_i)^{-1}\sum_{\substack{L_f,L_i\\M_f,M_i}} i^{L_i-L_f}e^{i(\sigma_{L_i}+\sigma_{L_f})} \\ &\times T^{M\Pi S}_{fL_fM_f,iL_iM_i}(q_f,q_i)Y_{L_fM_f}(\hat{\boldsymbol{q}}_f^{(\mathrm{b})})Y^*_{L_iM_i}(\hat{\boldsymbol{q}}_i^{(\mathrm{b})}). \end{aligned} \tag{4.41}$$

This physical body-frame T-matrix is used to obtain the laboratory-frame scattering amplitudes defined in equations (2.41) and (2.45) and cross sections as described in Section 2.2. For electronically homogeneous diatomic molecules the partial-wave term $A^{S(\mathrm{b})}_{fL_fM_f,iL_iM_i}(R)$ defined in Eq. (2.40), is more appropriately replaced by

$$\begin{aligned} &A^{M\Pi S(\mathrm{b})}_{fL_fM_f,iL_iM_i}(R)=-(2\pi)^2(q_fq_i)^{-1}i^{L_i-L_f} \\ &\times e^{i(\sigma_{L_i}+\sigma_{L_f})}T^{M\Pi S(\mathrm{b})}_{fL_fM_f,iL_iM_i}(q_f,q_i;R), \end{aligned} \tag{4.42}$$

where $T^{M\Pi S(\mathrm{b})}_{fL_fM_f,iL_iM_i}(q_f,q_i;R)\equiv T^{M\Pi S}_{fL_fM_f,iL_iM_i}(q_f,q_i)$ in equations (4.40) and (4.41).

4.3 V-matrix elements

4.3.1 V-matrix elements for $e^{\pm}$-H_2^+

The scattering system interaction potential $V_U^{SN}(\theta)$ (4.22) can be split into a sum of direct- and exchange-potential terms, noting that the exchange-interaction is only present in electron scattering. For H_2^+ the direct interaction potential is

$$V_U^{\mathrm{D}} = V_0 + V_{01} - \frac{z_{\mathrm{e}} Z_{\mathrm{Ion}}}{r_0} - U_0, \tag{4.43}$$

and the exchange-potential is

$$V_{\mathrm{Exch}}^{SN}(\theta) = -E\theta I_0^N - (-1)^S (E(1-\theta) - H) P_{\boldsymbol{r}_0 \boldsymbol{r}_1}. \tag{4.44}$$

Electron-H_2^+ V-matrix elements $V^{M\Pi S}_{fL_fM_f,iL_iM_i}(k_f, k_i)$ in (4.32) are evaluated by summing the direct and exchange terms. For notational purposes the target states of H_2^+ are represented by the form of Eq. (3.14). The direct part of the V-matrix element is given by

$$\begin{aligned}
&\langle k'L'M'(\boldsymbol{r}_0), n'm'\pi'(\boldsymbol{r}_1) : \bar{M}'\Pi'S' | V_U^D | kLM(\boldsymbol{r}_0), nm\pi(\boldsymbol{r}_1) : \bar{M}\Pi S \rangle \\
&\quad = \frac{2}{\pi} \delta_{\bar{M}',\bar{M}} \delta_{\Pi',\Pi} \delta_{S',S} \sum_{\alpha\gamma} C_\alpha^{(n')} C_\gamma^{(n)} \sum_{\lambda\mu} (-1)^{\lambda+\mu} C^{L0}_{L'0,\lambda 0} C^{L'M'}_{LM,\lambda-\mu} \\
&\quad \times \Bigg(\delta_{\mu,0} \delta_{l_\alpha,l_\gamma} \delta_{m_\alpha,m_\gamma} \int_0^\infty dr_1 \varphi_\alpha(r_1) \varphi_\gamma(r_1) \int_0^\infty dr_0 u_{L'}(r_0; k'; Z_{\mathrm{Ion}}) \\
&\quad \times (z_{\mathrm{e}}(1 + (-1)^\lambda) v_\lambda(r_0, R/2) - \delta_{\lambda,0} U(r_0)) u_L(r_0; k; Z_{\mathrm{Ion}}) \\
&\quad - z_{\mathrm{e}} \, (-1)^\lambda C^{l_\gamma 0}_{l_\alpha 0,\lambda 0} C^{l_\alpha m_\alpha}_{l_\gamma m_\gamma,\lambda\mu} \\
&\quad \times \int dr_0 dr_1 u_{L'}(r_0; k'; Z_{\mathrm{Ion}}) u_L(r_0; k; Z_{\mathrm{Ion}}) v_\lambda(r_0, r_1) \varphi_\alpha(r_1) \varphi_\gamma(r_1) \Bigg).
\end{aligned} \tag{4.45}$$

The exchange term of the V-matrix element, can also be split into one-electron terms and the electron-electron term. Firstly evaluating the ex-

change electron-electron term

$$\begin{aligned}
&\langle k'L'M'(\boldsymbol{r}_0), n'm'\pi'(\boldsymbol{r}_1) : \bar{M}'\Pi'S'|(-1)^S V_{01} P_{\boldsymbol{r}_0\boldsymbol{r}_1}|kLM(\boldsymbol{r}_0), nm\pi(\boldsymbol{r}_1) : \bar{M}\Pi S\rangle \\
&= (-1)^S \delta_{\bar{M}',\bar{M}}\delta_{\Pi',\Pi}\delta_{S',S}\frac{2}{\pi}\sum_{\alpha\gamma} C_\alpha^{(n')} C_\gamma^{(n)} \qquad (4.46)\\
&\quad\times \sum_{\lambda\mu}(-1)^\mu C^{l_\gamma 0}_{L'0,\lambda 0} C^{L'M'}_{l_\gamma m_\gamma,\lambda-\mu} C^{L0}_{l_\alpha 0,\lambda 0} C^{l_\alpha m_\alpha}_{LM,\lambda\mu} \\
&\quad\times \int dr_0 dr_1 \varphi_\gamma(r_0) u_{L'}(r_0;k';Z_{\rm Ion}) v_\lambda(r_0,r_1)\varphi_\alpha(r_1) u_L(r_1;k;Z_{\rm Ion}).
\end{aligned}$$

The one-electron terms are given by

$$\begin{aligned}
&\langle k'L'M'(\boldsymbol{r}_0), n'm'\pi'(\boldsymbol{r}_1) : \bar{M}'\Pi'S'|\left(-E\theta I_0^N\right. \\
&\qquad \left.-(-1)^S(E(1-\theta)-(H_0+H_T))P_{\boldsymbol{r}_0\boldsymbol{r}_1}\right)|kLM(\boldsymbol{r}_0), nm\pi(\boldsymbol{r}_1) : \bar{M}\Pi S\rangle \\
&= -(-1)^S \delta_{\bar{M}',\bar{M}}\delta_{\Pi',\Pi}\delta_{S',S}\left(\langle k'L'M'|nm\pi\rangle\langle n'm'\pi'|kLM\rangle \qquad (4.47)\right.\\
&\quad\times(E(1-\theta)-\varepsilon_{k'}-\varepsilon_k-1/R)-\langle k'L'M'|V_0-U_0|nm\pi\rangle \\
&\quad\left.-\langle n'm'\pi'|V_1-U_1|kLM\rangle\right) \\
&\quad-\delta_{n',n}\delta_{\bar{M}',\bar{M}}\delta_{\Pi',\Pi}\delta_{S',S}E\theta\langle k'L'M'|I_0^N|kLM\rangle,
\end{aligned}$$

where,

$$\begin{aligned}
&\langle k'L'M'|nm\pi\rangle \\
&\qquad = \sqrt{\frac{2}{\pi}}\sum_\gamma C_\gamma^{(n)}\delta_{L',l_\gamma}\delta_{M',m_\gamma}\int_0^\infty dr u_{L'}(r;k';Z_{\rm Ion})\varphi_\gamma(r), \qquad (4.48)\\
&\langle k'L'M'|V-U|nm\pi\rangle \\
&\qquad = \sqrt{\frac{2}{\pi}}\sum_\gamma C_\gamma^{(n)}\sum_{\lambda=0,2,4,..}(-1)^\lambda C^{l_\gamma 0}_{L'0,\lambda 0} C^{L'M'}_{l_\gamma m_\gamma,\lambda 0} \qquad (4.49)\\
&\qquad\quad\times\int_0^\infty dr u_{L'}(r;k';Z_{\rm Ion})(-2Zv_\lambda(r,R/2)-\delta_{\lambda,0}U(r))\varphi_\gamma(r).
\end{aligned}$$

V-matrix elements $V^{M\Pi S}_{fL_fM_f,iL_iM_i}(k_f,k_i)$ in (4.32) are a sum of (4.45), (4.46) and (4.47).

4.3.2 Positron scattering from H_2

Applying the CCC method to positron scattering from H_2, the interaction potential $V_U^{SN}(\theta)$ (4.22) and corresponding equations in Section 4.2 are re-

placed with the direct part of the interaction potential

$$V_U^{\mathrm{D}} = V_0 + 2V_{01} - U_0. \tag{4.50}$$

For single-centre positron scattering there is no exchange interaction, hence non-uniqueness is not an issue. Due to the complexity of the exchange-matrix elements electron scattering from H_2 is not included in this thesis. Following the submission of this thesis exchange-matrix elements will be implemented and electron scattering from H_2 will be investigated.

The V-matrix elements of positron-H_2 scattering are relatively straightforward and are given by

$$\begin{aligned}
&\langle k'L'M'(\boldsymbol{r}_0), n'm'\pi's'(\boldsymbol{r}_1,\boldsymbol{r}_2) : \bar{M}'\Pi'S'|V_U^{\mathrm{D}}|kLM(\boldsymbol{r}_0), nm\pi s(\boldsymbol{r}_1,\boldsymbol{r}_2) : \bar{M}\Pi S\rangle \\
&= \frac{2}{\pi}\delta_{\bar{M}',\bar{M}}\delta_{\Pi',\Pi}\delta_{S',S}\delta_{s',s}\sum_{\alpha\beta\gamma\delta} C^{(n')}_{\alpha,\beta}C^{(n)}_{\gamma,\delta}\langle\varphi_\beta|\varphi_\delta\rangle\delta_{l_\beta,l_\delta}\delta_{m_\beta,m_\delta} \\
&\quad\times\sum_{\lambda\mu}(-1)^{\lambda+\mu}C^{L0}_{L'0,\lambda0}C^{L'M'}_{LM,\lambda-\mu}\left(\delta_{\mu,0}\delta_{l_\alpha,l_\gamma}\delta_{m_\alpha,m_\gamma}\int_0^\infty dr_1\varphi_\alpha(r_1)\varphi_\gamma(r_1)\right. \\
&\quad\times\int_0^\infty dr_0 u_{L'}(k'r_0)u_L(kr_0)(z_{\mathrm{e}}Z(1+(-1)^\lambda)v_\lambda(r_0,R/2)-\delta_{\lambda,0}U(r_0)) \\
&\quad\left.-2z_{\mathrm{e}}(-1)^\lambda C^{l_\gamma 0}_{l_\alpha 0,\lambda 0}C^{l_\alpha m_\alpha}_{l_\gamma m_\gamma,\lambda\mu}\int dr_0dr_1u_{L'}(k'r_0)v_\lambda(r_0,r_1)u_L(kr_0)\varphi_\alpha(r_1)\varphi_\gamma(r_1)\right).
\end{aligned} \tag{4.51}$$

Here the target states of H_2 are represented by the form of Eq. (3.48).

4.4 Analytic Born subtraction technique

Practically CCC calculations can only be performed for a partial-wave expansion of limited size. To complete the expansion and save on computational resources an analytic Born subtraction method is utilised. The first-order Born approximation relies on the property that for large values of orbital angular momentum (long range interactions), T-matrix elements are equal to the direct-potential partial-wave V-matrix elements

$$T^{M\Pi S}_{fL_fM_f,iL_iM_i}(q_f,q_i) = \tilde{V}^{M\Pi}_{fL_fM_f,iL_iM_i}(q_f,q_i), \tag{4.52}$$

where q on the right-hand-side refers to a plane-wave and $\tilde{V}$ indicates the direct part of the interaction potential (4.22),

$$\tilde{V} = V_0 + \sum_{j=1}^{N_e} V_{0j} - \frac{z_{\rm e} Z_{\rm Ion}}{r_0}. \tag{4.53}$$

4.4.1 Analytic Born matrix elements

The direct-potential V-matrix can avoid the infinite series partial-wave expansion of the projectile by applying the Bethe-formula [234], which allows analytic integration over the projectile coordinate space. Here the analytic Born subtraction technique is only utilised for inelastic-scattering, hence by orthogonality of the target states the matrix elements of the non-spherical potential V_0 and asymptotic potential $\frac{z_{\rm e} Z_{\rm Ion}}{r_0}$ are zero. The analytic Born subtraction technique is not used for elastic scattering because in a close-coupling calculation the elastic cross section converges quickly with respect to the partial-wave expansion. Also to describe elastic scattering the effect of dipole polarisation must be included [217], which comes in at the second-order Born approximation.

Note that in the present formulation target states are defined in the body-frame of reference (refer Section 2.2). Here Born matrix elements are chosen to be evaluated in the body-frame. The analytic Born body-frame scattering amplitude is formulated and then transformed to the laboratory (lab) frame.

Writing out the direct-potential V-matrix for inelastic-scattering and substituting plane waves (2.1) normalised in momentum space ($N = (2\pi)^{-3/2}$)

$$\begin{aligned}\langle \boldsymbol{q}_f \Phi_f | \sum_{j=1}^{N_e} V_{0j} | \Phi_i \boldsymbol{q}_i \rangle = -\frac{1}{(2\pi)^3} \sum_{j=1}^{N_e} \int d\boldsymbol{r}_j \Phi_f(\boldsymbol{r}) \Phi_i(\boldsymbol{r}) \\ \times \int d\boldsymbol{r}_0 e^{i\boldsymbol{Q}\cdot\boldsymbol{r}_0} \frac{z_{\rm e}}{|\boldsymbol{r}_0 - \boldsymbol{r}_j|},\end{aligned} \tag{4.54}$$

where $\boldsymbol{r}$ represents all target electrons spatial coordinates collectively and $\boldsymbol{Q} = \boldsymbol{q}_i - \boldsymbol{q}_f$. Utilising the Bethe-formula [234]

$$-\int d\boldsymbol{r}_0 e^{i\boldsymbol{Q}\cdot\boldsymbol{r}_0} \frac{z_{\rm e}}{|\boldsymbol{r}_0 - \boldsymbol{r}_j|} = -\frac{4\pi z_{\rm e}}{Q^2} e^{i\boldsymbol{Q}\cdot\boldsymbol{r}_j}, \tag{4.55}$$

and the multipole expansion, Eq. (4.54) becomes

$$\langle \boldsymbol{q}_f \Phi_f | \sum_{j=1}^{N_e} V_{0j} | \Phi_i \boldsymbol{q}_i \rangle = -\frac{N_e z_\mathrm{e}}{2Q^2\pi^2} \int d\boldsymbol{r}_1 \Phi_f(\boldsymbol{r}) e^{i\boldsymbol{Q}\cdot\boldsymbol{r}_1} \Phi_i(\boldsymbol{r}). \tag{4.56}$$

To carry out analytic integration over the angular terms in Eq. (4.56) the exponential term $e^{i\boldsymbol{Q}\cdot\boldsymbol{r}_1}$ is expanded in partial-wave form

$$e^{i\boldsymbol{Q}\cdot\boldsymbol{r}_1} = 4\pi \sum_{\lambda\mu} i^\lambda j_\lambda(Qr_1) Y^*_{\lambda\mu}(\hat{\boldsymbol{Q}}) Y_{\lambda\mu}(\hat{\boldsymbol{r}}_1). \tag{4.57}$$

Substituting (4.57) into Eq. (4.56), the analytic Born matrix elements (labelled by superscript $^{(\mathrm{AB})}$) are conveniently expressed as

$$\langle \boldsymbol{q}_f \Phi_f | \sum_{j=1}^{N_e} V_{0j} | \Phi_i \boldsymbol{q}_i \rangle = \sum_{\lambda\mu} i^\lambda V^{(\mathrm{AB})}_{\substack{f,i \\ \lambda\mu}}(Q) Y^*_{\lambda\mu}(\hat{\boldsymbol{Q}}). \tag{4.58}$$

For H_2^+ the analytic Born matrix elements $V^{(\mathrm{AB})}_{\substack{f,i \\ \lambda\mu}}(Q)$ have the form

$$\begin{aligned} V^{(\mathrm{AB})}_{\substack{f,i \\ \lambda\mu}}(Q) = -(-1)^\lambda \frac{2z_\mathrm{e}\hat{\lambda}}{Q^2\pi^{3/2}} \sum_{\alpha\gamma} C^{(f)}_\alpha C^{(i)}_\gamma \\ \times C^{l_\gamma 0}_{l_\alpha 0,\lambda 0} C^{l_\alpha m_\alpha}_{l_\gamma m_\gamma,\lambda\mu} \int_0^\infty dr_1 \varphi_\alpha(r_1) j_\lambda(Qr_1) \varphi_\gamma(r_1), \end{aligned} \tag{4.59}$$

while for H_2

$$\begin{aligned} V^{(\mathrm{AB})}_{\substack{f,i \\ \lambda\mu}}(Q) = -(-1)^\lambda \frac{4z_\mathrm{e}\hat{\lambda}}{Q^2\pi^{3/2}} \sum_{\alpha\beta\gamma\delta} C^{(f)}_{\alpha,\beta} C^{(i)}_{\gamma,\delta} \langle \varphi_\beta | \varphi_\delta \rangle \delta_{l_\beta,l_\delta} \delta_{m_\beta,m_\delta} \\ \times C^{l_\gamma 0}_{l_\alpha 0,\lambda 0} C^{l_\alpha m_\alpha}_{l_\gamma m_\gamma,\lambda\mu} \int_0^\infty dr_1 \varphi_\alpha(r_1) j_\lambda(Qr_1) \varphi_\gamma(r_1). \end{aligned} \tag{4.60}$$

Noting the Clebsch-Gordan coefficient triangle rules and the $\delta_{m_\beta,m_\delta}$ in Eq. (4.60), $V^{(\mathrm{AB})}_{\substack{f,i \\ \lambda\mu}}(Q)$ in equations (4.59) and (4.60) must have $\mu = m_f - m_i$ to be non-zero.

4.4.2 Analytic Born orientation averaged differential cross section

In the above Section the analytic Born matrix elements (4.56) were evaluated in the body-frame. Following from the definition of the body-frame scattering amplitude in Eq. (2.44), the analytic Born body-frame scattering amplitude for the transition $iv_i \rightarrow fv_f$ is conveniently expressed as

$$F^{(\mathrm{AB})}_{fv_f,iv_i}(\Omega^{(\mathrm{b})}) = \sum_{\lambda\mu} \langle \nu_{fv_f} | A^{(\mathrm{AB})}_{\substack{f,i \\ \lambda\mu}}(Q^{(\mathrm{b})}) | \nu_{iv_i} \rangle_R Y^*_{\lambda\mu}(\hat{\boldsymbol{Q}}^{(\mathrm{b})}), \tag{4.61}$$

where superscript $^{(\mathrm{b})}$ indicates the body-frame of reference, $\nu_{nv_n}(R)$ is the vibrational wave function (approximated to be independent of rotational quantum number J),

$$A^{(\mathrm{AB})}_{\substack{f,i \\ \lambda\mu}}(Q^{(\mathrm{b})};R) = -(2\pi)^2 i^{\lambda} V^{(\mathrm{AB})}_{\substack{f,i \\ \lambda\mu}}(Q^{(\mathrm{b})};R) \tag{4.62}$$

and $V^{(\mathrm{AB})}_{\substack{f,i \\ \lambda\mu}}(Q^{(\mathrm{b})};R)$ is the body-frame fixed-nuclei analytic Born matrix elements defined in equations (4.59) and (4.60). Equation (4.62) comes from definition (2.24) and noting that in the first-Born approximation $\langle \boldsymbol{q}_f^{(-)} \Phi_f | T | \Phi_i \boldsymbol{q}_i^{(+)} \rangle = \langle \boldsymbol{q}_f \Phi_f | \tilde{V} | \Phi_i \boldsymbol{q}_i \rangle$.

To transform the analytic Born body-frame scattering amplitude $F^{(\mathrm{AB})}_{fv_f,iv_i}(\Omega^{(\mathrm{b})})$ to the lab-frame (labelled by superscript $^{(\mathrm{lab})}$), $\hat{\boldsymbol{q}}_i^{(\mathrm{b})}$ is rotated so that $\hat{\boldsymbol{q}}_i^{(\mathrm{lab})}$ is aligned with the lab-frame z-axis. The definition in Eq. (2.35) is again utilised as described in Section 2.2 such that

$$Y^*_{\lambda\mu}(\hat{\boldsymbol{Q}}^{(\mathrm{b})}) = \sum_{\rho} D^{\lambda *}_{\rho,\mu}(\hat{\boldsymbol{R}}^{(\mathrm{lab})}) Y^*_{\lambda\rho}(\hat{\boldsymbol{Q}}^{(\mathrm{lab})}), \tag{4.63}$$

where in the lab-frame of reference the angle of $\hat{\boldsymbol{Q}}^{(\mathrm{lab})}$ with respect to the lab-frame z-axis (or $\hat{\boldsymbol{q}}_i^{(\mathrm{lab})}$)

$$\theta^{(\mathrm{lab})}_{\boldsymbol{Q}} \quad = \quad \arccos\left(\left(q_i - q_f \cos(\theta^{(\mathrm{lab})}_{\hat{\boldsymbol{q}}_f}) \right) / Q^{(\mathrm{lab})} \right) \tag{4.64}$$

and $\theta^{(\mathrm{lab})}_{\hat{\boldsymbol{q}}_f}$ is the angle between the lab-frame z-axis (or $\hat{\boldsymbol{q}}_i^{(\mathrm{lab})}$) and $\hat{\boldsymbol{q}}_f^{(\mathrm{lab})}$. Note that $\theta^{(\mathrm{lab})}_{\hat{\boldsymbol{q}}_f} = \theta^{(\mathrm{b})}_{\hat{\boldsymbol{q}}_i \hat{\boldsymbol{q}}_f}$, where $\theta^{(\mathrm{b})}_{\hat{\boldsymbol{q}}_i \hat{\boldsymbol{q}}_f}$ is the angle between $\hat{\boldsymbol{q}}_i^{(\mathrm{b})}$ and $\hat{\boldsymbol{q}}_f^{(\mathrm{b})}$. $|\boldsymbol{Q}|$

has the same form in both the body- and lab-frames of reference

$$Q = Q^{(\mathrm{b})} = Q^{(\mathrm{lab})} = |\boldsymbol{Q}| \quad = \quad |\boldsymbol{q}_i - \boldsymbol{q}_f| = \sqrt{q_i^2 + q_f^2 - 2\boldsymbol{q}_i \cdot \boldsymbol{q}_f}, \tag{4.65}$$

where vectors $\boldsymbol{q}_i$ and $\boldsymbol{q}_f$ are in the same frame as $\boldsymbol{Q}$. The analytic Born lab-frame scattering amplitude is now defined as

$$F_{f,i}^{(\mathrm{AB})}(\Omega^{(\mathrm{lab})}, \hat{\boldsymbol{R}}^{(\mathrm{lab})}) = \sum_{\lambda\mu} \langle \nu_{fv_f} | A_{\substack{f,i \\ \lambda\mu}}^{(\mathrm{AB})}(Q^{(\mathrm{b})}) | \nu_{iv_i} \rangle_R \times \sum_{\rho} D_{\rho,\mu}^{\lambda *}(\hat{\boldsymbol{R}}^{(\mathrm{lab})}) Y_{\lambda\rho}^{*}(\hat{\boldsymbol{Q}}^{(\mathrm{lab})}). \tag{4.66}$$

The analytic Born differential cross section is obtained by substituting $F_{f,i}^{(\mathrm{AB})}(\Omega^{(\mathrm{lab})}, \hat{\boldsymbol{R}}^{(\mathrm{lab})})$ into the orientation averaged differential cross section Eq. (2.46). The final form of the analytic Born differential cross section is

$$\frac{d\sigma_{fv_f,iv_i}^{(\mathrm{AB})}}{d\Omega^{(\mathrm{lab})}} = \frac{1}{4\pi} \sum_{\lambda\mu} |\langle \nu_{fv_f} | A_{\substack{f,i \\ \lambda\mu}}^{(\mathrm{AB})}(Q^{(\mathrm{b})}) | \nu_{iv_i} \rangle_R|^2. \tag{4.67}$$

For a full derivation of the analytic Born differential cross section see Appendix B.1. The orientation averaged integrated cross sections are calculated by numerically integrating over $\theta_{\hat{\boldsymbol{q}}_f}^{(\mathrm{lab})}$, noting that $Q^{(\mathrm{b})}$ is dependent upon $\theta_{\hat{\boldsymbol{q}}_f}^{(\mathrm{lab})}$ (refer to Eq. (4.65)).

4.4.3 Analytic Born subtraction method

The analytic Born subtraction method is generally used to top-up partial-wave differential and integrated cross sections. In this thesis the analytic Born subtraction method is only used for integrated cross sections.

Utilising the Born subtraction method orientationally averaged fixed-nuclei integrated cross sections are calculated via

$$\sigma_{f,i}^{S} = \sum_{M\Pi} (\sigma_{f,i}^{M\Pi S} - \tilde{\sigma}_{f,i}^{M\Pi}) + \sigma_{f,i}^{\mathrm{AB}}, \tag{4.68}$$

where orientationally averaged fixed-nuclei partial-wave integrated cross sections $\sigma_{f,i}^{M\Pi S}$ are calculated with Eq. (2.53) and the partial-wave scattering amplitude given in Eq. (4.42). The orientationally averaged partial-wave Born integrated cross sections $\tilde{\sigma}_{f,i}^{M\Pi}$ are calculated with Eq. (2.53)

and the partial-wave scattering amplitude given in Eq. (4.42) but with $e^{i(\sigma_{L_i}+\sigma_{L_f})}T^{M\Pi S}_{fL_fM_f,iL_iM_i}(q_f,q_i)$ replaced by $\tilde{V}^{M\Pi}_{fL_fM_f,iL_iM_i}(q_f,q_i)$. Orientationally averaged analytic Born integrated cross sections $\sigma^{\mathrm{AB}}_{f,i}$ are calculated from the analytic Born differential cross sections (4.67) via numerical integration over $\theta^{(\mathrm{lab})}_{\hat{\boldsymbol{q}}_f}$.

Chapter 5

Electron scattering from H_2^+ and its isotopologues

Adiabatic-nuclei convergent close-coupling (CCC) results of electron scattering from vibrationally excited H_2^+ and its isotopologues (D_2^+, T_2^+, HD^+, HT^+ and TD^+) are presented from 10 to 1000 eV. For impact energies below 10 eV significant indirect resonant electron attachment processes [155] are unaccounted for and hence are not presented here. Vibrationally weighted and resolved cross sections are presented for dissociative ionisation (DI) and proton production (PP) cross sections, which is a sum of the dissociative excitation (DE) and DI cross sections such that $\sigma_{\rm PP} = \sigma_{\rm DE} + 2\sigma_{\rm DI}$. Preliminary results were published in Ref. [171], while the results presented here are an extension of those published in Ref. [91].

5.1 Convergence studies of electron-H_2^+ scattering

In this section convergence studies are presented for electron scattering from H_2^+ in the fixed-nuclei approximation. By investigating the variation of results with respect to the calculation size (close-coupling and partial-wave expansions), an estimate of the collision data uncertainty can be determined. Uncertainty estimates of calculated collision data has been stressed by the International Atomic Energy Agency [235].

5.1.1 United atom limit: electron scattering from He^+

In the molecular CCC code calculations can be performed in the united atom limit ($R = 0$ a_0) of H_2^+. Omitting the internuclear Coulomb repulsion term $1/R$ this is equivalent to modelling He^+. The accuracy of the molecular CCC calculations is demonstrated by comparing $R = 0$ a_0 results with the atomic CCC code. The molecular CCC code is tested against the atomic CCC code for electron-He^+ scattering calculations [15]. The difference between the two codes is that the atomic CCC calculations conserve total orbital angular momentum $\bar{J}$, total orbital angular projection M, parity Π and spin S, while molecular calculations conserve total orbital angular projection M, parity Π and spin S. Consequently the formulation of the atomic and electronic molecular target states, V-matrix elements and the set of coupled equations are very different. Here atomic CCC calculations are different to those published in Ref. [15]. The atomic and molecular CCC calculations both use the same size Laguerre basis with $N_l = 15 - l$, $l_{\max} = 4$ and Laguerre basis functions with exponential fall-offs $\alpha_l = 1.4$. The atomic code diagonalisation generated 65 states, while the molecular code produced 305 states. For these two calculations the highest-energy pseudostates were omitted for the reasons discussed in Section 3.1.2. Omitting these states, 61-state atomic CCC calculations and 289-state molecular CCC calculations were performed. Atomic CCC calculations were performed up to $\bar{J} = 15$ for both singlet and triplet spin S. The molecular CCC calculations were performed with a projectile partial-wave expansion with maximum orbital angular momentum $L_{\max} = 8$. The singlet and triplet spin S, odd and even parity Π and maximum total orbital angular projection $M_{\max} = 8$ channels were included, where $-M_{\max} \leq M \leq M_{\max}$. Both codes use the analytic Born subtraction (ABS) method to top-up the partial-wave expansion. Total ionisation cross sections (TICS) of electron scattering from the ground-state of He^+ are presented in Fig. 5.1. The atomic and molecular CCC code calculations are compared with the experimental measurements of Peart et al. [16]. The atomic and molecular CCC results are in excellent agreement with each other and experiment across the entire energy range. Because the atomic CCC code has been rigorously tested, this result indicates that the molecular CCC code was developed successfully.

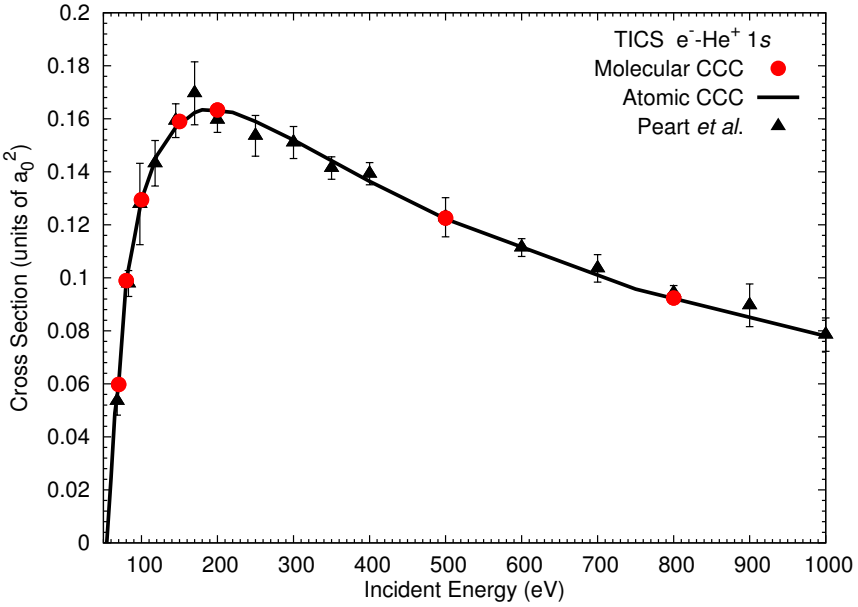

Figure 5.1: Total ionisation cross section (TICS) of electron scattering from the He^+ ground state. The molecular convergent close-coupling (CCC) calculations for the united atom limit ($R = 0$ a_0) of H_2^+ are compared with the atomic CCC code calculations [15] and the measurements of Peart et al. [16].

5.1.2 Convergence with the number of states

Here calculations of electron scattering from H_2^+ utilise the structure b model described in Section 3.1.2, which from here is referred to as the 351-state calculation. Molecular CCC calculations were conducted over the energy range from 10 to 1000 eV and performed with partial waves up to orbital angular momentum $L_{\max} = 9$, total orbital angular projection $M_{\max} = 9$, singlet and triplet spin S and odd and even parity Π. The orientationally averaged ABS method (described in Section 4.4) was used to top-up the partial-wave expansion.

Convergence studies of the close-coupling expansion are investigated for electron scattering from H_2^+ at the equilibrium distance $R_0 = 2.0$ a_0. The 351-state CCC calculation is compared with a 289-state and 227-state CCC calculation. Note for the reasons discussed in Section 3.1.2, these scattering calculations omitted the highest energy pseudostates from the structure models described below. These structure models utilise the same molecular

orbital method (described in Section 3.1.1) for the $1s\sigma_g$ and $2p\sigma_u$ orbitals, which were produced with a large basis that had $N_l = 60 - l$ functions with $l_{\max} = 9$ and $\alpha_l = 1.4$. The 289 states used in the scattering calculation were generated with a second Laguerre basis that had $N_l = 15 - l$, $l_{\max} = 4$ and Laguerre basis functions with exponential fall-offs $\alpha_l = 1.4$. The 227 states used in the CCC calculation were generated with the same second Laguerre basis as that used to generate the 351 states, however in this model Laguerre basis functions were restricted up to $l_{\max} = 3$. 351-, 289- and 227-state molecular CCC calculations are presented in Fig. 5.2 for $R_0 = 2.0$ a_0 PP and DI cross sections. These calculations yield practically the same results and are therefore convergent in N_l and $l_{\max}$. The PP cross section feature at 20 eV is from the newly opened $2p\pi_u$ states contribution to the cross section.

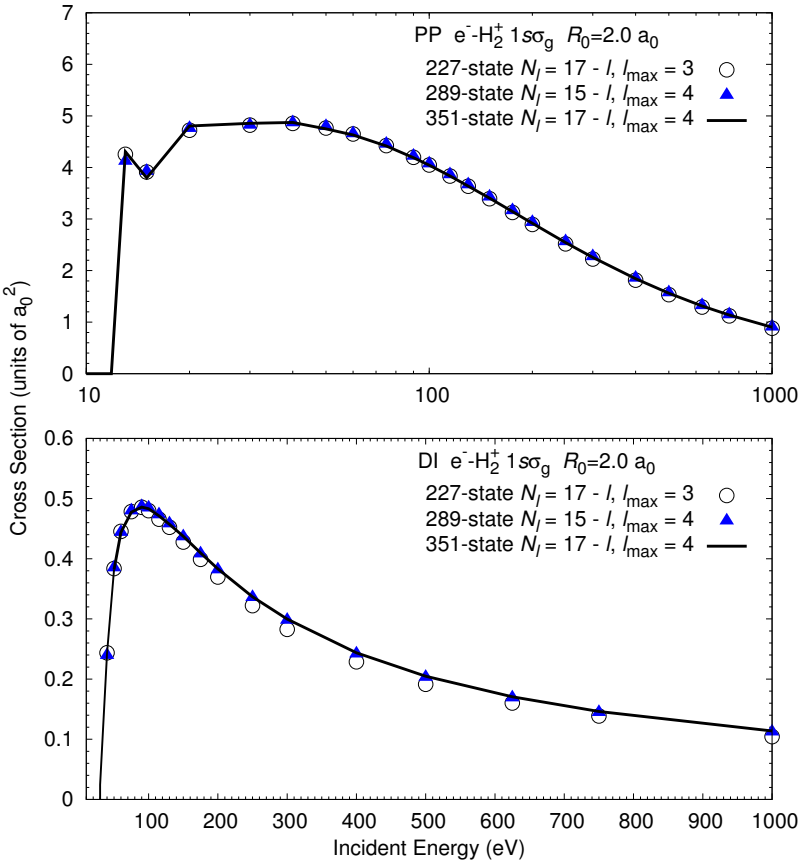

Figure 5.2: Convergence studies of electron scattering from H_2^+ at the equilibrium distance $R_0 = 2.0\ a_0$. 351-, 289- and 227-state convergent close-coupling (CCC) calculations are presented for proton production (PP) and dissociative ionisation (DI) cross sections. Target states are calculated with N_l Laguerre basis functions for each orbital angular momentum l up to $l_{\max}$.

5.1.3 Convergence of the partial-wave expansion

Convergence of electron-H_2^+ $R_0 = 2.0\ a_0$ calculations is investigated with respect to the size of the projectile-electron partial-wave expansion. Partial-wave expansions of different size are used to calculate 351-state CCC results, which are presented in Fig. 5.3. These results are also compared with the time-dependent close-coupling (TDCC) $R_0 = 2.0\ a_0$ results [17]. CCC calculations use partial-wave expansions with maximum orbital angular momentum $L_{\max}$ and maximum total orbital angular projection $M_{\max}$. An orientationally averaged ABS method is also used to top-up results. Referring to

Fig. 5.3 it is shown that convergence is achieved in the partial-wave expansion for maximum orbital angular momentum $L_{\max} = 7$ and maximum total orbital angular projection $M_{\max} = 7$. The TDCC results were calculated with a partial-wave expansion up to $L_{\max} = 5$ and $M_{\max} = 2$ and utilised a distorted-wave top-up for the higher terms up to $L_{\max} = M_{\max} = 16$. TDCC results are approximately 20% larger than the converged CCC results at the cross section peak. This demonstrates that the published TDCC results [17] are not fully converged in the size of the partial-wave expansion. The CCC results here are the first demonstration of convergence in both the partial-wave and close-coupling expansions for electron-molecule scattering.

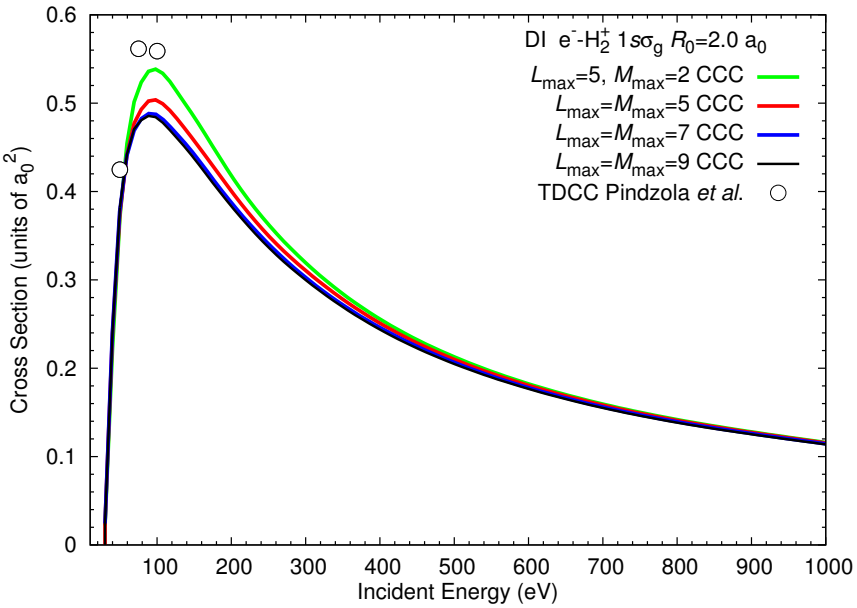

Figure 5.3: The dissociative ionisation (DI) cross section of electron scattering from H_2^+ at the equilibrium distance $R_0 = 2.0\ a_0$. Convergent close-coupling (CCC) results are calculated using a partial-wave expansion with maximum orbital angular momentum $L_{\max}$ and maximum total orbital angular projection $M_{\max}$. An orientationally averaged analytic Born subtraction method is used to top-up CCC results. CCC results are compared with the time-dependent close-coupling (TDCC) results of Pindzola et al. [17], which used a $L_{\max} = 5$, $M_{\max} = 2$ partial-wave expansion with a distorted-wave top-up to $L_{\max} = M_{\max} = 16$.

5.1.4 Investigation of partial-wave top-up procedures

In this Section the plane-wave ABS method and the unitarised Coulomb Born approximation (UCBA) top-up procedures are investigated. The UCBA approximates Eq. (4.36) as

$$K^{M\Pi S}_{fL_fM_f,iL_iM_i}(k_f,k_i) = \tilde{V}^{M\Pi S}_{fL_fM_f,iL_iM_i}(k_f,k_i), \tag{5.1}$$

where k indicates a distorted Coulomb wave and $\tilde{V}$ indicates the direct part of the interaction potential (4.43) V-matrix elements. To test the current top-up procedure, the 351-state CCC results are calculated with different sized partial-wave expansions that utilise the UCBA to top-up results up to $L_{\max} = M_{\max} = 16$ and the orientationally averaged ABS technique to top-up results for the higher terms ($M_{\max} > 16$). These results are compared in Fig. 5.4 with the TDCC results [17] and 351-state CCC results that utilise just the orientationally averaged ABS method to top-up results. Firstly the $L_{\max} = 5$ $M_{\max} = 2$ CCC results that utilise the UCBA top-up procedure are in excellent agreement with the corresponding TDCC results. For the unconverged partial-wave expansions a notable difference is seen in the CCC results different top-up procedures. There is only a very minor difference in the converged partial-wave expansion results ($L_{\max} = M_{\max} = 7$ and $L_{\max} = M_{\max} = 9$). Therefore the orientationally averaged plane-wave ABS method is sufficiently accurate for close-coupling calculations with a converged partial-wave expansion.

5.2 Electron scattering from vibrationally excited H_2^+ and its isotopologues

As mentioned in Section 1.3.1, experimentally H_2^+ is produced by electron impact-ionisation of H_2 which leaves H_2^+ in a range of vibrational states. To compare with experiment, cross sections are weighted according to the vibrational population of the beam

$$\bar{\sigma}_{f,i} = \sum_{v_i=0}^{N_v} p_{v_i}\sigma_{f,iv_i} \Bigg/ \left(\sum_{v_i=0}^{N_v} p_{v_i}\right), \tag{5.2}$$

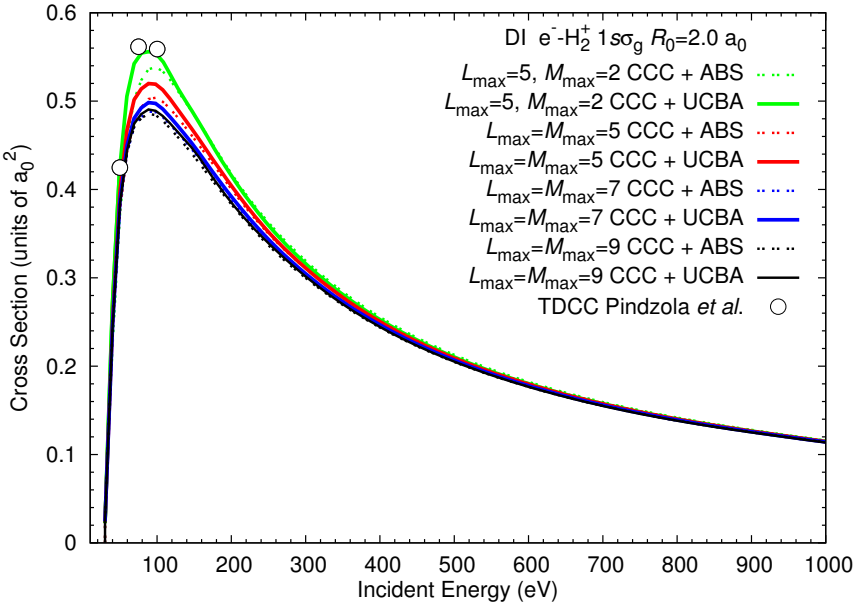

Figure 5.4: The dissociative ionisation (DI) cross section of electron scattering from H_2^+ at the equilibrium distance $R_0 = 2.0\ a_0$. Convergent close-coupling (CCC) results are calculated with a partial-wave expansion up to orbital angular momentum $L_{\max}$ and maximum total orbital angular projection $M_{\max}$. CCC results utilise the orientationally averaged analytic Born subtraction (ABS) method to top-up results or the unitarised Coulomb Born approximation (UCBA) method to top-up results to $L_{\max} = M_{\max} = 16$ and then the ABS method for the higher terms. CCC results are compared with the time-dependent close-coupling (TDCC) results of Pindzola et al. [17], which used a $L_{\max} = 5$, $M_{\max} = 2$ partial-wave expansion with a distorted-wave top-up to $L_{\max} = M_{\max} = 16$.

where p_{v_i} are the Franck-Condon (FC) or von Busch and Dunn [12] (BD) vibrational distribution weights, N_v is the last vibrational state of the population and σ_{f,iv_i} is calculated using Eq. (2.52). In the adiabatic-nuclei approximation, calculations of σ_{f,iv_i} are performed as post processing of fixed-nuclei scattering results and requires scattering calculations to be conducted at a (large) number of internuclear distances. Results for electron scattering from D_2^+ and its isotopologues can be obtained by using the same fixed-nuclei scattering results in Eq. (2.52) with appropriate vibrational wave functions of the target.

Here 351-state CCC scattering calculations were conducted over a 23 point R grid within the interval $1.2 \leq R \leq 5.5\ a_0$. In Fig. 5.5 resulting DI and DE cross sections are presented as a function of internuclear distance

R at an impact energy of 100 eV. PP cross sections $\sigma_{\rm PP}(R)$ and DI cross sections $\sigma_{\rm DI}(R)$ were found to be smooth as a function of R away from excitation threshold. The PP cross section is found to be much more sensitive to variations of R than the DI cross section. This result is not surprising if one considers the static dipole polarisability contribution from the DE and ionisation continuum states as a function of R. Analysing our calculations of the polarisability, the contribution from the continuum states increases much more slowly with R than the contribution from the DE states.

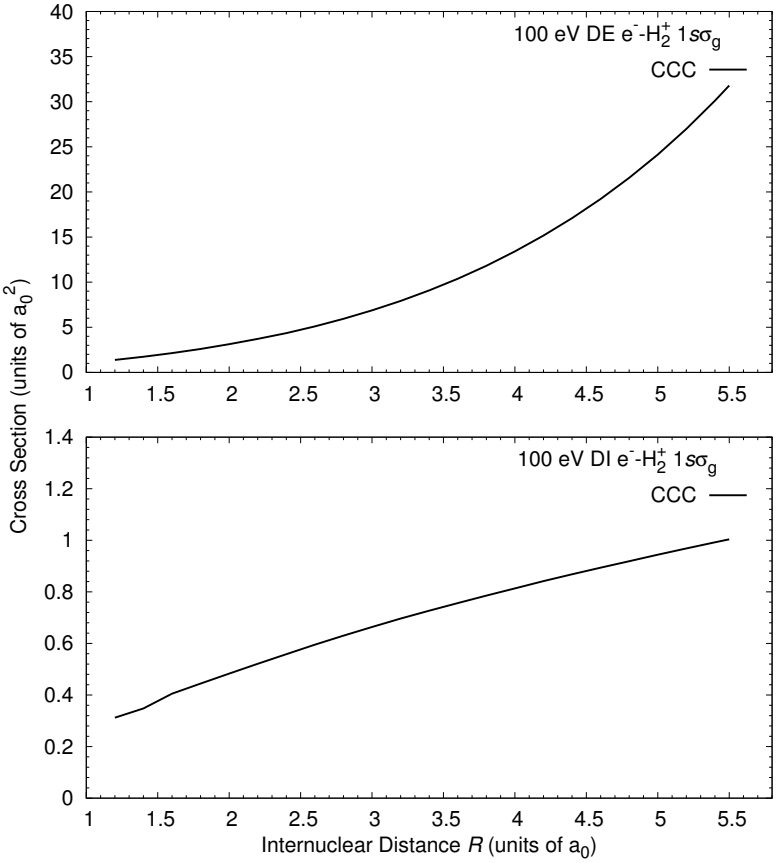

Figure 5.5: Convergent close-coupling (CCC) results of dissociative ionisation (DI) and dissociative excitation (DE) cross sections as a function of the internuclear distance R for 100 eV electrons scattering from H_2^+.

Cross sections were interpolated and extrapolated across the grid $1.0 \leq R \leq 18.0\ a_0$, which is the span of the highest excited vibrational levels. Extrapolation outside the interval $1.2 \leq R \leq 5.5\ a_0$ introduces uncertainty in the vibrationally resolved and weighted cross sections. To check this ex-

trapolation method vibrationally resolved and weighted analytic Born cross sections for the transition $1s\sigma_g \rightarrow 2p\sigma_u$ are compared with the plane-wave first Born approximation (FBA) results of Peek and Green [19]. Firstly, the fixed-nuclei $R_0 = 2.0\ a_0$ analytic Born results are compared with the FBA calculations of Peek [18] in Fig. 5.6. Here the present results are in excellent agreement with the corresponding FBA calculations of Peek [18].

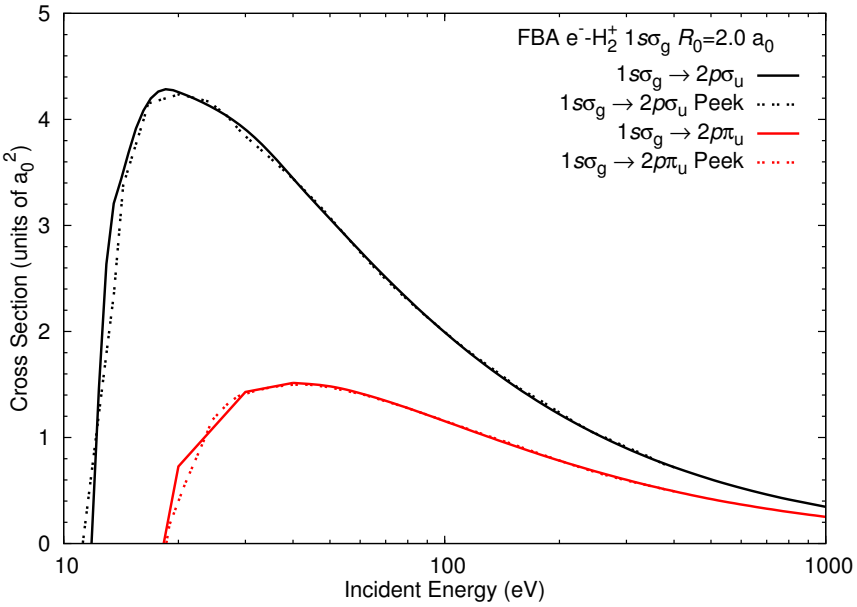

Figure 5.6: First Born approximation (FBA) results of electron scattering from H_2^+ at the equilibrium distance $R_0 = 2.0\ a_0$ for the transitions $1s\sigma_g \rightarrow 2p\sigma_u$ and $1s\sigma_g \rightarrow 2p\pi_u$. The present analytic Born cross sections are compared with the FBA results of Peek [18].

The vibrationally resolved $1s\sigma_g \rightarrow 2p\sigma_u$ excitation cross sections of Peek and Green [19] are constructed with the Bethe-asymptotic formula

$$\sigma_{f,iv_i} = \frac{8\pi}{q_i^2}\left(A\ln(q_i) + B^*\right), \tag{5.3}$$

where the respective parameters for A and $B^* = B - \alpha + \alpha^*$ are taken from Table I in [19]. Note that Eq. (5.3) is only valid in the energy range where the Born approximation is accurate [236] ($q_i^2/2$ is sufficiently larger than the binding energies of the target electrons). For this reason results are only presented for impact energies above 20 eV. The present analytic Born vibrationally resolved results are presented in Fig. 5.7 and are generally in

good agreement with those of Peek and Green [19]. For the $v_i \leq 9$ vibrational states (where no extrapolation is used) there is a minor difference between results in the intermediate-energy region (20-100 eV). This difference come primarily from the inaccuracy of the Bethe-asymptotic formula (5.3) and the different vibrational wave functions used. Both of these calculations use different vibrational wave functions, where Peek and Green [19] have a bound $v = 19$ H_2^+ state. This could be the reason for the large difference in the $v_i = 18$ state results. Considering the difference in results of the $v_i = 18$ state, the FC and BD vibrationally weighted results in Fig. 5.8 are in good agreement with the results of Peek and Green [19]. It is estimated that the vibrationally weighted CCC cross sections $\tilde{\sigma}_{f,i}$ have a maximum error of 5% from the extrapolation.

An estimate of the associated uncertainty in the final cross sections is important in many practical applications. These uncertainties arise from numerical integrations in the matrix elements, the momentum quadrature integration in Eq. (4.37), the size of the close-coupling and partial-wave expansions and the closure approximation used to calculate σ_{f,iv_i} (2.52), which breaks down near respective transition thresholds. By performing convergence studies, the close-coupling fixed-nuclei cross sections are estimated to be accurate to less than 5% accuracy. Uncertainty in the extrapolation procedure to larger internuclear distances R is estimated to be less than 5%. From the investigation by Peek and Green [19] utilising the Bethe-asymptotic formula (described above), the error associated with the adiabatic closure approximation is estimated to be less than 1% in the intermediate- and high-energy (100-1000 eV) regions [19]. Vibrationally weighted cross sections are estimated to be accurate within 5% for DI and 10% for PP. PP cross sections have a larger uncertainty estimate due to their higher sensitivity to extrapolation to large R. Note that the vibrational population weighting also has an associated uncertainty, however, this is dependent on the experiment or application.

5.2.1 H_2^+

Adiabatic-nuclei CCC results of vibrationally weighted PP cross sections are presented in Fig. 5.9 for electron scattering from H_2^+. Adiabatic-nuclei CCC results have been vibrationally weighted according to the BD and FC distributions, and are compared with the CCC $R_0 = 2.0$ a_0 fixed-nuclei cal-

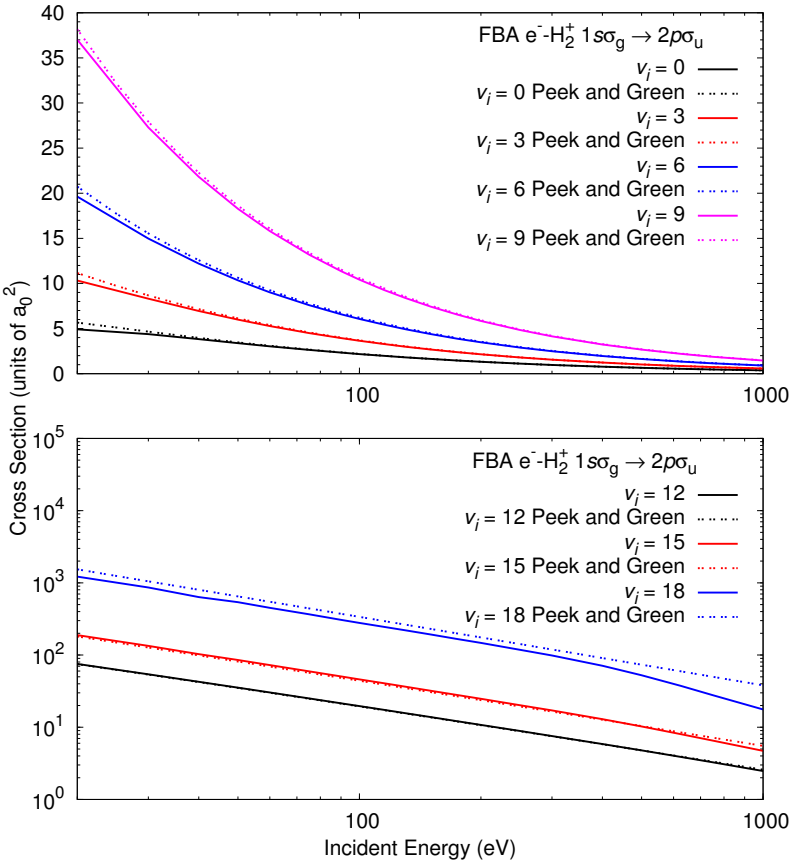

Figure 5.7: First Born approximation (FBA) results of electron-impact excitation of H_2^+ in the electronic ground vibrational state v_i to the $2p\sigma_u$ state. The present analytic Born cross sections are compared with the FBA results of Peek and Green [19].

culations, vibrationally weighted total inelastic (TI) Born cross sections of Peek [20], the TI measurements of Peart and Dolder [21] and the PP measurements of El Ghazaly *et al.* [22], Dunn *et al.* [23, 24] and Dance et al. [25]. Noting that the DI cross sections are an order of magnitude lower than the PP cross sections [21, 237, 238], the TI cross sections $\sigma_{\rm TI} = \sigma_{\rm DE} + \sigma_{\rm DI}$ and PP cross sections can be compared with each other. Firstly comparing the BD and FC vibrationally weighted results, a large difference of approximately 20% is seen in the low-energy region (10-20 eV), which indicates an extremely large dependence on the vibrational state of the molecule. FC weighting leads to a larger cross section due to their slightly heavier weighting on the highly excited vibrational states. In the low-energy re-

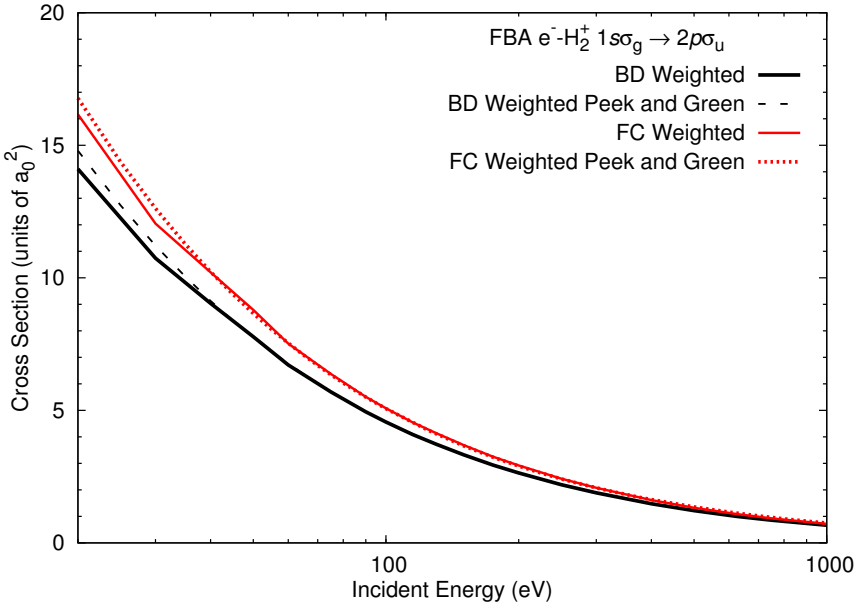

Figure 5.8: Adiabatic-nuclei first Born approximation (FBA) calculations of electron scattering from the electronic ground, vibrationally excited states of H_2^+. Franck-Condon (FC) and von Busch and Dunn [12] (BD) vibrationally weighted results of the $1s\sigma_g \rightarrow 2p\sigma_u$ transition. The present analytic Born cross sections are compared with the FBA results of Peek and Green [19].

gion vibrationally weighted PP results have the maximum assigned uncertainty. This is because the uncertainty associated with the extrapolation of fixed-nuclei results to large R directly effects the high-lying vibrational levels cross section contribution, which are very sensitive in low-energy region. In the intermediate-energy region the vibrationally weighted results are within 10% of each other and in the high-energy region vibrationally weighted results are practically the same. Comparing fixed-nuclei and vibrationally weighted results, the vibrationally weighted cross sections are around four times larger in the low-energy region. A significant difference is also seen in the intermediate- and high-energy regions. This again indicates the importance of accounting for the vibrational distribution of H_2^+. Further investigations found that including the complete vibrational population (even the high-lying vibrational levels) was very important.

The measurements of Peart and Dolder [21], El Ghazaly *et al.* [22], Dunn *et al.* [23, 24] and Dance et al. [25] have a large variation in the low-energy region. Peart and Dolder [21] have outlined some possible rea-

sons for this large variation. This variation is probably due to the different vibrational populations of H_2^+ produced in experiment and the sensitivity of the DE cross sections with respect to the initial vibrational state of H_2^+. In the experiment of El Ghazaly *et al.* [22] measurements of the vibrational population of H_2^+ indicated that H_2^+ ions were not produced in the $v \geq 14$ states, while the experiments of Peart and Dolder [21] and Dunn *et al.* [23, 24] were designed to produce H_2^+ ions in a vibrational population given by the FC factors. Comparing the vibrationally weighted PP cross sections with experimental data, BD and FC CCC results are within the experimental error bars of the Dance et al. [25], Dunn *et al.* [23, 24] and Peart and Dolder [21] measurements in the low- and intermediate-energy regions. In the high-energy region, both vibrationally weighted PP cross sections are in good agreement with all experiments and the vibrationally weighted Born cross sections of Peek [20]. The Born results of Peek [20] are approximately 35% larger than the respective CCC results in the low- and intermediate-energy regions. This is expected low-energy behaviour of results calculated with a first-order method.

DI cross sections are presented in Fig. 5.10 for electron scattering from vibrationally excited H_2^+. The FC and BD vibrationally weighted CCC results are compared with the $R_0 = 2.0\ a_0$ results and the measurements of Peart and Dolder [26] and El Ghazaly *et al.* [22]. Vibrationally weighted CCC results are approximately 20% larger than the fixed-nuclei results. The difference between these results and the FC and BD weighted results suggests that the DI cross sections are relatively insensitive to the vibrational distribution compared to the PP cross sections. Comparing CCC results with experiment, the FC and BD weighted DI results disagree with the measurements of El Ghazaly *et al.* [22] in the high-energy region. Noting that the DI cross sections are relatively insensitive to the vibrational distribution, this disagreement is not likely due to the different vibrational populations (assumed here and produced in experiment). The experiment of El Ghazaly *et al.* [22] measured the kinetic energy release of H^+ ions after electron-impact dissociation of H_2^+. To differentiate protons resulting from DI or DE, it was assumed that the DI cross sections are not dependent upon R, i.e. $\sigma_{\mathrm{DI}}(R)$ is constant. The DI cross section can then be extracted from the tail of the measured kinetic energy release spectrum by extrapolating the tail signal [239]. This procedure was expected to produce inaccurate DI cross

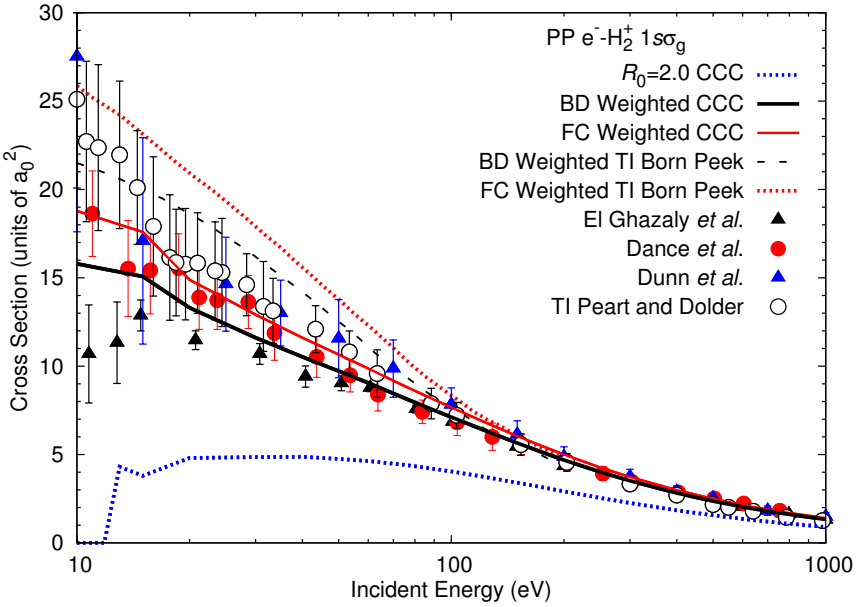

Figure 5.9: Adiabatic-nuclei convergent close-coupling (CCC) calculations of electron scattering from the electronic ground, vibrationally excited states of H_2^+. Franck-Condon (FC) and von Busch and Dunn [12] (BD) vibrationally weighted proton production (PP) cross sections are compared with the CCC $R_0 = 2.0\ a_0$ calculations, vibrationally weighted total inelastic (TI) Born calculations of Peek [20], the TI measurements of Peart and Dolder [21] and the PP experiments of El Ghazaly *et al.* [22], Dunn *et al.* [23, 24] and Dance et al. [25].

sections only near threshold [22], however there is still disagreement with CCC results in the high-energy region. As shown in Fig. 5.5 the DI cross section has a linear dependence on R. This dependence on R is not surprising considering that the single-photon ionisation cross sections of H_2^+ have a significant dependence on R [240]. The FC and BD vibrationally weighted CCC results are in excellent agreement with the measurements of Peart and Dolder [26]. This experiment differentiated DE and DI processes by measuring protons arriving at detectors in coincidence, which is an expected result of a homonuclear diatomic molecule undergoing a Coulomb explosion. This agreement is most encouraging and suggests that the experiment of El Ghazaly *et al.* [22] mixed signals from DE and DI processes.

Here vibrationally resolved cross sections are presented for initial vibrational states v_i which have a probability density function that is spanned within the range $1.0 \leq R \leq 5.5\ a_0$. Therefore vibrationally resolved cross

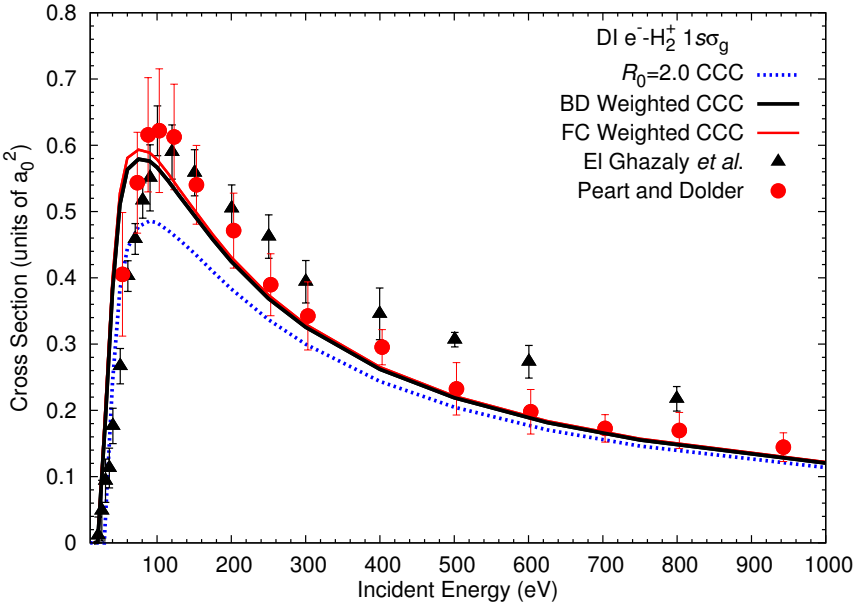

Figure 5.10: Adiabatic-nuclei convergent close-coupling (CCC) calculations of electron scattering from the electronic ground, vibrationally excited states of H_2^+. Franck-Condon (FC) and von Busch and Dunn [12] (BD) vibrationally weighted dissociative ionisation (DI) cross sections are compared with the CCC $R_0 = 2.0\ a_0$ results, and the measurements of Peart and Dolder [26] and El Ghazaly *et al.* [22].

sections presented here do not utilise the extrapolation procedure to large R and hence do not have the associated uncertainty. For H_2^+ the vibrational state $v_i = 9$ spans over the range $1.0 \leq R \leq 5.5\ a_0$. In Fig. 5.11 the DE and DI cross sections are presented as a function of the initial vibrational state v_i for H_2^+. DE and DI cross sections have a major dependence on v_i in the low- and intermediate-energy regions, as v_i increases the cross sections monotonically increase across the entire energy range. For example at 100 eV the $v_i = 9$ DI cross section is almost 60% larger than the $v_i = 0$ DI cross section. Both the DE and DI cross-section peak shifts to lower energies as v_i increases. For DI, the $v_i = 9$ cross section peak at 60 eV is about 70% larger than the $v_i = 0$ cross section peak at 90 eV. The DE cross section sensitivity with respect to v_i is seen particularly in the low-energy region, for example at 20 eV the $v_i = 9$ DE cross section is five times larger than the $v_i = 0$ state. DE and DI cross sections also have a significant dependence on v_i at higher energies. Looking at the DI cross section at 750 eV, the $v_i = 9$ cross section is 30% larger than $v_i = 0$ cross section. While for the DE cross sec-

tion at 750 eV the $v_i = 9$ results are about two times larger than the $v_i = 0$ results. This behaviour of the DE cross sections is qualitatively consistent with the results of Peek [172, 173]. The monotonic increase and peak shift in the cross section comes from a lower excitation or ionisation threshold as R increases. This increase in R also pushes electronic dissociative states into the ionisation continuum, which increases the DI cross section. It is interesting to note that the high-energy DI cross sections do not converge to the high-energy TICS of He^+.

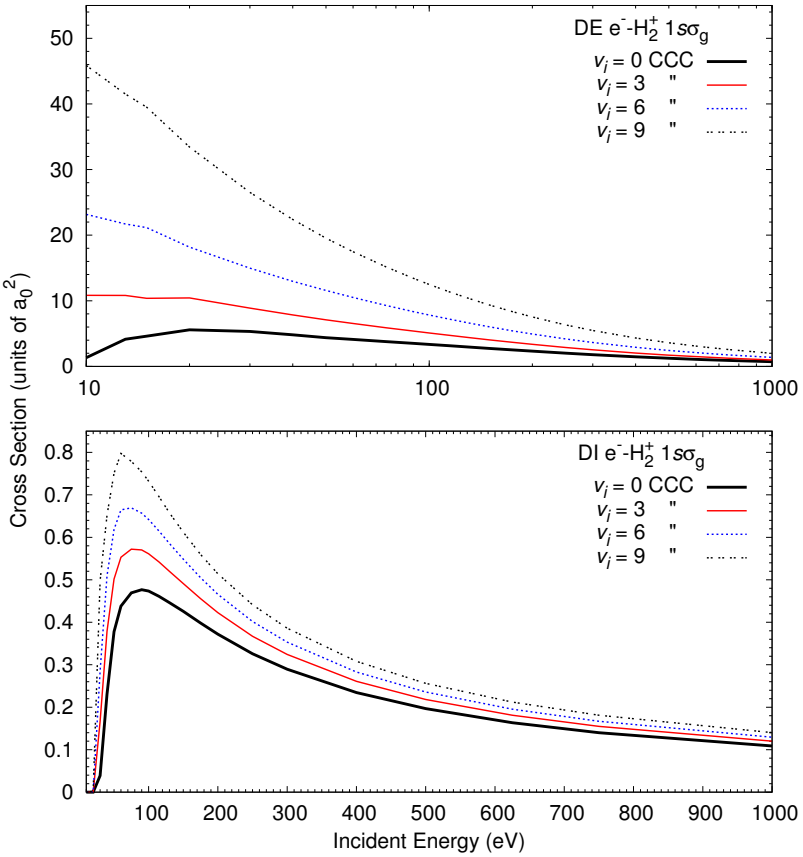

Figure 5.11: Electron scattering from the electronic ground state of H_2^+ in the vibrational state v_i. Convergent close-coupling (CCC) results are presented for dissociative excitation (DE) and dissociative ionisation (DI) cross sections.

5.2.2 D_2^+

Results for electron-D_2^+ scattering are obtained by substituting the D_2^+ vibrational wave functions into Eq. (2.52). Vibrationally weighted deuteron production (DP) cross sections are calculated using Eq. (5.2) with the FC vibrational weights presented in Table 3.10. Adiabatic-nuclei CCC results of electron scattering from vibrationally excited D_2^+ are presented in Fig. 5.12 for DP cross sections. Vibrationally weighted results are compared with the experiments of El Ghazaly *et al.* [22] and Dunn and Van Zyl [24]. In the low-energy region CCC results are 15% larger than the measurements of El Ghazaly *et al.* [22]. Like the results for H_2^+ the DE cross sections are highly sensitive to the vibrational population in the low-energy region hence this discrepancy could be due to the different vibrational population assumed here and that which was produced in experiment. Results in the intermediate- and high-energy regions are in excellent agreement with both experiments [22, 24]. Comparing measurements of PP for H_2^+ and DP for D_2^+, measurements are within the error bars of each other. The CCC PP and DP vibrationally weighted cross sections are practically on top of each other in the intermediate- and high-energy regions, a minor variation is seen in the low-energy region. These isotopic effects will be discussed further in the following Section.

In Fig. 5.13 D_2^+ vibrationally weighted DI cross sections are compared with the measurements of El Ghazaly *et al.* [22]. The adiabatic-nuclei CCC results do not agree with the measurements of El Ghazaly *et al.* [22] in the high energy-region (like the comparison for H_2^+). Reasons for this discrepancy were pointed out in the previous Section. Comparing the vibrationally weighted DI CCC results for H_2^+ and D_2^+, the FC weighted results are within 1% of each other.

As mentioned in the previous Section, vibrationally resolved cross sections are presented up to the vibrational state which spans the range $1.0 \leq R \leq 5.5\ a_0$, for D_2^+ the $v_i = 13$ state spans this range. D_2^+ DE and DI vibrationally resolved cross sections are presented in Fig. 5.14 up to $v_i = 13$. Like H_2^+, the D_2^+ cross sections are significantly dependent on the initial vibrational state of the molecule. This dependence is most pronounced at the peak of the cross section and in the intermediate-energy region. For example the $v_i = 13$ DI cross section peak at 60 eV is 70% larger than the $v_i = 0$ cross section peak at 90 eV. This difference is very

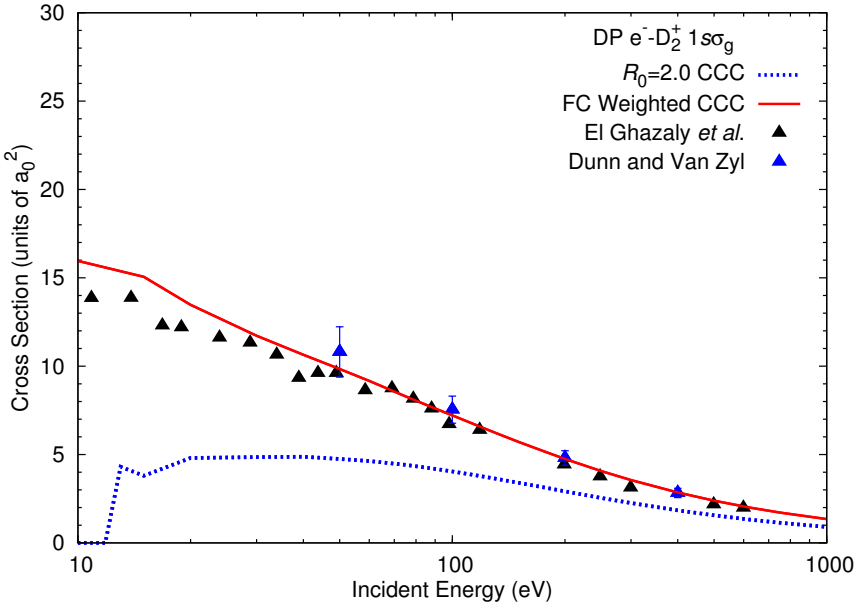

Figure 5.12: Adiabatic-nuclei convergent close-coupling (CCC) calculations of electron scattering from the electronic ground, vibrationally excited states of D_2^+. Franck-Condon (FC) vibrationally weighted deuteron production (DP) cross sections are compared with the CCC $R_0 = 2.0$ a_0 results and the experiments of El Ghazaly *et al.* [22] and Dunn and Van Zyl [24].

similar to the difference found in the H_2^+ $v_i = 0$ and $v_i = 9$ DI cross section peaks. Comparing H_2^+ and D_2^+ vibrationally resolved results for DE and DI respectively, little difference is seen in results for vibrational states that spans the same range of R. For instance the DE cross sections of D_2^+ in the $v_i = 13$ and H_2^+ in the $v_i = 9$ state (which also spans the range $1.0 \leq R \leq 5.5$ a_0) are within 1.5% of each other across the entire energy range considered. The DI cross section peak for D_2^+ $v_i = 13$ (at 60 eV) is 0.05% larger than the H_2^+ $v_i = 9$ cross section peak (also at 60 eV). A notable difference in the vibrational states cross sections (that span the same R) is seen near the respective threshold, however, this where the closure method is inaccurate. The H_2^+ $v_i = 0$ DE cross section is approximately 5% larger than the corresponding D_2^+ cross section in the low- and intermediate-energy regions. This difference is less pronounced in the $v_i = 0$ DI cross section. It is important to note that the ground vibrational states of H_2^+ and D_2^+ do not span the same range of R (refer to Fig. 3.3), which is the source of this difference. For D_2^+ the $v_i = 0$ state probability density function approximately spans the

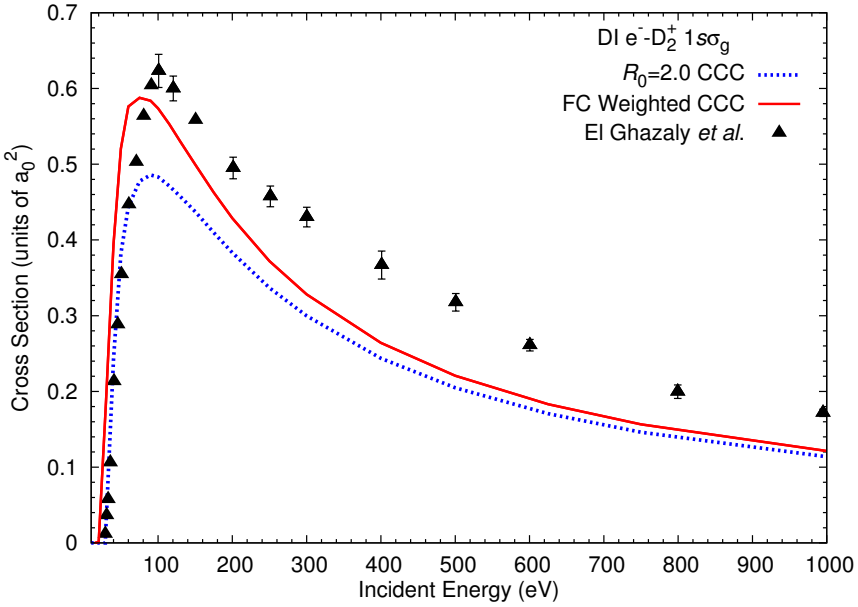

Figure 5.13: Adiabatic-nuclei convergent close-coupling (CCC) calculations of electron scattering from the electronic ground, vibrationally excited states of D_2^+. Franck-Condon (FC) vibrationally weighted dissociative ionisation (DI) cross sections are compared with the CCC $R_0 = 2.0$ a_0 results and the experiment of El Ghazaly *et al.* [22].

range $1.5 \leq R \leq 2.7$ a_0 and has a mean internuclear distance $R_m = 2.044$ a_0, while the H_2^+ $v_i = 0$ state probability density function approximately spans the range $1.4 \leq R \leq 2.8$ a_0 and $R_m = 2.063$ a_0.

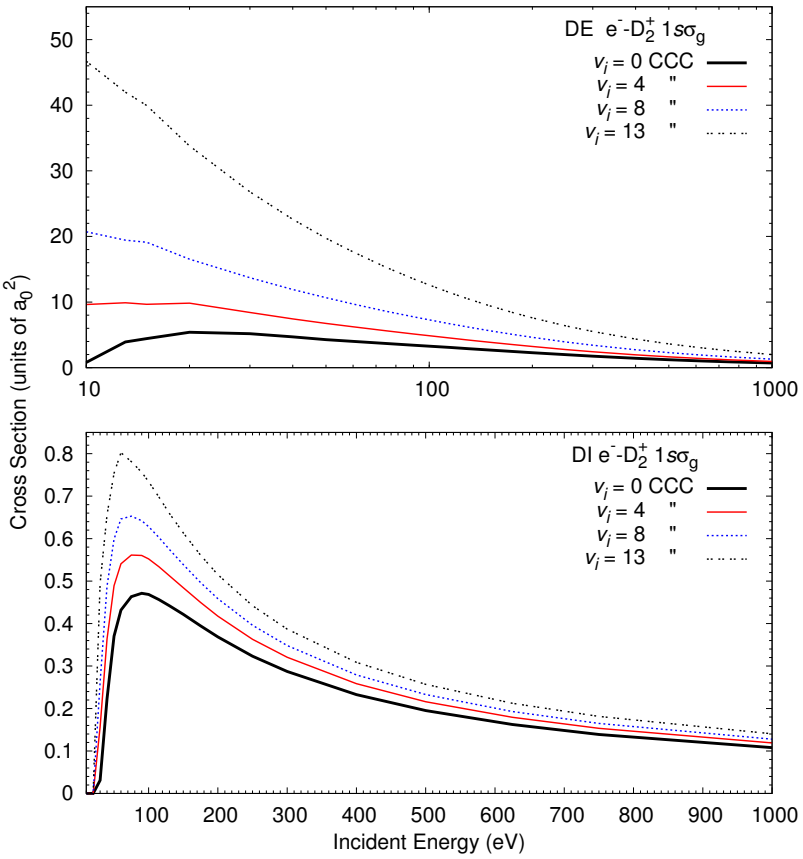

Figure 5.14: Electron scattering from the electronic ground state of D_2^+ in the vibrational state v_i. Convergent close-coupling (CCC) results are presented for dissociative excitation (DE) and dissociative ionisation (DI) cross sections.

5.2.3 T_2^+

CCC vibrationally weighted triton production (TP) cross sections are presented in Fig. 5.15 and compared with FC weighted PP and DP cross sections for H_2^+ and D_2^+ respectively. Isotopic effects are evident in the low- and intermediate-energy regions. At 10 eV H_2^+ PP cross sections are 30% larger than the TP cross sections of T_2^+. In the intermediate-energy region the difference is less pronounced. For example at 60 eV H_2^+ PP cross sections are 10% larger than the TP cross sections of T_2^+. In the high-energy region there is little difference between results. Here FC factors of the molecular ions are calculated for the single-ionisation process of the corresponding ground state

neutral molecule (like experiments) i.e. for the transition $H_2(X^1\Sigma_g^+, 0, 0) \rightarrow H_2^+(1s\sigma_g, v, 0)$. A heavy neutral molecule (T_2) has a more compact vibrational ground state compared to its lighter isotopologues (e.g. H_2, refer to Fig. 3.3). These lighter isotopologues have a more diffuse ground state that reaches larger and smaller values of R. For lighter molecules this makes the normalised FC distribution have a slightly heavier weighting on highly excited vibrational states. This results in lighter molecules having higher vibrationally weighted cross sections and leads to isotopic effects.

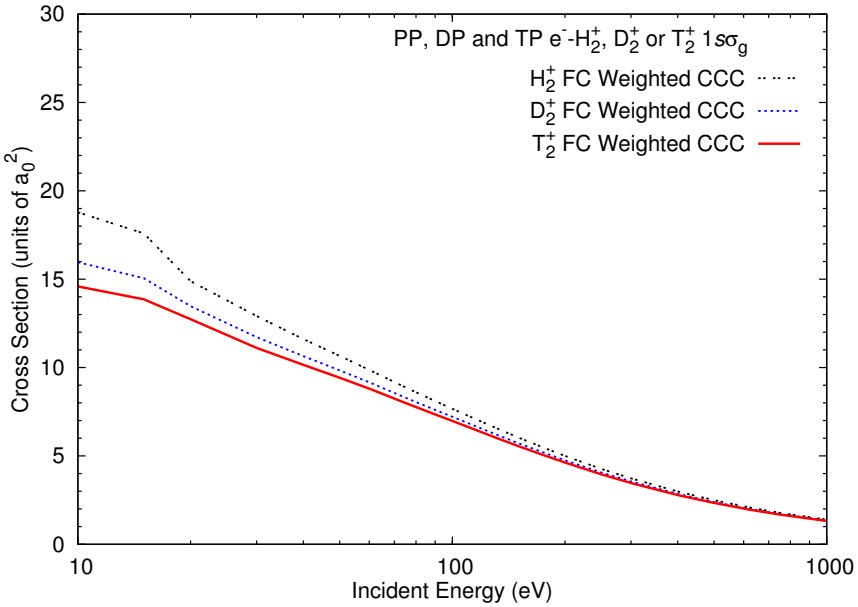

Figure 5.15: Adiabatic-nuclei convergent close-coupling (CCC) calculations of electron scattering from the electronic ground, vibrationally excited states of H_2^+, D_2^+ or T_2^+. Franck-Condon (FC) vibrationally weighted proton production (PP), deuteron production (DP) and triton production (TP) cross sections are presented.

In Fig. 5.16 the PP, DP and TP FC weighted cross sections are presented as a function of individual vibrational-state cross section contribution for 20 and 100 eV electrons, while in Fig. 5.17 100 eV FC weighted DI cross sections are presented for H_2^+, D_2^+ and T_2^+ as a function of the individual vibrational-state contribution. Results in Figs. 5.16 and 5.17 resemble the FC population of the respective molecule, as seen in Fig. 3.2, however the 20 eV results in Fig. 5.16 shows a higher contribution from highly excited vibrational states.

This is due to the vibrationally excited states very large DE excitation cross section as a consequence of the decrease in DE threshold. At 100 eV the individual contribution from the highly excited vibrational states is more pronounced for the DE (PP, DP and TP) cross sections compared to the DI cross sections. For example at 100 eV the H_2^+ $v_i = 15$ state contributes 1.6% to the FC weighted PP cross section, while for DI the $v_i = 15$ state contributes 0.4%. As described in Section 5.2, by analysing the static dipole polarisability the DE cross sections are expected to be more sensitive to changes in R than the DI cross sections.

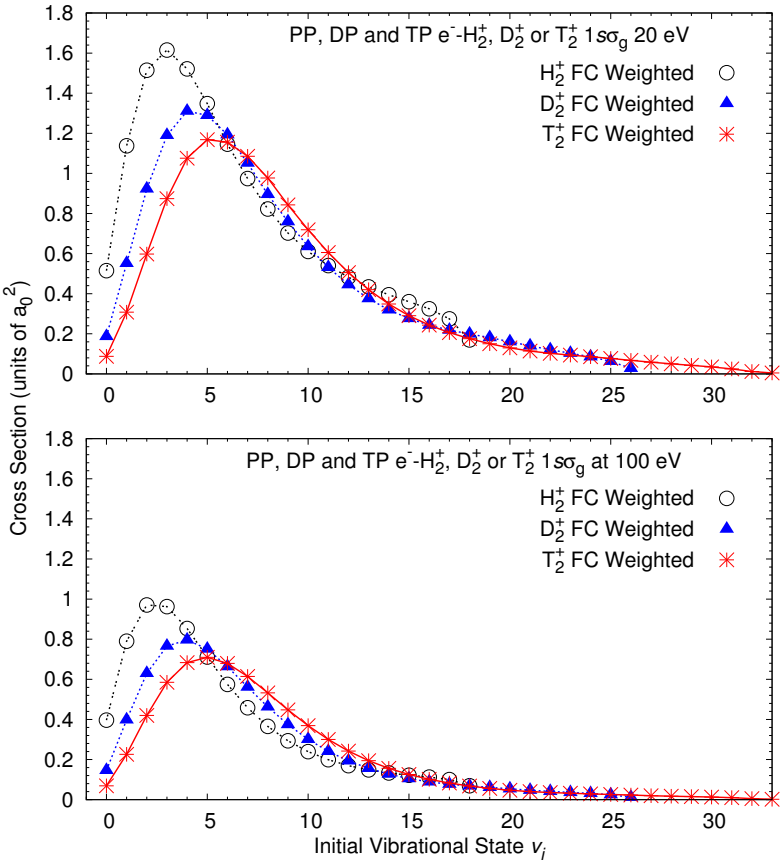

Figure 5.16: Adiabatic-nuclei convergent close-coupling (CCC) calculations of 20 and 100 eV electrons scattering from the electronic ground, vibrationally excited states of H_2^+, D_2^+ or T_2^+. Franck-Condon (FC) vibrationally weighted proton production (PP), deuteron production (DP) and triton production (TP) cross sections are presented as a function of the initial vibrational state v_i of the molecule.

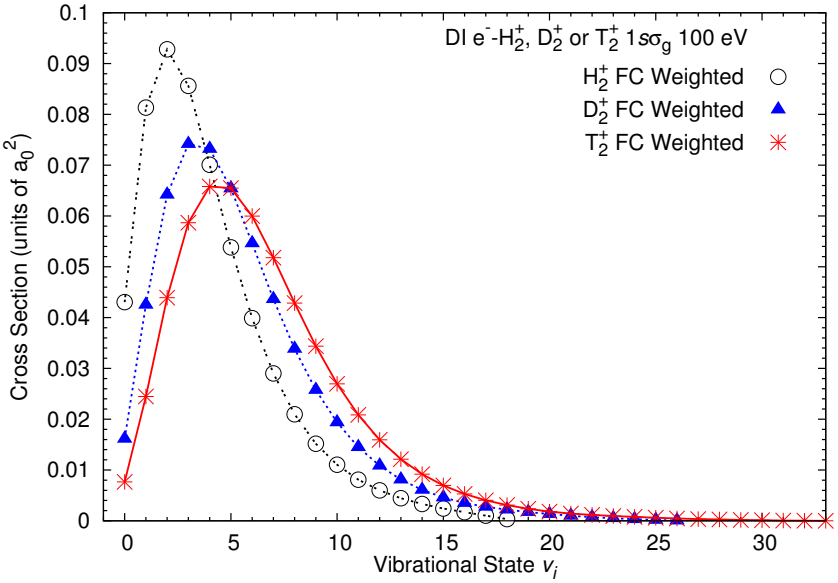

Figure 5.17: Adiabatic-nuclei convergent close-coupling (CCC) calculations of 100 eV electrons scattering from the electronic ground, vibrationally excited states of H_2^+, D_2^+ or T_2^+. Franck-Condon (FC) vibrationally weighted dissociative ionisation (DI) cross sections are presented as a function of the initial vibrational state v_i of the molecule.

In Fig. 5.18 DE and DI cross sections are presented as a function of the initial vibrational states of T_2^+ up to $v_i = 17$ (approximately spans the range $1.0 \leq R \leq 5.5\ a_0$). Like H_2^+ and D_2^+ the DE and DI cross sections are highly dependent upon the initial vibrational state of the molecule.

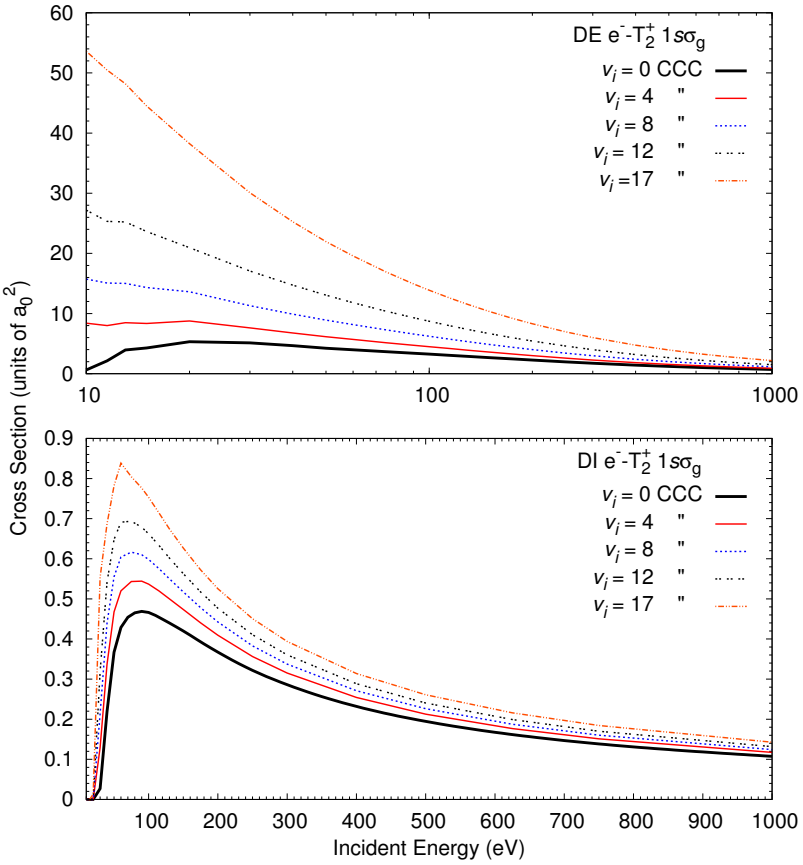

Figure 5.18: Electron scattering from the electronic ground state of T_2^+ in the vibrational state v_i. Convergent close-coupling (CCC) results are presented for dissociative excitation (DE) and dissociative ionisation (DI) cross sections.

5.2.4 HD^+

Unlike the homonuclear molecular ions H_2^+, D_2^+ and T_2^+ the heterogeneous molecular ions HD^+, HT^+ and DT^+ all have a permanent electric dipole-moment and internally cool via rotational-vibrational radiative transitions [91]. This allows experiments to prepare the HD^+, HT^+ and DT^+ molecules in the ground vibrational state [27]. For this reason averaging over the vibrational distribution is not required and weighted cross sections are not presented for HD^+, HT^+ and DT^+.

DE and DI cross sections of HD^+ in the vibrationally excited state v_i are presented up to $v_i = 11$ in Fig. 5.19. Firstly the $v_i = 0$ DE cross section

is compared with the experiment of Andersen et al. [27] in the top panel of Fig. 5.19. Above 13 eV the adiabatic-nuclei CCC results are in excellent agreement with experiment. The poor agreement with experiment below 13 eV comes from the near threshold error in the closure approximation and the indirect resonant electron attachment processes neglected in the current formalism. For HD^+ in the vibrational ground state the direct DE mechanism (excitation to the $2p\sigma_u$) starts to contribute to the DE cross section at approximately 9 eV, while the indirect mechanism contribution starts to diminish at 9 eV and practically goes to zero at approximately 13 eV [153]. The reasonably good agreement between the adiabatic-nuclei CCC results and experiment indicates the dominance of the direct-scattering process above 10 eV, which is consistent with findings of Duca and Fifirig [153] and Fifirig and Stroe [155]. DE and DI cross sections of HD^+ have the same dependence on v_i as the other isotopologues described above. The major difference between isotopologues vibrationally resolved cross sections is just the density and spacing of the vibrational state cross sections, which comes from number of bound vibrational states in the same range of R.

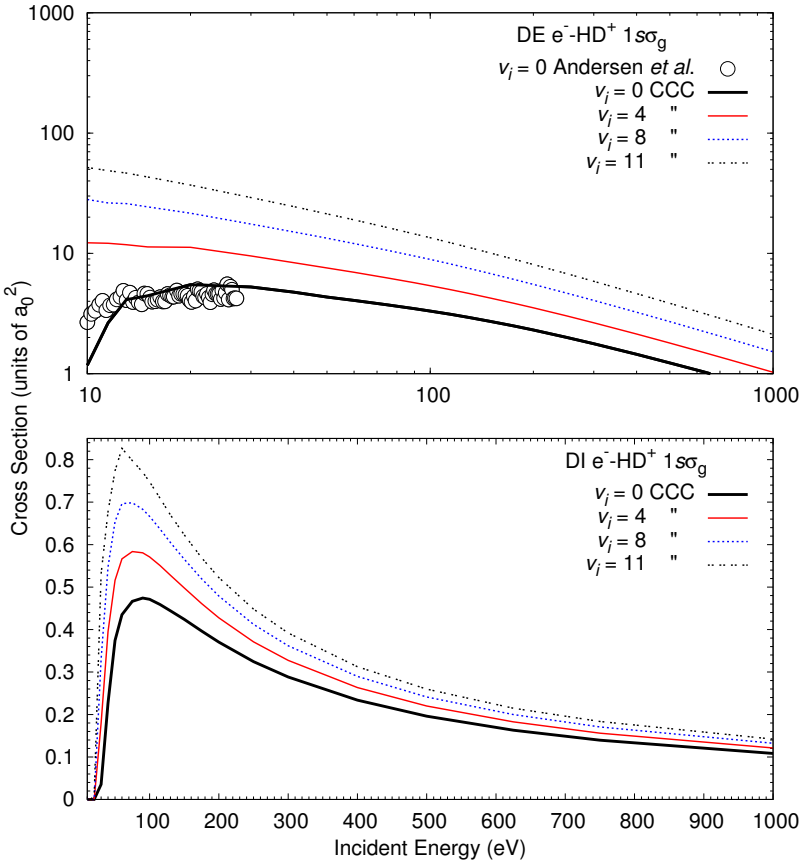

Figure 5.19: Dissociative excitation (DE) and dissociative ionisation (DI) cross sections for electron scattering from HD^+ in the electronic ground, vibrational state v_i. DE results of HD^+ in the vibrational ground state are compared with the experiment of Andersen et al. [27].

5.2.5 HT^+

Vibrationally resolved DE and DI cross sections of HT^+ are presented in Fig. 5.20 up to $v_i = 12$. These cross sections have a large dependence on the initial vibrational state of the molecule and monotonically increase as v_i increases.

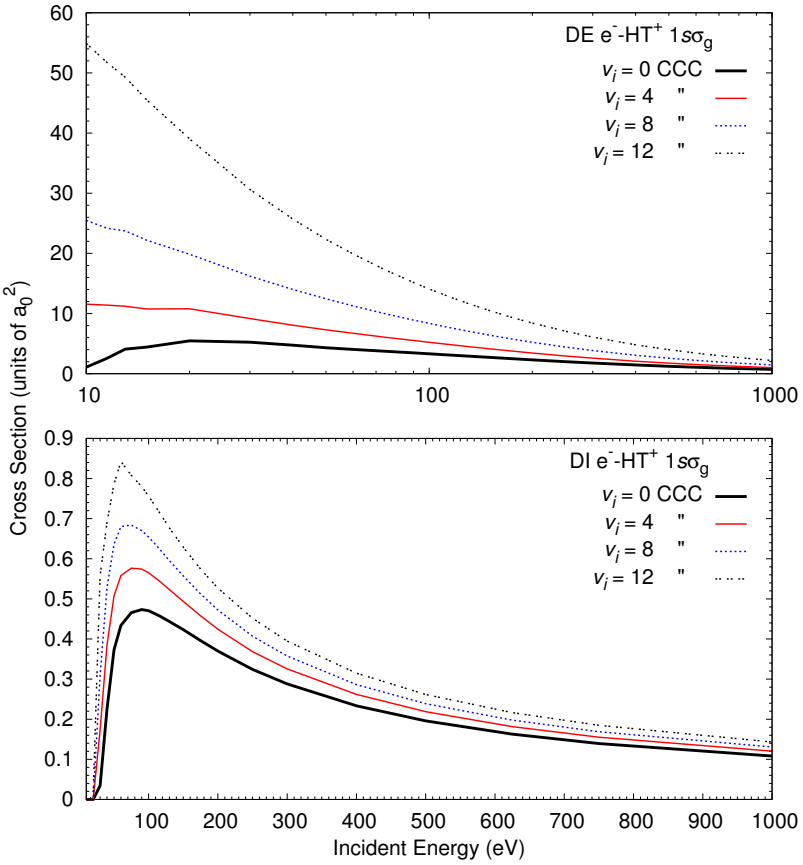

Figure 5.20: Electron scattering from the electronic ground state of HT^+ in the vibrational state v_i. Convergent close-coupling (CCC) results are presented for dissociative excitation (DE) and dissociative ionisation (DI) cross sections.

5.2.6 DT^+

Vibrationally resolved DE and DI cross sections of DT^+ are presented in Fig. 5.21 up to $v_i = 15$. Like the other isotopologues of H_2^+, the DE and DI cross sections of HD^+ have a major dependence on v_i. The DE and DI cross sections monotonically increase as v_i increases.

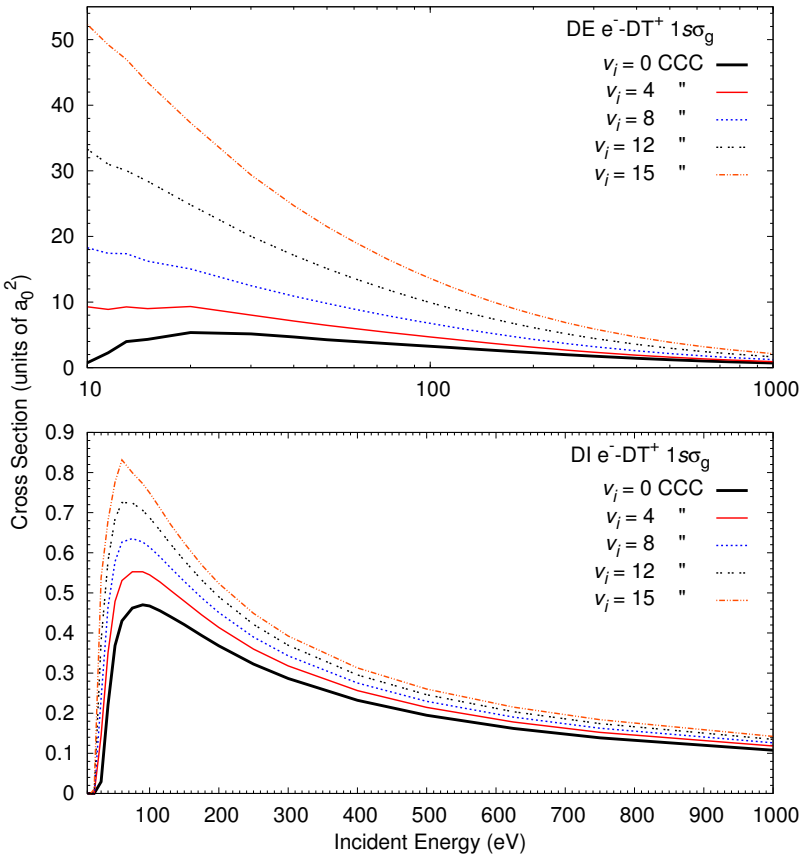

Figure 5.21: Electron scattering from the electronic ground state of DT^+ in the vibrational state v_i. Convergent close-coupling (CCC) results are presented for dissociative excitation (DE) and dissociative ionisation (DI) cross sections.

Chapter 6

Positron scattering from H_2

Adiabatic-nuclei convergent close-coupling (CCC) results of positron scattering from the $v_i = 0$ and $v_i = 1$ vibrational states of H_2 are presented up to 1000 eV. CCC fixed-nuclei results were found to be a good approximation of the adiabatic-nuclei $v_i = 0$ CCC results. The fixed internuclear distance chosen here is the mean internuclear distance of the H_2 vibrational ground state $R_m = 1.448\ a_0$. Results are presented for elastic integrated and differential cross sections, the vibrational $0 \rightarrow 1$ excitation cross section, the electronic $X^1\Sigma_g^+ \rightarrow B^1\Sigma_u^+$ excitation cross section, grand total cross section (GTCS) and total ionisation cross section (TICS), which is the sum of positronium (Ps) formation (1.9) and direct ionisation (1.14) cross sections. Preliminary results have been published in Ref. [170].

Cross sections calculated with the adiabatic-nuclei approximation of Eq. (2.52) and the fixed-nuclei approximation utilise the closure-method to sum over all vibrational and rotational excitations. The GTCS is the sum of all transition cross sections, including rotational and vibrational excitations.

The 1013-state model described in Section 3.2.1 is used to perform CCC calculations. The present results have been calculated using a projectile partial-wave expansion with maximum orbital angular momentum $L_{\max} = 8$. The total spin $S = 1/2$, odd and even parity Π and maximum total orbital angular projection $M_{\max} = 8$ channels were included, where $-M_{\max} \leq M \leq M_{\max}$. The orientationally averaged analytic Born subtraction (ABS) method (described in Section 4.4) was used to top-up the partial-wave expansion. In this Chapter the dash-dotted vertical lines at 8.6 and 15.4 eV in the figures, respectively indicate the Ps-formation and

ionisation thresholds of H_2 in the ground state. Note that with the present $R_m = 1.448\ a_0$ fixed-nuclei structure model, the Ps-formation and ionisation thresholds are at 9.34 and 16.14 eV respectively.

6.1 Convergence studies of positron-H_2 scattering

6.1.1 Convergence with the number of states

To investigate convergence, results of this model are compared with 694- and 884-state CCC calculations at the mean internuclear distance $R_m = 1.448$ a_0 (of H_2 vibrational ground state). The 694-state calculation was produced with the same 1013-state model described in Section 3.2.1, however the "outer" electron orbitals were constructed from Laguerre basis functions that had maximum orbital angular momentum $l_{\max} = 6$, which produced target states with maximum orbital angular projection $m_{\max} = 6$. The 884-state model was produced with the same 1013-state model described in Section 3.2.1, except the "outer" electron orbitals were constructed with $N_l = 15 - l$, $l_{\max} = 8$ Laguerre basis functions that have exponential fall-offs $\alpha_l = 1.2$ for $l \leq 5$ and $\alpha_l = 1.0$ for $l \geq 6$. The 694-, 884- and 1013-state GTCS and TICS are presented in Figs. 6.1 and 6.2 respectively. These results are practically the same and hence the 1013-state calculations are converged in the close-coupling expansion for both the number of Laguerre basis functions N_l and maximum orbital angular momentum $l_{\max}$. The convergence of the 694- and 1013-state calculations indicate that the $m_{\max} = 6$ pseudostates model is sufficiently accurate enough to describe the long-range correlations and (virtual) Ps-formation (in the low-energy region and) above the ionisation threshold. Note that the sharp rise in the TICS just above the ionisation threshold is from the Ps-formation and direct ionisation flux captured by the open positive-energy pseudostates. Hence a larger CCC calculation is expected to have sharper TICS rise just above the ionisation threshold. CCC results presented from here onwards are calculated with the 1013-state model described in Section 3.2.1.

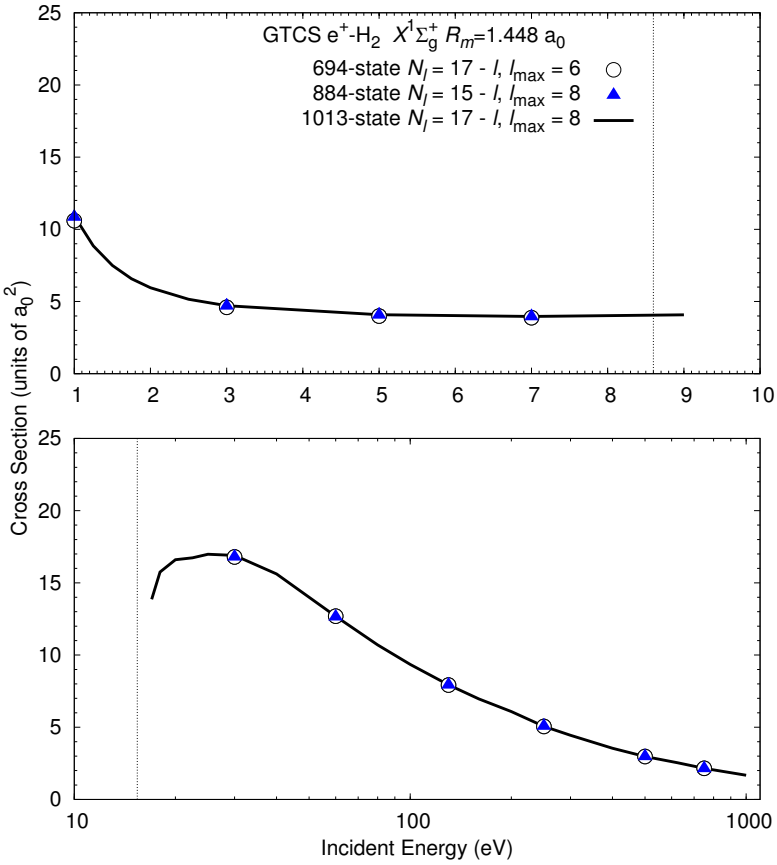

Figure 6.1: Convergence studies of positron scattering from H_2 at the mean vibrational ground state fixed-nuclear distance of $R_m = 1.448\ a_0$. 694-, 884- and 1013-state convergent close-coupling (CCC) calculations are presented for the grand total cross section (GTCS). A Laguerre basis with N_l functions for each orbital angular momentum l up to $l_{\max}$ is used to construct the "outer" electron orbitals. The dash-dotted vertical lines at 8.6 and 15.4 eV indicate the positronium-formation and ionisation thresholds of H_2 in the ground state.

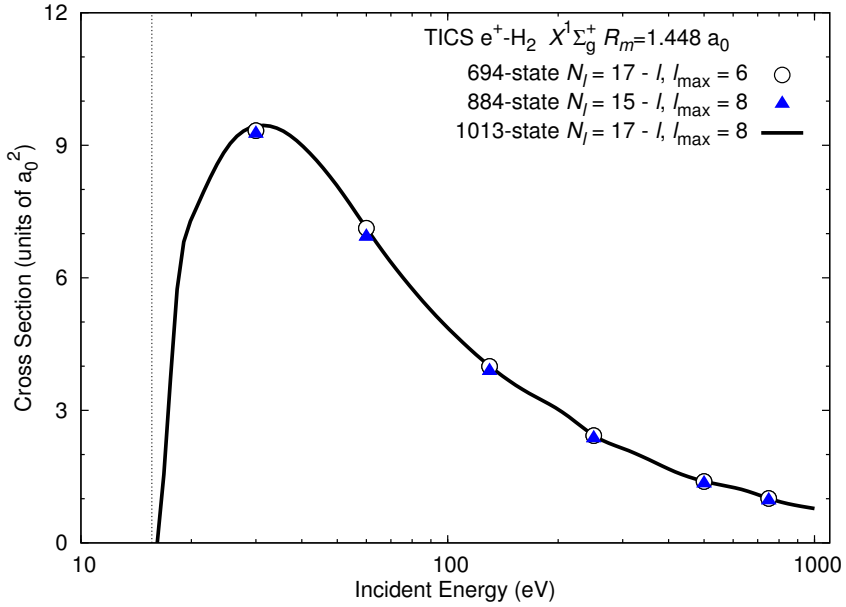

Figure 6.2: Convergence studies of positron scattering from H_2 at the mean vibrational ground state fixed-nuclear distance of $R_m = 1.448\ a_0$. 694-, 884- and 1013-state convergent close-coupling (CCC) calculations are presented for the total ionisation cross section (TICS). A Laguerre basis with N_l functions for each orbital angular momentum l up to $l_{\max}$ is used to construct the "outer" electron orbitals. The dash-dotted vertical line at 15.4 eV indicates the ionisation threshold of H_2 in the ground state.

6.1.2 Convergence of the partial-wave expansion

Convergence of the GTCS and TICS is investigated in Figs. 6.3 and 6.4 with respect to the size of the projectile partial-wave expansion. The 1013-state CCC calculations at the fixed-nuclear distance of $R_m = 1.448\ a_0$ were performed for partial-wave expansions with $L_{\max} = M_{\max} = 7$, $L_{\max} = M_{\max} = 8$ and $L_{\max} = M_{\max} = 9$, which were then topped-up using the ABS method. The $L_{\max} = M_{\max} = 8$ and $L_{\max} = M_{\max} = 9$ GTCS and TICS are practically the same, where the GTCS maximum is within 1% of each other. A noticeable difference is seen at the TICS peak, where the $L_{\max} = M_{\max} = 7$ cross section is approximately 2.5% and 3.8% lower than the $L_{\max} = M_{\max} = 8$ and $L_{\max} = M_{\max} = 9$ results respectively. Testing the convergence of the partial-wave expansion of the 694-state calculations described in the Section above (which have $m_{\max} = 6$ states),

it was found that $L_{\max} = M_{\max} = 7$ TICS peak is within 2.4% of the $L_{\max} = M_{\max} = 8$ cross section. By construction the $L_{\max} = M_{\max} = 7$ partial-wave expansion fully couples all states in the 694-state calculation. For the 1013-state calculations, the $L_{\max} = M_{\max} = 7$ partial-wave expansion does not fully couple the $|m| = 8$ states by construction. This indicates that the incomplete coupling of the $L_{\max} = M_{\max} = 7$ partial-wave expansion to the $|m| = 8$ states is not the major contributor to this difference. Practically the $L_{\max} = M_{\max} = 8$ and $L_{\max} = M_{\max} = 9$ TICS and GTCS are the same across the entire energy-range and are therefore converged.

The 1013-state CCC results presented here are converged in both the projectile partial-wave and close-coupling expansions. From here onwards the following results have been calculated using the 1013-state model and a partial-wave expansion with maximum orbital angular momentum and maximum total orbital angular projection $L_{\max} = M_{\max} = 8$. Convergence studies suggest that the present fixed-nuclei $R_m = 1.448\ a_0$ 1013-state CCC results are estimated to be accurate to within 5% for the GTCS and TICS. This accuracy estimate does not include uncertainty associated with the fixed-nuclei approximation.

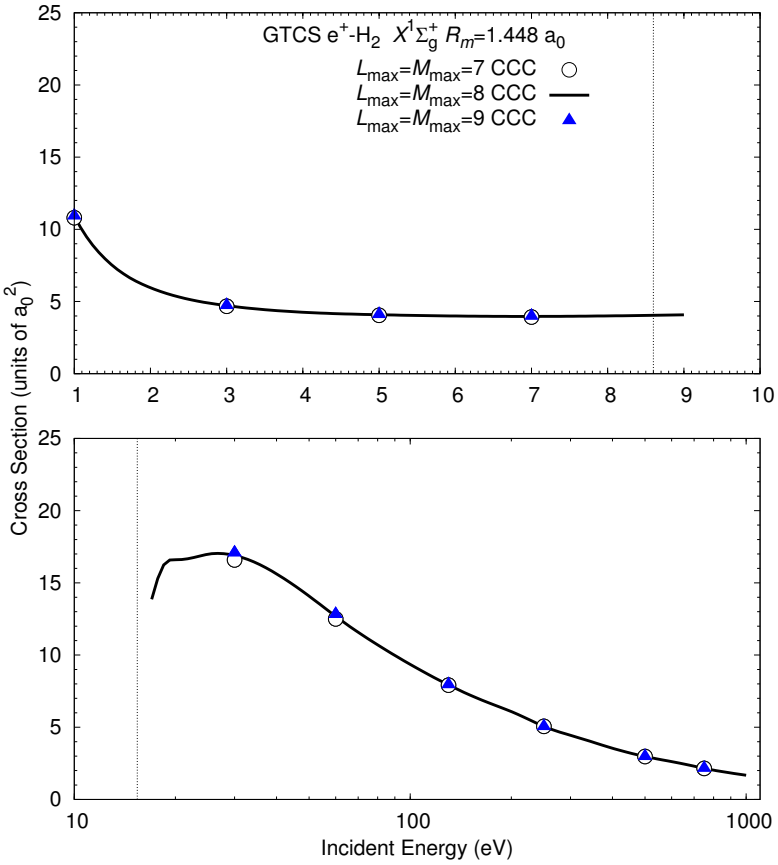

Figure 6.3: Convergence studies of the grand total cross section (GTCS) for positron scattering from H_2 at the mean vibrational ground state fixed-nuclear distance of $R_m = 1.448\ a_0$. 1013-state convergent close-coupling (CCC) results are calculated using a partial-wave expansion with maximum orbital angular momentum $L_{\max}$ and maximum total orbital angular projection $M_{\max}$. An orientationally averaged analytic Born subtraction method is used to top-up results. The dash-dotted vertical lines at 8.6 and 15.4 eV indicate the positronium-formation and ionisation thresholds of H_2 in the ground state.

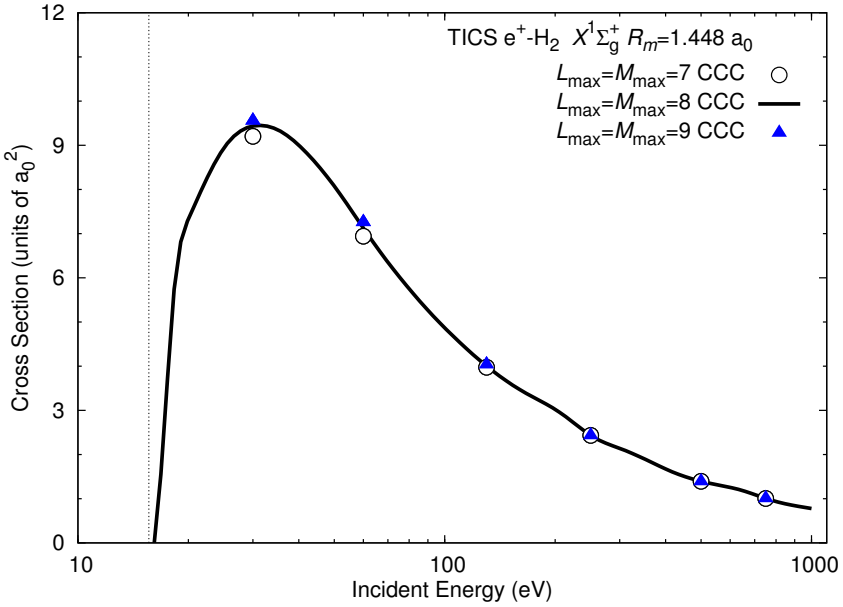

Figure 6.4: Convergence studies of the total ionisation cross section (TICS) for positron scattering from H_2 at the mean vibrational ground state fixed-nuclear distance of $R_m = 1.448\ a_0$. 1013-state convergent close-coupling (CCC) results are calculated using a partial-wave expansion with maximum orbital angular momentum $L_{\max}$ and maximum total orbital angular projection $M_{\max}$. An orientationally averaged analytic Born subtraction method is used to top-up results. The dash-dotted vertical line at 15.4 eV indicates the ionisation threshold of H_2 in the ground state.

6.2 Positron scattering from vibrationally excited H_2

Adiabatic-nuclei 1013-state CCC calculations were performed with a $L_{\max} = M_{\max} = 8$ partial-wave expansion and the ABS method was used to top-up results for the higher terms. CCC calculations were conducted over a eight point R grid within the interval $0.8 \leq R \leq 2.2\ a_0$. CCC results were found to be smooth as a function of R and were interpolated in this interval of R. Referring to Fig. 3.3 this interval approximately spans the range of the H_2 $v = 0$ and $v = 1$ vibrational state probability density functions. Using Eq. (2.52) adiabatic-nuclei CCC results are presented for positron scattering from the $v_i = 0$ and $v_i = 1$ vibrational states of H_2.

CCC calculations were performed at sufficiently low-energies to calculate the scattering length A, where

$$A = \pm\sqrt{\frac{\sigma(0)}{4\pi}}, \tag{6.1}$$

and $\sigma(0)$ is the GTCS at 0 eV [205].

For positron-H_2 accurate calculations of the scattering length have been performed by Zhang *et al.* [28, 29]. Zhang *et al.* [28, 29] determined the scattering length using the Kohn variational method and described the trial total wave function with a set of energy-optimised explicitly correlated Gaussians. In these calculations the H_2 electronic ground state is accurate to 10^{-5}% at the equilibrium distance $R_0 = 1.4\ a_0$ and convergence with respect to the basis size has variations of 1% in the scattering length [28]. To investigate the accuracy of the adiabatic-nuclei CCC results, the CCC scattering lengths are compared with the accurate calculations of Zhang *et al.* [28, 29] as a function of R in Fig. 6.5. CCC results are in excellent agreement with the calculations of Zhang *et al.* [28, 29] in the interval $0.8 \leq R \leq 2.0\ a_0$. This excellent agreement indicates that the current CCC calculations model virtual Ps-formation sufficiently accurately. At $R = 2.2\ a_0$ there is a difference of approximately 5% between the CCC results and the calculations of Zhang *et al.* [28, 29]. This difference comes for the 1013-state structure model, where the low-lying excited states of H_2 start to become more diffuse and the present structure model becomes less accurate. The $v_i = 0$ and $v_i = 1$ adiabatic-nuclei results of H_2 only have a minor contribution from cross sections $\sigma_{f,i}(R)$ for $R \geq 2.2\ a_0$. Referring to Eq. (2.52) and Fig. 3.3, this is because the respective probability density function is very small at these values of R. Utilising Eq. (2.52), the adiabatic-nuclei CCC scattering length was calculated as $A = -2.76\ a_0$ for the $v_i = 0$ state, which compares well to the fixed-nuclei $R_m = 1.448\ a_0$ CCC result of $A = -2.65\ a_0$ and the $R = 1.45\ a_0$ results of Zhang *et al.* [29] who calculated $A = -2.71\ a_0$. Second-order derivative corrections were applied to the results of Zhang *et al.* [29] (refer Eq. (2.56) and the discussion in Ref. [29]) and their scattering length was estimated as $A = -2.74\ a_0$ for the $v_i = 0$ state, which is in excellent agreement with the corresponding CCC results. The $v_i = 1$ state CCC scattering length was calculated as $A = -3.35\ a_0$, which is 21% larger than the $v_i = 0$ scattering length. Note that the present adiabatic-nuclei re-

sults are approximately a 4% increase from the fixed-nuclei results, while the second-order derivative corrections of Zhang *et al.* [29] are approximately a 1% increase.

To investigate the second-order derivative corrections of Zhang *et al.* [29] fixed-nuclei results, here their $v_i = 0$ and $v_i = 1$ scattering lengths are calculated with the adiabatic-nuclei approximation Eq. (2.52). Transforming their scattering lengths $A(R)$ to cross sections $\sigma(R)$ via Eq. (6.1), Zhang *et al.* [29] $\sigma(R)$ and H_2 vibrational wave functions (calculated here) are substituted into Eq. (2.52). The vibrationally resolved scattering length was then calculated via Eq. (6.1). Zhang *et al.* [29] adiabatic-nuclei scattering lengths via Eq. (2.52) were calculated as $A = -2.78\ a_0$ for the $v_i = 0$ state and $A = -3.31\ a_0$ for the $v_i = 1$ state, which are in excellent agreement with the CCC results. Zhang *et al.* [29] adiabatic-nuclei $v_i = 0$ scattering length was 2.6% larger than the fixed-nuclei results.

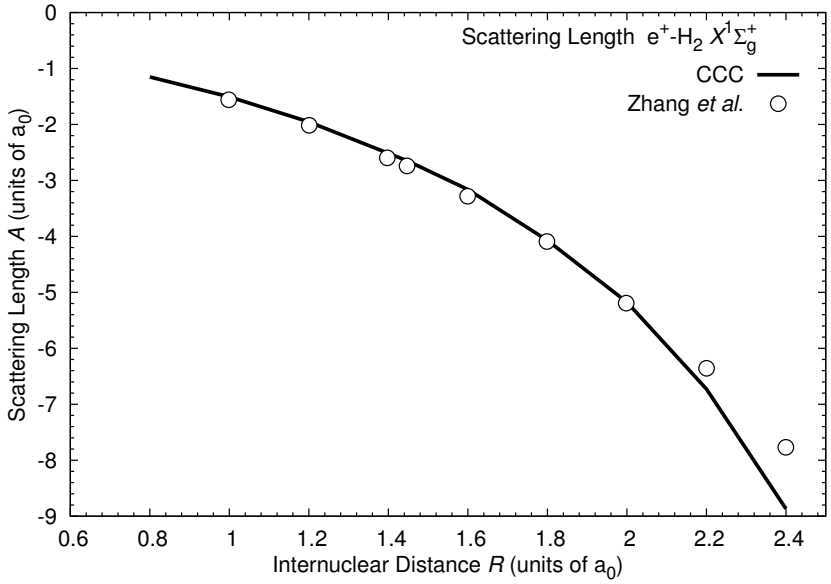

Figure 6.5: The scattering length A of positron scattering from the ground state of H_2 is presented as function of the internuclear distance R. Convergent close-coupling (CCC) results are compared with the calculations of Zhang *et al.* [28, 29].

The low-energy (below 10 eV) GTCS is presented in Fig. 6.6 for positron scattering from the ground state of H_2. Fixed-nuclei $R_m = 1.448\ a_0$ 1013-state CCC results are compared with equilibrium distance $R_0 = 1.4\ a_0$ fixed-

nuclei theoretical results calculated with the continued fractions method of Tenfen et al. [30], the molecular R-matrix with pseudostates (MRMPS) method of Zhang et al. [31], Schwinger multichannel (SMC) method of Sanchez and Lima [32] and the first-order (ad hoc) method of Reid et al. [33]. It is important to note that the fixed-nuclei $R_m = 1.448\ a_0$ results are approximately 10% larger than the $R_0 = 1.4\ a_0$ CCC results. There is still, however, a large variation between fixed-nuclei single-centre close-coupling methods (CCC, MRMPS and SMC) results, where CCC results are 20-30% larger than the MRMPS and SMC results. Here the CCC, MRMPS and SMC methods model Ps-formation indirectly by coupling basis functions that have large orbital angular momentum, refer Section 2.3.8. The variation in these methods results comes primarily from the different size close-coupling expansions utilised in their calculations. The SMC and MRMPS calculations utilise basis expansions that have $l_{\max} = 3$ and $l_{\max} = 5$, respectively. Noting that the CCC calculations utilise a basis expansion with $l_{\max} = 8$ suggests that the SMC and MRMPS calculations have not modelled virtual Ps-formation to convergence. CCC calculations with the same sized basis as the MRMPS calculations [31] were performed, these CCC and MRMPS results were almost identical. All theoretical results have the same qualitative behaviour except for the results of Reid et al. [33] near the Ps-formation threshold. The present CCC results are in good agreement with the body-frame vibrational close-coupling (BFVCC) calculations of Gianturco and Mukherjee [34] above 4 eV.

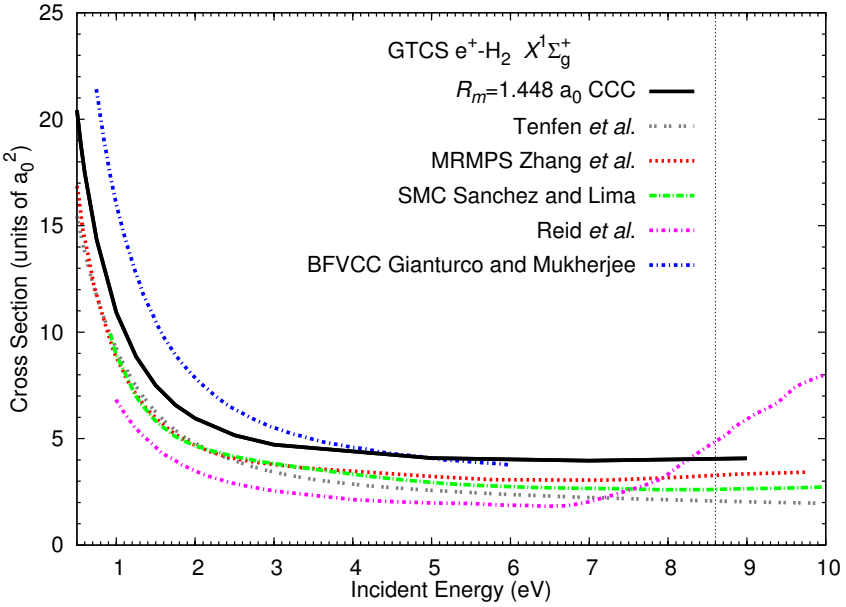

Figure 6.6: The grand total cross section (GTCS) for positron scattering from the ground state of H_2. The mean internuclear distance $R_m = 1.448$ a_0 fixed-nuclei convergent close-coupling (CCC) results are compared with equilibrium $R_0 = 1.4$ a_0 fixed-nuclei results from the method of continued fractions calculation of Tenfen et al. [30], the molecular R-matrix with pseudostates (MRMPS) calculations of Zhang et al. [31], Schwinger multichannel (SMC) calculations of Sanchez and Lima [32] and first-order method of Reid et al. [33]. Results are also compared with the body-frame vibrational close-coupling (BFVCC) calculations of Gianturco and Mukherjee [34]. The dash-dotted vertical line at 8.6 eV indicates the positronium-formation threshold of H_2 in the ground state.

The adiabatic-nuclei GTCS is presented in Fig. 6.7 for positron scattering from the $v_i = 0$ and $v_i = 1$ states of H_2. Firstly in the low-energy region the adiabatic-nuclei CCC $v_i = 1$ results are between 20-30% larger than the $v_i = 0$ results. This significant difference between the $v_i = 0$ and $v_i = 1$ cross sections and scattering lengths is likely to be important in transport models [65, 66]. In the intermediate-energy region (10-100 eV) the $v_i = 1$ results are at most 10% larger than the $v_i = 0$ results. As the incident projectile energy increases the $v_i = 0$ and $v_i = 1$ cross sections converge and by 250 eV results are practically the same. Comparing the adiabatic-nuclei $v_i = 0$ results and the the fixed-nuclei mean internuclear distance $R_m = 1.448$ a_0 results,

cross sections are practically the same. In the energy-range presented here the largest difference is approximately 3% (in the low-energy region). Note that the adiabatic-nuclei $v_i = 0$ CCC results are approximately 15% larger than the equilibrium $R_0 = 1.4\ a_0$ fixed-nuclei CCC results. This suggests that for fixed-nuclei calculations the mean internuclear distance is a better approximation than the equilibrium distance. Therefore for the $v_i = 0$ state GTCS the mean internuclear distance $R_m = 1.448\ a_0$ fixed-nuclei results are a good approximation of the adiabatic-nuclei results.

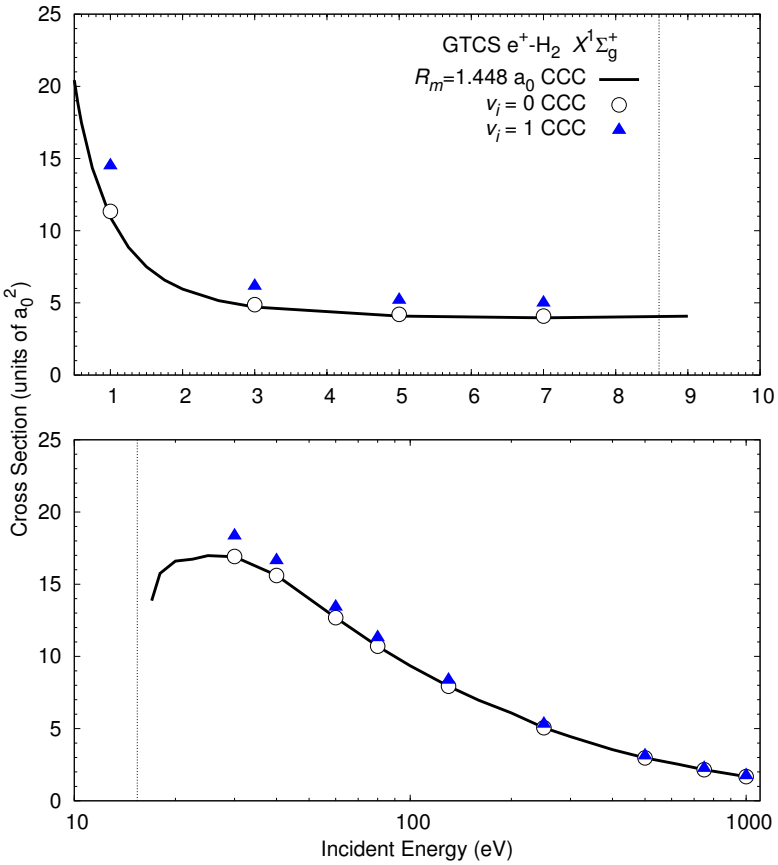

Figure 6.7: The grand total cross section (GTCS) for positron scattering from the $v_i = 0$ and $v_i = 1$ vibrational states of H_2. Adiabatic-nuclei convergent close-coupling (CCC) results are compared with the mean internuclear distance $R_m = 1.448\ a_0$ fixed-nuclei CCC calculations. The dash-dotted vertical lines at 8.6 and 15.4 eV indicate the positronium-formation and ionisation thresholds of H_2 in the ground state.

In Fig. 6.8 the GTCS is compared with experiments for positron scattering from the ground state of H_2. The fixed-nuclei $R_m = 1.448\ a_0$ 1013-state CCC results are compared with the measurements of Machacek et al. [35], Karwasz et al. [36], Zecca et al. [37], Hoffman et al. [38], Charlton et al. [39] Zhou et al. [40] and Deuring et al. [41]. Machacek et al. [35] have also corrected their low-energy measurements to account for scattering to forward angles. In the low-energy region experimental results show large variations. These variations are primarily due to differing experimental resolution of scattering to forward angles [35, 37]. The resolution of Zecca et al. [37], Karwasz et al. [36] and Machacek et al. [35] experiments are the most superior [37, 241]. The experiments of Hoffman et al. [38], Charlton et al. [39] Zhou et al. [40] and Deuring et al. [41] have likely missed scattering to forward angles and measured lower cross sections [37]. For example at 5 eV the measurements of Machacek et al. [35] had scattering resolution above 10 degrees, while the experiment of Hoffman et al. [38] had scattering resolution above 25 degrees. Note that the angular resolution of a measurement is dependent on the projectile, target and projectile-energy [38]. CCC results are in the best agreement with the measurements of Zecca et al. [37] and Karwasz et al. [36]. At very low energies (below 2 eV) the agreement with the measurements of Zecca et al. [37] is expected to improve when the missed scattering to forward angles is accounted for.

Above the ionisation threshold (lower panel of Fig. 6.8) all experiments [35, 37–41] are in good agreement with each other. CCC results are in good agreement with all experiments. The good agreement with experiment at the cross section maximum (25 eV) suggests that the 1013-state CCC calculations are sufficiently large to model Ps-formation. It is interesting to note that the GTCS measurements of Machacek et al. [35] are consistently higher than other experiments [38, 40, 41] and the CCC results at high energies, where Ps-formation is negligible and experimental angular resolution should not be an issue. Note that in the high-energy region the positron-H_2 GTCS is approximately two-three times larger than the positron-He GTCS [242].

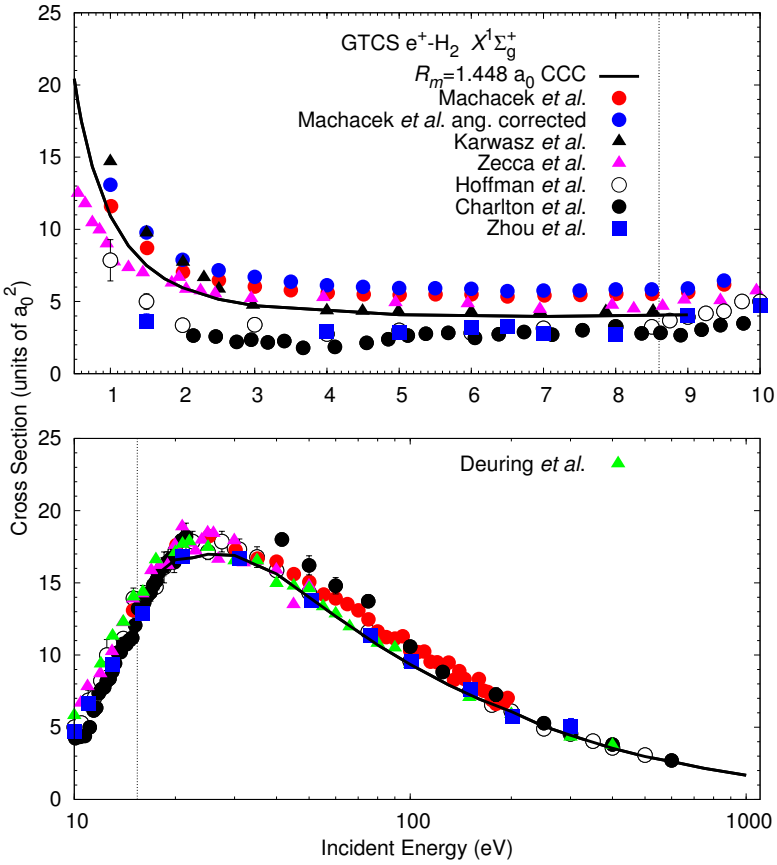

Figure 6.8: Convergent close-coupling (CCC) results of the grand total cross section (GTCS) for positron scattering from the ground state of H_2. The mean internuclear distance $R_m = 1.448\ a_0$ fixed-nuclei CCC results are compared with the measurements of Machacek et al. [35], Karwasz et al. [36], Zecca et al. [37], Hoffman et al. [38], Charlton et al. [39], Zhou et al. [40] and Deuring et al. [41]. The dash-dotted vertical lines at 8.6 and 15.4 eV indicate the positronium-formation and ionisation thresholds of H_2 in the ground state.

Low-energy elastic differential cross sections (DCS) are presented in Fig. 6.9 for positron scattering from the ground state of H_2. The experiment of Machacek et al. [35] measures the elastic cross section as the electronic elastic cross section summed over all final vibrational and rotational transitions. Note that fixed-nuclei CCC DCS and integrated cross sections are analytically summed over all vibrational and rotational excitations, refer Section 2.2 and Lane [208]. The experiment of Machacek et al. [35] sums measure-

ments of the DCS at θ and $180^\circ - \theta$. Here the fixed-nuclei $R_m = 1.448\ a_0$ CCC results are combined in the same way to compare with experiment. Note that the fixed-nuclei CCC results at 10 eV have a mismatch of boundary conditions as Ps-formation is open and direct ionisation is closed. CCC results are in good qualitative agreement with the 3.0, 7.0 and 10 eV measured DCS but underestimate experimental measurements in the forward (and backward) scattering angles. For the 1.0 eV DCS, CCC results do not agree with the shape or magnitude of the measurements. The rapid rise of the GTCS around 1 eV (see Fig. 6.6) is possibly a contributing factor. However even taking into account the uncertainty estimates of the present fixed-nuclei CCC results, there is still a significant difference between theory and experiment at the forward scattering angles. As shown in Section 6.1 the CCC results are converged in both the close-coupling and partial-wave expansions. Hence these calculations can only be improved by coupling to vibrational and rotational states.

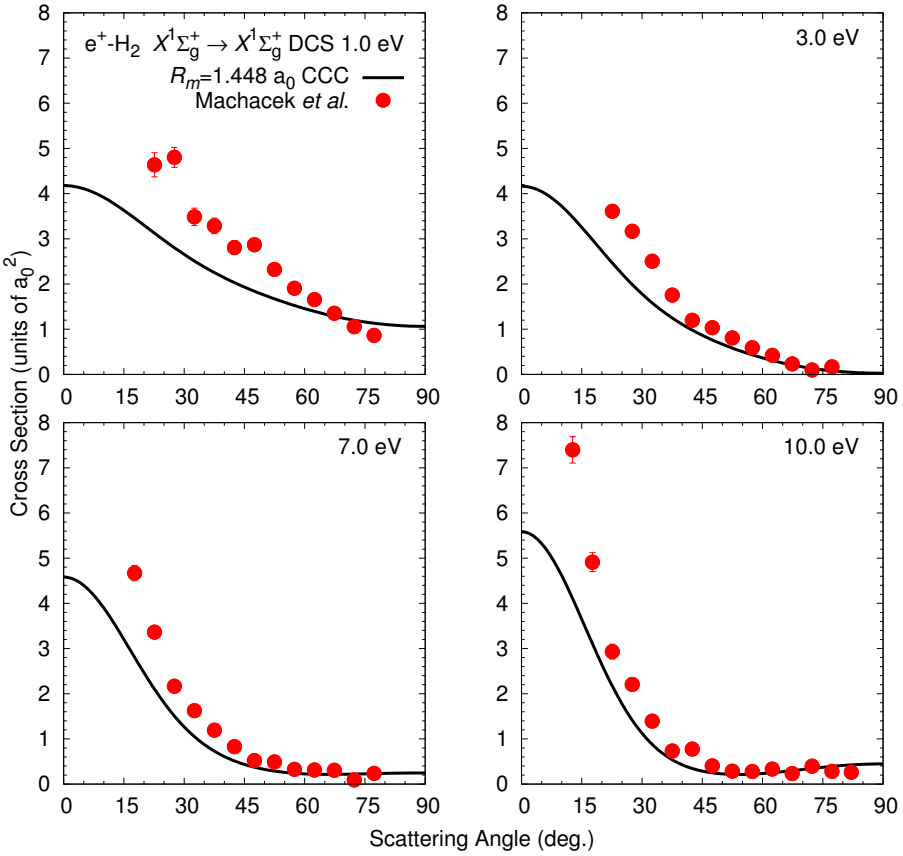

Figure 6.9: 1.0, 3.0, 7.0 and 10 eV elastic (summed over all vibrational and rotational excitations) differential cross sections (DCS) for positron scattering from the ground state of H_2. The mean internuclear distance $R_m = 1.448$ a_0 fixed-nuclei convergent close-coupling (CCC) results and the measurements of Machacek et al. [35] have summed the DCS at θ and $180° - \theta$.

The positron-H_2 vibrational $0 \rightarrow 1$ excitation cross section is presented in Fig. 6.10. Adiabatic-nuclei CCC results are compared with the adiabatic-nuclei SMC projection-operator calculations of Varella and Lima [42], BFVCC calculations of Gianturco and Mukherjee [34] and the measurements of Sullivan et al. [43]. The adiabatic-nuclei CCC results are calculated with an approximation to Eq. (2.48), which was utilised by El Ghazaly *et al.* [22]

$$\sigma^S_{fv_f,iv_i} = |\langle \nu_{fv_f} | \sqrt{\sigma^S_{f,i}(R)} | \nu_{iv_i} \rangle_R|^2. \tag{6.2}$$

The vibrational excitation cross section forms given by equations (2.48) and (6.2) violate the conservation of energy (due to vibrational transition) and the cross section will not go to zero at threshold. Several adiabatic-nuclei correction methods have been summarised in Section 2.1.2 and are expected to lower the adiabatic-nuclei CCC cross section and have the correct threshold behaviour. The present adiabatic-nuclei CCC results from Eq. (6.2) are in excellent agreement with experiment. CCC results are also in reasonable agreement with the adiabatic-nuclei SMC projection-operator results [42] and BFVCC calculations of Gianturco and Mukherjee [34].

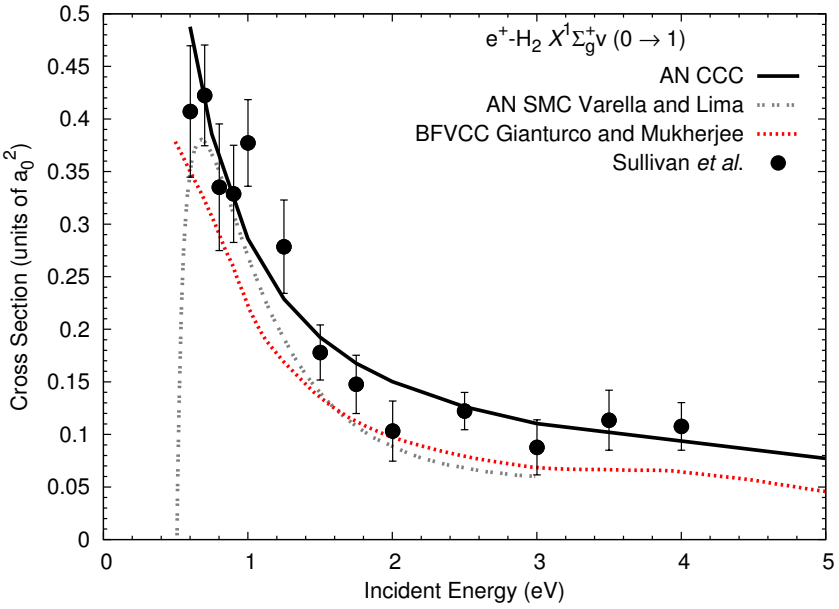

Figure 6.10: Positron scattering from the ground state of H_2 adiabatic-nuclei (AN) convergent close-coupling (CCC) vibrational $0 \rightarrow 1$ excitation cross section. Results are compared with the AN Schwinger multichannel (SMC) calculations of Varella and Lima [42], body-frame vibrational close-coupling (BFVCC) calculations of Gianturco and Mukherjee [34] and the measurements of Sullivan et al. [43].

The adiabatic-nuclei CCC TICS of positron scattering from the $v_i = 0$ and $v_i = 1$ vibrational states of H_2 are presented in Fig. 6.11. The $v_i = 1$ state TICS is noticeably larger than the $v_i = 0$ results in the intermediate-energy region. The largest difference is at the peak of the cross section (at 30 eV), where the $v_i = 1$ TICS is approximately 7% larger than the $v_i = 0$ TICS. Again the $v_i = 1$ results converge to the $v_i = 0$ results at larger energies. By 130 eV the $v_i = 0$ and $v_i = 1$ TICS are practically the

same. Comparing the $v_i = 0$ and the fixed-nuclei $R_m = 1.448\ a_0$ calculations, results are practically the same over the entire energy range. The difference between these results is less than 1%, therefore the $R_m = 1.448\ a_0$ calculations are a good approximation of the $v_i = 0$ TICS.

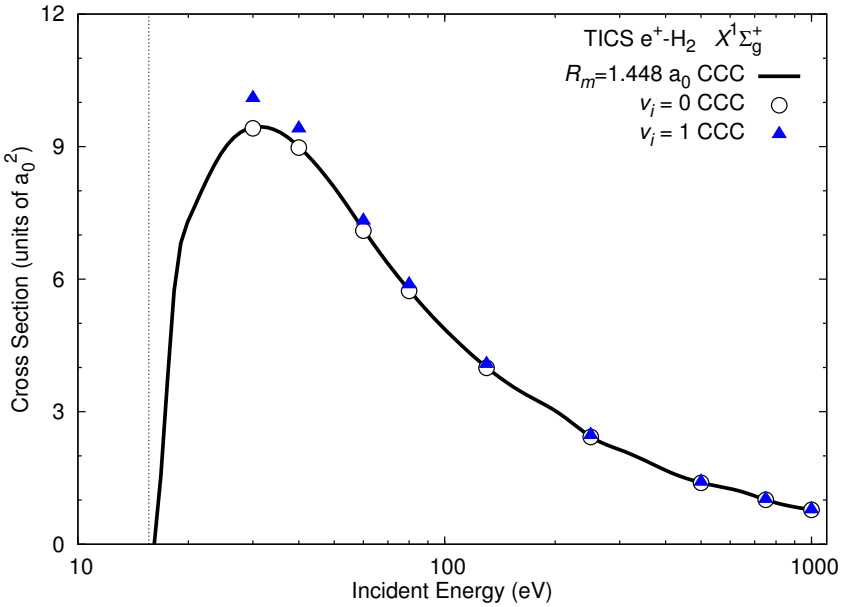

Figure 6.11: The total ionisation cross section (TICS) for positron scattering from the $v_i = 0$ and $v_i = 1$ vibrational states of H_2. Adiabatic-nuclei convergent close-coupling (CCC) results are compared with the mean internuclear distance $R_m = 1.448\ a_0$ fixed-nuclei CCC calculations. The dash-dotted vertical line at 15.4 eV indicates the ionisation threshold of H_2 in the ground state.

The ground state TICS of H_2 are compared with experiments and presented in Fig. 6.12. The $R_m = 1.448\ a_0$ CCC TICS is compared with the measurements of Fromme et al. [44] and Moxom et al. [45]. The TICS maximum at approximately 30 eV has the largest contribution from the Ps-formation cross section compared to the direct ionisation cross section (DICS), which is measured by Jacobsen et al. [46] and Knudsen et al. [47]. Just above the ionisation threshold the CCC TICS increases rapidly as more positive energy pseudostates become energetically open. The good agreement at the cross section maximum between the CCC TICS and the TICS measurements of Fromme et al. [44] and Moxom et al. [45] suggests that the 1013-state CCC calculations have a sufficiently large close-coupling expansion to indirectly model Ps-formation. As the projectile energy increases

the Ps-formation cross section diminishes and becomes negligible at approximately 130 eV [35]. Above 130 eV the CCC TICS can be compared with the DICS measurements of Jacobsen et al. [46] and Knudsen et al. [47]. Here CCC results are in good agreement with both experiments. Note that in the high-energy region the TICS is approximately two times larger than the positron-He TICS [242].

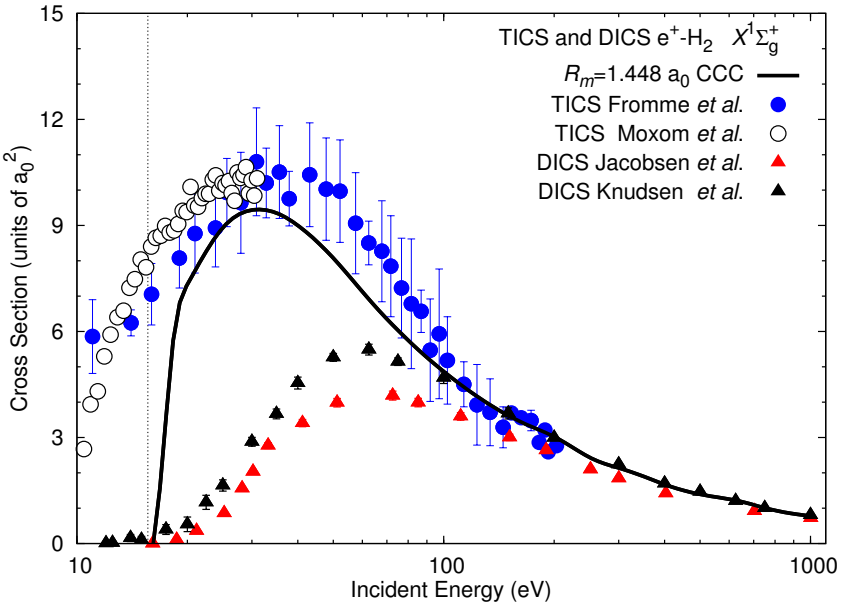

Figure 6.12: Convergent close-coupling (CCC) results of the total ionisation cross section (TICS) for positron scattering from the ground state of H_2. The mean internuclear distance $R_m = 1.448\ a_0$ fixed-nuclei CCC results are compared with the measurements of Fromme et al. [44] and Moxom et al. [45] and the direct ionisation cross sections (DICS) measured by Jacobsen et al. [46] and Knudsen et al. [47]. The dash-dotted vertical line at 15.4 eV indicates the ionisation threshold of H_2 in the ground state.

The adiabatic-nuclei CCC elastic (summed over all vibrational and rotational excitations) integrated cross section is presented in Fig. 6.13 for positron scattering from the $v_i = 0$ and $v_i = 1$ vibrational states of H_2. Firstly comparing the fixed-nuclei $R_m = 1.448\ a_0$ and adiabatic-nuclei $v_i = 0$ CCC results, cross sections are practically the same. The difference between the $v_i = 0$ and $v_i = 1$ results is relatively minor, where the $v_i = 1$ cross section is at most 8% larger than the $v_i = 0$ results.

The $R_m = 1.448\ a_0$ fixed-nuclei CCC elastic (summed over all vibrational and rotational excitations) integrated cross section is compared with the

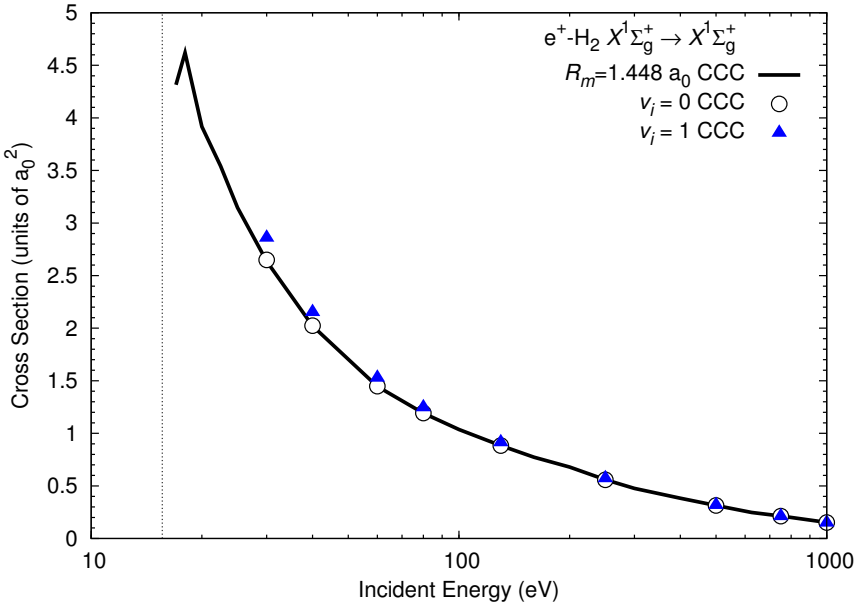

Figure 6.13: Convergent close-coupling (CCC) results of the elastic (summed over all vibrational and rotational excitations) integrated cross section for positron scattering from the $v_i = 0$ and $v_i = 1$ vibrational states of H_2. The mean internuclear distance $R_m = 1.448\ a_0$ fixed-nuclei results are compared with the adiabatic-nuclei CCC. The dash-dotted vertical line at 15.4 eV indicates the ionisation threshold of H_2 in the ground state.

corresponding measurements of Machacek et al. [35] in Fig. 6.14 for H_2 in the $v_i = 0$ state. As a consequence of distinguishing between the elastic and inelastic scattering processes, the elastic measurements of Machacek et al. [35] missed a larger portion of forward angle scattering compared to the measurements of the GTCS. These measurements of Machacek et al. [35] are expected to rise when scattering to forward angles is better accounted for. Given the large variation and uncertainty in the measurements it is difficult to draw any solid conclusions regarding the comparison with theory. The $R_m = 1.448\ a_0$ fixed-nuclei CCC results are within the uncertainties of almost all experimental points.

In Fig. 6.15 the $v_i = 0$ and $v_i = 1$ states of H_2 $X^1\Sigma_g^+ \rightarrow B^1\Sigma_u^+$ electronic excitation cross sections are presented. The adiabatic-nuclei $v_i = 0$ and $v_i = 1$ state CCC results show a significant difference across the entire energy range. For example at 30 eV the $v_i = 1$ cross section is 20% larger than the $v_i = 0$ cross section. Even at high energies there is still a significant difference between $v_i = 0$ and $v_i = 1$ results, where at 750 eV there is a 14%

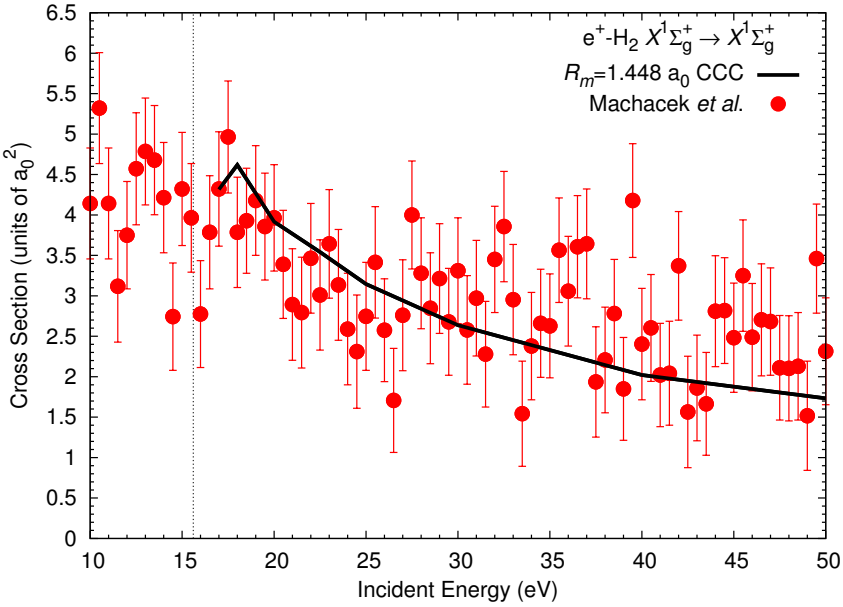

Figure 6.14: Convergent close-coupling (CCC) results of the elastic (summed over all vibrational and rotational excitations) integrated cross section for positron scattering from the ground state of H_2. The mean internuclear distance $R_m = 1.448\ a_0$ fixed-nuclei results are compared with the measurements of Machacek et al. [35]. The dash-dotted vertical line at 15.4 eV indicates the ionisation threshold of H_2 in the ground state.

difference. The adiabatic-nuclei $v_i = 0$ results are less than 2% larger than the $R_m = 1.448\ a_0$ fixed-nuclei results. Hence the $R_m = 1.448\ a_0$ fixed-nuclei results are a good approximation of the adiabatic-nuclei $v_i = 0$ results.

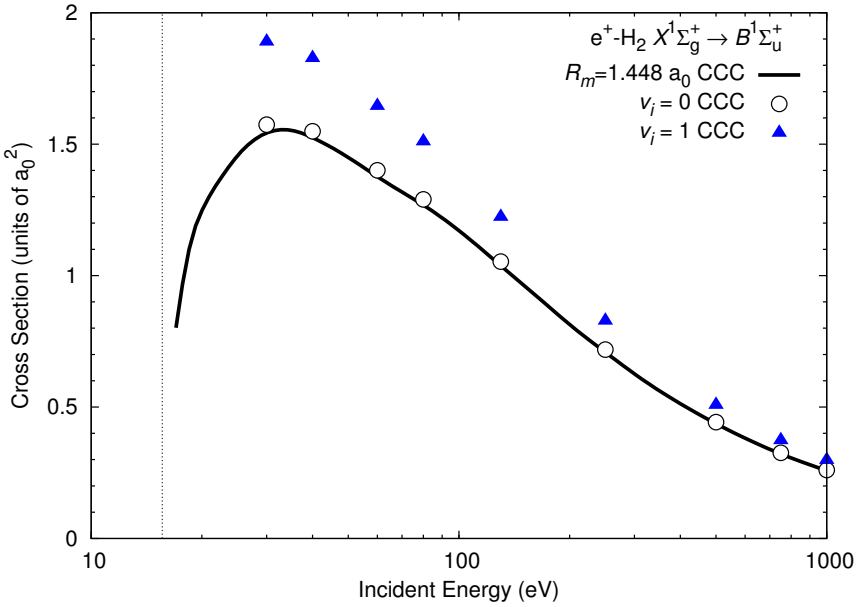

Figure 6.15: Positron scattering from H_2 in the $v_i = 0$ and $v_i = 1$ vibrational states for the electronic $X^1\Sigma_g^+ \rightarrow B^1\Sigma_u^+$ excitation cross section. Adiabatic-nuclei convergent close-coupling (CCC) results are compared with the mean internuclear distance $R_m = 1.448\ a_0$ fixed-nuclei CCC calculations. The dash-dotted vertical line at 15.4 eV indicates the ionisation threshold of H_2 in the ground state.

The fixed-nuclei $R_m = 1.448\ a_0$ CCC results are compared with the measurements of Sullivan *et al.* [43, 185] and the fixed-nuclei $R_0 = 1.4\ a_0$ SMC calculations of Lino et al. [48] and Arretche and Lima [49] in Fig. 6.16, for the $X^1\Sigma_g^+ \rightarrow B^1\Sigma_u^+$ electronic excitation cross section of H_2 in the ground state. The calculations of Lino et al. [48] used Hartree-Fock target state wave functions, while the scattering calculation was just a two-state approximation. This type of calculation is not expected to yield physically accurate results but was simply used as a first attempt at a multichannel calculation. Arretche and Lima [49] have performed a 5-state SMC calculation, which is expected to be more accurate than the calculations of Lino et al. [48]. The 1013-state CCC results are in good agreement with experiment below 25 eV, however above 25 eV CCC results do not follow the shape of the experimental measurements or the 2-state SMC results. Experiment shows a cross section peak at approximately 20 eV, while both the CCC and 5-state SMC [49] results do not show a cross section peak below 25 eV. Referring

to Fig. 6.15, CCC results show a cross section peak at approximately 30 eV. Confidence in the CCC results is increased by noting that convergence studies suggest that the fixed-nuclei CCC results are accurate to within 5% (for this cross section) and that the good agreement with experiment for the GTCS, TICS and elastic cross section in this energy region suggest that by unitarity the CCC results for other processes should be sufficiently accurate.

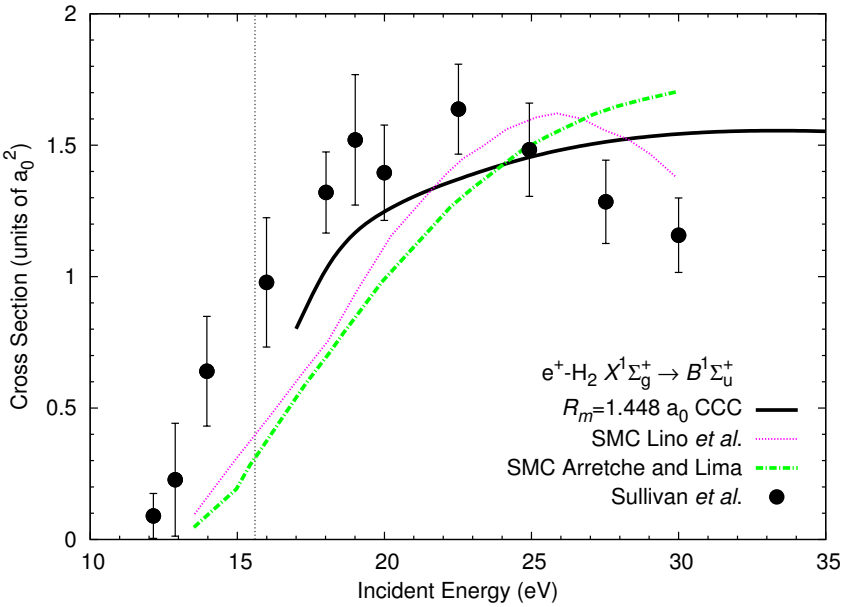

Figure 6.16: Positron scattering from the ground state of H_2 for the electronic $X^1\Sigma_g^+ \rightarrow B^1\Sigma_u^+$ excitation cross section (summed over all vibrational and rotational excitations). The mean internuclear distance $R_m = 1.448\ a_0$ fixed-nuclei convergent close-coupling (CCC) results are compared with the $R_0 = 1.4\ a_0$ fixed-nuclei Schwinger multichannel (SMC) calculations of Lino et al. [48] and Arretche and Lima [49] and the measurements of Sullivan et al. [43]. The dash-dotted vertical line at 15.4 eV indicates the ionisation threshold of H_2 in the ground state.

Chapter 7

Summary and conclusions

7.1 Summary

In this thesis the adiabatic-nuclei convergent close-coupling (CCC) method was successfully developed for electron scattering from vibrationally excited H_2^+ and single-centre positron scattering from vibrationally excited H_2. The CCC computer code developed during this thesis was written in Fortran 90 and is over 35000 lines in length. An OpenMP-MPI hybrid parellelisation scheme was implemented to allow calculations to be of arbitrary size and utilise modern day supercomputing facilities. The largest calculations presented in this thesis were run on the Pawsey centre Magnus supercomputer and required 15 nodes (360 cores, 960 GB of memory).

Electron- and positron-molecule scattering calculations demonstrated convergence in the the fixed-nuclei close-coupling (target state) and projectile partial-wave expansions. Hence the results presented here are expected to be the most accurate in the literature. The collision data presented in this thesis has been requested by the National Institute of Standards and Technology (NIST) and the International Atomic Energy Agency (IAEA) to contribute to internationally agreed publicly accessible standards for molecular collision data. This data will be useful to plasma modellers and has already become useful in transport property models [66].

7.1.1 Electron scattering from H_2^+ and its isotopologues

Calculations were performed for electron scattering from vibrationally excited H_2^+ and its isotopologues (D_2^+, T_2^+, HD^+, HT^+ and TD^+). Dissociative

excitation and dissociative ionisation cross sections are presented from 10 to 1000 eV as a function of the initial vibrational state of the isotopologues. To compare with experiments, CCC vibrationally resolved cross sections were weighted according to the vibrational populations of experiment (Franck-Condon factors). Adiabatic-nuclei CCC results were found to be in excellent agreement with experiment. Inaccuracies were identified in dissociative ionisation measurements [22] and time-dependent close-coupling [17] calculations (not fully converged in the projectile partial-wave expansion). The present results have been published in *Phys. Rev. A* **88**(6):062709, 2013 and *Phys. Rev. A* **90**(2):022711, 2014.

For the first time:

- Convergence is achieved in electron-molecule scattering calculations for both the fixed-nuclei close-coupling (target state) and projectile partial-wave expansions.
- Accurate *ab initio* calculations are presented over a broad energy-range for dissociative excitation and dissociative ionisation cross sections of H_2^+ and its isotopologues as a function of the initial vibrational state.
- Excellent agreement with experiment is seen over a broad energy-range for proton production and dissociative ionisation cross sections of vibrationally weighted H_2^+ and its isotopologues.

7.1.2 Positron scattering from H_2

Single-centre CCC calculations were performed for positron scattering from vibrationally excited H_2. Results are presented from threshold to 1000 eV for the elastic integrated and differential cross sections, the vibrational $0 \rightarrow 1$ excitation cross section, the electronic $X^1\Sigma_g^+ \rightarrow B^1\Sigma_u^+$ excitation cross section, grand total cross section and total ionisation cross section, which is the sum of positronium formation (1.9) and direct ionisation (1.14) cross sections. In general these results are in good agreement with experiment. The scattering length is also presented as function of the internuclear distance and is in excellent agreement with the accurate calculations of Zhang *et al.* [28, 29]. A rapid communications paper was published in *Phys. Rev. A* **87**(2):020701, 2013. A more detailed manuscript is currently in preparation.

For the first time:

- Convergence is achieved in positron-molecule scattering calculations for both the single-centre fixed-nuclei close-coupling (target state) and projectile partial-wave expansions.
- Accurate *ab initio* results of positron-molecule scattering are calculated above the ionisation threshold.
- Results are in excellent agreement with experiment for the grand total and total ionisation cross sections over a broad energy-range.
- Accurate elastic scattering and electronic $X^1\Sigma_g^+ \rightarrow B^1\Sigma_u^+$ excitation cross sections are presented over a broad energy-range and are in good agreement with experiment.
- Accurate results are presented for positron scattering from the $v_i = 1$ vibrational state of H_2 over a broad energy-range.

7.2 Conclusions

As a first attempt at electron- and positron-molecule CCC calculations, the method has shown great promise. Integrated cross sections for the elastic, electronic excitation and single-ionisation processes are in good agreement with experiment over a broad energy-range. The accurate structure models used in these calculations are calculated from a complete Laguerre basis. Achieving convergent results with respect to the size of the projectile partial-wave and target state (Laguerre basis) expansions indicate that scattering cross sections are accurate. With this solid foundation the CCC method is expected to be successful describing more complicated molecular collision systems.

7.3 Future work

The atomic and molecular CCC methods are the same in principle, and are expected to have the same advantages and disadvantages. Future development of the molecular CCC code will be aligned with the interest of the scientific community and successful developments of the atomic CCC method. One of the major successes of the atomic CCC method was its application to electron-He scattering [219], which produced very accurate

results that are used as a benchmark for theorists and experimentalists. The next step for the molecular CCC method is to extend it to electron scattering from H_2, which like the atomic CCC application to electron-He scattering [203, 219], should produce reliable results.

The single-centre approach is particularly suited for modelling targets with a heavy centre, like molecular hydrides [243–245]. Electron scattering from the hydrides HeH^+, LiH^+, LiH, BeH^+, BeH, BeH_2 and BeH_2^+ are particularly important in the modelling of fusion plasmas [235]. The theory behind the two-electron target HeH^+ is similar to H_2 and would require only a few minor modifications to the code. It is worth noting that hydrides have a strong permanent dipole moment, which in scattering calculations require a large partial-wave expansion to achieve convergence [69]. This can be overcome by utilising the analytic Born subtraction technique described in Section 4.4.

The second major step will be to develop and generalise the single-centre molecular CCC code so it can model scattering from multi-electron molecular hydrides. In the atomic CCC method alkali atoms (Li, Na, K, Rb, Cs, Fr) and alkaline-earth atoms (Be, Mg, Ca, Sr, Ba) are accurately modelled as quasi one- and two-electron targets above an inert Hartree-Fock frozen-core [196, 199, 203]. For electron scattering from Be and its ions the atomic CCC code has produced benchmark results [246, 247]. The quasi one-electron target LiH^+ is synonymous with atomic Li, Be^+ or B^{2+}, which have successfully been modelled with the atomic CCC code for positron [248] and electron scattering [199, 249, 250]. BeH^+ and LiH are quasi two-electron targets that are similar to Be and B^+.

Currently the atomic CCC method is being extended to perform single-centre calculations of positron scattering from arbitrary atomic targets. Similarly, we expect that by utilising these techniques the molecular CCC method will be able to perform single-centre calculations of positron scattering from arbitrary linear molecules, such as N_2, O_2, CO_2, CO, OH and HCl etc. N_2 and CF_4 gasses are interesting targets because they are used as energy loss mechanisms to cool down positrons in beam line experiments [251].

The third major development of the molecular CCC method will be an extension to polyatomic hydrides such as H_3^+, CH_4 and H_2O. H_3^+ is one of the most common ions in the universe and plays a key role in hy-

drogen plasmas [53, 57]. Electron scattering from this tightly bound two-electron target should be accurately modelled within the molecular single-centre CCC method. Positron scattering from CH_4 and H_2O is synonymous with positron scattering from Ne, where CH_4 and H_2O are Ne-like targets. Recently single-centre CCC calculations of positron-Ne produced results in good agreement with experiment [204], and hence the same success is expected for these molecular scattering systems.

Appendix A

Scattering cross section

Here the scattering cross section is derived from the asymptotic form of the total scattering wave function $\bar{\Psi}(\boldsymbol{r}_0, \mathfrak{R})$, where $\boldsymbol{r}_0$ refers to the projectile spatial coordinates and $\mathfrak{R}$ represents all target electrons and nuclear spatial coordinates collectively. Figure 2.1 shows the setup of a typical scattering experiment that measures integrated and differential cross sections. In these experiments particles are detected at asymptotic distances from the scattering centre. For a transition from the initial state i to the final state f, the total wave function has the asymptotic form

$$\bar{\Psi}^{(+)}_{f,i}(\boldsymbol{r}_0, \mathfrak{R}) \xrightarrow[\boldsymbol{r_0}\to\infty]{} N\left(e^{iq_i z_0}\bar{\Phi}_i(\mathfrak{R})\delta_{f,i} + \frac{e^{iq_f r_0}}{r_0}F_{f,i}(\theta,\phi)\bar{\Phi}_f(\mathfrak{R})\right), \qquad \text{(A.1)}$$

where N is a normalisation constant, q_i is the incident linear momentum of the projectile and q_f is the outgoing linear momentum of the scattered particle.

Referring to Fig. 2.1, a detector located at (θ, ϕ), has a face which takes up the solid angle $d\Omega$. The number of particles detected dN_{D} at (θ, ϕ), per unit time dt, per solid angle $d\Omega$ the detector face subtends with the target, is proportional to the incident number of particles dN_{Inc} per unit time per unit area dA. Hence the number of particles counted by the detector is proportional to the incident current of the beam $\boldsymbol{j}_{\mathrm{Inc}}(\boldsymbol{r}_0)$ and the solid angle subtended by the detector. For a particular transition $i \to f$, the number

of particles detected can be expressed by

$$\frac{dN_{\mathrm{D}}}{dt} = \boldsymbol{j}_{\mathrm{Inc}}(\boldsymbol{r}_0)\sigma_{f,i}(\theta,\phi)d\Omega \tag{A.2}$$

$$= \boldsymbol{j}_{\mathrm{Inc}}(\boldsymbol{r}_0)\frac{\sigma_{f,i}(\theta,\phi)}{r^2}dA, \tag{A.3}$$

where, $\sigma_{f,i}(\theta,\phi)$ is a proportionality factor, $d\Omega$ is a dimensionless quantity, r is the distance of the detector from the scattering centre and dA is the unit area, where $dA = r^2 d\Omega$. Dividing Eq. (A.3) by dA, one can substitute $\boldsymbol{j}_{\mathrm{Scat}}(\boldsymbol{r}_0)$ on the LHS and obtain

$$\boldsymbol{j}_{\mathrm{Scat}}(\boldsymbol{r}_0) = \boldsymbol{j}_{\mathrm{Inc}}(\boldsymbol{r}_0)\frac{\sigma_{f,i}(\theta,\phi)}{r^2}, \tag{A.4}$$

where $\boldsymbol{j}_{\mathrm{Scat}}(\boldsymbol{r}_0)$ is the scattered portion of the incident current detected at the angle (θ,ϕ). Note that the detector measures the scattered particles at $r = r_0$. Rearranging the above equation in terms of $\sigma_{f,i}(\theta,\phi)$

$$\sigma_{f,i}(\theta,\phi) = \frac{r_0^2\boldsymbol{j}_{\mathrm{Scat}}(\boldsymbol{r}_0)}{\boldsymbol{j}_{\mathrm{Inc}}(\boldsymbol{r}_0)}, \tag{A.5}$$

and is known as the differential cross section.

Classically, current $\boldsymbol{j}(\boldsymbol{r})$ is defined as the number of particles passing through a unit area per unit of time, or alternatively as the density ρ multiplied by velocity $\boldsymbol{v}$. It has units $\frac{N_{\mathrm{P}}}{m^2 s}$, where N_{P} is the number of particles. Quantum mechanically the density is represented by the the probability density wave function $|\psi(\boldsymbol{r})|^2$. The momentum operator $\hat{P} = \frac{1}{i}\nabla$ is used to determine the velocity operator $\hat{v} = \frac{1}{\mu}\hat{P}$ of a quantum mechanical system. Hence the quantum mechanical current is defined as

$$\boldsymbol{j}(\boldsymbol{r}) = \rho(r)\boldsymbol{v} = \mathrm{Re}\left[\psi^*(\boldsymbol{r})\frac{1}{i\mu}\nabla\psi(\boldsymbol{r})\right], \tag{A.6}$$

where, ∇ is given in Eq. (C.41) and (C.42).

The incident particle is described by a plane-wave $\psi_{\mathrm{Inc}}(\boldsymbol{r}_0) = Ne^{iq_i z_0}$.

Utilising (C.41) the incident current $\boldsymbol{j}_{\text{Inc}}(\boldsymbol{r}_0)$ is

$$\begin{aligned}
\boldsymbol{j}_{\text{Inc}}(\boldsymbol{r}_0) &= \text{Re}\left[\psi^*_{\text{Inc}}(\boldsymbol{r}_0)\frac{1}{i\mu}\nabla_0\psi_{\text{Inc}}(\boldsymbol{r}_0)\right] && \text{(A.7)}\\
&= \text{Re}\left[(Ne^{-iq_iz_0})\frac{1}{i\mu}\nabla_0(Ne^{iq_iz_0})\right]\\
&= \text{Re}\left[Ne^{-iq_iz_0}\frac{1}{i\mu}(Niq_ie^{iq_iz_0}\hat{\boldsymbol{z}})\right]\\
&= N^2\frac{q_i}{\mu}\hat{\boldsymbol{z}} && \text{(A.8)}\\
&= N^2\boldsymbol{v}_{\text{in}}. && \text{(A.9)}
\end{aligned}$$

The scattered particle wave is described by $\psi_{\text{Scat}}(\boldsymbol{r}_0) = N\frac{e^{iq_fr_0}}{r_0}F_{f,i}(\theta,\phi)$. Substituting the scattered particle wave and (C.42) into the current (A.6), the resulting scattered particle current $\boldsymbol{j}_{\text{Scat}}(\boldsymbol{r}_0)$ is

$$\begin{aligned}
\boldsymbol{j}_{\text{Scat}}(\boldsymbol{r}_0) &= \text{Re}\left[\psi^*_{\text{Scat}}(\boldsymbol{r}_0)\frac{1}{i\mu}\nabla_0\psi_{\text{Scat}}(\boldsymbol{r}_0)\right] && \text{(A.10)}\\
&= \text{Re}\left[\left(N\frac{e^{-iq_fr_0}}{r_0}F^*_{f,i}(\theta,\phi)\right)\frac{1}{i\mu}\nabla_0\left(N\frac{e^{iq_fr_0}}{r_0}F_{f,i}(\theta,\phi)\right)\right]\\
&= \text{Re}\left[\left(N\frac{e^{-iq_fr_0}}{r_0}F^*_{f,i}(\theta,\phi)\right)\frac{1}{i\mu}\right.\\
&\quad\times\left(Niq_f\frac{e^{iq_fr_0}}{r_0}F_{f,i}(\theta,\phi)\hat{\boldsymbol{r}} - N\frac{e^{iq_fr_0}}{r_0^2}F_{f,i}(\theta,\phi)\hat{\boldsymbol{r}}\right.\\
&\quad\left.\left.+\ N\frac{e^{iq_fr_0}}{r_0^2}\frac{\partial F_{f,i}(\theta,\phi)}{\partial\theta}\hat{\boldsymbol{\theta}} + N\frac{e^{iq_fr_0}}{r_0^2\sin(\theta)}\frac{\partial F_{f,i}(\theta,\phi)}{\partial\phi}\hat{\boldsymbol{\phi}}\right)\right]\\
&= \frac{N^2}{\mu r_0^2}\text{Re}\left[F^*_{f,i}(\theta,\phi)\left(q_fF_{f,i}(\theta,\phi)\hat{\boldsymbol{r}} - \frac{F_{f,i}(\theta,\phi)}{ir_0}\hat{\boldsymbol{r}}\right.\right.\\
&\quad\left.\left.+\ \frac{1}{ir_0}\frac{\partial F_{f,i}(\theta,\phi)}{\partial\theta}\hat{\boldsymbol{\theta}} + \frac{1}{ir_0\sin(\theta)}\frac{\partial F_{f,i}(\theta,\phi)}{\partial\phi}\hat{\boldsymbol{\phi}}\right)\right]. && \text{(A.11)}
\end{aligned}$$

The asymptotic form of the wave function (A.1) is used to calculate the asymptotic current $\boldsymbol{j}_{\text{Scat}}(\boldsymbol{r}_0)$, hence terms that fall off faster than $\frac{1}{r_0^2}$ can be dropped

$$\begin{aligned}
\boldsymbol{j}_{\text{Scat}}(\boldsymbol{r}_0) &= N^2\frac{|F_{f,i}(\theta,\phi)|^2}{r_0^2}\frac{q_f}{\mu}\hat{\boldsymbol{r}} && \text{(A.12)}\\
&= N^2\frac{|F_{f,i}(\theta,\phi)|^2}{r_0^2}\boldsymbol{v}_{\text{out}}. && \text{(A.13)}
\end{aligned}$$

From (A.13) and (A.9), the scattered particle current can also be expressed as

$$\boldsymbol{j}_{\text{Scat}}(\boldsymbol{r}_0) = \boldsymbol{j}_{\text{Inc}}(\boldsymbol{r}_0)\frac{|F_{f,i}(\theta,\phi)|^2}{r_0^2}\frac{\boldsymbol{v}_{\text{out}}}{\boldsymbol{v}_{\text{in}}}, \tag{A.14}$$

or alternatively

$$\frac{\boldsymbol{j}_{\text{Scat}}(\boldsymbol{r}_0)}{\boldsymbol{j}_{\text{Inc}}(\boldsymbol{r}_0)} = \frac{|F_{f,i}(\theta,\phi)|^2}{r_0^2}\frac{\boldsymbol{v}_{\text{out}}}{\boldsymbol{v}_{\text{in}}}. \tag{A.15}$$

Now substituting (A.15) into (A.5), the differential cross section $\sigma_{f,i}(\theta,\phi)$ is defined as

$$\begin{aligned}
\sigma_{f,i}(\theta,\phi) &= \frac{r_0^2\boldsymbol{j}_{\text{Scat}}(\boldsymbol{r}_0)}{\boldsymbol{j}_{\text{Inc}}(\boldsymbol{r}_0)} && \text{(A.16)}\\
&= \frac{\boldsymbol{v}_{\text{out}}}{\boldsymbol{v}_{\text{in}}}|F_{f,i}(\theta,\phi)|^2 && \text{(A.17)}\\
&= \frac{\boldsymbol{q}_f}{\boldsymbol{q}_i}|F_{f,i}(\theta,\phi)|^2. && \text{(A.18)}
\end{aligned}$$

$\sigma_{f,i}(\theta,\phi)d\Omega$ is the cross-sectional area of the incident beam that is intercepted by the target and scattered into a cone defined by θ, ϕ and $d\Omega$. $\sigma_{f,i}(\theta,\phi)$ is alternatively written as $\frac{d\sigma_{f,i}}{d\Omega}(\theta,\phi)$ and is known as the differential cross section for the transition $i \to f$. The integrated cross section for the transition $i \to f$ can be obtained by integrating $\frac{d\sigma_{f,i}}{d\Omega}(\theta,\phi)$ over all angles

$$\sigma_{f,i} = \int \frac{d\sigma_{f,i}}{d\Omega}(\theta,\phi)d\Omega. \tag{A.19}$$

Appendix B

Orientation averaged differential cross sections

The orientation averaged differential cross section (DCS) [93, 214–216] for the transition $iv_i \to fv_f$ is written as

$$\frac{d\sigma^S_{fv_f,iv_i}}{d\Omega^{(\mathrm{lab})}} = \frac{q_f}{q_i}\frac{1}{4\pi}\int_0^{2\pi}\int_0^{\pi} |F^S_{fv_f,iv_i}(\boldsymbol{q}_f^{(\mathrm{lab})}, \boldsymbol{q}_i^{(\mathrm{lab})}, \hat{\boldsymbol{R}}^{(\mathrm{lab})})|^2 d\Omega_{R^{(\mathrm{lab})}}, \quad \text{(B.1)}$$

where

$$F^S_{fv_f,iv_i}(\boldsymbol{q}_f^{(\mathrm{lab})}, \boldsymbol{q}_i^{(\mathrm{lab})}, \hat{\boldsymbol{R}}^{(\mathrm{lab})}) = (\sqrt{4\pi})^{-1} \sum_{\substack{L_f,L_i \\ M_f,M_i}} \hat{L}_i \quad \text{(B.2)}$$

$$\times \langle \nu_{fv_f} | A^{S(\mathrm{b})}_{fL_fM_f,iL_iM_i} | \nu_{iv_i} \rangle_R \sum_{\kappa} D^{L_f}_{\kappa,M_f}(\hat{\boldsymbol{R}}^{(\mathrm{lab})}) D^{L_i*}_{0,M_i}(\hat{\boldsymbol{R}}^{(\mathrm{lab})}) Y_{L_f\kappa}(\hat{\boldsymbol{q}}_f^{(\mathrm{lab})}),$$

$^{(\mathrm{lab})}$ denotes the lab-frame of reference, $^{(\mathrm{b})}$ denotes the body-frame of reference, $\hat{\boldsymbol{q}}$ is the projectile momentum vector, $\hat{\boldsymbol{R}}$ is the internuclear separation orientation angle, $\hat{L} = \sqrt{(2L+1)}$ and $A^{S(\mathrm{b})}_{fL_fM_f,iL_iM_i}$ contains the partial-wave fixed-nuclei T-matrix elements and is defined in Eq. (4.42) for homonuclear diatomic molecules. Note that vibrational wave functions $\nu_{nvJ}(R)$ have a very minor dependence on J and it can be assumed the vibrational wave functions are independent of J, i.e. ν_{fv_f}. Substituting the

lab-frame scattering amplitude (B.2) into the DCS (B.1)

$$\frac{d\sigma^{S}_{fv_f,iv_i}}{d\Omega^{(\mathrm{lab})}} = \frac{q_f}{q_i}\frac{1}{4\pi}\sum_{\substack{L_f,L_i\\M_f,M_i}}\sum_{\substack{L'_f,L'_i\\M'_f,M'_i}}\hat{L}_i\hat{L}'_i \tag{B.3}$$
$$\times\langle\nu_{fv_f}|A^{S(\mathrm{b})}_{fL_fM_f,iL_iM_i}|\nu_{iv_i}\rangle_R\langle\nu^*_{fv_f}|A^{S(\mathrm{b})*}_{fL'_fM'_f,iL'_iM'_i}|\nu^*_{iv_i}\rangle_{R'}$$
$$\times\sum_{\kappa\kappa'}\Bigg((4\pi)^{-1}\int_0^{2\pi}\int_0^{\pi}D^{L_f}_{\kappa,M_f}(\phi_{\hat{\boldsymbol{R}}},\theta_{\hat{\boldsymbol{R}}},0)D^{L_i*}_{0,M_i}(\phi_{\hat{\boldsymbol{R}}},\theta_{\hat{\boldsymbol{R}}},0)D^{L'_f*}_{\kappa',M'_f}(\phi_{\hat{\boldsymbol{R}}},\theta_{\hat{\boldsymbol{R}}},0)$$
$$\times D^{L'_i}_{0,M'_i}(\phi_{\hat{\boldsymbol{R}}},\theta_{\hat{\boldsymbol{R}}},0)d\phi_{\hat{\boldsymbol{R}}}\sin(\theta_{\hat{\boldsymbol{R}}})d\theta_{\hat{\boldsymbol{R}}}\Bigg)Y_{L_f\kappa}(\hat{\boldsymbol{q}}^{(\mathrm{lab})}_f)Y^*_{L'_f\kappa'}(\hat{\boldsymbol{q}}^{(\mathrm{lab})}_f).$$

Utilising definition (C.3) $D^{L_f}_{\kappa,M_f}(\hat{\boldsymbol{R}}) = (-1)^{\kappa-M_f}D^{L_f*}_{-\kappa,-M_f}(\hat{\boldsymbol{R}})$. Definitions (C.5) and (C.6) are then used to reduce the Wigner-D functions

$$D^{L_i*}_{0,M_i}(\hat{\boldsymbol{R}})D^{L'_i}_{0,M'_i}(\hat{\boldsymbol{R}}) = (-1)^{-M_i}\sum_j(2j+1) \tag{B.4}$$
$$\times\begin{pmatrix}L_i & L'_i & j\\ 0 & 0 & 0\end{pmatrix}\begin{pmatrix}L_i & L'_i & j\\ -M_i & M'_i & M_i-M'_i\end{pmatrix}D^{j*}_{0,M_i-M'_i}(\hat{\boldsymbol{R}})$$
$$(-1)^{\kappa-M_f}D^{L_f*}_{-\kappa,-M_f}(\hat{\boldsymbol{R}})D^{L'_f*}_{\kappa',M'_f}(\hat{\boldsymbol{R}}) = (-1)^{\kappa-M_f}\sum_{j'}(2j'+1) \tag{B.5}$$
$$\times\begin{pmatrix}L_f & L'_f & j'\\ \kappa & -\kappa' & \kappa'-\kappa\end{pmatrix}\begin{pmatrix}L_f & L'_f & j'\\ M_f & -M'_f & M'_f-M_f\end{pmatrix}D^{j'}_{\kappa-\kappa',M_f-M'_f}(\hat{\boldsymbol{R}}),$$

and substituted back into (B.3)

$$\frac{d\sigma^{S}_{fv_f,iv_i}}{d\Omega^{(\mathrm{lab})}} = \frac{q_f}{q_i}\frac{1}{4\pi}\sum_{\substack{L_f,L_i\\M_f,M_i}}\sum_{\substack{L'_f,L'_i\\M'_f,M'_i}}(-1)^{-M_f-M_i}\hat{L}_i\hat{L}'_i \tag{B.6}$$

$$\times\langle\nu_{fv_f}|A^{S(\mathrm{b})}_{fL_fM_f,iL_iM_i}|\nu_{iv_i}\rangle_R\langle\nu^*_{fv_f}|A^{S(\mathrm{b})*}_{fL'_fM'_f,iL'_iM'_i}|\nu^*_{iv_i}\rangle_{R'}$$

$$\times\sum_{j'j\kappa\kappa'}(-1)^{\kappa}(2j'+1)(2j+1)\begin{pmatrix}L_i & L'_i & j\\ 0 & 0 & 0\end{pmatrix}\begin{pmatrix}L_i & L'_i & j\\ -M_i & M'_i & M_i-M'_i\end{pmatrix}$$

$$\times\begin{pmatrix}L_f & L'_f & j'\\ \kappa & -\kappa' & \kappa'-\kappa\end{pmatrix}\begin{pmatrix}L_f & L'_f & j'\\ M_f & -M'_f & M'_f-M_f\end{pmatrix}$$

$$\times\left((4\pi)^{-1}\int_0^{\pi}\int_0^{2\pi}D^{j*}_{0,M_i-M'_i}(\phi_{\hat{\boldsymbol{R}}},\theta_{\hat{\boldsymbol{R}}},0)\right.$$

$$\left.\times D^{j'}_{\kappa-\kappa',M_f-M'_f}(\phi_{\hat{\boldsymbol{R}}},\theta_{\hat{\boldsymbol{R}}},0)d\phi_{\hat{\boldsymbol{R}}}\sin(\theta_{\hat{\boldsymbol{R}}})d\theta_{\hat{\boldsymbol{R}}}\right)Y_{L_f\kappa}(\hat{\boldsymbol{q}}^{(\mathrm{lab})}_f)Y^*_{L'_f\kappa'}(\hat{\boldsymbol{q}}^{(\mathrm{lab})}_f).$$

The spherical harmonic $Y^*_{L'_f\kappa'}(\hat{\boldsymbol{q}}^{(\mathrm{lab})}_f)$ is transformed with definition (C.29) and definition (C.8) is used to evaluate the integration over $\hat{\boldsymbol{R}}$

$$\frac{d\sigma^{S}_{fv_f,iv_i}}{d\Omega^{(\mathrm{lab})}} = \frac{q_f}{q_i}\frac{1}{4\pi}\sum_{\substack{L_f,L_i\\M_f,M_i}}\sum_{\substack{L'_f,L'_i\\M'_f,M'_i}}(-1)^{-M_f-M_i}\hat{L}_i\hat{L}'_i \tag{B.7}$$

$$\times\langle\nu_{fv_f}|A^{S(\mathrm{b})}_{fL_fM_f,iL_iM_i}|\nu_{iv_i}\rangle_R\langle\nu^*_{fv_f}|A^{S(\mathrm{b})*}_{fL'_fM'_f,iL'_iM'_i}|\nu^*_{iv_i}\rangle_{R'}$$

$$\times\sum_{j'j\kappa\kappa'}(-1)^{\kappa'+\kappa}(2j'+1)(2j+1)\begin{pmatrix}L_i & L'_i & j\\ 0 & 0 & 0\end{pmatrix}\begin{pmatrix}L_i & L'_i & j\\ -M_i & M'_i & M_i-M'_i\end{pmatrix}$$

$$\times\begin{pmatrix}L_f & L'_f & j'\\ \kappa & -\kappa' & \kappa'-\kappa\end{pmatrix}\begin{pmatrix}L_f & L'_f & j'\\ M_f & -M'_f & M'_f-M_f\end{pmatrix}$$

$$\times(4\pi)^{-1}\left(\frac{4\pi}{(2j+1)}\delta_{j,j'}\delta_{0,\kappa-\kappa'}\delta_{M_i-M'_i,M_f-M'_f}\right)$$

$$\times Y_{L_f\kappa}(\hat{\boldsymbol{q}}^{(\mathrm{lab})}_f)Y_{L'_f-\kappa'}(\hat{\boldsymbol{q}}^{(\mathrm{lab})}_f).$$

Now $\delta_{0,\kappa-\kappa'}$ implies $\kappa'=\kappa$, the 3-j symbols are expressed with (C.20) in terms of Clebsch-Gordan coefficients $C^{lm}_{l_1m_1,l_2m_2}$ and the spherical harmonics

are collapsed using (C.33)

$$\frac{d\sigma^{S}_{fv_f,iv_i}}{d\Omega^{(\mathrm{lab})}} = \frac{q_f}{q_i}\frac{1}{4\pi}\sum_{\substack{L_f,L_i\\M_f,M_i}}\sum_{\substack{L'_f,L'_i\\M'_f,M'_i}}(-1)^{-M_f-M_i}\hat{L}_i\hat{L}'_i \tag{B.8}$$

$$\times\langle\nu_{fv_f}|A^{S(\mathrm{b})}_{fL_fM_f,iL_iM_i}|\nu_{iv_i}\rangle_R\langle\nu^*_{fv_f}|A^{S(\mathrm{b})*}_{fL'_fM'_f,iL'_iM'_i}|\nu^*_{iv_i}\rangle_{R'}$$

$$\times\sum_{j\kappa}(2j+1)\left(\frac{(-1)^{3L_i+L'_i}}{\hat{j}}C^{j0}_{L_i0,L'_i0}\right)$$

$$\times\left(\frac{(-1)^{3L_i+L'_i+(M_i-M'_i)}}{\hat{j}}C^{jM'_i-M_i}_{L_i-M_i,L'_iM'_i}\right)$$

$$\times\left(\frac{(-1)^{3L_f+L'_f}}{\hat{j}}C^{j0}_{L_f\kappa,L'_f-\kappa}\right)$$

$$\times\left(\frac{(-1)^{3L_f+L'_f+(M'_f-M_f)}}{\hat{j}}C^{jM_f-M'_f}_{L_fM_f,L'_f-M'_f}\right)$$

$$\times\left(\sum_{j'}\frac{\hat{L}_f\hat{L}'_f}{4\pi}C^{j'0}_{L_f0,L'_f0}C^{j'0}_{L_f\kappa,L'_f-\kappa}P_{j'}(\cos(\theta^{(\mathrm{lab})}))\right)\delta_{M_i-M'_i,M_f-M'_f}$$

$$= \frac{q_f}{q_i}\frac{1}{(4\pi)^2}\sum_{\substack{L_f,L_i\\M_f,M_i}}\sum_{\substack{L'_f,L'_i\\M'_f,M'_i}}(-1)^{M'_f-M'_i}\hat{L}_i\hat{L}'_i\hat{L}_f\hat{L}'_f \tag{B.9}$$

$$\times\langle\nu_{fv_f}|A^{S(\mathrm{b})}_{fL_fM_f,iL_iM_i}|\nu_{iv_i}\rangle_R\langle\nu^*_{fv_f}|A^{S(\mathrm{b})*}_{fL'_fM'_f,iL'_iM'_i}|\nu^*_{iv_i}\rangle_{R'}$$

$$\times\sum_{j'j}(2j+1)^{-1}C^{j0}_{L_i0,L'_i0}C^{jM'_i-M_i}_{L_i-M_i,L'_iM'_i}C^{jM_f-M'_f}_{L_fM_f,L'_f-M'_f}C^{j'0}_{L_f0,L'_f0}$$

$$\times P_{j'}(\cos(\theta^{(\mathrm{lab})}))\delta_{M_i-M'_i,M_f-M'_f}\sum_{\kappa}C^{j0}_{L_f\kappa,L'_f-\kappa}C^{j'0}_{L_f\kappa,L'_f-\kappa}.$$

Summing over κ with the Clebsch-Gordan orthogonality condition (C.21), the final form of the orientation averaged DCS is

$$\begin{aligned}\frac{d\sigma^S_{fv_f,iv_i}}{d\Omega^{(\mathrm{lab})}} &= \frac{q_f}{q_i}\frac{1}{(4\pi)^2}\sum_{\substack{L_f,L_i\\M_f,M_i}}\sum_{\substack{L'_f,L'_i\\M'_f,M'_i}}(-1)^{M'_f-M'_i}\hat{L}_i\hat{L}'_i\hat{L}_f\hat{L}'_f \\ &\times\langle\nu_{fv_f}|A^{S(\mathrm{b})}_{fL_fM_f,iL_iM_i}|\nu_{iv_i}\rangle_R\langle\nu^*_{fv_f}|A^{S(\mathrm{b})*}_{fL'_fM'_f,iL'_iM'_i}|\nu^*_{iv_i}\rangle_{R'} \\ &\times\sum_j(2j+1)^{-1}C^{j0}_{L_i0,L'_i0}C^{jM'_i-M_i}_{L_i-M_i,L'_iM'_i}C^{jM_f-M'_f}_{L_fM_f,L'_f-M'_f}C^{j0}_{L_f0,L'_f0} \\ &\times P_j(\cos(\theta^{(\mathrm{lab})}))\delta_{M_i-M'_i,M_f-M'_f}.\end{aligned} \tag{B.10}$$

The integrated cross section is calculated by integrating over all final angles of the scattered particle

$$\sigma^S_{fv_f,iv_i} = \int_0^{2\pi}d\phi_{q_f}\int_0^{\pi}\sin(\theta_{q_f})\frac{d\sigma^S_{fv_f,iv_i}}{d\Omega^{(\mathrm{lab})}}d\theta_{q_f}. \tag{B.11}$$

Noting that $P^m_0(x) = 1$, definition (C.34) is utilised to integrate over all final angles

$$\int_0^{2\pi}d\phi_{q_f}\int_0^{\pi}P_L(\cos(\theta_{q_f}))\sin(\theta_{q_f})d\theta_{q_f} = 4\pi\delta_{L,0}. \tag{B.12}$$

Utilising (B.12) to integrate over all final angles of the DCS and noting the Clebsch-Gordan coefficient $C^{lm}_{l_1m_1,l_2m_2}$ triangle rule $|m| \leq l$, the orientation averaged integrated cross section is calculated

$$\begin{aligned}\sigma^S_{fv_f,iv_i} &= \int d\Omega_{q_f}\frac{d\sigma^S_{fv_f,iv_i}}{d\Omega^{(\mathrm{lab})}} \\ &= \frac{q_f}{q_i}\frac{1}{4\pi}\sum_{\substack{L_f,L_i\\M_f,M_i}}\sum_{\substack{L'_f,L'_i\\M'_f,M'_i}}(-1)^{M'_f-M'_i}\hat{L}_i\hat{L}'_i\hat{L}_f\hat{L}'_f \\ &\times\langle\nu_{fv_f}|A^{S(\mathrm{b})}_{fL_fM_f,iL_iM_i}|\nu_{iv_i}\rangle_R\langle\nu^*_{fv_f}|A^{S(\mathrm{b})*}_{fL'_fM'_f,iL'_iM'_i}|\nu^*_{iv_i}\rangle_{R'} \\ &\times C^{00}_{L_i0,L'_i0}C^{00}_{L_i-M_i,L'_iM'_i}C^{00}_{L_fM_f,L'_f-M'_f}C^{00}_{L_f0,L'_f0}\delta_{M_i-M'_i,M_f-M'_f}.\end{aligned} \tag{B.13}$$

Using definition (C.25) to evaluate the Clebsch-Gordan coefficients

$$\sigma^{S}_{fv_f,iv_i} = \frac{q_f}{q_i}\frac{1}{4\pi}\sum_{\substack{L_f,L_i\\M_f,M_i}}\sum_{\substack{L'_f,L'_i\\M'_f,M'_i}}(-1)^{M'_f-M'_i}\hat{L}_i\hat{L}'_i\hat{L}_f\hat{L}'_f \tag{B.14}$$
$$\times\langle\nu_{fv_f}|A^{S(\mathrm{b})}_{fL_fM_f,iL_iM_i}|\nu_{iv_i}\rangle_R\langle\nu^*_{fv_f}|A^{S(\mathrm{b})*}_{fL'_fM'_f,iL'_iM'_i}|\nu^*_{iv_i}\rangle_{R'}$$
$$\times\left(\frac{(-1)^{L_i}}{\hat{L}_i}\delta_{L_i,L'_i}\right)\left(\frac{(-1)^{L_i+M_i}}{\hat{L}_i}\delta_{L_i,L'_i}\delta_{M'_i,M_i}\right)$$
$$\times\left(\frac{(-1)^{L_f-M_f}}{\hat{L}_f}\delta_{L_f,L'_f}\delta_{-M'_f,-M_f}\right)\left(\frac{(-1)^{L_f}}{\hat{L}_f}\delta_{L_f,L'_f}\right)\delta_{M_i-M'_i,M_f-M'_f}.$$

The final form of the integrated cross section is

$$\sigma^{S}_{fv_f,iv_i} = \frac{q_f}{q_i}\frac{1}{4\pi}\sum_{\substack{L_f,L_i\\M_f,M_i}}|\langle\nu_{fv_f}|A^{S(\mathrm{b})}_{fL_fM_f,iL_iM_i}|\nu_{iv_i}\rangle_R|^2. \tag{B.15}$$

B.1 Analytic Born cross section

Following from Section 4.4.2 the analytic Born body-frame scattering amplitude for the transition $iv_i \to fv_f$ is defined in Eq. (4.61). The analytic Born lab-frame scattering amplitude is defined as

$$F^{(\mathrm{AB})}_{f,i}(\Omega^{(\mathrm{lab})},\hat{\boldsymbol{R}}^{(\mathrm{lab})}) = \sum_{\lambda\mu}\langle\nu_{fv_f}|A^{(\mathrm{AB})}_{\substack{f,i\\\lambda\mu}}(Q^{(\mathrm{b})})|\nu_{iv_i}\rangle_R \times\sum_{\rho}D^{\lambda*}_{\rho,\mu}(\hat{\boldsymbol{R}}^{(\mathrm{lab})})Y^*_{\lambda\rho}(\hat{\boldsymbol{Q}}^{(\mathrm{lab})}), \tag{B.16}$$

where the momentum transfer $\boldsymbol{Q} = \boldsymbol{q}_i - \boldsymbol{q}_f$ and $A^{(\mathrm{AB})}_{\substack{f,i\\\lambda\mu}}(Q^{(\mathrm{b})})$ is defined by Eq. (4.62). Substituting $F^{(\mathrm{AB})}_{f,i}(\Omega^{(\mathrm{lab})},\hat{\boldsymbol{R}}^{(\mathrm{lab})})$ into the orientation averaged DCS Eq. (B.1), the analytic Born DCS is

$$\frac{d\sigma^{(\mathrm{AB})}_{fv_f,iv_i}}{d\Omega^{(\mathrm{lab})}} = \sum_{\lambda\mu}\sum_{\lambda'\mu'}\langle\nu_{fv_f}|A^{(\mathrm{AB})}_{\substack{f,i\\\lambda\mu}}(Q^{(\mathrm{b})})|\nu_{iv_i}\rangle_R\langle\nu^*_{fv_f}|A^{(\mathrm{AB})*}_{\substack{f,i\\\lambda'\mu'}}(Q^{(\mathrm{b})})|\nu^*_{iv_i}\rangle_{R'} \tag{B.17}$$
$$\times\sum_{\rho\rho'}\frac{1}{4\pi}\int_0^{\pi}\int_0^{2\pi}D^{\lambda*}_{\rho,\mu}(\phi_{\hat{\boldsymbol{R}}},\theta_{\hat{\boldsymbol{R}}},0)D^{\lambda'}_{\rho',\mu'}(\phi_{\hat{\boldsymbol{R}}},\theta_{\hat{\boldsymbol{R}}},0)d\phi_{\hat{\boldsymbol{R}}}\sin(\theta_{\hat{\boldsymbol{R}}})d\theta_{\hat{\boldsymbol{R}}}$$
$$\times Y^*_{\lambda\rho}(\hat{\boldsymbol{Q}}^{(\mathrm{lab})})Y_{\lambda'\rho'}(\hat{\boldsymbol{Q}}^{(\mathrm{lab})}).$$

Utilising definition (C.8) to evaluate the integration over $\hat{\boldsymbol{R}}$

$$\begin{aligned}\frac{d\sigma^{(\mathrm{AB})}_{fv_f,iv_i}}{d\Omega^{(\mathrm{lab})}} &= \sum_{\lambda\mu}\sum_{\lambda'\mu'}\langle\nu_{fv_f}|A^{(\mathrm{AB})}_{\substack{f,i\\ \lambda\mu}}(Q^{(\mathrm{b})})|\nu_{iv_i}\rangle_R\langle\nu^*_{fv_f}|A^{(\mathrm{AB})*}_{\substack{f,i\\ \lambda'\mu'}}(Q^{(\mathrm{b})})|\nu^*_{iv_i}\rangle_{R'} \\ &\quad\times\sum_{\rho\rho'}\frac{1}{4\pi}\left(\frac{4\pi}{(2\lambda+1)}\delta_{\lambda,\lambda'}\delta_{\mu,\mu}\delta_{\rho,\rho'}\right)Y^*_{\lambda\rho}(\hat{\boldsymbol{Q}}^{(\mathrm{lab})})Y_{\lambda'\rho'}(\hat{\boldsymbol{Q}}^{(\mathrm{lab})}) \\ &= \sum_{\lambda\mu}\frac{1}{(2\lambda+1)}|\langle\nu_{fv_f}|A^{(\mathrm{AB})}_{\substack{f,i\\ \lambda\mu}}(Q^{(\mathrm{b})})|\nu_{iv_i}\rangle_R|^2 \\ &\quad\times\sum_{\rho}Y^*_{\lambda\rho}(\hat{\boldsymbol{Q}}^{(\mathrm{lab})})Y_{\lambda\rho}(\hat{\boldsymbol{Q}}^{(\mathrm{lab})}).\end{aligned} \tag{B.18}$$

Summing the spherical harmonics over ρ with definition (C.31), the final form of the analytic Born DCS is

$$\begin{aligned}\frac{d\sigma^{(\mathrm{AB})}_{fv_f,iv_i}}{d\Omega^{(\mathrm{lab})}} &= \sum_{\lambda\mu}\frac{1}{(2\lambda+1)}|\langle\nu_{fv_f}|A^{(\mathrm{AB})}_{\substack{f,i\\ \lambda\mu}}(Q^{(\mathrm{b})})|\nu_{iv_i}\rangle_R|^2\left(\frac{(2\lambda+1)}{4\pi}\right) \\ &= \frac{1}{4\pi}\sum_{\lambda\mu}|\langle\nu_{fv_f}|A^{(\mathrm{AB})}_{\substack{f,i\\ \lambda\mu}}(Q^{(\mathrm{b})})|\nu_{iv_i}\rangle_R|^2.\end{aligned} \tag{B.19}$$

Appendix C

Useful definitions

The following definition have been taken from Varshalovich et al. [252] and Edmonds [212]. In some cases extra definition have been derived.

Varshalovich et al. [252] and Edmonds [212] have different definitions of the Wigner-D functions. Here the following definitions and conventions are taken from Edmonds [212]. These definitions assume integer values of all J's and m's.

$$D^{J}_{m_1,m_2}(\alpha,\beta,\gamma) = e^{-im_1\alpha} d^{J}_{m_1,m_2}(\beta) e^{-im_2\gamma}, \tag{C.1}$$

$$D^{J*}_{m_1,m_2}(\boldsymbol{\beta}) = (-1)^{m_1-m_2} D^{J}_{-m_1,-m_2}(\boldsymbol{\beta}), \tag{C.2}$$

$$D^{J}_{m_1,m_2}(\boldsymbol{\beta}) = (-1)^{m_1-m_2} D^{J*}_{-m_1,-m_2}(\boldsymbol{\beta}), \tag{C.3}$$

$$\begin{aligned} D^{J_1}_{m_1,m_1'}(\boldsymbol{\beta}) D^{J_2}_{m_2,m_2'}(\boldsymbol{\beta}) = \sum_J (2J+1) & \begin{pmatrix} J_1 & J_2 & J \\ m_1 & m_2 & -m_1-m_2 \end{pmatrix} \\ & \times \begin{pmatrix} J_1 & J_2 & J \\ m_1' & m_2' & -m_1'-m_2' \end{pmatrix} D^{J*}_{-m_1-m_2,-m_1'-m_2'}(\boldsymbol{\beta}), \end{aligned} \tag{C.4}$$

$$\begin{aligned} D^{J_1*}_{m_1,m_1'}(\boldsymbol{\beta}) D^{J_2}_{m_2,m_2'}(\boldsymbol{\beta}) &= (-1)^{m_1-m_1'} \sum_J (2J+1) \begin{pmatrix} J_1 & J_2 & J \\ -m_1 & m_2 & m_1-m_2 \end{pmatrix} \\ &\quad \times \begin{pmatrix} J_1 & J_2 & J \\ -m_1' & m_2' & m_1'-m_2' \end{pmatrix} D^{J*}_{m_1-m_2,m_1'-m_2'}(\boldsymbol{\beta}) \\ &= (-1)^{m_2'-m_2} \sum_J (2J+1) \begin{pmatrix} J_1 & J_2 & J \\ m_1 & -m_2 & m_2-m_1 \end{pmatrix} \\ &\quad \times \begin{pmatrix} J_1 & J_2 & J \\ m_1' & -m_2' & m_2'-m_1' \end{pmatrix} D^{J}_{m_2-m_1,m_2'-m_1'}(\boldsymbol{\beta}). \end{aligned} \tag{C.5}$$

$$D^{J_1*}_{m_1,m_1'}(\boldsymbol{\beta})D^{J_2*}_{m_2,m_2'}(\boldsymbol{\beta}) = \sum_J (2J+1)\begin{pmatrix} J_1 & J_2 & J \\ -m_1 & -m_2 & m_1+m_2 \end{pmatrix} \times \begin{pmatrix} J_1 & J_2 & J \\ -m_1' & -m_2' & m_1'+m_2' \end{pmatrix} D^J_{-m_1-m_2,-m_1'-m_2'}(\boldsymbol{\beta}) = \sum_J (2J+1)\begin{pmatrix} J_1 & J_2 & J \\ m_1 & m_2 & -m_1-m_2 \end{pmatrix} \times \begin{pmatrix} J_1 & J_2 & J \\ m_1' & m_2' & -m_1'-m_2' \end{pmatrix} D^J_{-m_1-m_2,-m_1'-m_2'}(\boldsymbol{\beta}), \tag{C.6}$$

$$\int_0^{2\pi}\int_0^{\pi}\int_0^{2\pi} D^{J'*}_{m_1',m_2'}(\alpha,\beta,\gamma)D^J_{m_1,m_2}(\alpha,\beta,\gamma)d\alpha\sin(\beta)d\beta d\gamma = \frac{8\pi^2}{(2J+1)}\delta_{J',J}\delta_{m_1',m_1}\delta_{m_2',m_2}. \tag{C.7}$$

Utilising definition (C.7) and substituting (C.1)

$$\int_0^{2\pi}\int_0^{\pi}\int_0^{2\pi} D^{J'*}_{m_1',m_2'}(\alpha,\beta,0)D^J_{m_1,m_2}(\alpha,\beta,0)d\alpha\sin(\beta)d\beta d\gamma = \frac{8\pi^2}{(2J+1)}\delta_{J',J}\delta_{m_1',m_1}\delta_{m_2',m_2}$$
$$\int_0^{2\pi}d\gamma\int_0^{\pi}\int_0^{2\pi} e^{i(m_1'-m_1)\alpha}d^{J'*}_{m_1',m_2'}(\beta)d^J_{m_1,m_2}(\beta)d\alpha\sin(\beta)d\beta = \frac{8\pi^2}{(2J+1)}\delta_{J',J}\delta_{m_1',m_1}\delta_{m_2',m_2}$$
$$\int_0^{\pi}\int_0^{2\pi} e^{i(m_1'-m_1)\alpha}d^{J'*}_{m_1',m_2'}(\beta)d^J_{m_1,m_2}(\beta)d\alpha\sin(\beta)d\beta = \frac{4\pi}{(2J+1)}\delta_{J',J}\delta_{m_1',m_1}\delta_{m_2',m_2}$$
$$\int_0^{\pi}\int_0^{2\pi} D^{J'*}_{m_1',m_2'}(\alpha,\beta,0)D^J_{m_1,m_2}(\alpha,\beta,0)d\alpha\sin(\beta)d\beta = \frac{4\pi}{(2J+1)}\delta_{J',J}\delta_{m_1',m_1}\delta_{m_2',m_2}. \tag{C.8}$$

From Varshalovich et al. [252]

$$D^{J*}_{m_1,0}(\alpha,\beta,\gamma) = \sqrt{\frac{4\pi}{(2J+1)}}Y_{Jm_1}(\beta,\alpha), \tag{C.9}$$

$$D^{J}_{m_1,0}(\alpha,\beta,\gamma) = \sqrt{\frac{4\pi}{(2J+1)}}Y^*_{Jm_1}(\beta,\alpha). \tag{C.10}$$

Evaluating the common Wigner-D function integral

$$(8\pi^2)^{-1}\int D^{J_1*}_{m_1,m_1'}(\boldsymbol{\beta})D^{J_2*}_{m_2,m_2'}(\boldsymbol{\beta})D^{J_3}_{m_3,m_3'}(\boldsymbol{\beta})D^{J_4}_{m_4,m_4'}(\boldsymbol{\beta})d\boldsymbol{\beta}. \tag{C.11}$$

Using equations (C.6) and (C.4) to reduce $D^{J_1*}_{m_1,m_1'}(\boldsymbol{\beta})D^{J_2*}_{m_2,m_2'}(\boldsymbol{\beta})$ and

$D^{J_3}_{m_3,m'_3}(\boldsymbol{\beta})D^{J_4}_{m_4,m'_4}(\boldsymbol{\beta})$, respectively. Now Eq. (C.11) can be reduced to

$$
\begin{aligned}
&(8\pi^2)^{-1}\int D^{J_1*}_{m_1,m'_1}(\boldsymbol{\beta})D^{J_2*}_{m_2,m'_2}(\boldsymbol{\beta})D^{J_3}_{m_3,m'_3}(\boldsymbol{\beta})D^{J_4}_{m_4,m'_4}(\boldsymbol{\beta})d\boldsymbol{\beta}\\
&\quad=(8\pi^2)^{-1}\sum_{JJ'}(2J+1)(2J'+1)\begin{pmatrix}J_1 & J_2 & J\\ m_1 & m_2 & -m_1-m_2\end{pmatrix}\\
&\quad\times\begin{pmatrix}J_1 & J_2 & J\\ m'_1 & m'_2 & -m'_1-m'_2\end{pmatrix}\begin{pmatrix}J_3 & J_4 & J'\\ m_3 & m_4 & -m_3-m_4\end{pmatrix}\\
&\quad\times\begin{pmatrix}J_3 & J_4 & J'\\ m'_3 & m'_4 & -m'_3-m'_4\end{pmatrix}\\
&\quad\times\int D^{J}_{-m_1-m_2,-m'_1-m'_2}(\boldsymbol{\beta})D^{J'*}_{-m_3-m'_3,-m_4-m'_4}(\boldsymbol{\beta})d\boldsymbol{\beta}.
\end{aligned}
\tag{C.12}
$$

Using the Wigner-D functions normalisation condition (C.7), integral (C.12) now comes

$$
\begin{aligned}
&(8\pi^2)^{-1}\int D^{J_1*}_{m_1,m'_1}(\boldsymbol{\beta})D^{J_2*}_{m_2,m'_2}(\boldsymbol{\beta})D^{J_3}_{m_3,m'_3}(\boldsymbol{\beta})D^{J_4}_{m_4,m'_4}(\boldsymbol{\beta})d\boldsymbol{\beta}\\
&\quad=(8\pi^2)^{-1}\sum_{JJ'}(2J+1)(2J'+1)\begin{pmatrix}J_1 & J_2 & J\\ m_1 & m_2 & -m_1-m_2\end{pmatrix}\\
&\quad\times\begin{pmatrix}J_1 & J_2 & J\\ m'_1 & m'_2 & -m'_1-m'_2\end{pmatrix}\begin{pmatrix}J_3 & J_4 & J'\\ m_3 & m_4 & -m_3-m_4\end{pmatrix}\\
&\quad\times\begin{pmatrix}J_3 & J_4 & J'\\ m'_3 & m'_4 & -m'_3-m'_4\end{pmatrix}\\
&\quad\times\left(\frac{8\pi^2}{(2J+1)}\delta_{J,J'}\delta_{-m_1-m_2,-m_3-m'_3}\delta_{-m'_1-m'_2,-m'_3-m'_4}\right)\\
&\quad=\sum_{J}(2J+1)\begin{pmatrix}J_1 & J_2 & J\\ m_1 & m_2 & -m_1-m_2\end{pmatrix}\begin{pmatrix}J_1 & J_2 & J\\ m'_1 & m'_2 & -m'_1-m'_2\end{pmatrix}\\
&\quad\times\begin{pmatrix}J_3 & J_4 & J\\ m_3 & m_4 & -m_3-m_4\end{pmatrix}\begin{pmatrix}J_3 & J_4 & J\\ m'_3 & m'_4 & -m'_3-m'_4\end{pmatrix}\\
&\quad\times\delta_{-m_1-m_2,-m_3-m_4}\delta_{-m'_1-m'_2,-m'_3-m'_4}\\
&\quad=\sum_{J}(2J+1)\begin{pmatrix}J_2 & J_1 & J\\ m_2 & m_1 & -m_2-m_1\end{pmatrix}\begin{pmatrix}J_2 & J_1 & J\\ m'_2 & m'_1 & -m'_2-m'_1\end{pmatrix}\\
&\quad\times\begin{pmatrix}J_4 & J_3 & J\\ m_4 & m_3 & -m_4-m_3\end{pmatrix}\begin{pmatrix}J_4 & J_3 & J\\ m'_4 & m'_3 & -m'_4-m'_3\end{pmatrix}\\
&\quad\times\delta_{-m_2-m_1,-m_4-m_3}\delta_{-m'_2-m'_1,-m'_4-m'_3}.
\end{aligned}
\tag{C.13}
\tag{C.14}
$$

C.1 Clebsch-Gordan coefficients

These definition are from Varshalovich et al. [252].

$$C^{l_3 m_3}_{l_1 m_1, l_2 m_2} = (-1)^{l_1+l_2-l_3} C^{l_3 -m_3}_{l_1 -m_1, l_2 -m_2} \tag{C.15}$$
$$= (-1)^{l_1+l_2-l_3} C^{l_3 m_3}_{l_2 m_2, l_1 m_1}. \tag{C.16}$$

$$\begin{pmatrix} l_1 & l_2 & l_3 \\ m_1 & m_2 & m_3 \end{pmatrix} = (-1)^{l_1+l_2+l_3} \begin{pmatrix} l_1 & l_2 & l_3 \\ -m_1 & -m_2 & -m_3 \end{pmatrix} \tag{C.17}$$
$$= (-1)^{l_1+l_2+l_3} \begin{pmatrix} l_2 & l_1 & l_3 \\ m_2 & m_1 & m_3 \end{pmatrix} \tag{C.18}$$
$$= \frac{(-1)^{l_3+m_3+2l_1}}{\hat{l}_3} C^{l_3 m_3}_{l_1 -m_1, l_2 -m_2}. \tag{C.19}$$

Substituting (C.15) into (C.19)

$$\begin{pmatrix} l_1 & l_2 & l_3 \\ m_1 & m_2 & m_3 \end{pmatrix} = \frac{(-1)^{3l_1+l_2+m_3}}{\hat{l}_3} C^{l_3 -m_3}_{l_1 m_1, l_2 m_2}. \tag{C.20}$$

$$\sum_{m_1 m_2} C^{l_3 m_3}_{l_1 m_1, l_2 m_2} C^{l'_3 m'_3}_{l_1 m_1, l_2 m_2} = \delta_{l_3, l'_3} \delta_{m_3, m'_3}, \tag{C.21}$$
$$\sum_{m_1 m_3} C^{l_3 m_3}_{l_1 m_1, l_2 m_2} C^{l_3 m_3}_{l_1 m_1, l'_2 m'_2} = \frac{(2l_3+1)}{(2l_2+1)} \delta_{l_2, l'_2} \delta_{m_2, m'_2}, \tag{C.22}$$
$$\sum_{l_3 m_3} C^{l_3 m_3}_{l_1 m_1, l_2 m_2} C^{l_3 m_3}_{l_1 m'_1, l_2 m'_2} = \sum_{l_3} C^{l_3 m_1+m_2}_{l_1 m_1, l_2 m_2} C^{l_3 m'_1+m'_2}_{l_1 m'_1, l_2 m'_2} = \delta_{m_1, m'_1} \delta_{m_2, m'_2}. \tag{C.23}$$

$$C^{l_3 m_3}_{l_1 m_1, l_2 m_2} = (-1)^{l_1 - m_1} \frac{\hat{l}_3}{\hat{l}_2} C^{l_2 -m_2}_{l_1 m_1, l_3 -m_3}. \tag{C.24}$$

$$C^{00}_{l_1 m_1, l_2 m_2} = \frac{(-1)^{l_1 - m_1}}{\hat{l}_1} \delta_{l_1, l_2} \delta_{m_2, -m_1}, \tag{C.25}$$
$$C^{l_3 m_3}_{l_1 m_1, 00} = \delta_{l_1, l_3} \delta_{m_1, m_3}, \tag{C.26}$$
$$C^{l_3 m_3}_{00, l_2 m_2} = \delta_{l_2, l_3} \delta_{m_2, m_3}. \tag{C.27}$$

$$\sum_{m_1 m_2 m_3} (-1)^{l_1-m_1} C^{l_4 m_4}_{l_1 m_1, l_2 m_2} C^{l_5 m_5}_{l_3 m_3, l_2 m_2} C^{l_6 m_6}_{l_3 m_3, l_1 - m_1}$$
$$= (-1)^{l_2+l_4+l_3+l_6} \hat{l}_4 \hat{l}_6 C^{l_5 m_5}_{l_4 m_4, l_6 m_6} \begin{Bmatrix} l_1 & l_2 & l_4 \\ l_5 & l_6 & l_3 \end{Bmatrix}. \quad \text{(C.28)}$$

C.2 Spherical harmonics

The following definitions are from Varshalovich et al. [252].

$$Y^*_{lm}(\Omega) = (-1)^m Y_{l-m}(\Omega). \quad \text{(C.29)}$$

A spherical harmonic with angles $\Omega = (\theta,\phi)$ aligned along the z-axis

$$Y_{lm}\left(\pm\pi, \frac{\pi}{2}\right) = (-1)^l \sqrt{\frac{(2l+1)}{4\pi}} \delta_{m,0}. \quad \text{(C.30)}$$

$$\sum_{m=-l}^{l} Y_{lm}(\Omega) Y^*_{lm}(\Omega) = \frac{(2l+1)}{4\pi}, \quad \text{(C.31)}$$

$$Y_{l_1 m_1}(\Omega) Y_{l_2 m_2}(\Omega) = \sum_{l_3 m_3} \frac{\hat{l}_1 \hat{l}_2}{\sqrt{4\pi}\hat{l}_3} C^{l_3 0}_{l_1 0, l_2 0} C^{l_3 m_3}_{l_1 m_1, l_2 m_2} Y_{l_3 m_3}(\Omega), \quad \text{(C.32)}$$

$$Y_{l_1 m_1}(\Omega) Y_{l_2 - m_1}(\Omega) = \sum_{l_3} \frac{\hat{l}_1 \hat{l}_2}{4\pi} C^{l_3 0}_{l_1 0, l_2 0} C^{l_3 0}_{l_1 m_1, l_2 - m_1} P_{l_3}(\cos(\theta)). \quad \text{(C.33)}$$

$$\int_0^\pi P^m_j(\cos(\theta)) P^m_{j'}(\cos(\theta)) = \frac{2(j+m)!}{(2j+1)(j-m)!} \delta_{j,j'}. \quad \text{(C.34)}$$

$$\sum_{lm} Y_{lm}(\hat{r}_1) Y_{lm}(\hat{r}_2) = \delta(\hat{r}_1 - \hat{r}_2) \quad \text{(C.35)}$$
$$= \delta(\phi_1 - \phi_2)\delta(\cos(\theta_1) - \cos(\theta_2)). \quad \text{(C.36)}$$

$$\sqrt{\frac{4\pi}{2l_2+1}}\langle Y_{l_1m_1}(\hat{r})|Y_{l_2m_2}(\hat{r})|Y_{l_3m_3}(\hat{r})\rangle \tag{C.37}$$

$$= \sqrt{\frac{4\pi}{2l_2+1}}\int d\hat{r}Y^*_{l_1m_1}(\hat{r})Y_{l_2m_2}(\hat{r})Y_{l_3m_3}(\hat{r})$$

$$= (-1)^{m_1}\sqrt{\frac{4\pi}{2l_2+1}}\int_0^{2\pi}d\phi\int_0^{\pi}\sin(\theta)d\theta Y_{l_1-m_1}(\theta,\phi)Y_{l_2m_2}(\theta,\phi)Y_{l_3m_3}(\theta,\phi)$$

$$= (-1)^{m_1}\sqrt{\frac{4\pi}{2l_2+1}}\left(\frac{\hat{l}_1\hat{l}_2\hat{l}_3}{\sqrt{4\pi}}\begin{pmatrix}l_1 & l_2 & l_3\\ 0 & 0 & 0\end{pmatrix}\begin{pmatrix}l_1 & l_2 & l_3\\ -m_1 & m_2 & m_3\end{pmatrix}\right)$$

$$= (-1)^{m_1}\hat{l}_1\hat{l}_3\begin{pmatrix}l_1 & l_2 & l_3\\ 0 & 0 & 0\end{pmatrix}\begin{pmatrix}l_1 & l_2 & l_3\\ -m_1 & m_2 & m_3\end{pmatrix}. \tag{C.38}$$

Some of the alternative representations of (C.37) and hence (C.38) are

$$= (-1)^{m_1}\hat{l}_1\hat{l}_3\begin{pmatrix}l_1 & l_2 & l_3\\ 0 & 0 & 0\end{pmatrix}\begin{pmatrix}l_1 & l_2 & l_3\\ -m_1 & m_2 & m_3\end{pmatrix}$$

$$= (-1)^{m_1}\hat{l}_1\hat{l}_3\left(\frac{(-1)^{l_3+2l_1}}{\hat{l}_3}C^{l_30}_{l_10,l_20}\right)\left(\frac{(-1)^{l_3+m_3+2l_1}}{\hat{l}_3}C^{l_3m_3}_{l_1m_1,l_2-m_2}\right)$$

$$= (-1)^{m_1+2l_3+m_3}\frac{\hat{l}_1}{\hat{l}_3}C^{l_30}_{l_10,l_20}C^{l_3m_3}_{l_1m_1,l_2-m_2}, \tag{C.39}$$

or,

$$= (-1)^{m_1}\hat{l}_1\hat{l}_3\begin{pmatrix}l_1 & l_2 & l_3\\ 0 & 0 & 0\end{pmatrix}\begin{pmatrix}l_1 & l_2 & l_3\\ -m_1 & m_2 & m_3\end{pmatrix}$$

$$= (-1)^{m_1}\hat{l}_1\hat{l}_3\begin{pmatrix}l_1 & l_2 & l_3\\ 0 & 0 & 0\end{pmatrix}\left((-1)^{l_1+l_2+l_3}\begin{pmatrix}l_2 & l_1 & l_3\\ m_2 & -m_1 & m_3\end{pmatrix}\right)$$

$$= (-1)^{m_1+l_1+l_2+l_3}\hat{l}_1\hat{l}_3\begin{pmatrix}l_1 & l_2 & l_3\\ 0 & 0 & 0\end{pmatrix}\left(\begin{pmatrix}l_3 & l_2 & l_1\\ m_3 & m_2 & -m_1\end{pmatrix}\right)$$

$$= (-1)^{m_1+l_1+l_2+l_3}\hat{l}_1\hat{l}_3\left(\frac{(-1)^{3l_1+l_2}}{\hat{l}_3}C^{l_30}_{l_10,l_20}\right)\left(\frac{(-1)^{3l_3+l_2-m_1}}{\hat{l}_1}C^{l_1m_1}_{l_3m_3,l_2m_2}\right)$$

$$= (-1)^{3l_2}C^{l_30}_{l_10,l_20}C^{l_1m_1}_{l_3m_3,l_2m_2}. \tag{C.40}$$

$$\nabla = \frac{\partial}{\partial x}\hat{x} + \frac{\partial}{\partial y}\hat{y} + \frac{\partial}{\partial z}\hat{z} = \tag{C.41}$$

$$= \frac{\partial}{\partial r}\hat{r} + \frac{1}{r}\frac{\partial}{\partial \theta}\hat{\theta} + \frac{1}{r\sin(\theta)}\frac{\partial}{\partial \phi}\hat{\phi}. \tag{C.42}$$

Bibliography

[1] D. R. Bates, K. Ledsham, and A. L. Stewart, Proc. R. Soc. A **246**, 215 (1953).

[2] D. R. Bates, J. Chem. Phys. **19**, 1122 (1951).

[3] D. M. Bishop and L. M. Cheung, J. Phys. B **11**, 3133 (1978).

[4] D. R. Bates, R. T. S. Darling, S. C. Hawe, and A. L. Stewart, Proc. Phys. Soc. A **67**, 533 (1954).

[5] W. Kolos, K. Szalewicz, and H. J. Monkhorst, J. Chem. Phys. **84**, 3278 (1986).

[6] L. Wolniewicz and K. Dressler, J. Chem. Phys. **88**, 3861 (1988).

[7] W. Kolos and L. Wolniewicz, J. Chem. Phys. **46**, 1426 (1967).

[8] J. W. Liu and S. Hagstrom, Phys. Rev. A **48**, 166 (1993).

[9] T. E. Sharp, At. Data Nucl. Data Tables **2**, 119 (1970).

[10] S. E. Branchett and J. Tennyson, J. Phys. B **25**, 2017 (1992).

[11] W. Kolos and L. Wolniewicz, J. Chem. Phys. **49**, 404 (1968).

[12] F. von Busch and G. H. Dunn, Phys. Rev. A **5**, 1726 (1972).

[13] D. Wünderlich and U. Fantz, At. Data Nucl. Data Tables **97**, 152 (2011).

[14] J. S. Savage, D. V. Fursa, M. C. Zammit, and I. Bray, J. Phys. Conference Series **488**, 052016 (2014).

[15] I. Bray, I. E. McCarthy, J. Wigley, and A. T. Stelbovics, J. Phys. B **26**, L831 (1993).

[16] B. Peart, D. S. Walton, and K. T. Dolder, J. Phys. B **2**, 1347 (1969).

[17] M. S. Pindzola, F. Robicheaux, and J. Colgan, J. Phys. B **38**, L285 (2005).

[18] J. M. Peek, Physical Review **134**, A877 (1964).

[19] J. M. Peek and T. A. Green, Phys. Rev. **183**, 202 (1969).

[20] J. M. Peek, Phys. Rev. A **10**, 539 (1974).

[21] B. Peart and K. T. Dolder, J. Phys. B **4**, 1496 (1971).

[22] M. O. A. E. Ghazaly, J. Jureta, X. Urbain, and P. Defrance, J. Phys. B **37**, 2467 (2004).

[23] G. H. Dunn, B. Van Zyl, and R. N. Zare, Phys. Rev. Lett. **15**, 610 (1965).

[24] G. H. Dunn and B. Van Zyl, Phys. Rev. **154**, 40 (1967).

[25] D. F. Dance, M. F. A. Harrison, R. D. Rundel, and A. C. H. Smith, Proc. Phys. Soc. **92**, 577 (1967).

[26] B. Peart and K. T. Dolder, J. Phys. B **6**, 2409 (1973).

[27] L. H. Andersen, P. J. Johnson, D. Kella, H. B. Pedersen, and L. Vejby-Christensen, Phys. Rev. A **55**, 2799 (1997).

[28] J.-Y. Zhang, J. Mitroy, and K. Varga, Phys. Rev. Lett. **103**, 223202 (2009).

[29] J. Y. Zhang and J. Mitroy, Phys. Rev. A **83**, 022711 (2011).

[30] W. Tenfen, K. T. Mazon, S. E. Michelin, and F. Arretche, Phys. Rev. A **86**, 042706 (2012).

[31] R. Zhang, K. L. Baluja, J. Franz, and J. Tennyson, J. Phys. B **44**, 035203 (2011).

[32] S. d. A. Sanchez and M. A. P. Lima, Nucl. Instr. and Meth. B **266**, 447 (2008).

[33] D. D. Reid, W. B. Klann, and J. M. Wadehra, Phys. Rev. A **70**, 062714 (2004).

[34] F. A. Gianturco and T. Mukherjee, Phys. Rev. A **64**, 024703 (2001).

[35] J. R. Machacek, E. K. Anderson, C. Makochekanwa, S. J. Buckman, and J. P. Sullivan, Phys. Rev. A **88**, 042715 (2013).

[36] G. P. Karwasz, D. Pliszka, and R. S. Brusa, Nucl. Instr. and Meth. B **247**, 68 (2006).

[37] A. Zecca, L. Chiari, A. Sarkar, K. L. Nixon, and M. J. Brunger, Phys. Rev. A **80**, 032702 (2009).

[38] K. R. Hoffman, M. S. Dababneh, Y. F. Hsieh, W. E. Kauppila, V. Pol, J. H. Smart, and T. S. Stein, Phys. Rev. A **25**, 1393 (1982).

[39] M. Charlton, T. C. Griffith, G. R. Heyland, and G. L. Wright, J. Phys. B **13**, L353 (1980).

[40] S. Zhou, H. Li, W. E. Kauppila, C. K. Kwan, and T. S. Stein, Phys. Rev. A **55**, 361 (1997).

[41] A. Deuring, K. Floeder, D. Fromme, W. Raith, A. Schwab, G. Sinapius, P. W. Zitzewitz, and J. Krug, J. Phys. B **16**, 1633 (1983).

[42] M. T. d. N. Varella and M. A. P. Lima, Phys. Rev. A **76**, 052701 (2007).

[43] J. P. Sullivan, S. J. Gilbert, J. P. Marler, L. D. Barnes, S. J. Buckman, and C. M. Surko, Nucl. Instr. and Meth. B **192**, 3 (2002).

[44] D. Fromme, G. Kruse, W. Raith, and G. Sinapius, J. Phys. B **21**, L261 (1988).

[45] J. Moxom, G. Laricchia, and M. Charlton, J. Phys. B **26**, L367 (1993).

[46] F. M. Jacobsen, N. P. Frandsen, H. Knudsen, and U. Mikkelsen, J. Phys. B **28**, 4675 (1995).

[47] H. Knudsen, L. Brun-Nielsen, M. Charlton, and M. R. Poulsen, J. Phys. B **23**, 3955 (1990).

[48] J. L. S. Lino, J. S. E. Germano, and M. A. P. Lima, J. Phys. B **27**, 1881 (1994).

[49] F. Arretche and M. A. P. Lima, Phys. Rev. A **74**, 042713 (2006).

[50] R. K. Janev, Atomic and Plasma-Material Interaction Data for Fusion **9**, 1 (2001).

[51] S. Matt, T. Fiegele, G. Senn, K. Becker, H. Deutsch, O. Echt, A. Stamatovic, P. Scheier, and T. D. Märk, Atomic and Plasma-Material Interaction Data for Fusion **9**, 11 (2001).

[52] R. Celiberto, M. Capitelli, and A. Laricchiuta, Phys. Scr. **2002**, 32 (2002).

[53] R. Janev, D. Reiter, and U. Samm (2003), URL *http://www.eirene.de/reports/report_4105.pdf*.

[54] J. Meyer, F. Eder, S. Kurasch, V. Skakalova, J. Kotakoski, H. Park, S. Roth, A. Chuvilin, S. Eyhusen, G. Benner, et al., Phys. Rev. Lett. **108**, 196102 (2012).

[55] Q.-B. Lu, Phys. Rep. **487**, 141 (2010).

[56] J. L. Fox, M. I. Galand, and R. E. Johnson, Space Sci. Rev. **139**, 3 (2008).

[57] D. L. Huestis, S. W. Bougher, J. L. Fox, M. Galand, R. E. Johnson, J. I. Moses, and J. C. Pickering, Space Sci. Rev. **139**, 63 (2008).

[58] S. W. Bougher, P.-L. Blelly, M. Combi, J. L. Fox, I. Mueller-Wodarg, A. Ridley, and R. G. Roble, Space Sci. Rev. **139**, 107 (2008).

[59] M. Inokuti and M. J. Berger, Nucl. Instrum. Meth. B **27**, 249 (1987).

[60] M. Inokuti, M. A. Dillon, and M. Kimura, Int. J. Quantum Chem. **32**, 251 (1987).

[61] M. J. Berger and L. Paul, *Chapter 7 in Atomic and molecular data for radiotherapy and radiation research* (International Atomic Energy Agency, Vienna, 1995).

[62] L. Sanche, Eur. Phys. J. D **35**, 367 (2005).

[63] B. Boudaïffa, P. Cloutier, D. Hunting, M. A. Huels, and L. Sanche, Science **287**, 1658 (2000).

[64] I. Baccarelli, I. Bald, F. A. Gianturco, E. Illenberger, and J. Kopyra, Phys. Rep. **508**, 1 (2011).

[65] R. White, W. Tattersall, G. Boyle, R. Robson, S. Dujko, Z. Petrovic, A. Bankovic, M. Brunger, J. Sullivan, S. Buckman, et al., Appl. Radiat. Isotopes **83, Part B**, 77 (2014).

[66] G. J. Boyle, W. J. Tattersall, D. G. Cocks, S. Dujko, and R. D. White, Phys. Rev. A **91**, 052710 (2015).

[67] G. J. Schulz, Rev. Mod. Phys. **45**, 423 (1973).

[68] M. Stroe and M. Fifirig, J. Phys. B **42**, 205203 (2009).

[69] J. Tennyson, Phys. Rep. **491**, 29 (2010).

[70] G. J. Schulz, Rev. Mod. Phys. **45**, 378 (1973).

[71] S. J. Buckman and C. W. Clark, Rev. Mod. Phys. **66**, 539 (1994).

[72] T. Andersen, Phys. Rep. **394**, 157 (2004).

[73] K. Bartschat, I. Bray, P. G. Burke, and M. P. Scott, J. Phys. B **29**, 5493 (1996).

[74] S. B. Zhang, J. G. Wang, and R. K. Janev, Phys. Rev. Lett. **104**, 023203 (2010).

[75] E. T. Hudson, K. Bartschat, M. P. Scott, P. G. Burke, and V. M. Burke, J. Phys. B **29**, 5513 (1996).

[76] J. Gao, J. L. Peacher, and D. H. Madison, J. Chem. Phys. **123**, 204302 (2005).

[77] D. H. Madison and O. Al-Hagan, J. Atom. Mol. Opt. Phys. **2010**, 367180 (2010).

[78] A. Zecca, L. Chiari, G. García, F. Blanco, E. Trainotti, and M. J. Brunger, J. Phys. B **43**, 215204 (2010).

[79] A. G. Sanz, M. C. Fuss, F. Blanco, F. Sebastianelli, F. A. Gianturco, and G. García, J. Chem. Phys. **137**, 124103 (2012).

[80] M. C. Fuss, A. G. Sanz, F. Blanco, P. Limão Vieira, M. J. Brunger, and G. García, Eur. Phys. J. D **68**, 161 (2014).

[81] J. Gao, D. H. Madison, and J. L. Peacher, Phys. Rev. A **72**, 032721 (2005).

[82] J. Gao, D. H. Madison, and J. L. Peacher, J. Chem. Phys. **123**, 204314 (2005).

[83] A. Senftleben, T. Pflüger, X. Ren, O. Al-Hagan, B. Najjari, D. Madison, A. Dorn, and J. Ullrich, J. Phys. B **43**, 081002 (2010).

[84] Y. Itikawa and N. Mason, Phys. Rep. **414**, 1 (2005).

[85] S. Mazevet, M. A. Morrison, O. Boydstun, and R. K. Nesbet, J. Chem. Phys. **32**, 1269 (1999).

[86] M. Morrison, R. Crompton, B. Saha, and Z. Petrovic, Aust. J. Phys. **40**, 239 (1987).

[87] A. Florescu-Mitchell and J. Mitchell, Phys. Rep. **430**, 277 (2006).

[88] K. Takatsuka and V. McKoy, Phys. Rev. A **30**, 1734 (1984).

[89] T. Rescigno, C. McCurdy, A. Orel, and I. Lengsfield, B.H., in *Computational Methods for Electron-Molecule Collisions*, edited by W. Huo and F. Gianturco (Springer US, 1995), pp. 1–44.

[90] M. S. Pindzola, F. Robicheaux, S. D. Loch, J. C. Berengut, T. Topcu, J. Colgan, M. Foster, D. C. Griffin, C. P. Ballance, D. R. Schultz, et al., J. Phys. B **40**, R39 (2007).

[91] M. C. Zammit, D. V. Fursa, and I. Bray, Phys. Rev. A **90**, 022711 (2014).

[92] R. F. da Costa, F. J. da Paixão, and M. A. P. Lima, J. Phys. B **38**, 4363 (2005).

[93] R. F. da Costa and M. A. P. Lima, Phys. Rev. A **75**, 022705 (2007).

[94] J. D. Gorfinkiel and J. Tennyson, J. Phys. B **38**, 1607 (2005).

[95] R. R. Lucchese, K. Takatsuka, and V. McKoy, Phys. Rep. **131**, 147 (1986).

[96] K. Takatsuka and V. McKoy, Phys. Rev. A **24**, 2473 (1981).

[97] L. Mu-Tao, K. Takatsuka, and V. McKoy, J. Phys. B **14**, 4115 (1981).

[98] J. M. Blatt and J. D. Jackson, Phys. Rev. **76**, 18 (1949).

[99] K. Takatsuka and V. McKoy, Phys. Rev. A **23**, 2352 (1981).

[100] M. A. P. Lima and V. McKoy, Phys. Rev. A **38**, 501 (1988).

[101] K. Takatsuka, R. R. Lucchese, and V. McKoy, Phys. Rev. A **24**, 1812 (1981).

[102] R. R. Lucchese, G. Raseev, and V. McKoy, Phys. Rev. A **25**, 2572 (1982).

[103] H. Cho, Y. S. Park, E. A. y Castro, G. L. C. de Souza, I. Iga, L. E. Machado, L. M. Brescansin, and M.-T. Lee, J. Phys. B **41**, 045203 (2008).

[104] L. M. Brescansin, L. E. Machado, M.-T. Lee, H. Cho, and Y. S. Park, J. Phys. B **41**, 185201 (2008).

[105] R. F. da Costa, F. J. da Paixão, and M. A. P. Lima, J. Phys. B **37**, L129 (2004).

[106] F. Arretche, R. da Costa, S. d'A. Sanchez, A. Hisi, E. de Oliveira, M. do N. Varella, and M. Lima, Nucl. Instr. and Meth. B **247**, 13 (2006).

[107] M. H. F. Bettega, L. G. Ferreira, and M. A. P. Lima, Phys. Rev. A **47**, 1111 (1993).

[108] M. A. Khakoo, J. Muse, K. Ralphs, R. F. da Costa, M. H. F. Bettega, and M. A. P. Lima, Phys. Rev. A **81**, 062716 (2010).

[109] M. A. Khakoo, J. Blumer, K. Keane, C. Campbell, H. Silva, M. C. A. Lopes, C. Winstead, V. McKoy, R. F. da Costa, L. G. Ferreira, et al., Phys. Rev. A **77**, 042705 (2008).

[110] J. S. E. Germano and M. A. P. Lima, Phys. Rev. A **47**, 3976 (1993).

[111] P. Chaudhuri, M. T. do N. Varella, C. R. C. de Carvalho, and M. A. P. Lima, Phys. Rev. A **69**, 042703 (2004).

[112] E. P. da Silva, M. T. d. N. Varella, and M. A. P. Lima, Phys. Rev. A **72**, 062715 (2005).

[113] S. d. Sanchez, F. Arretche, and M. A. P. Lima, Phys. Rev. A **77**, 054703 (2008).

[114] F. Arretche, K. T. Mazon, S. E. Michelin, M.-T. Lee, and M. A. P. Lima, Phys. Rev. A **77**, 042708 (2008).

[115] M. H. F. Bettega, S. d'A. Sanchez, M. T. do N. Varella, M. A. P. Lima, L. Chiari, A. Zecca, E. Trainotti, and M. J. Brunger, Phys. Rev. A **86**, 022709 (2012).

[116] L. Chiari, A. Zecca, E. Trainotti, M. H. F. Bettega, S. d. Sanchez, M. T. d. N. Varella, M. A. P. Lima, and M. J. Brunger, Phys. Rev. A **87**, 032707 (2013).

[117] W. Kohn, Phys. Rev. **74**, 1763 (1948).

[118] T. Kato, Prog. Theor. Phys. **6**, 394 (1951).

[119] J. N. Cooper, M. Plummer, and E. A. G. Armour, J. Phys. A: Math. Theor. **43**, 175302 (2010).

[120] B. I. Schneider and T. N. Rescigno, Phys. Rev. A **37**, 3749 (1988).

[121] S. D. Parker, W. McCurdy, T. N. Rescigno, and B. H. Legsfield, Phys. Rev. A **43**, 3514 (1991).

[122] T. N. Rescigno and A. E. Orel, Phys. Rev. A **88**, 012703 (2013).

[123] C.-Y. Lin, C. W. McCurdy, and T. N. Rescigno, Phys. Rev. A **89**, 012703 (2014).

[124] B. H. Lengsfield, T. N. Rescigno, and C. W. McCurdy, Phys. Rev. A **44**, 4296 (1991).

[125] C.-Y. Lin, C. W. McCurdy, and T. N. Rescigno, Phys. Rev. A **89**, 052718 (2014).

[126] T. N. Rescigno, B. H. Lengsfield, C. W. McCurdy, and S. D. Parker, Phys. Rev. A **45**, 7800 (1992).

[127] T. N. Rescigno, A. E. Orel, and C. W. McCurdy, Phys. Rev. A **56**, 2855 (1997).

[128] C. S. Trevisan, A. E. Orel, and T. N. Rescigno, Phys. Rev. A **74**, 042716 (2006).

[129] C. S. Trevisan, A. E. Orel, and T. N. Rescigno, J. Phys. B **39**, L255 (2006).

[130] E. Armour, Phys. Rep. **169**, 1 (1988).

[131] E. A. G. Armour, D. J. Baker, and M. Plummer, J. Phys. B **23**, 3057 (1990).

[132] J. N. Cooper, E. A. G. Armour, and M. Plummer, J. Phys. B **41**, 245201 (2008).

[133] E. A. G. Armour and M. Plummer, J. Phys. B **24**, 4463 (1991).

[134] S. E. Branchett, J. Tennyson, and L. A. Morgan, J. Phys. B **23** (1990).

[135] S. E. Branchett, J. Tennyson, and L. A. Morgan, J. Phys. B **24**, 3479 (1991).

[136] C. S. Trevisan and J. Tennyson, J. Phys. B **34**, 2935 (2001).

[137] R. Zhang, A. Faure, and J. Tennyson, Phys. Scr. **80**, 015301 (2009).

[138] W. J. Brigg, J. Tennyson, and M. Plummer, J. Phys. B **47**, 185203 (2014).

[139] A. Dora, J. Tennyson, L. Bryjko, and T. van Mourik, J. Chem. Phys. **130**, 164307 (2009).

[140] G. Halmová and J. Tennyson, Phys. Rev. Lett. **100**, 213202 (2008).

[141] G. Halmová, J. D. Gorfinkiel, and J. Tennyson, J. Phys. B **41**, 155201 (2008).

[142] B. I. Schneider, M. LeDourneuf, and P. G. Burke, J. Phys. B **12**, L365 (1979).

[143] K. Pfingst, H. T. Thummel, and S. D. Peyerimhoff, J. Phys. B **25**, 2107 (1992).

[144] B. M. Nestmann and T. Beyer, Chem. Phys. **343**, 281 (2008), ISSN 0301-0104.

[145] L. A. Morgan, J. Phys. B **19**, L439 (1986).

[146] O. Zatsarinny, Comp. Phys. Comm. **174**, 273 (2006).

[147] O. Zatsarinny and K. Bartschat, J. Phys. B **46**, 112001 (2013).

[148] O. Zatsarinny and K. Bartschat, Phys. Rev. A **85**, 062709 (2012).

[149] O. Zatsarinny and K. Bartschat, Phys. Rev. A **85**, 062710 (2012).

[150] I. Sànchez and F. Martín, J. Phys. B **30**, 679 (1997).

[151] H. Bachau, E. Cormier, P. Decleva, J. E. Hansen, and F. Martin, Rep. Prog. Phys. **64**, 1815 (2001).

[152] E. S. Chang and U. Fano, Phys. Rev. A **6**, 173 (1972).

[153] M. Duca and M. Fifirig, Cent. Eur. J. Phys. **8**, 87 (2010).

[154] V. Ngassam, A. Florescu, L. Pichl, I. Schneider, O. Motapon, and A. Suzor-Weiner, Eur. Phys. J. D **26**, 165 (2003).

[155] M. Fifirig and M. Stroe, J. Phys. B **44**, 085202 (2011).

[156] K. Chakrabarti, D. R. Backodissa-Kiminou, N. Pop, J. Z. Mezei, O. Motapon, F. Lique, O. Dulieu, A. Wolf, and I. F. Schneider, Phys. Rev. A **87**, 022702 (2013).

[157] H. Takagi, Phys. Rev. A **70**, 022709 (2004).

[158] S. Niyonzima, F. Lique, K. Chakrabarti, A. Larson, A. E. Orel, and I. F. Schneider, Phys. Rev. A **87**, 022713 (2013).

[159] V. Kokoouline and C. H. Greene, Phys. Rev. A **68**, 012703 (2003).

[160] O. Motapon, N. Pop, F. Argoubi, J. Z. Mezei, M. D. E. Epee, A. Faure, M. Telmini, J. Tennyson, and I. F. Schneider, Phys. Rev. A **90**, 012706 (2014).

[161] O. Motapon, F. O. W. Tamo, X. Urbain, and I. F. Schneider, Phys. Rev. A **77**, 052711 (2008).

[162] M. S. Pindzola, F. Robicheaux, S. D. Loch, and J. P. Colgan, Phys. Rev. A **73**, 052706 (2006).

[163] M. S. Pindzola, S. A. Abdel-Naby, J. A. Ludlow, F. Robicheaux, and J. Colgan, Phys. Rev. A **85**, 012704 (2012).

[164] J. Colgan, M. S. Pindzola, F. Robicheaux, C. Kaiser, A. J. Murray, and D. H. Madison, Phys. Rev. Lett. **101**, 233201 (2008).

[165] J. Colgan, O. Al-Hagan, D. H. Madison, C. Kaiser, A. J. Murray, and M. S. Pindzola, Phys. Rev. A **79**, 052704 (2009).

[166] X. Ren, T. Pflüger, S. Xu, J. Colgan, M. S. Pindzola, A. Senftleben, J. Ullrich, and A. Dorn, Phys. Rev. Lett. **109**, 123202 (2012).

[167] J. Colgan, M. S. Pindzola, and F. Robicheaux, J. Phys. B **37**, L377 (2004).

[168] T. J. Reddish, J. Colgan, P. Bolognesi, L. Avaldi, M. Gisselbrecht, M. Lavollée, M. S. Pindzola, and A. Huetz, Phys. Rev. Lett. **100**, 193001 (2008).

[169] J. Colgan, T. J. Reddish, A. Huetz, P. Bolognesi, L. Avaldi, M. Gisselbrecht, M. Lavollèe, and M. S. Pindzola, J. Phys. Conference Series **141**, 012004 (2008).

[170] M. C. Zammit, D. V. Fursa, and I. Bray, Phys. Rev. A **87**, 020701 (2013).

[171] M. C. Zammit, D. V. Fursa, and I. Bray, Phys. Rev. A **88**, 062709 (2013).

[172] J. M. Peek, Phys. Rev. **140**, A11 (1965).

[173] J. M. Peek, Phys. Rev. **154**, 52 (1967).

[174] J. W. Liu, J. Phys. B **22**, 2605 (1989).

[175] M. J. Brunger and S. J. Buckman, Phys. Rep. **367**, 215 (2002).

[176] S. Trajmar, D. Register, and A. Chutjian, Phys. Rep. **97**, 219 (1983).

[177] H. Tawara, Y. Itikawa, H. Nishimura, and M. Yoshino, J. Phys. Chem. Ref. Data **19**, 617 (1990).

[178] J.-S. Yoon, M.-Y. Song, J.-M. Han, S. H. Hwang, W.-S. Chang, B. Lee, and Y. Itikawa, J. Phys. Chem. Ref. Data **37**, 913 (2008).

[179] J.-S. Yoon, Y.-W. Kim, D.-C. Kwon, M.-Y. Song, W.-S. Chang, C.-G. Kim, V. Kumar, and B. Lee, Phys. Rep. **73**, 116401 (2010).

[180] J. Wrkich, D. Mathews, I. Kanik, S. Trajmar, and M. A. Khakoo, J. Phys. B **35**, 4695 (2002).

[181] H. Kato, H. Kawahara, M. Hoshino, H. Tanaka, L. Campbell, and M. J. Brunger, Phys. Rev. A **77**, 062708 (2008).

[182] M. Tashiro, K. Morokuma, and J. Tennyson, Phys. Rev. A **74**, 022706 (2006).

[183] M. Charlton, T. C. Griffith, G. R. Heyland, and G. L. Wright, J. Phys. B **16**, 323 (1983).

[184] K. L. Baluja and A. Jain, Phys. Rev. A **45**, 7838 (1992).

[185] J. P. Sullivan, J. P. Marler, S. J. Gilbert, S. J. Buckman, and C. M. Surko, Phys. Rev. Lett. **87**, 073201 (2001).

[186] C. M. Surko, G. F. Gribakin, and S. J. Buckman, J. Phys. B **38**, R57 (2005).

[187] A. Zecca, L. Chiari, A. Sarkar, and M. J. Brunger, New J. Phys. **13** (2011).

[188] G. Danby and J. Tennyson, J. Phys. B **24**, 3517 (1991).

[189] C. R. de Carvalho, M. T. N. Varella, M. A. Lima, E. P. da Silva, and J. S. Germano, Nucl. Instr. and Meth. B **171**, 33 (2000).

[190] F. Arretche, K. Mazon, S. Michelin, M. Fujimoto, I. Iga, and M.-T. Lee, Nucl. Instr. and Meth. B **266**, 441 (2008).

[191] J. Tennyson and L. Morgan, J. Phys. B **20**, L641 (1987).

[192] H. Bluhme, N. P. Frandsen, F. M. Jacobsen, H. Knudsen, J. Merrison, K. Paludan, and M. R. Poulsen, J. Phys. B **31**, 4631 (1998).

[193] J. P. Marler and C. M. Surko, Phys. Rev. A **72**, 062713 (2005).

[194] G. Laricchia, J. Moxom, and M. Charlton, Phys. Rev. Lett. **70**, 3229 (1993).

[195] I. Bray and A. T. Stelbovics, Phys. Rev. A **46**, 6995 (1992).

[196] I. Bray, Phys. Rev. A **49**, 1066 (1994).

[197] I. Bray and D. V. Fursa, Phys. Rev. Lett. **76**, 2674 (1996).

[198] I. Bray, Phys. Rev. Lett. **89**, 273201 (2002).

[199] I. Bray, D. V. Fursa, A. S. Kheifets, and A. T. Stelbovics, J. Phys. B **35**, R117 (2002).

[200] D. V. Fursa and I. Bray, Phys. Rev. Lett. **100**, 113201 (2008).

[201] C. J. Bostock, D. V. Fursa, and I. Bray, Phys. Rev. A **89**, 032712 (2014).

[202] C. J. Bostock, J. Phys. B **44**, 083001 (2011).

[203] I. Bray, D. V. Fursa, A. S. Kadyrov, A. T. Stelbovics, A. S. Kheifets, and A. M. Mukhamedzhanov, Phys. Rep. **520**, 135 (2012).

[204] D. V. Fursa and I. Bray, New J. Phys. **14**, 035002 (2012).

[205] B. H. Bransden, *Atomic collision theory*, Lecture notes and supplements in physics (Benjamin/Cummings, Reading, Massachusetts, 1983), 2nd ed.

[206] J. M. Brown and A. Carrington, *Rotational Spectroscopy of Diatomic Molecules* (Cambridge University Press, 2003).

[207] D. M. Bishop and L. M. Cheung, Phys. Rev. A **16**, 640 (1977).

[208] N. F. Lane, Rev. Mod. Phys. **52**, 29 (1980).

[209] A. Faure, V. Kokoouline, C. H. Greene, and J. Tennyson, J. Phys. B **39**, 4261 (2006).

[210] E. Chang and A. Temkin, Phys. Rev. Lett. **23**, 399 (1969).

[211] R. Nesbet, Phys. Rev. A **19**, 551 (1979).

[212] A. R. Edmonds, *Angular Momentum in Quantum Mechanics* (Princeton University Press, 1957).

[213] Y. Itikawa, Theor. Chem. Acc. **105**, 123 (2000).

[214] G. A. Gallup, J. Phys. B **26**, 759 (1993).

[215] W. A. Isaacs and M. A. Morrison, Phys. Rev. A **53**, 4215 (1996).

[216] A. N. Feldt and M. A. Morrison, Phys. Rev. A **77**, 012726 (2008).

[217] I. Bray and A. T. Stelbovics, Adv. Atom. Mol. Phys. **35**, 209 (1995).

[218] L. S. Rodberg and R. M. Thaler, *Introduction to the Quantum Theory of Scattering* (Academic Press, New York, 1967).

[219] D. V. Fursa and I. Bray, Phys. Rev. A **52**, 1279 (1995).

[220] A. S. Kadyrov and I. Bray, Phys. Rev. A **66**, 012710 (2002).

[221] R. Utamuratov, A. S. Kadyrov, D. V. Fursa, I. Bray, and A. T. Stelbovics, J. Phys. B **43**, 125203 (2010).

[222] R. Utamuratov, A. S. Kadyrov, D. V. Fursa, M. C. Zammit, and I. Bray, Phys. Rev. A **92**, 032707 (2015).

[223] P. K. Biswas, J. S. E. Germano, and T. Frederico, J. Phys. B **35**, L409 (2002).

[224] J. T. Broad and W. P. Reinhardt, J. Phys. B **9**, 1941 (1976).

[225] H. A. Yamani and L. Fishman, J. Math. Phys. **16**, 410 (1975).

[226] H. A. Bethe and E. E. Salpeter, *Quantum Mechanics of One- and Two-Electron Atoms* (Springer, 1957).

[227] Y. Y. Qi, J. G. Wang, and R. K. Janev, Phys. Rev. A **80**, 032502 (2009).

[228] C. E. Moore, *Atomic Energy Levels as Derived from Analyses of Optical Spectra*, Circ. No. 467 Vol. 1 (Natl. Bur. Stand. (U.S.), U.S. GPO, Washington, DC, 1949).

[229] S. Kar and Y. K. Ho, Int. J. Quantum Chem. **108**, 1491 (2008).

[230] D. M. Bishop and R. W. Wetmore, Mol. Phys. **26**, 145 (1973).

[231] D. M. Bishop and R. W. Wetmore, Mol. Phys. **27**, 279 (1974).

[232] L. Wolniewicz and J. Poll, J. Mol. Spectrosc. **72**, 264 (1978).

[233] I. Bray, in *Computational Quantum Mechanics Lecture Notes* (private, 2013), chap. 7.

[234] M. Inokuti, Rev. Mod. Phys. **43**, 297 (1971).

[235] H.-K. Chung and B. J. Braams (2013), URL *https://www-amdis.iaea.org/publications/INDC/INDC_NDS-636.pdf*.

[236] Y.-K. Kim and M. Inokuti, Phys. Rev. **175**, 176 (1968).

[237] B. Peart and K. T. Dolder, J. Phys. B **5**, 1554 (1972).

[238] B. Peart and K. T. Dolder, J. Phys. B **5**, 860 (1972).

[239] E. M. Bahati, J. J. Jureta, D. S. Belic, H. Cherkani-Hassani, M. O. Abdellahi, and P. Defrance, J. Phys. B **34**, 2963 (2001).

[240] F. M. Chapman, J. Chem. Phys. **63**, 2101 (1975).

[241] K. Fedus, J. Franz, and G. P. Karwasz, Phys. Rev. A **91**, 062701 (2015).

[242] H. Wu, I. Bray, D. V. Fursa, and A. T. Stelbovics, J. Phys. B **37**, 1165 (2004).

[243] R. Moccia, J. Chem. Phys. **40**, 2164 (1964).

[244] R. Moccia, J. Chem. Phys. **40**, 2176 (1964).

[245] R. Moccia, J. Chem. Phys. **40**, 2186 (1964).

[246] D. V. Fursa and I. Bray, J. Phys. B **30**, L273 (1997).

[247] D. V. Fursa and I. Bray, J. Phys. B **30**, 5895 (1997).

[248] K. D. Winkler, D. H. Madison, and I. Bray, J. Phys. B **32**, 1987 (1999).

[249] A. Starobinets, I. Bray, L. A. Vainstein, Y. V. Ralchenko, and Y. Maron, Phys. Scr. **67**, 500 (2003).

[250] I. Bray, J. Phys. B **28**, L247 (1995).

[251] J. P. Sullivan, A. Jones, P. Caradonna, C. Makochekanwa, and S. J. Buckman, Rev. Sci. Instrum. **79**, 113105 (2008).

[252] D. A. Varshalovich, A. N. Moskalev, and V. K. Khersonskii, *Quantum theory of angular momentum* (World Scientific Pub., Philadelphia, 1988), 1st ed.